

“Devices’ application using oxides and chalcogenides nanomaterials”

A Thesis

**Submitted in partial fulfilment of the requirements for the Degree of
Doctor of Philosophy (Science)
Jadavpur University**



By

Pubali Das

Department of Physics

Jadavpur University

Kolkata-700032

India

December 2023



*Dedicated
To
My Beloved Maa & Baba*



CERTIFICATE FROM THE SUPERVISOR

This is to certify that the thesis entitled “**Devices’ application using oxides and chalcogenides nanomaterials**” submitted by **Miss Pubali Das**, who got her name registered on 13.04.2016 for the award of Ph.D. (Science) degree of Jadavpur University, is absolutely based upon her own work under supervision of **Dr. Partha Pratim Ray**, Professor, Department of Physics, Jadavpur University. It is also certified that neither this thesis nor any part of it has been submitted for either any degree or any other academic award else before.

Partha Pratim Ray
20/12/23



Dr. Partha Pratim Ray
Professor
Department of Physics
Jadavpur University



CERTIFICATE FROM THE CO-SUPERVISOR

This is to certify that the thesis entitled “**Devices’ application using oxides and chalcogenides nanomaterials**” submitted by Miss **Pubali Das**, who got her name registered on 13.04.2016 for the award of Ph.D. (Science) degree of Jadavpur University, is absolutely based upon her own work under co-supervision of **Dr. Animesh Layek**, Assistant Professor, Department of Physics, Jadavpur University. It is also certified that neither this thesis nor any part of it has been submitted for either any degree or any other academic award else before.

Animesh Layek
20.12.2013
Dr. Animesh Layek
Assistant Professor
Department of Physics
Jadavpur University
Kolkata - 700032



Acknowledgement

I'd want to take this occasion to express my deepest appreciation to everyone who has helped me with this thesis or made an indispensable contribution.

My first priority is to express my profound appreciation to my supervisor, Prof. Partha Pratim Ray, for all of the encouragement and guidance he has given me throughout my time here. For the chance to work and learn from him, I'd like to express my gratitude. He has been wonderful to me as his PhD student for the past few years. It's been a fantastic privilege and educational experience to work under his supervision.

To my co-supervisor, Dr. Animesh Layek, I am indebted for all the inspiration and help he has given me throughout the work. In any case, I appreciate his allowing me to learn from him. As his PhD student, he has guided me as an elder brother over these years. The time spent working under his guidance has been extremely rewarding and enjoyable.

I'd want to give a heartfelt shout-out to my wonderful lab mates, without whom none of this would have been possible. My deepest gratitude goes to my seniors Dr. Mrinmay Das, Dr. Joydeep Datta, Dr. Arka Dey, Dr. Rajkumar Jana and Dr. Sayantan Sil. They took me under their wing from the moment I stepped foot in the lab and showed me the ropes of conducting research. I'd want to give a shout-out to my longtime buddy and current lab partner, Mrs. Baishakhi Pal. I felt like I could have meaningful conversations with him about a range of issues. Mr. Joydeep Dhar, my another senior, has also helped me out tremendously, and I appreciate it. In addition to Mrs. Soumi Halder and Mr. Mainak Das, I'd like to thank Mr. Animesh Biswas, Mr. Dhananjay Das, Mr. Supravat Ghosh and Mr. Ramjan Sk for their hard work and dedication in the lab. We've had some amazing times together thus far. Without you guys, it would have been nearly impossible to do this research.

In my PhD tenure, I got the opportunity to work in collaboration with Dr. Chittaranjan Sinha (Jadavpur University), Dr. Souvik Chattopadhyay, Dr. Bibhuti Bhushan Shaw (Jadavpur University), Mr. Manik Shit (Jadavpur University), Dr. Mohammad Hedayetullah Mir (Alia University) and Ms. Sanobar Naaz (Alia University). It was a great working experience.

I express my sincere gratitude to the esteemed faculty members of my former physics department Prof. Pabitra Kumar Paul, Prof. Sukhen Das, Prof. Sanjay Kumar, and Dr. Kaustuv Das for their invaluable counsel and provision of numerous research resources. Although it is impracticable to list all of the acquaintances I made during my time at this university in this space, their company certainly brightened my existence. Special recognition is extended to the entire office staff for their assistance with official matters that are either directly or indirectly associated with my work.

I have no idea how to show gratitude to my parents Mr. Kamalakanta Das and Mrs. Arati Das. Without their constant encouragement, I never would have made it this far. There is nothing I can say or do that will ever be sufficient to prove their significance specially my mother. The simple dedication of this thesis is to my "maa" and "baba".

Again, words fall short of expressing how much my dearest siblings (Mrs. Sibali Das and Mr. Sovanlal Das) means to me or how much they helped me get here. My nephews (Mr. Satrajit Das and Mr. Shreyan Das) are too little to understand, but I want to tell him how much I love him anyhow. A look of their innocent face, their heavenly smile, or their silliness would instantly fill me with delight and rejuvenate my spirit at any point during these years of my studies when I felt fatigued. Thanks to my brother-in-law, Bibekananda Das and sister-in-law, Sumana Maity also. My aunt Mrs. Tripti Maity and her family also have helped me out are likewise appreciated as they granted me as one of their family members and not allow me to feel that I am away from my home.

Last but not least, I'd like to thank my bestie, Mr. Bikash Maity. Without your unwavering support, I would not have been able to persevere. A simple "thank you" would not be enough to express how much I appreciate you being there for me through all of my difficulties.

Thanks to all.

The "Department of Science and Technology (DST), Government of India" is to be thanked for funding my INSPIRE Fellowship; it is listed at the end of this section. Their funding made it possible for me to pursue my Ph.D.

Pubali Das
(Pubali Das)

Preface

The search for novel semiconductor materials and the improvement of existing ones are major research topics in the field of materials science. Because of their distinct material properties, compound semiconductor microsystems are rapidly gaining popularity for use in electronic, optoelectronic and sensing applications. These materials outperform the well-established silicon technology because of their unique properties, such as a higher saturation velocity of electrons, operation at high temperatures and frequencies, piezo-electricity, piezo-resistivity, variable thermal conductivity, direct or indirect band gap, and variation of band gap (from zero via narrow to wide).

One of the most promising nanomaterials is graphene, which consists of a single layer of graphite or carbon atoms organised in a honeycomb lattice. Graphene is also the best electrical and thermal conductor and has the world's highest strength-to-weight ratio. But having some unavoidable difficulty of use, it allows rGO (reduced graphene oxide) to make place in the field of electronics. rGO is a 2D material with strong chemical stability, carrier mobility, and a large specific surface area. So, Composite using rGO and compound semiconductor can have a huge advantage in electronic device application.

On other side, the Schottky diode is a majority carrier device, i.e., electrons in N-type material. This provides a huge performance boost over a standard diode since it is not dependent on the recombination of holes or electrons when they enter the opposite sort of area. Because of their low turn-on voltage, quick recovery time, and negligible energy loss at higher frequencies, Schottky diodes are widely utilised in electronic devices. Due to their fast switching between conducting and blocking states, Schottky diodes are able to rectify an alternating current.

Therefore, improving future semiconductor technology requires research into the use of compound semiconductor and rGO based nanocomposites on Schottky

barrier device and thorough device characterization. In addition, a thorough understanding of the metal semiconductor junction in these devices and its charge transport properties is crucial.

Therefore, the study reported in this thesis is concerned with the method of synthesis, the detailed characterization, and their application in thin film Schottky barrier diodes of various compound semiconductor and rGO based semiconducting nanocomposites. Both the charge transport and photo-response characteristics are examined in depth.

The thesis is divided in 9 chapters and a brief discussion on the content of each chapter is given below.

Chapter 1 provides a glimpse into the world of compound semiconductors and rGO nanocomposite. This chapter provides a brief description of the research on inorganic compound semiconductor, rGO and rGO nanocomposite. The unique and extraordinary properties of different semiconducting materials, rGO and rGO-nanocomposite are discussed. It also demonstrates why Schottky barriers are such an integral feature of modern electronics. The theory behind how Schottky barriers form has been outlined.

Chapter 2 describes the coprecipitation, hydrothermal/solvothermal synthesis procedure. Also, characterizations techniques and their importance in nanomaterial production is also narrated. Fabrication of sandwiched metal semiconductor junction is concisely delineated.

Chapter 3 demonstrates the outline of the whole thesis precisely.

Chapter 4 reports the hydrothermal synthesis of reduced graphene oxide–Tin dioxide composite (rGO–SnO₂) and its use in a Schottky barrier diode. Results show that combining rGO with SnO₂ nanoparticles boosts device performance. The report also show how rGO can improve device performance by illustrating the carriers' charge transfer properties. Derived diode as a photodetector is

analyzed by investigating the photosensitivity, photoresponsivity and specific detectivity.

Chapter 5 demonstrates the temperature dependent performance of the rGO-SnO₂ based Schottky barrier diode. The temperature-dependent changes in the Schottky parameters are discussed. Due to barrier height inhomogeneities at the metal-semiconductor interface, the Richardson constant value acquired from experimental measurements deviates from theoretical values, which can be explained by assuming a Gaussian distribution of the barrier heights.

Chapter 6 reports the co-precipitation and hydrothermal synthesis of Zinc Oxide (ZnO) and their changing properties depending on synthesis procedure. The study shows device application and the improvement in device performance for hydrothermally synthesized material. The charge transport properties of the carriers are also illustrated.

Chapter 7 illustrates annealing effect on hydrothermally synthesized cobalt sulfide (CoS₂). Effect of annealing temperature on device performance is also studied. Charge carrier mobility and carrier diffusion length are extracted from impedance analysis and current-voltage characteristics. Magnetic study and magnetic parameter extraction is illustrated.

Chapter 8 provides the effect of the synthesis temperature on properties of molybdenum di-selenide (MoSe₂) and Schottky performance of the individuals. Impedance analysis, ac conductivity and charge transport of the devices are also elaborated and compared.

Chapter 9 presents a brief summary and conclusion of the entire work.

All the references in this thesis are given in the following format:

Initial and surname of the authors, Journal abbreviation, Year, Volume, Page number.

Example: P. Das, B. Pal, J. Datta, M. Das, S. Sil and P. P. Ray, Journal of Physics and Chemistry of Solids, 2021, 148, 109706.

Chapter 1

An Introduction to Inorganic nano- semiconductor and Metal- Semiconductor (MS) interface

1.1. *Introduction:*

This chapter presents an overview of the physics of metal-semiconductor devices. It is a very important aspect of the extensive research on nano-semiconductors and MS devices that has been published to date. The physical and chemical properties of semiconductor materials inevitably influence the performance of semiconductor devices. This also includes topics that are directly related to the fabrication and operation of MS device.

In last few decades, compound semiconductors, have attracted great attention as they are inexpensive and can easily be processed by varying synthesis conditions. Functionality of the materials can be controlled by tailoring molecular design and chemical synthesis. Their band gap, absorption and electrical conductivity can be varied by changing the particle sizes. Properties related to device application can be tuned by varying their nanomorphology.

Most compound semiconductors of different structure that enables piezoelectricity, opening up exciting possibilities for use in sensing [1, 2, 3, 4]. Compound semiconductors with other different structure have also been used as gas sensor [5, 6], as ohmic contacts [7] in power devices [8, 9, 10], in electronic and optoelectronic devices [11, 12], for energy conversion, energy storage and electrocatalysis [13, 14] including solar cells [15, 16, 17], various junction based electronic devices like FET, MOSFET [18, 19, 20, 21] etc.

1.2. *World of semiconductor:*

A solid substance whose conductivity (from 10^{-6} to $10^4 \text{ ohm}^{-1} \text{ m}^{-1}$) lies between that of an insulator and that of metals, is generally called as a semiconductor. It is a material with specific electrical properties that allow it to serve as the basis for different electronic devices. When the carriers within a

semiconductor are depleted, a charge density is left behind, as a result generation of an electric field and sometimes a barrier potential is occurred.

Experiments on the electrical characteristics of materials lay the groundwork for the development of semiconductor knowledge. As early as the 19th century, researchers were able to observe the time-temperature coefficient of resistance, rectification, and light-sensitivity features. In 1821, Thomas Johann Seebeck discovered the first effect caused by semiconductors. In 1874, Karl Ferdinand Braun fabricated the first semiconductor device, the crystal detector. In the second part of the twentieth century, significant advances in electronics have had a profound impact on our way of life and culture. The integrated circuit (IC), made primarily of element semiconductor is a key component in this development.

Element semiconductors, like silicon (Si) and germanium (Ge) before it (Ge served as a precursor to Si as the first transistor material), are composed of a single element. Elemental semiconductors include antimony (Sb), arsenic (As), boron (B), carbon (C), selenium (Se), sulphur (S) and tellurium (Te). The most famous of these is undoubtedly silicon because of the following reasons-

- a) Due to the utilization of well-established processing procedures, the expenses are relatively low.
- b) The market for crystalline Silicon (Si) is enormous.
- c) It is quite effective.
- d) Large wafers may be handled safely and damage-free because to their hardness.

The semiconducting materials can be classified into two main categories-

(i) Intrinsic and (ii) Extrinsic type.

Pure semiconductors, also known as intrinsic semiconductors, lack any trace of impurities or doping. A sufficient amount of impurity is added to these

semiconductors to create extrinsic semiconductors. Intrinsic semiconductors include silicon and germanium, while there are doped with additional elements such as aluminium (Al), indium (In), phosphorus (P), arsenic (As), etc. called extrinsic.

In materials science, the quest for novel semiconductors and the upgrading of current semiconductors are a crucial area of study. From the years ago silicon is an eminent material as a semiconductor in the field of electronics. With a lot of advantages, it has some unavoidable drawbacks like cost, brittleness and short life cycles. To overcome these problems a bunch of different compound semiconductors have been discovered and yet to discover.

Compound semiconductors are the materials with semiconducting properties that are made using more than one elemental material. They are generated from the ionic bonding of various semiconductor types. Ionic bonded materials are insulators because of the high electrostatic interaction between the ions. When combined with a specific set of anions and cations, their mild electrostatic force of attraction transforms them into semiconductors. There have been several advancements in the development and commercialization of compound semiconductors and compound semiconductor devices in the past. These compound semiconductors, like III-V, II-VI, and IV-IV, are categorised according to the group number of the elements that make them up in the periodic table. Widely known III-V compound semiconductors are GaAs (Gallium Arsenide), InP (Indium Phosphate), GaN (Gallium Nitride), and AlN (Aluminium Nitride). Well-known II-VI and IV-IV semiconductors are ZnSe (Zinc Selenide), ZnS (Zinc Sulphide), CaTe (Calcium Telluride), and SiC (Silicon Carbide), SiGe (Silicon-Germanium), respectively.

Compound semiconductors are primarily of three types. They are inorganic, organic and hybrid (mixture of inorganic and organic compound) semiconductor respectively. Mostly used compound semiconductor materials are inorganic solids with crystalline structure in nature. There are two types of

semiconductors for both extrinsic semiconductor and compound semiconductor. One is known as n type and the other one is p type. They are named with respect to their majority carrier. Electrons play role as majority carrier for n-type where holes take the responsibility for p-type. The electron vacancy in a material creates a hole. Using the polarity of the Hall voltage, a semiconductor type can be determined. Hot probe method can also be used for the same.

Variation of semiconductor materials lead to a prominent variation in their properties. Rather than greatly used silicon, compound semiconductors come with some advantages. They provide a faster operational speed regarding higher electron mobility [22, 23], a successful generation of high frequency signal like microwave signal [24, 25], and where required can operate in a low voltage as necessary for lighter and longer lasting, low voltage batteries used for different portable devices. [26, 27]. Besides light emission properties (visible as well as infrared light, used in lasers and LEDs) [28, 29, 30], they are also sensitive to light (used for photodetectors application) [31] and magnetism (useful in sensor applications) [32, 33, 34]. Including all of above they are resistant to heat and radiation for which they are also useful in space applications, such as solar cells for satellites [35, 36]. Type of band gap i.e., direct or indirect band gap, variation of band gap from zero via narrow up to wide band gap [37, 38, 39, 40], piezoelectricity [41, 42, 43], piezo-resistivity [44, 45], variation in their thermal conductivity, higher saturation velocity of conductive electrons, operation possibility at higher temperature and frequencies, [46, 47] and so on are just a few of the inherent properties of these materials that set them apart from the well-developed silicon technology.

This chapter emphasizes on the types of important inorganic compound semiconductor materials and physics behind the generation of metal-semiconductor junction.

The metal oxide semiconductors are first one to discuss about.

1.2.1. *Metal Oxide Semiconductors:*

Metal oxides are crystalline solids composed of metal cation and oxygen anion. In terms of their designing concepts, electronic structure, mechanisms attributed to charge transport, different defect states, processing of their thin-film, and various optoelectronic properties, metal oxide semiconductors are notably distinct from typical semiconductors such as silicon and Germanium, facilitating entirely new functions with conventional. Recent developments in metal oxide semiconductors for electronics include the invention and characterization of all new transparent conducting oxides [48, 49], the understanding of p-type as well as formal n-type metal oxide semiconductors for transistors [50, 51, 52, 53], p–n junctions [54, 55], MS (metal-semiconductor) junctions [56], and complementary circuits, formulations for printing metal oxide electronics, and, most importantly, an initial alternating electrode material for photovoltaic devices [57, 58].

Metal oxide semiconductors are two types according to their chemical properties- (i) Basic Oxides and (ii) Amphoteric Oxides. Sodium Oxide (Na_2O), Calcium Oxide (CaO), Barium Oxide (BaO) are few examples of basic oxides, where Gallium Oxide (Ga_2O_3), Aluminium Oxide (Al_2O_3), Zinc Oxide (ZnO), Tin (IV) Oxide (SnO_2) etc. are belongs to the category of Amphoteric Oxides based semiconductor. In consonance with occurrence of major and minor carriers, they are divided as (a) n-type and (b) p-type.

Various characteristics of two n-type amphoteric oxides SnO_2 and ZnO are discussed here with, which are taken under investigations.

1.2.1 (a) *Tin (IV) Oxide (SnO_2):*

Tin (IV) oxide, also named as stannic oxide, is a chemically stable metal oxide compound with the chemical formula SnO_2 . Stannic oxide forms crystals with rutile structure. The Tin atoms have six coordinates and oxygen atoms have three.

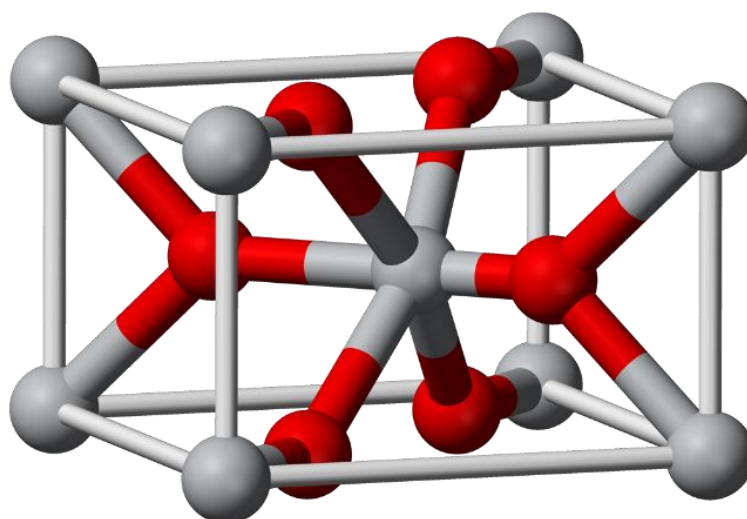


Figure 1.1: Rutile structure of SnO_2 [Gray Tin Red Oxygen, adapted from wikipedia]

It is an n-type wide band gap semiconducting material with a direct-bandgap about 3.6 eV [59, 60] for bulk. SnO_2 has reported a bulk carrier mobility nearly $240 \text{ cm}^2 \text{ V}^{-1}\text{s}^{-1}$ [61] which is much higher than the mobility of many metal oxide semiconductors such as Titanium Oxide, Cupric Oxide, Cobalt oxide etc. It has various applications in industrial polishes, glass and ceramic coatings, a broad range of construction materials, lithium-ion batteries and gas sensor devices [62, 63].

1.2.1 (b) *Zinc Oxide (ZnO):*

Zinc Oxide is a chemically stable metal oxide compound with the chemical formula ZnO , is another n-type metal oxide semiconductor with a tetrahedral configuration of bonding. In this type of bonding configuration an anion is bounded with four cations at the corners of a tetrahedron acquiring the sp^3 covalent bonding. There are two primary crystallization forms of Zinc Oxide: hexagonal wurtzite and cubic zincblende.

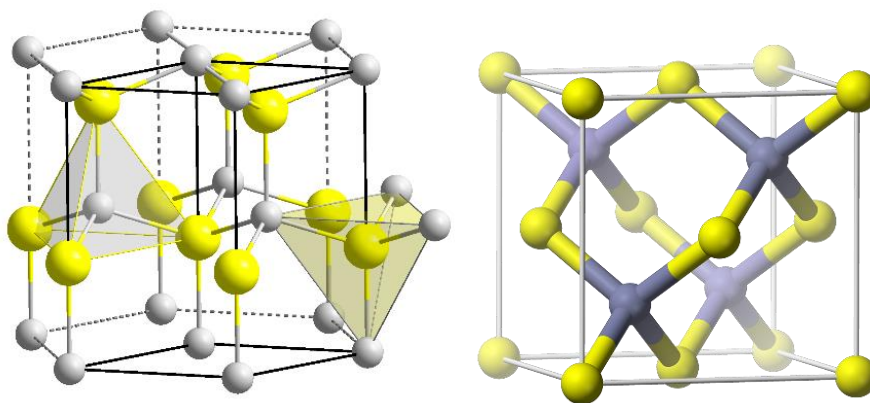


Figure 1.2: (a) Hexagonal wurtzite and (b) Cubic zinc blende Structure [adapted from wikipedia]

As an important compound, it can be called a multifunctional material due to its unique chemical, physical, electrical and optical absorption properties. The material has a wide direct band gap (about 3.3 eV) and a high exciton binding energy (60 meV) [64]. Positive characteristics of zinc oxide like high electron mobility, strong luminescence at room temperature make it valuable for a number of emerging applications, including transparent electrodes in liquid crystal displays, gas sensing, energy-efficient or heat-resistant windows, and light-emitting diodes in electronics [65, 66].

In similar way another two inorganic compound semiconductor CoS_2 and MoSe_2 , of metal chalcogenides group, are used in my experimental work, are discussed below.

1.2.2. *Metal Chalcogenides:*

Metal chalcogenides are another type of inorganic chemical compound consist of at least one chalcogen anion and at least one more electropositive (called cation) metal element. While oxides and polonium compounds also belong to the VIA group, sulphides, selenides, and tellurides are most commonly referred to as metal chalcogenides. This is because the metallic nature of the elements rises as the Periodic Table's VIA group goes down [67]. Thus, oxygen's

extremely strong non-metallic qualities and Polonium's (Po) strong metallic properties distinguish them from the other three members (S, Se, Te) of the group. Therefore, the chalcogenide class may be described as semimetal. There are numerous metal chalcogenides with various structures and chemical compositions. Due to their potential utility in numerous technological applications, metal chalcogenides have emerged as a significant class of materials. Metal chalcogenides are a diverse class of 2D materials that naturally avoid graphene's gapless nature. The diverse composition, tuneable crystal structure and unique morphology enrich them with exceptional physical, chemical, electronic and optical properties. These differences make them favourable for a variety of applications, as for field of electronics/optoelectronics, catalysis, in energy storage devices and for energy conversion, in different type of sensors, in biomedicine, and water remediation [68, 69, 70].

1.2.2. (a) *Cobalt di-sulphide (CoS₂)*:

In recent years, Cobalt di-sulphide of chemical formula CoS₂, a metal chalcogenide with pyrite structure has greatly noticed due to its efficient application in catalysis, as semiconductor, and magnetic materials, in lithium-ion batteries, and many more fields [71]. It is known that CoS₂ possesses higher electrical conductivity about $6.7 \times 10^5 \text{ Sm}^{-1}$ [72] and thermal stability compared to other metal sulphides. The wide range of tuneable direct band gap of 2.76 eV [73] for the material indicates that it can be used in the fabrication of optical and photonic devices also [74].

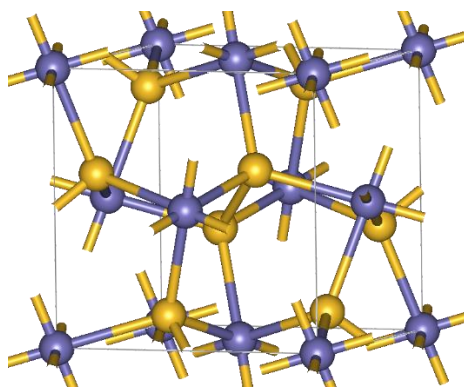


Figure 1.3: Pyrite structure [adapted from wikipedia]

1.2.2. (b) *Molybdenum di-selenide (MoSe₂)*:

Molybdenum di-selenide (MoSe₂), a metal chalcogenide with a variety of promising applications in electrochemical, photocatalytic, and optoelectronic systems, is another interesting member of this family. This is because it has several benefits over other metal chalcogenides, including the popular molybdenum disulfide (MoS₂). The ability of MoSe₂ to host counterions in electrochemical energy storage systems like lithium-ion and sodium-ion batteries arises from the combination of its layered structure with Se's size and electrical conductivity [75]. The metal ion in these compounds is surrounded by six Se²⁻ ions. The electron mobility 50 cm² V⁻¹ s⁻¹ [76] of MoSe₂ is significantly higher. MoSe₂ has a direct band gap of 1.6 eV [77], suggesting applications in different electronic devices [78].

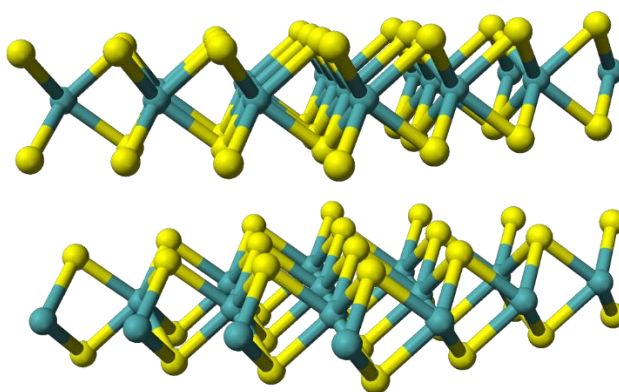


Figure 1.4: Molybdenum di-selenide (a) monolayer (b) multilayer structure [adapted from wikipedia]

To improve the overall device performance making of semiconductor, several attempts of making composite of the preferred semiconductor with graphene is becoming a great area of interest from the day of its revealing. Khan et al. (2015) conducted a comprehensive study of graphene-based metal and metal oxide nanocomposites, discussing their synthesis, characteristics, and applications. Both top-down and bottom-up approaches were used in the various preparations [79]. There is a lot of room for growth in the electronics, electrochemical, and electrical domains for graphene-based inorganic nanocomposites. Three-dimensional graphene-based composites were synthesised and used in various applications, as reported in 2016 by Shi et al. [80]. They talked mostly about how to make them and how they can be used as electrode materials for energy storage and conversion. Simultaneously, Pham et al. summarised the use of hybrid graphene-semiconductor quantum dot photovoltaics and photodetectors [81]. But then again, the question is...

1.3. What is graphene?

Graphene is a two-dimensional (2D) material which is basically a monolayer of carbon atoms. In this material the carbon atoms are ordered such that a hexagonal honeycomb lattice is formed. It is a different form of carbon in which a plane of sp^2 -bonded atoms exists having an inter-molecular bond length about 0.142 nanometres [82]. Compounds with thin layers of graphite were reduced and burned to create soot by Boehm and colleagues. Having only one carbon layer, these items were given the term "graphene platelets" in 1944. It was first exfoliated from graphite by Andre Geim and Konstantin Novoselov in 2004. Graphene's exceptional physicochemical characteristics set it apart from other materials. These characteristics include a huge surface area ($2630 \text{ m}^2/\text{g}$), high tensile strength, outstanding thermal conductivity, and rapid electron transport

[83, 84, 85]. There's no denying that graphene has been at the forefront of materials science for a number of years, and that trend shows no signs of abating.

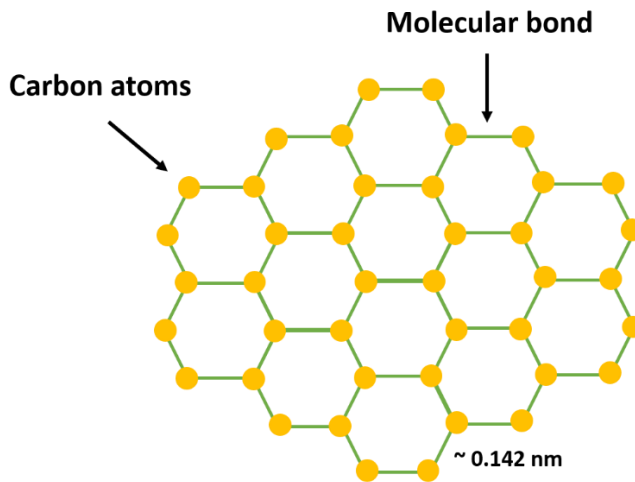


Figure 1.5: Schematic image of graphene

1.3.1. Hurdles in using pristine graphene:

Current graphene production methods, both top-down and bottom-up, are costly, energy- and resource-intensive, and produce too little material, too slowly. As an excellent electrical conductor, graphene cannot be turned off. In this concern my research work has been performed with reduced Graphene Oxide.

1.3.2. Advantage of reduced graphene oxide (rGO):

Reduced Graphene Oxide (rGO) is less expensive and simpler to produce than graphene although it shows graphene-like behaviour; therefore, it may enter mass production and use sooner. Because of its heterogeneous structure, which consists of a graphene-like basal plane adorned with structural flaws and inhabited with patches containing oxidised chemical groups, it shares the same mechanical, optoelectronic, or conductive capabilities as pure graphene. Also, rGO can be readily combined with various polymers and other materials to improve the tensile strength, elasticity, conductivity, and other properties of composite materials [86, 87, 88, 89].

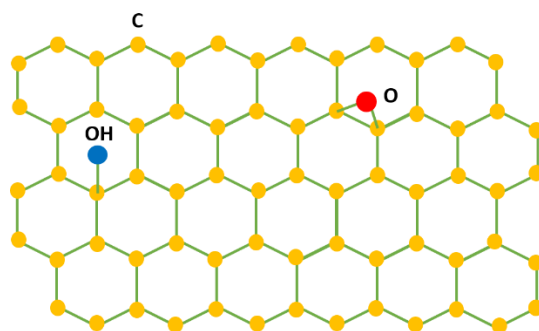


Figure 1.6: Schematic image of rGO

1.3.3. Synthesis of Reduced Graphene Oxide:

The reduction of graphene oxide (GO) is considered to be an attractive route to obtain reduced graphene oxide. GO can be prepared through the exfoliation of graphite powder as suggested in modified Hummer's method [90] and proceeding a reduction with hydrazine hydrate (reducing agent) to produce rGO. Thermal reduction of GO can also be adapted using high temperature (350°C) treatment [91]. Other procedures for reduction of GO are UV irradiation and microwave assisted method [92].

1.3.4. rGO-nanocomposite with inorganic semiconductors:

Typically composites of reduced graphene oxide (rGO) and other materials, including metals and metal oxides, have been prepared using a variety of methods. upon combining graphene nanosheet with some inorganic semiconductors, the zero-gap shortcomings could be significantly reduced or eliminated. rGO can be patterned with size constrictions to create an electronic band gap. Many inorganic semiconductors have been reported as compatible to form composites with graphene but the compatibility of these materials with graphene depends upon the synthesis procedure of graphene. It has significant effect on charge transport properties of the composite materials. Typically, in an inorganic semiconductor, charge carriers are activated under light irradiation [93, 94, 95]. The ensuing electronic interactions between graphene and the

semiconductor will facilitate efficient charge separation and transportation [96, 97, 98]. In the composite graphene works as the electron conductor which inhibit fast recombination of electron and holes. P. Wang, J. Wang and others has reported enhanced photocatalytic activity of TiO_2 after rGO addition [99]. K Wang, X Dong and authors has reported superior cyclability in supercapacitor made of rGO nanocomposite [100]. M. Azarang, A. Shuhaimi also reported about improvement in photocurrent due to rGO addition [101]. The enhanced field emission behaviour also observed for the rGO nanocomposite [102].

In this art of work, a nanocomposite of SnO_2 along with rGO is used as exploring material.

1.3.4.1. *rGO/SnO₂ nanocomposite:*

Several articles on the production and use of SnO_2 -rGO nanocomposites have been published to date. There are lots of reported paper on different applications of the SnO_2 /rGO heterostructure like gas sensing performance [103, 104], photocatalytic capabilities [105], Lithium-ion batteries [106, 107], Medical science [108] etc. In my experimental endeavour SnO_2 composited with rGO which results improvement in adsorption.

1.4. *Nanomaterial/Nanocrystal:*

In recent past nanomaterials have attracted a huge attention mainly because of the property tuning, that is not possible in bulk materials and there is a possible appearance of quantum effects at the nanoscale. Nanotechnology was first proposed in 1959 by Richard Feynman, an American physicist and Nobel laureate. Feynman delivered a talk titled "There's Plenty of Room at the Bottom" at Caltech for the American Physical Society meeting. In 1974, fifteen years after initial proposal, Japanese scientist Norio Taniguchi used the term as "nanotechnology" and defined it as "the processing of separation, consolidation,

and deformation of materials by one atom or one molecule." [109]. Many benefits of nanomaterials over bulk materials stem from their many unique physical and chemical characteristics, including their extremely high surface-to-volume ratio, extreme porosity, and unusual chemistry. Their small size makes them ideal for use in electronics, and they can also be put to use in the removal of harmful substances from the environment by binding to them. Nanocrystals possess also unique optical, electrical, and magnetic properties that cannot be found in their bulk counterparts. They are more conductive than their larger-scale (called bulk) counterparts.

A crystal is distinguished by its well-structured, periodic arrangement of atoms. A nanocrystal is a microscopic particle comprised primarily of crystalline components and with at least one dimension smaller than 1000 nano-meters exhibiting novel nanoscale physical and chemical characteristics. Nano-powder is just one form of nanomaterial; others include nanofilaments, nanotubes, nanowires, nanocables, nano-thin film, dendrimers, quantum dots, composite materials, and many more [110]. Most of the nano-dynamics are governed by the understanding of terms: crystallites, grain and particle.

1.4.1. *Crystallite, Grain and particle:*

Crystallite is the smallest - most likely single crystal in powder form. Grain refers to the volume of a material within which the crystal structure and the orientation of the crystal is same. A grain can be formed with a single crystallite or a bunch of crystallites. A particle may have one or more grains within it.

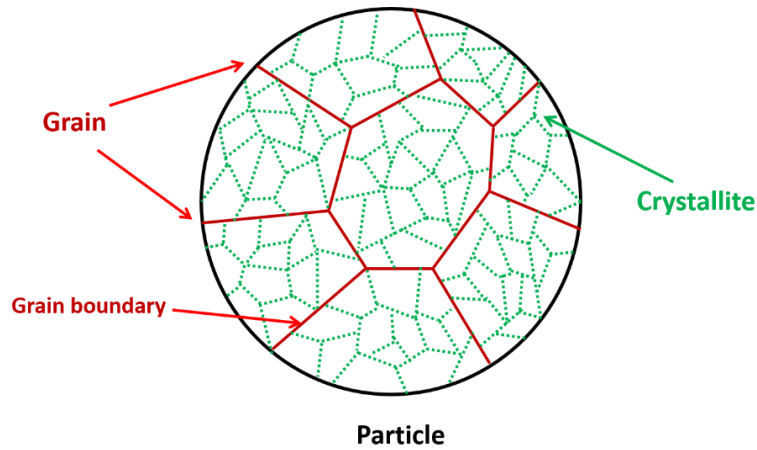


Figure 1.7: Schematic diagram of a particle

1.4.2. *Size and shape of nanomaterials:*

Nanomaterials can be divided into four distinct groups based on their size and shape: (1) zero-dimensional (0D) clusters and particles, (2) 1D nanotubes and nanowires, (3) 2D nanoplates and layers, and (4) 3D bundles of nanowires, nanotubes, and multi-nanolayers [111]. They come in a wide variety of shapes and sizes, including spherical, tubular, ellipsoidal, and irregular, and can exist singly, fused, aggregated, or agglomerated.

1.4.2. (a) *Zero-dimensional nanomaterial:*

In the context of nanotechnology, spheres of nanoparticles are the universal symbol for 0D nanomaterials. Nanoscale cubic and polygonal shapes are also included in this category. Amorphous, single-crystalline, and polycrystalline forms are all possible. This category encompasses all nano-sized uniform materials, including molecules, different clusters, fullerene and fullerene like structures, rings, particles, and grains. Examples of this category include nanoparticles of metals like silver and gold nanoparticles, quantum dots having uniform arrays of particles or with core-shell, heterogeneous particle arrays, hollow spheres, and nano-lenses [112, 113, 114, 115]. They come in a wide variety of ceramic and polymeric materials, shapes, and sizes.

1.4.2. (b) *One-dimensional nanomaterial:*

Needle-like in appearance, 1D nanomaterials are nanometer-sized in two dimensions but much longer in the third (>100 nm). Most 1D nanomaterials can be categorised as either carbon nanotubes (CNT), metal or metal oxide nanowires, nanowires or nanofibers nanowires or nanofibers with polymeric structure, or a hybrid material [114, 115, 116]. The high-aspect-ratio structural feature of 1D nanomaterials, combined with their exceptional mechanical, electrical, and optical capabilities, gives these materials a distinct edge.

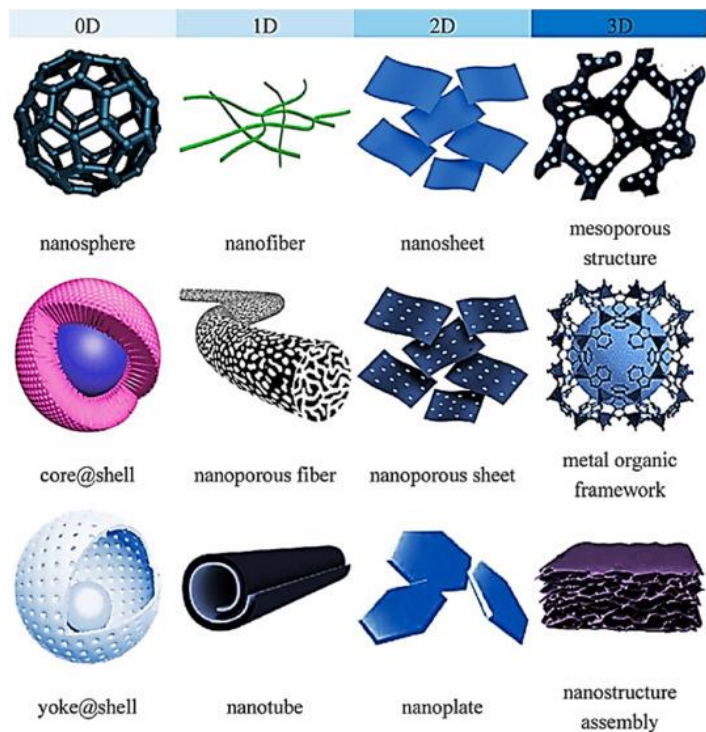


Figure 1.8: Different nanocrystal structure [reference no:111]

1.4.2. (c) *Two-dimensional nanomaterial:*

The dimensions of two-dimensional (2D) nanomaterials, which are typically atomically thin sheets, are not limited to the nanoscale. Two-dimensional nanomaterials typically take the form of nanofilms, nanolayers, or nano-coatings due to their flat, plate-like structures.

Graphene, a single carbon layer in the honeycomb structure of graphite, is the most recent member of this class [114, 115].

1.4.2. (d) *Three-dimensional nanomaterial:*

Nanomaterials that extend into the third dimension are said to be 3D nanomaterials. They have three dimensions over 100 nm that are completely arbitrary. On the other hand, 3D nanomaterials involve a nanocrystalline structure or nanoscale characteristics [115, 117]. Bulk nanomaterials can have a nanocrystalline structure that consists of a variety of configurations of nano-size crystals with varying orientations. 3D nanomaterials can include a wide variety of nanoscale properties, including nanoparticle dispersions, nanowire and nanotube bundles, and multi-nanolayer structures.

As the main objective of this chapter is to illustrate the understanding of the behaviour of metal-semiconductor junction, consequently there should have some discussion on following topics in vivid manner.

1.5. *Different Junction formation:*

Wherever two or more conductors or semiconductors come together, electrical junctions form. Primarily junctions can be classified by (1) Metal-Metal, (2) Semiconductor-Semiconductor and (3) Metal-Semiconductor.

In solid-state physics, a metal–metal (M–M) junction is a type of electrical junction in which a metal with a certain work function (ϕ_{m1}) comes in close contact with another metal of different work function (ϕ_{m2}). An electric double layer with opposite charges is risen in this type of junction. At equilibrium a contact potential is developed which is simply the difference between two work functions. Peltier effect and Seebeck effect are important effects correspond to M-M junction. Additional heat generation in M-M junction has made it also called as thermoelectric junction.

A Semiconductor-Semiconductor (S-S) junction is a semiconductor interface that occurs between layers of similar semiconductor with different doping or different semiconductors. As define above, there is clearly two types of S-S junctions (i) Homojunctions and (ii) Heterojunctions. A homojunction arise between layers of same semiconductor having different doping (i.e., type of doping or concentration of doping or both). The junction between two layers or regions of different semiconductors is called a heterojunction. A depletion layer is found in every S-S junction.

The rest is metal-semiconductor junction which is the important part of my research methodology, is elaborated accordingly.

1.5.1. *Metal Semiconductor Interface:*

A metal-semiconductor (M-S) junction is a specific form of electrical junction that occurs when a metal and a semiconductor are in physical contact with one another. As far as known, this is the first ever semiconductor device. Metal-semiconductor (M-S) junctions can behave as either Schottky contacts (rectifying) or as Ohmic contacts (non-rectifying), depending on the interface properties. Interfaces between metal and semiconductor may be found almost everywhere in contemporary electronics. Current can flow in both directions between the metal and the semiconductor through an Ohmic contact, which is a low-resistance junction that does not undergo rectification. Theoretically, the relationship between the applied voltage and the resulting current should be linear with instantaneous reaction to even the smallest voltage. Ohmic contacts come in two varieties: The ideal nonrectifying barriers and the tunnelling barriers. After reaching thermal equilibrium, electrons will begin to flow from the metal into the lower energy levels of the semiconductor in ideal nonrectifying barrier kind of contacts. If a positive bias was provided to the metal portion, these electrons would flow back into the metal portion unimpeded. When a negative bias is applied, electrons are pushed from the metal into the semiconductor despite the

low barrier they encounter. However, the tunnelling probability through the barrier is enhanced by increasing the doping concentration in a semiconductor, which reduces the depletion zone.

1.5.1.1. Schottky Barrier Diode (SBD):

A metal-semiconductor diode having a small forward voltage drop and quick switching action, called the Schottky diode, goes by a few other names as well like hot carrier diode or low voltage diode. Because of its ability to prevent current from flowing in the opposite direction, the Schottky diode is often utilized as discharge protection and called blocking diode.

1.5.1.2. History of SBD:

Braun, who in 1874 observed how the total resistance of a point contact depends on the polarity of the applied voltage and on the particular surface characteristics [118], is generally credited as conducting the first systematic examination into metal semiconductor rectifying devices. Beginning in 1904 [119], J. C. Bose and others put the point contact rectifier to use in a variety of contexts. Wilson developed the semiconductor transport theory in 1931 [120] using concepts from the solid-state band theory. The concept is then used to explain the behaviour of metal-semiconductor interactions. Without a chemical layer, Walter H. Schottky hypothesised in 1938 that the potential barrier may be generated by stable space charges in the semiconductor itself [121]. The Schottky barrier model is based on this thinking. Mott also created the Mott barrier, a more accurate theoretical model for swept-out metal-semiconductor interactions, in the same year [122]. Bethe refined these models further in 1942 to create the thermionic emission model, which successfully captures the electrical behaviour of metal semiconductor contacts [123]. Bardeen [124] proposed in 1947 that the barrier height of a covalent semiconductor may be fixed by pinning it at the Fermi level. This theory is useful in many real-world examples because it explains why

the barrier heights of Schottky diodes were not always governed by the variations in the metal semiconductors' work functions. The tunnelling process of the carriers, known as field emission, was first described by Conley et al. [125] and Stratton [126] in the early 1960s. The tunnelling process of thermally excited carriers lifting the barrier was later considered by Padovani and Stratton, Crowell and Rideout, and Chang and Sze [127, 128, 129]. Finally, Crowell and Sze integrated Schottky's diffusion theory with Bethe's thermionic emission theory to establish a single thermionic diffusion model [130].

1.5.1.3. *Applications of Schottky diode:*

Schottky diodes are the favoured rectifying devices for use in circuit applications demanding high current and low voltage [131]. Schottky diodes can be used as quick switches in digital logic systems [132, 133, 134]. In optical communications and optical measurements, high-speed Schottky photodiodes are used [135, 136]. Low-cost solar cells based on Schottky junction technology are also in use [137, 138]. In addition, metal-semiconductor contacts play crucial roles in many electronic devices, including as field-effect transistor gate electrodes, MOSFET drain and source contacts, IMPATT oscillator electrodes, and the third terminal in a transferred-electron device [139, 140, 141, 142, 143, 144, 145].

1.5.1.4. *Advantages of Schottky diode:*

Because of their low capacitance and status as majority carrier devices, junction-based devices benefit greatly from rapid switching times. When switching from the conducting to the nonconducting state, Schottky diodes have an extremely fast reverse recovery time. The reversal of current in a p-n junction takes 5–100 ns. In comparison, Schottky diodes often flip on and off in less than 1 nanosecond. Also, its fast-switching speed doesn't allow the diode to reach saturation, which makes the Schottky diode useful for high-frequencies and

digital applications. Low forward voltage drop is another useful property of a Schottky device. In contrast to a p-n junction, the barrier height in a Schottky diode can be adjusted throughout the design process. The Schottky junction has this benefit over the p-n junction as well.

The transport behaviour within this junction-based device is ruled by the energy band and the Fermi energy level.

1.5.1.5. *Fermi level:*

The Fermi Level is the point of highest energy that an electron can have at zero Temperature. Probability of electron occupancy at various energy levels is defined by the Fermi level. It is easier for valence electrons to move into the conduction band if the Fermi level gets closer to the energy of conduction band.

In conductors, the Fermi level is located in the conduction band, in insulators in the valence band, and in semiconductors in the band gap between conduction and valence band.

1.5.1.6. *Dynamics of Schottky interface:*

Occurrence of rectifying contact in metal semiconductor junction depends on the position of Fermi level in both metal and semiconductor, and the type of semiconductor (n-type or p-type). The work function of any material is determined by the energy required to shift an electron from Fermi level (E_F) to vacuum level (E_0) or simply the net energy difference between the Fermi level and the vacuum level. The work function is different for various metal and semiconductor. If the work function of the n-type semiconductor (ϕ_s) is less than the metal work function (ϕ_m) i.e., if $\phi_s < \phi_m$ then the contact would be rectifying in nature. And for the p-type they should satisfy the condition $\phi_s > \phi_m$.

1.5.1.7. Conduction mechanism with band theory:

Energy band diagram concept is used to understand the current conduction mechanism of Schottky barrier. **Figure 1.9** shows the ideal band diagram of n-type semiconductor and metal having work function ϕ_s and ϕ_m respectively, before and after close contact. At the metal-semiconductor (M-S) interface, a potential barrier will be formed when the metal makes intimate contact with the semiconductor. The potential barrier is caused by the separation of charges at the metal-semiconductor interface, which results in the formation of a mobile-carrier-depleted, high-resistance region in the semiconductor. Schottky and Mott introduced the first model to explain the height of the barrier. **Figure 1.9(a)** clearly shows that work function of metal is higher than semiconductor, where vacuum level is considered as reference level. Although the work function of a semiconducting material is a variable quantity as the position of Fermi level in the semiconductor varies with doping, doping has no effect on a semiconductor's electron affinity. Typically, the work functions and electron affinities are in electron volt (eV).

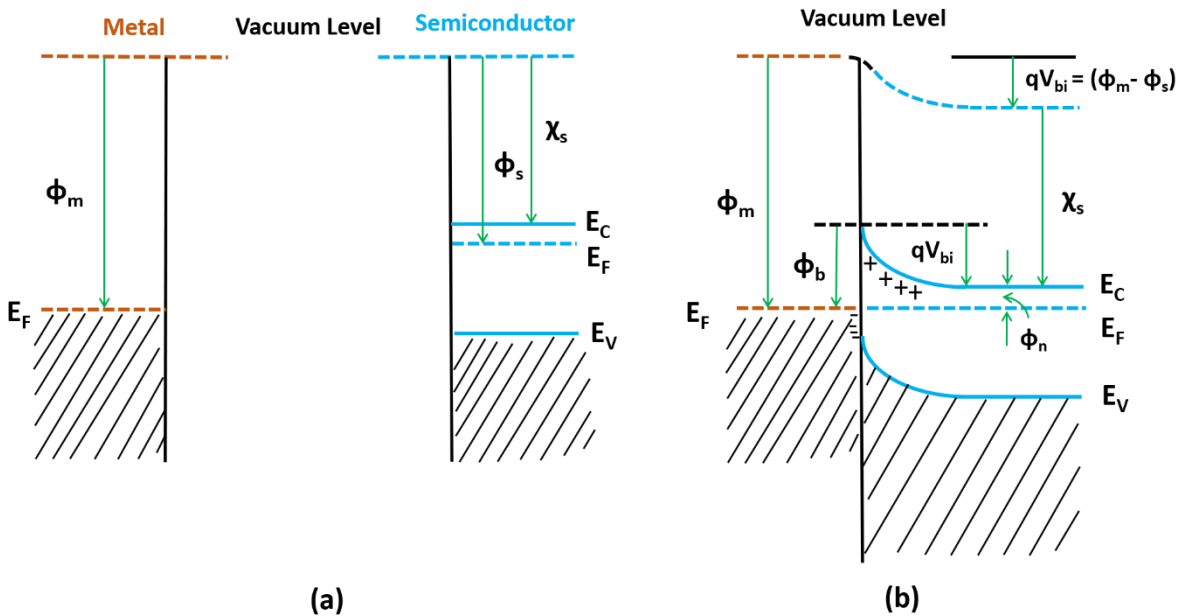


Figure 1.9: Electron energy band diagrams of metal contact to n-type semiconductor with $\phi_m > \phi_s$ (a) Neutral materials separated from each other and (b) thermal equilibrium situation after the contact has been made

After intimate contact in thermal equilibrium (**Figure 1.9b**), the higher-energy electrons from the semiconductor's conduction band (CB) flow into the lower-energy metal. This exchange will continue until both sides' Fermi levels are equalised. As electrons leave the semiconductor and enter the metal on the other side of the border, the concentration of free electrons in the semiconductor zone declines. The gap between the conduction band edge E_C and the Fermi level E_F widens as the electron density falls. **Figure 1.9(b)** depicts the upward bending of the CB edge as a result of the constant Fermi level at thermal equilibrium. The semiconductor region next to the metal loses mobile electrons as a result of the CB electrons, crossing over to the metal and a positive charge of ionised donors is left behind. Hence, the semiconductor side of the interface takes on a positive charge and a tiny layer of negative charge forms on the metal side. This leads to a rise of semiconductor-to-metal electric field. Since the semiconductor's band gap is unaffected by metal contact, the VB edge E_V shifts upward in tandem with E_C . Since the semiconductor's electron affinity is not variable, the vacuum level tracks changes in the same way as conduction energy level at semiconductor side. In order to maintain uniformity, this vacuum eventually approaches the vacuum level of metal side. Therefore, the difference between the two vacuum levels corresponding to metal and semiconductor side is equivalent to the difference between the work functions of two, and so the amount of band bending is simply equal to this difference. The value of this difference is given by $qV_{bi} = (\phi_m - \phi_s)$ where V_{bi} represents contact potential difference, also known as built in potential of the junction and is expressed in Volt. A semiconductor electron entering a metal must, of course, overcome this potential barrier. However, looking through the metal into the semiconductor results in a different barrier, which is given by

$$\phi_b^e = \phi_m - \chi_s \quad (1.1)$$

From figure,

$$\phi_s = \chi_s + \phi_n \quad (1.2)$$

So,

$$\phi_b^e = qV_{bi} + \phi_n \quad (1.3)$$

Where $\phi_n = (E_C - E_F)$ and q is the electronic charge.

Equation (1.1) was stated by Schottky and independently by Mott.

In a state of equilibrium, no net current flows because the rate at which electrons cross the barrier from the metal into the semiconductor is equal to the rate at which electrons cross the barrier from the semiconductor into the metal.

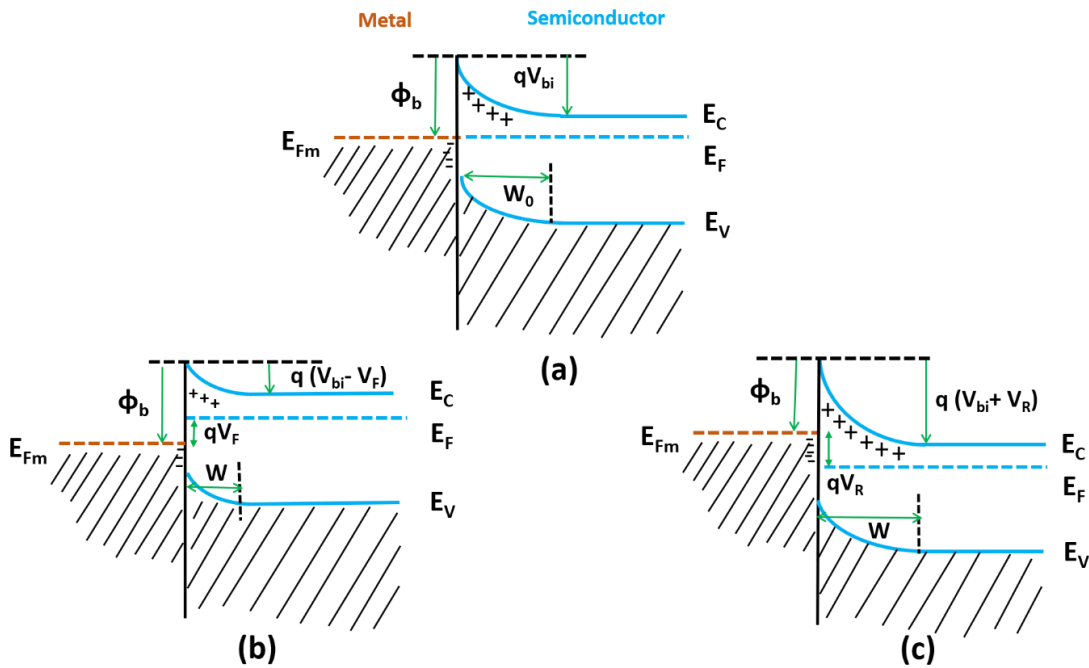


Figure 1.10: Electron energy band diagrams of rectifying metal contact on n-type semiconductor. (a) Thermal equilibrium situation; (b) forward bias; and (c) reverse bias

When the metal is biased positive against the semiconductor by a voltage of V_F , the width of the depletion region at MS interface decreases leading a reduction of the voltage across this region from V_{bi} to $(V_{bi} - V_F)$ [**Figure 1.10(b)**]. Since the barrier for semiconductor-side electrons has been lowered, more electrons can move from the semiconductor to the metal than they could during thermal equilibrium. However, this bias voltage does not affect ϕ_b . This means that the equilibrium level of electron flow from the metal to the semiconductor remains constant. With a negative bias, electrons will flow from the

semiconductor into the metal, creating a current that will flow from the metal into the semiconductor. The junction is then said to be forward biased. As voltage V_F is raised, the forward current rises exponentially.

The potential drop across the depletion area grows to $(V_{bi} + V_R)$ when the semiconductor is positively biased with respect to the metal by a voltage $V = -V_R$. Therefore, the equilibrium value of the electron flow from the semiconductor towards the metal is dropped below, but the electron flow from the metal side is unaffected. This triggers a reversal in the direction of the current flow, from the semiconductor to the metal. When compared to the forward current, this current is obviously negligible. This means the MS contact acts like a rectification junction.

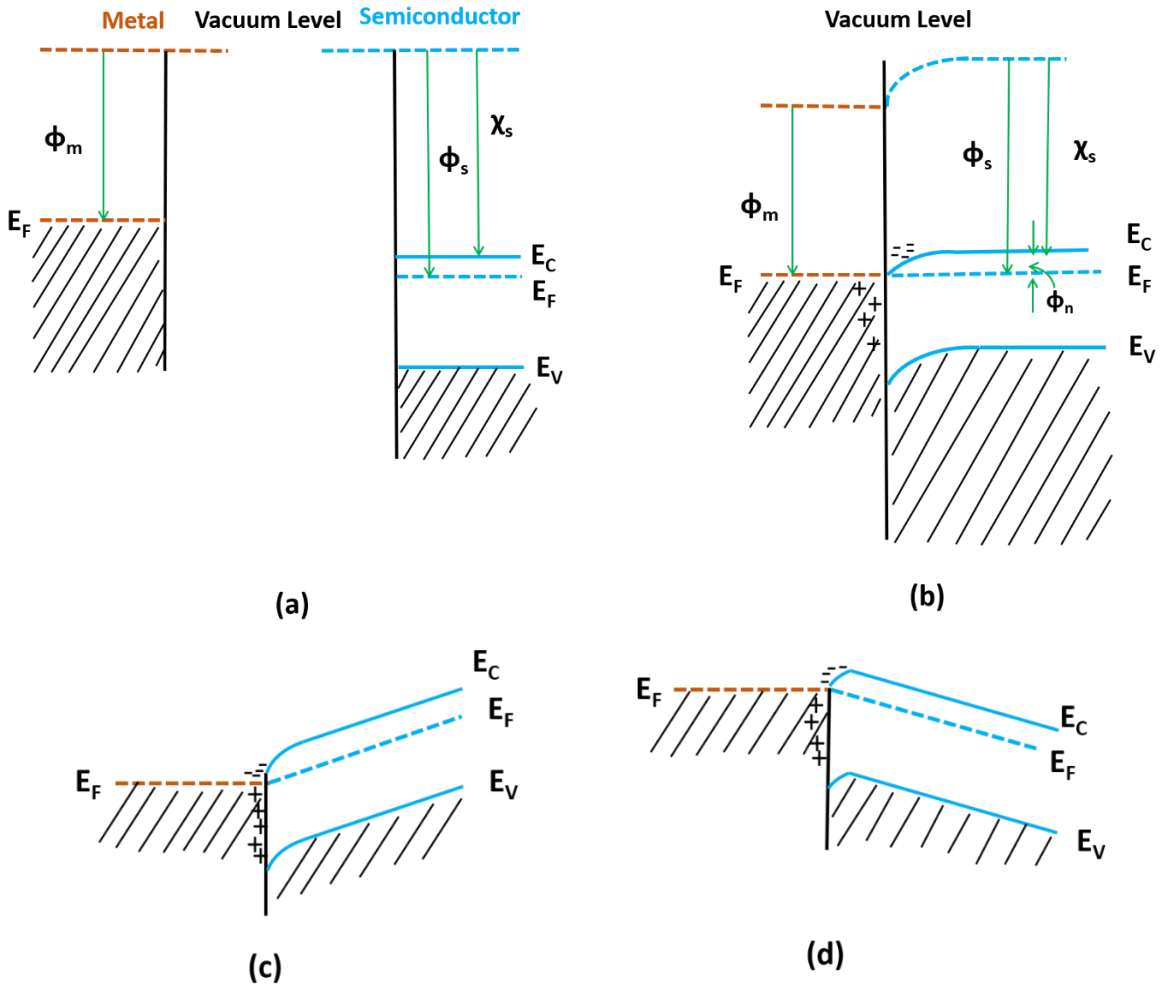


Figure 1.11: Electron energy band diagrams of metal contact on n-type semiconductor with $\phi_m < \phi_s$ (a) Neutral materials separated from each other; (b) contact under thermal equilibrium; (c) negative bias on the semiconductor; and (d) positive bias on the semiconductor.

Only n-type semiconductors, where $\phi_s < \phi_m$, fit the aforementioned description. For an n-type semiconductor with $\phi_m < \phi_s$, the electron energy band diagrams are depicted in **Figure 1.11**. The energy bands for isolated substances are depicted in **Figure 1.11(a)**. Electrons accumulate on the semiconductor side of the CB after the contact as they flow from the metal into the semiconductor. This leaves the metal positively charged. As can be seen in **Figure 1.11(b)**, when equilibrium is established, the Fermi level in the semiconductor is increased by a value $(\phi_s - \phi_m)$. The semiconductor's accumulation layer charge is effectively a surface charge since it is limited to a very thin layer, on the order of the Debye length. The positive charge on the metal side is also a surface charge due to the extremely high electron concentration in the metal. There is a higher concentration of electrons close to the interface, and the bulk semiconductor has the highest resistance in the system. As can be seen in Figure, the majority of the applied voltage is distributed across this large area. For the two current flows, in **Figure 1.11(c)** and **1.11(d)**, this makes the resistance of the bulk region the determining factor in the current, rather than the orientation of the bias. An ohmic contact is a common term for such non-rectifying contact.

The inverse phenomena are applicable for a contact between a metal and a p-type semiconductor. From **Figure 1.12(a)**, electrons flow from the metal into the semiconductor when the contact is made, bringing the Fermi levels of the two materials into phase. In a p-type semiconductor, these electrons constitute a small fraction of the total carriers. They recombine with holes once they reach the semiconductor, giving birth to an ionised acceptor layer in the space charge region, as shown in **Figure 1.12(b)**. When compared to the acceptor concentration, the density of holes in the space charge area is extremely low.

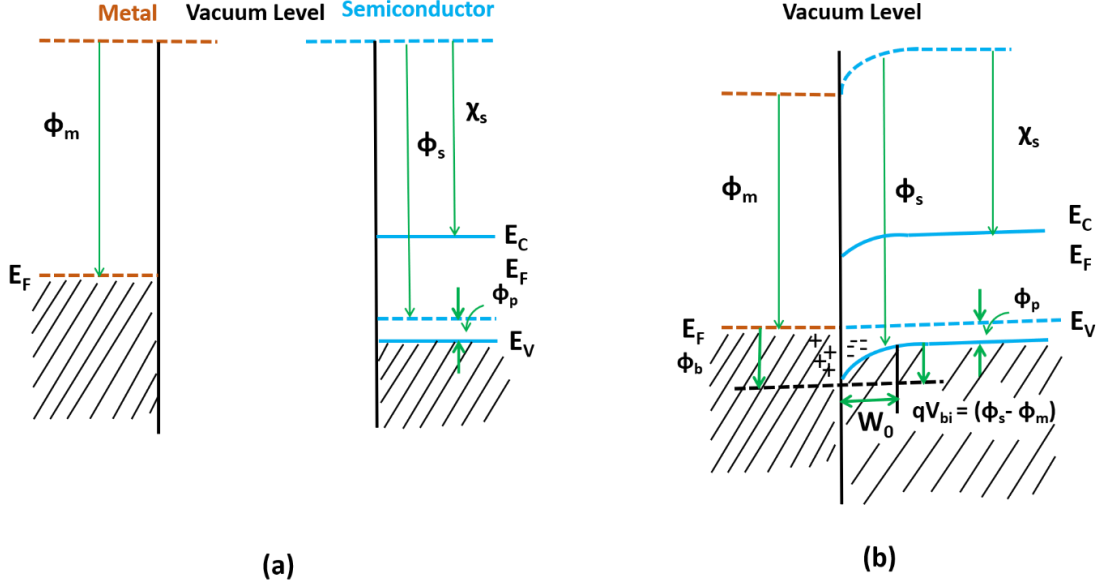


Figure 1.12: Electron energy band diagrams of metal contact on p-type semiconductor with $\phi_m < \phi_s$ (a) Neutral and separated materials and (b) thermal equilibrium situation after the contact has been made

Therefore, a depletion layer with thickness W_0 , proportional to the number of ionised acceptor atoms can be found on the semiconductor side of the space charge area. From above figure the hole barrier height is

$$\phi_b^h = \chi_s + E_g - \phi_m \quad (1.4)$$

where E_g is the band gap of the semiconductor.

From equation (1) and (4)

$$\phi_b^e + \phi_b^h = E_g \quad (1.5)$$

As discuss in the above section for n-type semiconductor, it can be shown for p-type semiconductor that the junction is non-rectifying for $\phi_m > \phi_s$. Typically the junction between metal and p-type semiconductor cause a smaller barrier height and also rarely used in practical devices as the majority carriers in p-type (holes) are heavier than electrons that causes more energy to drive a hole in device resulting a poor performance.

Practical MS contacts don't obey the ideal theory. Particularly the barrier height does not increase linearly with increase of the metal work function, as

expressed in *equation 1.1*. Only ionic semiconductors obey *equation 1.1*. But in many of covalent semiconductors the barrier height is less dependent of metal work function. However, in some cases it is almost independent of ϕ_m . These facts led to a modification in Schottky theory.

1.5.1.8. Modifications to Schottky Theory:

Bardeen, was the first to explain why barrier height is independent of metal work function in covalently linked semiconductors by emphasising the role of localised surface states in this process [124]. The semiconductor's surface marks the end of the crystal lattice's periodicity. On the semiconductor side of a covalent crystal, the surface atoms have neighbours with whom they can form covalent bonds. However, there is no such neighbours to create covalent bonds, on the vacuum side i.e., only one broken covalent bond, having only one electron is present in each surface atom. These bonds are called dangling bonds. Energy levels in the forbidden gap are generated at the semiconductor surface due to dangling bonds. These surface states, typically denoted by the neutral level '0', are continuously distributed in the band gap. This neutral level is located in such a way that all of the semiconductor's states are filled with electrons up to '0' in the absence of band bending, rendering the surface electrically neutral.

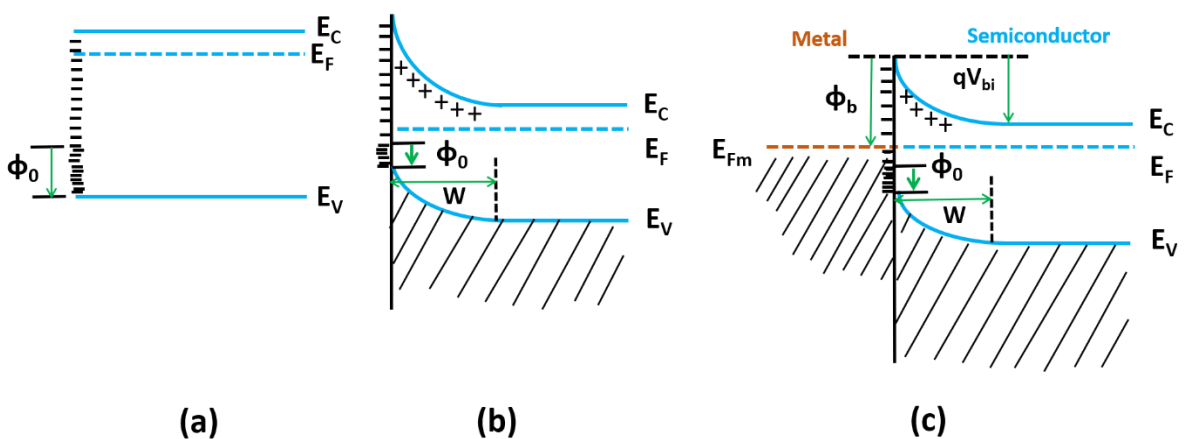


Figure 1.13: Electron energy band diagrams of n-type semiconductor with surface states. The diagrams show (a) flat band at the surface, (b) surface in thermal equilibrium with the bulk, and (c) semiconductor in contact with a metal

Donor states are those below ϕ_0 , which are unaffected by occupancy and produce a positive value while unoccupied. The states above ϕ_0 obviously act like acceptors. The number of surface atoms and the number of surface states are proportional on clean surfaces of covalent semiconductors. A significant reduction in density may occur if absorbed layers of foreign atoms repair the broken covalent connections.

The height of the barrier is affected by how the surface states change the charge in the depletion region. In **Figure 1.13(a)**, the electron energy band diagram for a flat-band n-type semiconductor is shown. Non-equilibrium exists until the surface Fermi level is equal to the bulk Fermi level and electrons from the neighbouring semiconductor are in states above ϕ_0 . The semiconductor region close to the surface is then ionised, creating a depletion layer of ionised donors, and the surface becomes negatively charged. This dipole creation results in a potential barrier, as seen in **Figure 1.13(b)**, when gazing from the surface into the semiconductor. The Fermi level in the semiconductor must vary by an amount equivalent to the contact potential through charge exchange with the metal when equilibrium is established. Metal-surface state interactions dominate charge transfer if the density of surface states at the semiconductor surface is very considerable, while the space charge in the semiconductor is hardly impacted. In this case as shown in **Figure 1.13(c)**, the barrier height becomes independent of metal work function and can be expressed as

$$\phi_b^e = E_g - \phi_0 \quad (1.6)$$

Barrier height is ‘pinned’ here by surface states.

1.5.1.9. Interfacial layer in Schottky junction:

During surface preparation of a highly polarizable semiconductor, there is always some residual insulating layer on the semiconductor's surface. This layer, also known as interfacial layer must have much lower thickness ($< 20\text{\AA}$) for a

satisfactory Schottky contact. The energy band diagram of an M-S contact having a formation of insulating interfacial layer on the semiconductor surface prior to metal contact is shown in **Figure 1.14**.

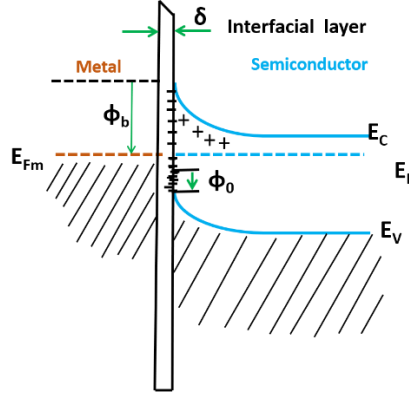


Figure 1.14: Electron energy band diagram of a metal-semiconductor contact with surface states and interfacial layer

As was previously said, the vacuum level is continuous throughout the interface, where the Fermi level is uniform throughout the system. Since this layer is believed to be a perfect insulator with no charge, a linear decrease in potential across the interfacial layer is clearly seen in **Figure 1.14**. The vacuum level is thought to be below the insulator's conduction band's lower edge.

For a very thin interfacial layer (i.e., $< 20 \text{ \AA}$) voltage drop across this layer is low enough to make it negligible with respect to the voltage drop due to the depletion region of the semiconductor. This type of interfacial layer allows electrons to tunnel through it in both directions, making itself effectively transparent to electrons. For these reasons, the existence of a thin interfacial layer has essentially little effect on the barrier height or the contact potential difference of the Schottky junction.

Clean intimate connections are more difficult to analyse theoretically than contacts with a small insulating layer between the metal and semiconductor. This is because the metal and semiconductor can be considered as independent systems in presence of an insulating layer. Then, any changes in the surface dipole

contributions to the work functions of the metal and the semiconductor can be disregarded, and the interface states can be considered a property of the specific semiconductor-insulator combination. Obviously, these simplifications can't be made when clean contacts are involved.

1.5.2. Theories govern carrier transport within M-S junction:

Unlike p-n junctions, where minority carriers are responsible for current transmission, metal-semiconductor interactions rely mostly on majority carriers to carry current. There are five basic transport processes in a M-S junction diode- (1) emission of electrons (majority charge carrier) from the side into the metal part over junctional potential barrier, (2) quantum mechanical tunnelling of majority carriers through the junctional barrier, (3) recombination occurs from electron hole pair in the space-charge region, (4) electron diffusion in the depletion region, and (5) injection of holes from the metal part that diffuse in the semiconductor side.

The current flow in typical high-mobility semiconductors can be explained by the thermionic-emission theory, while the diffusion theory can be used for low-mobility semiconductors. There is also a generalized theory obtained from these two which is named as thermionic-emission-diffusion theory. However, for heavily doped semiconductors and/or for lower operating temperature of the device, contribution of tunnelling current gets more significance and taken into consideration with thermionic emission current.

1.5.2.1. Thermionic-emission (TE) theory:

The word “thermionic” is related to the emission of charged particles like electrons (called thermions) from materials at high temperature. Thermionic emission, also known as the Edison effect, is the release of thermions from the

surface of a charged substance when the vibrational energy of heat overcomes the electrostatic attraction of the electrons there.

Owen Willans Richardson, a British scientist, started researching what would become known as "thermionic emission" after J. J. Thomson's 1897 discovery of the electron [146].

The necessary criteria for the thermionic emission to be the controlling mechanism is that the collision or the drift-diffusion process with barrier layer to be negligible (Fig. 1.15).

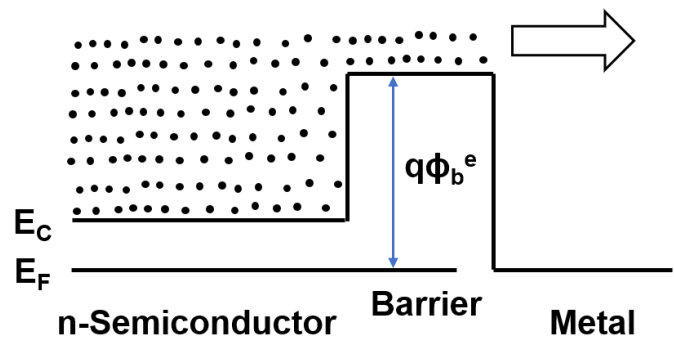


Figure 1.15: Energy band diagram showing thermionic emission of electrons over the barrier

Bethe has proposed his hypothesis of thermionic emission- (i) the barrier height is $\gg kT$, (ii) the plane that determines emission is in thermal equilibrium, and (iii) the presence of net current flow does not affect this thermal equilibrium.

According to these assumptions, the two respective current fluxes, i.e., one from the direction of metal to semiconductor and the other from the side of semiconductor to metal, each have their own quasi-Fermi level, and may be simply superimposed.

According to Fermi-Dirac statistics, above the conduction band edge, the density of electrons in n-type substrate drops exponentially. The density of carriers at non-zero energies is not zero at any non-zero temperature. The integral of the number of carriers that are above the barrier height is of particular

importance here. These newly formed carriers contribute to the thermionic emission current because they are no longer trapped by the barrier after being created thermally.

The total current density,

$$J = J_{TE}[\exp \frac{qV}{kT} - 1] \quad (1.7)$$

Where the saturation current density for thermionic emission,

$$J_{TE} = A^*T^2 \exp \left(\frac{-q\phi_b}{kT} \right) \quad (1.8)$$

Here q , k , T , and A^* are electronic charge (i.e., charge of one free electron = 1.602×10^{-19} Coulombs approx.), Boltzman constant ($= 1.380649 \times 10^{-23} \text{ J} \cdot \text{K}^{-1}$), operating temperature at absolute scale, and modified Richardson constant of semiconductor respectively.

1.5.2.2. Diffusion theory:

Diffusion refers to the transmission especially by contact. Transport of charges occurs via diffusion of charge carriers because of the semiconductor's non-uniform concentration of charged particles. Diffusion can perturb the carrier motion. The diffusion is based on the principle that the net flow of carriers occurs from regions of higher concentration to regions of low concern under the influence of concentration gradient.

The diffusion theory, proposed by Schottky is mainly based on the following assumptions:

- (i) The height of the formed junctional barrier is significantly larger than kT
- (ii) Within the depletion region, the impact of electron collisions, or diffusion, is also taken into account

(iii) The carrier concentration through the entire region of the semiconductor is unaffected by current flow

and

(iv) The semiconductor's impurity concentration is non-degenerate

The current density expression of diffusion theory is basically very similar to the expression of thermionic emission theory (eqⁿ 1.7) having saturation current density,

$$J_D = q\mu N_C \xi_m \exp\left(\frac{-q\phi_b}{kT}\right) \quad (1.9)$$

in the maximum field strength ξ_m with carrier concentration N_C (i.e., the number of free charge carriers in unit volume of semiconductor). This J_D depends on the applied bias voltage and has less sensitivity to the device temperature compared to J_{TE} .

1.5.2.3. Thermionic-emission-diffusion (TED) theory:

The thermionic emission model assumes that carriers do not scatter, while the diffusion theory of the MS diode predicts that the space charge region has numerous mean-free-paths.

The Crowell-Sze “ballistic-to-diffusive treatment of the metal-semiconductor (MS) diode” (130) forms the basis of the strategy of mixing up these two approaches. This strategy originates from the boundary condition of a velocity generated near the metal-semiconductor contact including the barrier lowering due to thermionic recombination.

The theory introduces a recombination velocity of carriers (v_R) associated with thermionic emission and diffusion velocity (v_D) in depletion region. The recombination velocity is also known as surface recombination velocity in semiconductor, defined as the quantity of excess bulk carriers at the line of separation between the quasi-neutral and space-charge zones that are

recombining on the surface per unit area per unit time per unit volume. Diffusion velocity of carrier is the velocity subjected to the process of movement of charge carriers due to concentration gradient along the semiconductor. The saturation current density,

$$J_{TED} = \frac{qN_C v_R}{1 + \left(\frac{v_R}{v_D}\right)} \exp\left(\frac{-q\phi_b}{kT}\right) \quad (1.10)$$

1.5.2.4. Tunnelling:

Electron tunnelling is a quantum mechanical phenomenon in which an electron passes through a potential energy barrier having higher energy than the electron. The process is illustrated in Fig.1.16.

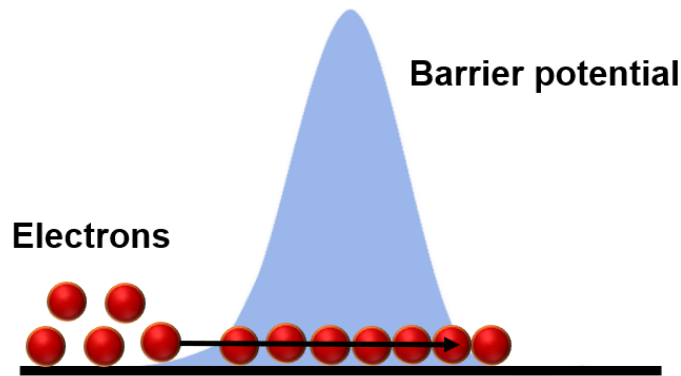


Figure 1.16: Electron tunnelling through barrier

1.5.3. Parameters of Schottky diode:

Performance of a practical Schottky device depends upon its characteristic parameters like ideality factor (I.F.), barrier height (B.H.), and series resistance.

I.F. defines how good a diode is that is quality of a diode. The ideal diode equation assumes that all the recombination of electron and hole occurs during current transport is mainly via band to band or through traps in the bulk areas of the device i.e., there is no incident of recombination found in junctional area. Thus, the I.F. for ideal diode is considered as '1'.

For practical diode recombination happens in other ways and in junctions also. Deviations in I.F. from one indicate that either there are unusual recombination mechanisms taking place or the amount of recombination is changing.

The electric field formed in the depletion region acts as a barrier. To get electrons to go over the electric field's barrier, further energy must be applied. The term "barrier potential" or "barrier height" refers to the minimum difference in potential energy over which electrons must go in order to traverse the electric field. So, the lower barrier height indicates lower turn on voltage. B.H. of device depends upon the materials of the device and also on operating temperature.

The series resistance in MS diode is arising from the metal (which is negligible), from the semiconductor, from the connections. Series resistance lowers the effective voltage applied to the junction leading to generation of lower current in device.

The above-mentioned parameters can be extracted using different measurement characteristics of Schottky device - (i) Current (I) – Voltage (V) measurement, (ii) Activation energy (I-V-T) Measurement, (iii) Capacitance (C) – Voltage (V) measurement and (iv) Photoelectric Measurement

1.5.3.1. Current (I) – Voltage (V) Characteristics:

For a Schottky diode fabricated with n-type semiconductor and metal is said to be forward biased when its metal part is linked to the positive battery terminal and its n-type semiconductor is connected to the negative battery terminal (Fig.1.17a).

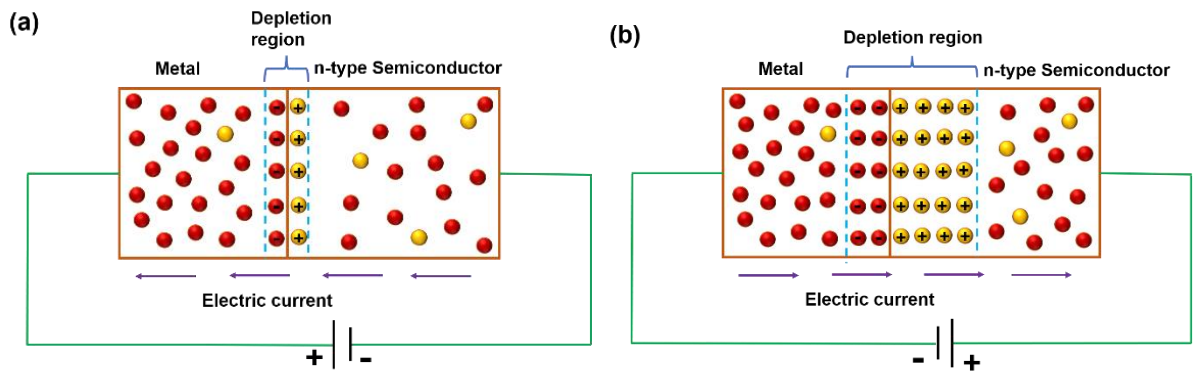


Figure 1.17: Schematic diagram of a metal/n-type semiconductor SBD when (a) forward biased and (b) reverse biased

Applying a forward bias voltage to the Schottky diode causes the n-type semiconductor and metal to release a high number of free electrons. Free electrons flow from metal to n-type semiconductor across the junction after reached at turn on voltage resulting a net current flow from n-type semiconductor to metal.

The Schottky diode is reverse biased when the battery's negative terminal is connected to the metal and the positive terminal is connected to the n-type semiconductor (Fig. 1.17b). The depletion width of a Schottky diode expands in response to a reverse bias voltage. Therefore, there is an end to the flow of electricity. However, a tiny leakage current does flow because the metal's electrons are thermally stimulated.

The I-V curve of an SBD typically looks like the Fig.1.18. There is a "knee" or "turn on" voltage at which the current begins to increase exponentially in the forward direction.

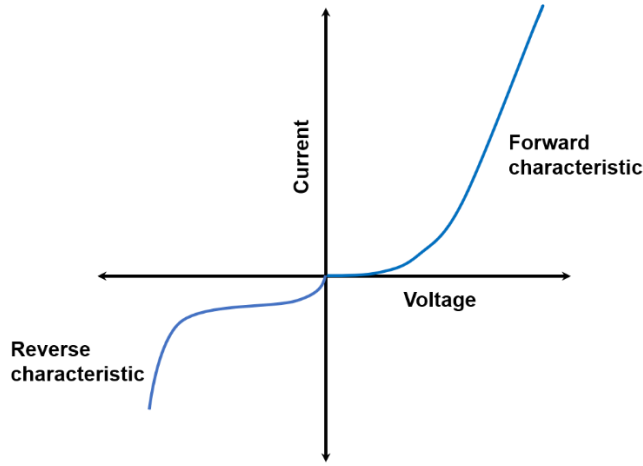


Figure 1.18: I-V characteristic curve of SBD

From Fig.1.17, an abrupt increase in electric current is seen when the reverse bias voltage is significantly raised. Damage to the device could be permanent if the electric current suddenly rises, which breaks down the depletion region.

When semiconductors having high carrier mobility are used to fabricate Schottky barrier devices, the current in the device is mainly due to thermionic emission of carriers over the barrier along with some tunnelling current.

In this case, the forward current of the device in terms of applied bias voltage V , caused by both the thermionic emission and tunnelling, can be expressed as,

$$I = I_0 \left[\exp \frac{qV}{\eta kT} - 1 \right] \quad (1.11)$$

where, reverse saturation current

$$I_0 = AA^*T^2 \exp \frac{-q\phi_b}{kT} \quad (1.12)$$

Here η , and A are ideality factor, and effective device area respectively.

From applied bias voltage $3kT/q$ the plot of $\ln I$ versus V forms a straight line. By extrapolating this straight line to $V=0$, the value of reverse saturation

current can be obtained. When all the other parameters are known the value of barrier height ϕ_b can be easily extracted using above equation (eqⁿ 1.12).

The practical devices often show the deviation from the ideal behaviour. For a typical Schottky device a series resistance arises due to the resistances of metal, semiconductor and the connectors which effectively lowers the applied bias voltage to the junction. That's why it is very important to take this series resistance into consideration and V is replaced by V_{eff} in equation 1.11 where $V_{eff} = V - IR_s$

i.e.,

$$I = I_0 \left[\exp \frac{qV_{eff}}{\eta kT} - 1 \right] \quad (1.13)$$

1.5.3.2. Activation energy measurement:

Activation energy is the amount of energy needed to generate the intermediate, also referred to as an activated complex. When a device is operated at different temperature the conductivity of the device changes with temperature but the activation energy is independent of temperature.

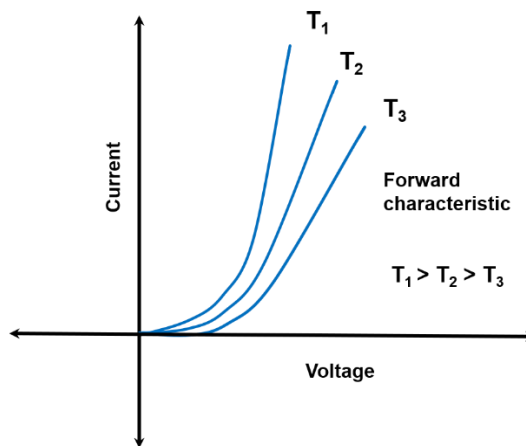


Figure 1.19: I-V curve of SBD at different temperature

In this concept, Arrhenius equation for the conductivity in terms of activation energy is given by the following equation,

$$\sigma = \sigma_0 \exp\left(-\frac{E_a}{kT}\right) \quad (1.14)$$

The activation energy, symbolized by E_a and σ_0 , named the pre-exponential factor can be calculated with help of the straight line in the Arrhenius plot (activation energy plot, Fig.1.20) for a single rate-limited thermally activated process.

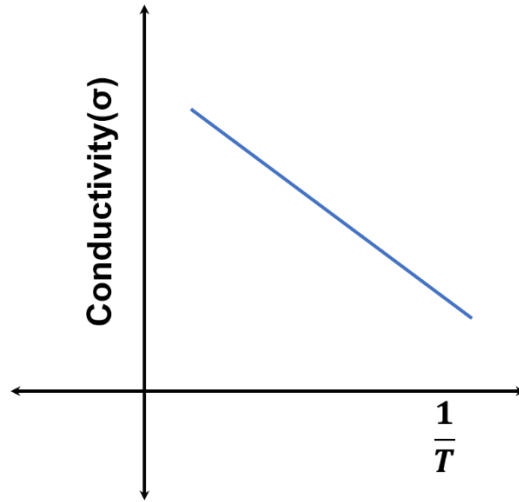


Figure 1.20: Activation energy of conductivity

Even if the modified Richardson constant is unknown, the barrier height can be calculated using this method. The primary benefit of activation energy measurement for determining the Schottky barrier is that it does not require the assumption of electrically active area. This is especially useful in studying atypical metal-semiconductor interfaces, where the actual value of the contacting area is typically unknown and must be estimated.

The electrically active region may represent a very small percentage of the total geometric area in the case of inadequately cleaned or incompletely reacted surfaces. However, a robust metallurgical reaction may produce a rough nonplanar metal-semiconductor contact with an electrically active region bigger than the apparent geometric size.

In these cases, the forward bias I-V data at different operating temperature (Fig.1.19) is recorded and reverse saturation current for each temperature is obtained using above mentioned procedure. Then a plot of $\ln(I_0/T^2)$ against $1/T$ can be drawn which gives a straight line and from the slope value one can determine the value of barrier height,

$$\ln\left(\frac{I_0}{T^2}\right) = \ln(AA^*) - \frac{q\phi_b}{kT} \quad (1.15)$$

The barrier height, determined through this method at absolute zero temperature is slightly greater than the barrier height at room temperature.

If the active area is known, from the intercept Richardson constant can be determined and the vice versa.

1.5.3.3. Capacitance (C) – Voltage (V) Measurement:

As discussed before, when reverse bias of a Schottky diode increases depletion layer width also increases. Hence the capacitance gets smaller due to the increased distance between the conducting areas.

The capacitance of a diode based on the amount of reverse bias that is given to the diode is measured in this purpose. The capacitance C of the depletion area of the diode under a small applied ac voltage is defined as follows:

$$C = A \left[\frac{\epsilon_s q N_D}{2(V_{bi} + V_R - \frac{kT}{q})} \right]^{\frac{1}{2}} \quad (1.16)$$

where ϵ_s is the relative permittivity of the semiconductor, the applied reverse voltage is denoted by V_R , N_D is donor concentration (concentration of atoms that can “donate” electrons to the conduction band) and all other symbols indicate their usual meanings. This equation is based on the assumptions that the diode does not have a significant interfacial oxide layer and that the donor concentration in the n-type semiconductor is constant.

It is clear from the above equation that $1/C^2$ versus V_R plot demonstrates a straight line having a slope of $\frac{2}{A^2 \epsilon_s q N_D}$ and a voltage axis intercept $V_0 = \left(V_{bi} - \frac{kT}{q}\right)$ (Fig.1.21).

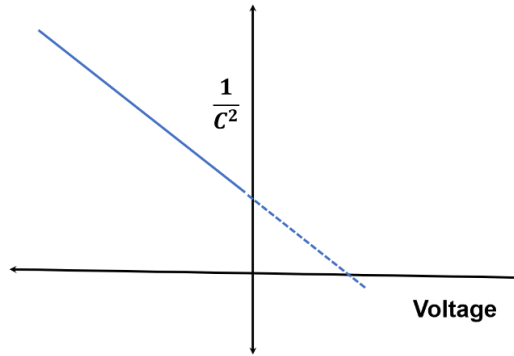


Figure 1.21: $1/C^2$ versus voltage plot in reverse bias

Replacing the value of V_{bi} in equation (3) the barrier height is as follows:

$$\phi_b^e = qV_0 + \phi_n + kT \quad (1.17)$$

The majority carrier contribution to the space charge is the source of the kT factor.

1.5.3.4. Photoelectric Measurement:

When a photon with enough energy enters in a diode, an electron-hole pair is formed. The mechanism is called as inner photoelectric effect.

When it comes to measuring barrier height, the photoelectric approach is both the most precise and direct option. It is possible to generate a photocurrent when a metal surface is exposed to a monochromatic light source. There are two possible mechanisms for carrier excitation in a Schottky barrier diode, both of which contribute to the device's photocurrent. One is excitation over the barrier and another is band to band excitation. For the measurement of barrier height first process is useful.

When a photon with energy $h\nu$ (h is Planck's constant and ν is frequency of photon), larger than barrier height but smaller than the band gap of the semiconductor, in on the metal having a contact with semiconductor, the incident photon will energize the electron from the metal to semiconductor over the barrier. The Fowler theory [147] gives the value of photocurrent (an electric current produced due to radiation of light)

$$I_{ph} = B(h\nu - \phi_b^e)^2 \quad (1.18)$$

Where, $(h\nu - \phi_b^e) \gg 3kT$

here B is a constant of proportionality.

When I_{ph} is plotted against $h\nu$, a straight line is obtained whose intercept on the $h\nu$ axis directly provides the barrier height.

References:

1. A. Dehe, K. Fricke, K. Mutamba and H. L. Hartnag, *A piezoresistive GaAs pressure sensor with GaAs/AlGaAs membrane technology*, Journal of Micromechanics and Microengineering, 1995, **5**, 139.
doi.org/10.1088/0960-1317/5/2/021
2. K. Fobelets, R. Vounckx and G. Borghs, *A GaAs pressure sensor based on resonant tunnelling diodes*, Journal of Micromechanics and Microengineering, 1994, **4**, 123
doi.org/10.1088/0960-1317/4/3/005
3. S. Kanaparthi and S. G. Singh, *Simultaneous Detection of CO and NH₃ Gases at Room Temperature with an Array of ZnS Chemiresistive Sensors and the Superposition Principle*, Analytical Chemistry, 2022, **94**, 11, 4602–4609
doi.org/10.1021/acs.analchem.1c04319
4. S. Park, S. An, H. Ko, S. Lee, and C. Lee, *Synthesis, structure, and UV-enhanced gas sensing properties of Au-functionalized ZnS nanowires*, Sensors and Actuators B: Chemical, 2013, **188**, 1270-1276
doi.org/10.1016/j.snb.2013.07.076
5. T. Inoue, K. Ohtsuka, Y. Yoshida, Y. Matsuura, and Y. Kajiyama, *Metal oxide semiconductor NO₂ sensor*, Sensors and Actuators B: Chemical, 1995, **25**, 1–3, 388-391
doi.org/10.1016/0925-4005(95)85087-2
6. S. Kumar, V. Pavelyev, P. Mishra, N. Tripathi, P. Sharma, and F. Calle, *A review on 2D transition metal di-chalcogenides and metal oxide nanostructures based NO₂ gas sensors*, Materials Science in Semiconductor Processing, 2020, **107**, 104865
doi.org/10.1016/j.mssp.2019.104865
7. T. C. Shen, G. B. Gao, and H. Morkoç, *Recent developments in ohmic contacts for III–V compound semiconductors*, Journal of Vacuum Science & Technology B, 1992, **10**, 5, 2113–2132
doi.org/10.1116/1.586179
8. C.E. Weitzel, J.W. Palmour, C.H. Carter, K. Moore, K.K. Nordquist, S. Allen, C. Thero, and M. Bhatnagar, *Silicon carbide high-power devices*, IEEE Transactions on Electron Devices, 1996, **43**, 10, 1732 – 1741
doi.org/ 10.1109/16.536819
9. B. Ozpineci, L. M. Tolbert, S. K. Islam, and M. Hasanuzzaman, *Effects of silicon carbide (SiC) power devices on HEV PWM inverter losses*, IECON'01. 27th Annual Conference of the IEEE Industrial Electronics Society, 2001, **2**, 1061-1066,
doi.org/10.1109/IECON.2001.975927

10. K. S. Boutros, R. Chu, and B. Hughes, *GaN power electronics for automotive application*, 2012 IEEE Energytech, 2012, 1-4
doi.org/10.1109/EnergyTech.2012.6304646
11. M. Razeghi, *Optoelectronic devices based on III-V compound semiconductors which have made a major scientific and technological impact in the past 20 years*, IEEE Journal of Selected Topics in Quantum Electronics, 2000, **6**, 6, 1344 - 1354
doi.org/10.1109/2944.902188
12. X. Yu, T. J. Marks, and A. Facchetti, *Metal oxides for optoelectronic applications*, Nature materials, 2016, **15**, 4, 383-96
doi.org/10.1038/nmat4599
13. M. R. Gao, Y. F. Xu, J. Jiang, and S. H. Yu, *Nanostructured metal chalcogenides: synthesis, modification, and applications in energy conversion and storage devices*, Chemical Society Reviews, 2013, **42**, 2986-3017
doi.org/10.1039/C2CS35310E
14. Y. Zhang, Q. Zhou, J. Zhu, Q. Yan, S. X. Dou, and W. Sun, *Nanostructured metal chalcogenides for energy storage and electrocatalysis*, Advanced Functional Materials, 2017, **27**, 35, 1702317
doi.org/10.1002/adfm.201702317
15. F. Dimroth, *High-efficiency solar cells from III-V compound semiconductors*, physica status solidi c, 2006, **3**, 3, 373-379
doi.org/10.1002/pssc.200564172
16. S. Siebentritt, *Chalcopyrite compound semiconductors for thin film solar cells*, Current Opinion in Green and Sustainable Chemistry, 2017, **4**, 1-7
doi.org/10.1016/j.cogsc.2017.02.001
17. M. Afzaal, and P. O'Brien, *Recent developments in II-VI and III-VI semiconductors and their applications in solar cells*, Journal of Materials Chemistry, 2006, **16**, 1597-1602
doi.org/10.1039/B512182E
18. H. Hasegawa, and T. Sawada, *Electrical modeling of compound semiconductor interface for FET device assessment*, IEEE Transactions on Electron Devices, 1980, **27**, 6, 1055 – 1061
doi.org/10.1109/T-ED.1980.19986
19. B. R. Bennett, M. G. Ancona, and J. B. Boos, *Compound semiconductors for low-power p-channel field-effect transistors*, MRS bulletin, 2009, **34**, 7, 530 - 536 doi.org/10.1557/mrs2009.141
20. P. D. Ye, G. D. Wilk, J. Kwo, B. Yang, H.-J. L. Gossmann, M. Frei, S. N. G. Chu, J. P. Mannaerts, M. Sergent, M. Hong, K. K. Ng, and J. Bude, *GaAs*

- MOSFET with oxide gate dielectric grown by atomic layer deposition*, IEEE Electron Device Letters, 2003, 24, 4, 209 – 211
doi.org/ 10.1109/LED.2003.812144
21. J. A. Del Alamo, *Nanometre-scale electronics with III–V compound semiconductors*, Nature, 2011, **479**, 317–323
doi.org/10.1038/nature10677
 22. A. J. Rosenberg, and T. C. Harman, *Cd₃As₂—A Noncubic Semiconductor with Unusually High Electron Mobility*, Journal of Applied Physics, 1959, **30**, 1621–1622
doi.org/10.1063/1.1735019
 23. E. Otsuka, *High electron mobility in p-type III-V compound semiconductors*, Japanese journal of applied physics, 1983, **22**, 292
doi.org/10.1143/JJAP.22.292
 24. A. Choudhury, and D. Mukhopadhyay, *Optimum second harmonic generation efficiency in II-VI compound semiconductors at 77 K*, Phys. Status Solidi B, 1982, K49-K51
doi.org/10.1002/pssb.2221130154
 25. K. Tabuse, J. Goto, and T. Kaitsuji, *Next generation microwave dielectric heating apparatus: A preliminary fundamental electric study*, Journal of Microwave Surgery, 2007, **25**, 21-29
doi.org/10.3380/jmicrowavesurg.25.21
 26. R. Chau, S. Datta, M. Doczy, B. Doyle, B. Jin, J. Kavalieros, A. Majumdar, M. Metz, and M. Radosavljevic, *Benchmarking nanotechnology for high-performance and low-power logic transistor applications*, IEEE transactions on nanotechnology, 2005, **4**, 2, 153 – 158
doi.org/ 10.1109/TNANO.2004.842073
 27. I. D. Kim, Y. W. Choi, and H. L. Tuller, *Low-voltage ZnO thin-film transistors with high- K. Bi_{1.5}Zn_{1.0}Nb_{1.5}O₇ gate insulator for transparent and flexible electronics*, Applied Physics Letters, 2005, **87**, 4, 043509
doi.org/10.1063/1.1993762
 28. S. Nakamura, *Growth of In_xGa_(1-x)N compound semiconductors and high-power InGaN/AlGaIn double heterostructure violet-light-emitting diodes*, Microelectronics Journal, 1994, **25**, 8, 651-659
doi.org/10.1016/0026-2692(94)90131-7
 29. J. M. Zavada, and D. Zhang, *Luminescence properties of erbium in III–V compound semiconductors*, Solid-State Electronics, 1995, **38**, 7, 1285-1293
doi.org/10.1016/0038-1101(94)00286-O
 30. S. S. Lin, *Light-emitting two-dimensional ultrathin silicon carbide*, The Journal of Physical Chemistry C, 2012, **116**, 6, 3951–3955
doi.org/10.1021/jp210536m

31. A. Kumar, and D. N. Bose, *Compound semiconductor photodetectors: A Review*, IETE Journal of Research, 1997, **43**, 2-3, 257-265
doi.org/10.1080/03772063.1997.11415985
32. G. Döll, A. Anghel, J. R. Baumann, E. Bucher, A. P. Ramirez, and K. J. Range, *Structural and Magnetic Properties of the Ternary Manganese Compound Semiconductors $MnAl_2Te_4$, $MnIn_2Te_4$, and $MnIn_2Se_4$* , physica status solidi (a), 1991, **126**, 1, 237-244
doi.org/10.1002/pssa.2211260127
33. J. Heremans, D. L. Partin, C. M. Thrush, and L. Green, *Narrow-gap semiconductor magnetic-field sensors and applications*, Semiconductor Science and Technology, 1993, **8**, S424
doi.org/10.1088/0268-1242/8/1S/093
34. M. W. Pelczynski, J. J. Heremans, and S. Schwed, *Compound semiconductor applications for automotive sensors*, MRS Online Proceedings Library (OPL), 1999, **607**, 65
doi.org/10.1557/PROC-607-65
35. A. W. Bett, F. Dimroth, G. Stollwerck, and O. V. Sulima, *III-V compounds for solar cell applications*, Applied Physics A, 1999, **69**, 119–129
doi.org/10.1007/s003390050983
36. F. Dimroth, C. Baur, A. W. Bett, M. Meusel, and G. Strobl, *3-6 junction photovoltaic cells for space and terrestrial concentrator applications*, Conference Record of the Thirty-first IEEE Photovoltaic Specialists Conference, 2005,
doi.org/10.1109/PVSC.2005.1488185
37. J. O. Sofo, and G. D. Mahan, *Electronic structure of $CoSb_3$: A narrow-band-gap semiconductor*, Physical Review B, 1998, **58**, 15620
doi.org/10.1103/PhysRevB.58.15620
38. J. Wu, W. Walukiewicz, W. Shan, K. M. Yu, J. W. Ager III, E. E. Haller, H. Lu, and W. J. Schaff, *Effects of the narrow band gap on the properties of InN* , Physical Review B, 2002, **66**, 201403
doi.org/10.1103/PhysRevB.66.201403
39. D. K. Ferry, *High-field transport in wide-band-gap semiconductors*, Physical Review B, 1975, **12**, 2361
doi.org/10.1103/PhysRevB.12.2361
40. J. H. Edgar, *Prospects for device implementation of wide band gap semiconductors*, Journal of materials research, 1992, **7**, 1, 235 – 252
doi.org/10.1017/S088429140009693X
41. P. K. Basu, and B. R. Nag, *Piezoelectric scattering in quantised surface layers in semiconductors*, Journal of Physics C: Solid State Physics, 1981, **14**, 1519
doi.org/10.1088/0022-3719/14/10/019

42. W. H. Hirschwald, *Zinc Oxide: An Outstanding Example of a Binary Compound Semiconductor*, Acc. Chem. Res. 1985, **18**, 228-234
43. F. Boxberg, N. Søndergaard, and H. Q. Xu, *Photovoltaics with piezoelectric core–shell nanowires*, Nano letters, 2010, **10**, 4, 1108–1112
doi.org/10.1021/nl9040934
44. L. E. Hollander, G. L. Vick, and T. J. Diesel, *The piezoresistive effect and its applications*, Review of Scientific Instruments, 1960, **31**, 323–327
doi.org/10.1063/1.1716967
45. Y. W. Hsu, S. S. Lu, and P. Z. Chang, *Piezoresistive response induced by piezoelectric charges in n-type GaAs mesa resistors for application in stress transducers*, Journal of applied physics, 1999, **85**, 333–340
doi.org/10.1063/1.369452
46. A. Owens, and A. Peacock, *Compound semiconductor radiation detectors*, Nuclear Instruments and Methods in Physics Research Section A: Accelerators, Spectrometers, Detectors and Associated Equipment, 2004, **531**, 1–2, 18-37
doi.org/10.1016/j.nima.2004.05.071
47. T. P. Chow, and R. Tyagi, *Wide bandgap compound semiconductors for superior high-voltage power devices*, Proceedings of the 5th International Symposium on Power Semiconductor Devices and ICs, 1993, 84-88
doi.org/10.1109/ISPSD.1993.297113
48. T. Minami, *Substitution of transparent conducting oxide thin films for indium tin oxide transparent electrode applications*, Thin solid films, 2008, **516**, 7, 1314-1321
doi.org/10.1016/j.tsf.2007.03.082
49. T. Hitosugi, N. Yamada, S. Nakao, Y. Hirose, and T. Hasegawa, *Properties of TiO₂-based transparent conducting oxides*, Physica status solidi (a), 2010, **207**, 7, 1529-1537
doi.org/10.1002/pssa.200983774
50. C. T. Lee, H. W. Chen, and H. Y. Lee, *Metal–oxide–semiconductor devices using Ga₂O₃ dielectrics on n-type GaN*, Applied physics letters, 2003, **82**, 4304–4306
doi.org/10.1063/1.1584520
51. M. Ershov, S. Saxena, H. Karbasi, S. Winters, S. Minehane, J. Babcock, R. Lindley, P. Clifton, M. Redford, and A. Shibkov, *Dynamic recovery of negative bias temperature instability in p-type metal–oxide–semiconductor field-effect transistors*, Applied Physics Letters, **83**, 8, 1647–1649
doi.org/10.1063/1.1604480

52. M. Dekkers, G. Rijnders, and D. H. A. Blank, *ZnIr₂O₄, a p-type transparent oxide semiconductor in the class of spinel zinc-d6-transition metal oxide*, Applied physics letters, 2007, **90**, 2, 021903
doi.org/10.1063/1.2431548
53. U. A. Joshi, and P. A. Maggard, *CuNb₃O₈: A p-Type Semiconducting Metal Oxide Photoelectrode*, The journal of physical chemistry letters, 2012, **3**, 11, 1577–1581
doi.org/10.1021/jz300477r
54. G. Dai, J. Yu, and G. Liu, *Synthesis and Enhanced Visible-Light Photoelectrocatalytic Activity of p–n Junction BiOI/TiO₂ Nanotube Arrays*, The Journal of Physical Chemistry C, 2011, **115**, 15, 7339–7346
doi.org/10.1021/jp200788n
55. T. Xie, G. Liu, B. Wen, J. Y. Ha, N. V. Nguyen, A. Motayed, and R. Debnath, *Tunable ultraviolet photoresponse in solution-processed p–n junction photodiodes based on transition-metal oxides*, ACS Applied Materials & Interfaces, 2015, **7**, 18, 9660–9667
doi.org/10.1021/acsami.5b01420
56. T. Shimizu, and H. Okushi, *The properties of a metal/oxide semiconductor junction prepared using a high-purity ozone surface treatment*, Applied physics letters, 1995, **67**, 10, 1411–1413
doi.org/10.1063/1.114510
57. R. Argazzi, N. Y. M. Iha, H. Zabri, F. Odobel, and C. A. Bignozzi, *Design of molecular dyes for application in photoelectrochemical and electrochromic devices based on nanocrystalline metal oxide semiconductors*, Coordination Chemistry Reviews, 2004, **248**, 1299–1316
doi.org/10.1016/j.ccr.2004.03.026
58. N. K. Elumalai, C. Vijila, R. Jose, A. Uddin, and S. Ramakrishna, *Metal oxide semiconducting interfacial layers for photovoltaic and photocatalytic applications*, Materials for Renewable and Sustainable Energy, 2015, **4**, 11
doi.org/10.1007/s40243-015-0054-9
59. K. Reimann, and M. Steube, *Experimental determination of the electronic band structure of SnO₂*, Solid State Communications, 1998, **105**, 10, 649–652
doi.org/10.1016/S0038-1098(97)10151-X
60. S. Chacko, M. J. Bushiri, and V. K. Vaidyan, *Photoluminescence studies of spray pyrolytically grown nanostructured tin oxide semiconductor thin films on glass substrates*, Journal of Physics D: Applied Physics, 2006, **39**, 4540
doi.org/10.1088/0022-3727/39/21/004
61. G. K. Dalapati, H. Sharma, A. Guchhait, N. Chakrabarty, P. Bamola, Q. Liu, G. Saianand, A. M. S. Krishna, S. Mukhopadhyay, A. Dey, T. K. S. Wong,

- S. Zhuk, S. Ghosh, S. Chakraborty, C. Mahata, S. Biring, A. Kumar, C. S. Ribeiro, S. Ramakrishna, A. K. Chakraborty, S. Krishnamurthy, P. Sonar, and M. Sharma, Tin oxide for optoelectronic, photovoltaic and energy storage devices: a review, *Journal of materials chemistry A*, 2021, **9**, 16621-16684 doi.org/10.1039/D1TA01291F
62. D. P. Dubal, N. R. Chodankar, P. Gomez-Romero, and D.-H. Kim, *4 - Fundamentals of Binary Metal Oxide-Based Supercapacitors*, *Metal Oxides in Supercapacitors*, 2017, 79-98
doi.org/10.1016/B978-0-12-810464-4.00004-8
 63. L. Zaraska, K. Gawlak, M. Gurgul, K. Mika, M. Zych, and G. D. Sulka, *Nanostructured semiconductor oxides formed by anodic oxidation of metallic Sn*, *Anodic Metal Oxides*, 2020, 349-384
doi.org/10.1016/B978-0-12-816706-9.00011-X
 64. A. Barhoum, H. Rahier, M. Benelmekki, and G. V. Assche, *Recent trends in nanostructured particles: synthesis, functionalization, and applications*, *Fundamentals of Nanoparticles*, 2018, 605-639
doi.org/10.1016/B978-0-323-51255-8.00024-0
 65. Z. Yang, C. Wang, and X. Lu, *Nanofibrous materials*, *Electrospinning: Nanofabrication and Applications*, 2019, 53-92
doi.org/10.1016/B978-0-323-51270-1.00003-0
 66. R. Sharma, and S. Yoo, *ZnO in organic electronics*, *Nanostructured Zinc Oxide*, 2021, 697-715
doi.org/10.1016/B978-0-12-818900-9.00004-8
 67. M. M. Khan, *Introduction and fundamentals of chalcogenides and chalcogenides-based nanomaterials*, *Chalcogenide-based nanomaterials as photocatalysts*, 2021, 1-6
doi.org/10.1016/B978-0-12-820498-6.00001-9
 68. J. Yin, J. Jin, H. Lin, Z. Yin, J. Li, M. Lu, L. Guo, P. Xi, Y. Tang, and C. H. Yan, *Optimized metal chalcogenides for boosting water splitting*, *Advanced Science*, 2020, **7**, 10, 1903070
doi.org/10.1002/advs.201903070
 69. M. D. Regulacio, D. T. Nguyen, R. Horia, and Z. W. Seh, *Designing nanostructured metal chalcogenides as cathode materials for rechargeable magnesium batteries*, *Small*, 2021, **17**, 25, 2007683
doi.org/10.1002/sml.202007683
 70. D. Zhang, L. Li, and Y. Zhang, *Metal chalcogenides-based materials for high-performance metal ion capacitors*, *Journal of Alloys and Compounds*, 2021, **869**, 159352
doi.org/10.1016/j.jallcom.2021.159352

71. Q. Wang, L. Jiao, Y. Han, H. Du, W. Peng, Q. Huan, D. Song, Y. Si, Y. Wang, and H. Yuan, *CoS₂ Hollow Spheres: Fabrication and Their Application in Lithium-Ion Batteries*, The Journal of Physical Chemistry C, 2011, **115**, 16, 8300–8304
doi.org/10.1021/jp111626a
72. J. Pu, Z. Shen, J. Zheng, W. Wu, C. Zhu, Q. Zhou, H. Zhang, and F. Pan, *Multifunctional Co₃S₄@sulfur nanotubes for enhanced lithium-sulfur battery performance*, Nano energy, 2017, **37**, 7-14
doi.org/10.1016/j.nanoen.2017.05.009
73. P. Ganesan, A. Sivanantham, and S. Shanmugam, *CoS₂–TiO₂ hybrid nanostructures: efficient and durable bifunctional electrocatalysts for alkaline electrolyte membrane water electrolyzers*, Journal of Materials Chemistry A, 2018, **6**, 1075-1085
doi.org/10.1039/C7TA09096J
74. M. B. Muradov, O. O. Balayeva, A. A. Azizov, A. M. Maharramov, L. R. Qahramanli, G. M. Eyvazova, and Z. A. Aghamaliyev, *Synthesis and characterization of cobalt sulfide nanoparticles by sonochemical method*, Infrared Physics & Technology, 2018, **89**, 255-262
doi.org/10.1016/j.infrared.2018.01.014
75. A. Eftelthari, *Molybdenum diselenide (MoSe₂) for energy storage, catalysis, and optoelectronics*, Applied Materials Today, 2017, **8**, 1-7
doi.org/10.1016/j.apmt.2017.01.006
76. H. Arora, and A. Erbe, *Recent progress in contact, mobility, and encapsulation engineering of InSe and GaSe*, InfoMat, 2021, **3**, 6, 662-693
doi.org/10.1002/inf2.12160
77. Rassay, and S. Shashikant, *Electrical, electronic and optical properties of MoSe₂ and WSe₂*, 2016, Theses. 8
78. D. J. Sathe, P. A. Chate, P. P. Hankare, A. H. Manikshete, and A. S. Aswar, *A novel route for synthesis, characterization of molybdenum diselenide thin films and their photovoltaic applications*, Journal of Materials Science: Materials in Electronics, 2013, **24**, 438–442
doi.org/10.1007/s10854-012-0705-x
79. M. Khan, M. N. Tahir, S. F. Adil, H. U. Khan, M. R. H. Siddiqui, A. A. Al-Warthan, and W. Tremel, *Graphene based metal and metal oxide nanocomposites: synthesis, properties and their applications*, Journal of Materials Chemistry A, 2015, **3**, 37, 18753-18808
doi.org/10.1039/C5TA02240A
80. Q. Shi, Y. Cha, Y. Song, J. I. Lee, C. Zhu, X. Li, M. K. Song, D. Du, and Y. Lin, *3D graphene-based hybrid materials: synthesis and applications in energy storage and conversion*, Nanoscale, 2016, **8**, 15414-15447
doi.org/ 10.1039/C6NR04770J

81. C. Van Pham, A. F. Madsuha, T. V. Nguyen, and M. Krueger, *Graphene-quantum dot hybrid materials on the road to optoelectronic applications*, Synthetic Metals, 2016, **219**, 33-43
doi.org/10.1016/j.synthmet.2016.04.029
82. V Berry, *Impermeability of graphene and its applications*, Carbon, 2013, **62**, 1-10
doi.org/10.1016/j.carbon.2013.05.052
83. M. D. Stoller, S. Park, Y. Zhu, J. An, and R. S. Ruoff, *Graphene-based ultracapacitors*, Nano letters, 2008, **8**, 10, 3498–3502
doi.org/10.1021/nl802558y
84. N. Yang, J. Zhai, D. Wang, Y. Chen, and L. Jiang, *Two-dimensional graphene bridges enhanced photoinduced charge transport in dye-sensitized solar cells*, ACS nano, 2010, **4**, 2, 887–894
doi.org/10.1021/nn901660v
85. A. Amiri, M. Naraghi, G. Ahmadi, M. Soleymaniha, and M. Shanbedi, *A review on liquid-phase exfoliation for scalable production of pure graphene, wrinkled, crumpled and functionalized graphene and challenges*, FlatChem, 2018, **8**, 40-71
doi.org/10.1016/j.flatc.2018.03.004
86. J. M. Xue, L. K. Wu, N. Hu, J. Qiu, C. Chang, S. Atobe, H. Fukunaga, T. Watanabe, Y. L. Liu, H. M. Ning, J. Li, Y. Li, and Y. Zhao, *Evaluation of piezoelectric property of reduced graphene oxide (rGO)–poly (vinylidene fluoride) nanocomposites*, Nanoscale, 2012, **4**, 7250-7255
doi.org/10.1039/C2NR32185H
87. G. Liu, Y. Wang, F. Qiu, L. Li, L. Jiao, and H. Yuan, *Synthesis of porous Ni@ rGO nanocomposite and its synergetic effect on hydrogen sorption properties of MgH₂*, Journal of Materials Chemistry, 2012, **22**, 22542-22549
doi.org/10.1039/C2JM34730J
88. S. Ebrahimi, A. Bordbar-Khiabani, B. Yarmand, and M. A. Asghari, *Improving optoelectrical properties of photoactive anatase TiO₂ coating using rGO incorporation during plasma electrolytic oxidation*, Ceramics International, 2019, **45**, 2, 1746-1754
doi.org/10.1016/j.ceramint.2018.10.057
89. J Sun, S Bai, Y Tian, Y Zhao, N Han, R Luo, D Li, and A. Chen, *Hybridization of ZnSnO₃ and rGO for improvement of formaldehyde sensing properties*, Sensors and Actuators B: Chemical, 2018, **257**, 29-36
doi.org/10.1016/j.snb.2017.10.015
90. N. I. Zaaba, K. L. Foo, U. Hashim, S. J. Tan, W. W. Liu, and C. H. Voon, *Synthesis of Graphene Oxide using Modified Hummers Method: Solvent Influence*, Procedia Engineering, 2017, **184**, 469-477
doi.org/10.1016/j.proeng.2017.04.118

91. S. N. Alam, N. Sharma, and L. Kumar, *Synthesis of graphene oxide (GO) by modified hummers method and its thermal reduction to obtain reduced graphene oxide (rGO)*, Graphene, 2017, **6**, 1-18
doi.org/10.4236/graphene.2017.61001
92. X. Xiang, Y. Zhu, C. Gao, H. Du, and C. Guo, *Study on the structure of reduced graphene oxide prepared by different reduction methods*, Carbon Letters, 2022, **32**, 557–566
doi.org/10.1007/s42823-021-00287-6
93. R. M. N. Yerga, M. C. Á. Galván, F. D. Valle, J. A. Villoria de la Mano, and J. L. G. Fierro, *Water splitting on semiconductor catalysts under visible-light irradiation*, ChemSusChem: Chemistry & Sustainability Energy & Materials, 2009, **2**, 6, 471-485
doi.org/10.1002/cssc.200900018
94. H. Yu, Z. Bao, and J. H. Oh, *High-performance phototransistors based on single-crystalline n-channel organic nanowires and photogenerated charge-carrier behaviors*, Advanced Functional Materials, 2013, **23**, 5, 629-639
doi.org/10.1002/adfm.201201848
95. K. H. Reddy, S. Martha, and K. M. Parida, *Fabrication of Novel p-BiOI/n-ZnTiO₃ Heterojunction for Degradation of Rhodamine 6G under Visible Light Irradiation*, Inorganic Chemistry, 2013, **52**, 11, 6390–6401
doi.org/10.1021/ic400159m
96. G. K. Pradhan, D. K. Padhi, and K. M. Parida, *Fabrication of α -Fe₂O₃ Nanorod/RGO Composite: A Novel Hybrid Photocatalyst for Phenol Degradation*, ACS applied materials & Interfaces, 2013, **5**, 18, 9101–9110
doi.org/10.1021/am402487h
97. J. Yang, X. Duan, W. Guo, D. Li, H. Zhang, and W. Zheng, *Electrochemical performances investigation of NiS/rGO composite as electrode material for supercapacitors*, Nano Energy, 2014, **5**, 74-81
doi.org/10.1016/j.nanoen.2014.02.006
98. J. Selvaraj, S. Gupta, R. Anand, S. Fiechter, and V. R. Subramanian, *How Beneficial Is Reduced Graphene Oxide (RGO) for Long-Term Photo Generated Charge Transport in Bismuth Titanate–RGO Nanocomposite Films?*, Journal of The Electrochemical Society, 2015, **163**, H147
doi.org/10.1149/2.0911602jes
99. P. Wang, J. Wang, X. Wang, H. Yu, J. Yu, M. Lei, and Y. Wang, *One-step synthesis of easy-recycling TiO₂-rGO nanocomposite photocatalysts with enhanced photocatalytic activity*, Applied Catalysis B: Environmental, 2013, **132-133**, 452-459
doi.org/10.1016/j.apcatb.2012.12.009

100. K. Wang, X. Dong, C. Zhao, X. Qian, and Y. Xu, *Facile synthesis of Cu₂O/CuO/RGO nanocomposite and its superior cyclability in supercapacitor*, *Electrochimica Acta*, 2015, **152**, 433-442
doi.org/10.1016/j.electacta.2014.11.171
101. M. Azarang, A. Shuhaimi, R. Yousefi, and M. Sookhakian, *Effects of graphene oxide concentration on optical properties of ZnO/RGO nanocomposites and their application to photocurrent generation*, *Journal of Applied Physics*, 2014, **116**, 8, 084307
doi.org/10.1063/1.4894141
102. C. S. Rout, P. D. Joshi, R. V. Kashid, D. S. Joag, M. A. More, A. J. Simbeck, M. Washington, S. K. Nayak, and D. J. Late, *Superior Field Emission Properties of Layered WS₂-RGO Nanocomposites*, *Scientific reports*, 2013, **3**, 3282
doi.org/10.1038/srep03282
103. L. Li, S. He, M. Liu, C. Zhang, and W. Chen, *Three-Dimensional Mesoporous Graphene Aerogel-Supported SnO₂ Nanocrystals for High-Performance NO₂ Gas Sensing at Low Temperature*, *Analytical chemistry*, 2015, **87**, 3, 1638–1645 **doi.org/10.1021/ac503234e**
104. G. Neri, S. G. Leonardi, M. Latino, N. Donato, S. Baek, D. E. Conte, P. A. Russo, and N. Pinna, *Sensing behavior of SnO₂/reduced graphene oxide nanocomposites toward NO₂*, *Sensors and Actuators B: Chemical*, 2013, **179**, 61-68
doi.org/10.1016/j.snb.2012.10.031
105. H. Seema, K. C. Kemp, V. Chandra, and K. S. Kim, *Graphene–SnO₂ composites for highly efficient photocatalytic degradation of methylene blue under sunlight*, *Nanotechnology*, 2012, **23**, 355705
doi.org/10.1088/0957-4484/23/35/355705
106. S. Li, W. Xie, S. Wang, X. Jiang, S. Peng, and D. He, *Facile synthesis of rGO/SnO₂ composite anodes for lithium ion batteries*, *Journal of Materials Chemistry A*, 2014, **2**, 17139-17145
doi.org/10.1039/C4TA03907F
107. L. Wang, D. Wang, Z. Dong, F. Zhang, and J. Jin, *Interface Chemistry Engineering for Stable Cycling of Reduced GO/SnO₂ Nanocomposites for Lithium Ion Battery*, *Nano letters*, 2013, **13**, 4, 1711–1716
doi.org/10.1021/nl400269d
108. S. J. Choi, B. H. Jang, S. J. Lee, B. K. Min, A. Rothschild§, and Il-Doo Kim, *Selective Detection of Acetone and Hydrogen Sulfide for the Diagnosis of Diabetes and Halitosis Using SnO₂ Nanofibers Functionalized with Reduced Graphene Oxide Nanosheets*, *Applied Materials & Interfaces*, 2014, **6**, 4, 2588–2597
doi.org/10.1021/am405088q

109. N. Taniguchi, C. Arakawa, and T. Kobayashi, *On the basic concept of nanotechnology*, Proceedings of the International Conference on Production Engineering, Tokyo, Japan. 1974
110. A. B. Asha, and R. Narain, *Nanomaterials properties*, Polymer science and nanotechnology, 2020, 343-359
doi.org/10.1016/B978-0-12-816806-6.00015-7
111. M. Byakodi, N. S. Shrikrishna, R. Sharma, S. Bhansali, Y. Mishra, A. Kaushik, and S. Gandhi, *Emerging 0D, 1D, 2D, and 3D nanostructures for efficient point-of-care biosensing*, Biosensors and Bioelectronics: X, 2022, **12**, 100284
doi.org/10.1016/j.biosx.2022.100284
112. Y. S. Zhao, H. Fu, A. Peng, Y. Ma, D. Xiao, and J. Yao, *Low-dimensional nanomaterials based on small organic molecules: preparation and optoelectronic properties*, Advanced materials, 2008, **20**, 15, 2859-2876
doi.org/10.1002/adma.200800604
113. J. N. Tiwari, R. N. Tiwari, and K. S. Kim, *Zero-dimensional, one-dimensional, two-dimensional and three-dimensional nanostructured materials for advanced electrochemical energy devices*, Progress in Materials Science, 2012, **57**, 4, 724-803
doi.org/10.1016/j.pmatsci.2011.08.003
114. A. Mostofizadeh, Y. Li, B. Song, and Y. Huang, *Synthesis, properties, and applications of low-dimensional carbon-related nanomaterials*, Journal of nanomaterials, 2011, **2011**, 1–21
doi.org/10.1155/2011/685081
115. P. M. Visakh, and M. J. M. Morlanes, *Nanomaterials and nanocomposites: zero-to three-dimensional materials and their composites*, John Wiley & Sons, 2016
116. A. Niu, Y. Han, J. Wu, N. Yu, and Q. Xu, *Synthesis of one-dimensional carbon nanomaterials wrapped by silver nanoparticles and their antibacterial behavior*, The Journal of Physical Chemistry C, 2010, **114**, 29, 12728–12735
doi.org/10.1021/jp104720w
117. T. Fukui, and Y. Hatsugai, *Quantum Spin Hall Effect in Three Dimensional Materials: Lattice Computation of Z_2 Topological Invariants and Its Application to Bi and Sb*, Journal of the Physical Society of Japan, 2007, **76**, 053702
doi.org/10.1143/JPSJ.76.053702
118. F. Braun, *Über die Stromleitung durch Schwefelmetalle*, Ann. Phys. Chem., 1874, **153**, 556
119. J. C. Bose U.S. Patent 775, 1904, 840

120. A. H. Wilson, *The Theory of Electronic Semiconductors*, Proc. R. Soc. Lond. Ser. A, 1931, **133**, 458
121. W. Schottky, *Halbleitertheorie der Sperrschicht*, Naturwissenschaften, 1938, **26**, 843
122. N. F. Mott, *Note on the Contact between a Metal and an Insulator or Semiconductor*, Proc. Cambr. Philos. Soc., 1938, **34**, 568
123. H. A. Bethe, *Theory of the Boundary Layer of Crystal Rectifiers*, MIT Radiat. Lab. Rep., 1942, **43**, 12
124. J. Bardeen, *Surface states and rectification at a metal-semiconductor contact*, Phys. Rev., 1947, **71**, 717-727
doi.org/10.1103/PhysRev.71.717
125. J. W. Conley, C. B. Duke, G. D. Mahan and J. J. Tiemann, *Electron tunnelling in metal semiconductor barriers*, Phys. Rev., 1966, **150**, 466-469.
126. R. Stratton, *Theory of field emission from semiconductors*, Phys. Rev., 1962, **125**, 67-82
127. S.M. Sze, C. R. Crowell and D. Kahng, *Photoelectric determination of the image force dielectric constant for hot electrons in Schottky barriers*, Applied Physics, 1964, **35**, 2534-2536.
128. C. R. Crowell and S. M. Sze, *Quantum mechanical reflection of electrons at metal-semiconductor barriers: electron transport in semiconductor-metal-semiconductor structures*, Journal of Applied Physics, 1966, **37**, 2683-2689
129. F.A. Padovani and R. Stratton, *Field and thermionic field emission in Schottky barriers*, Solid State Electron, 1966, **9**, 695-707
130. C.R. Crowell and S. M. Sze, *Current transport in metal-semiconductor barriers*, Solid-State Electron, 1966, **9**, 1035-1048
131. B. J. Baliga, *Trends in power semiconductor devices*, IEEE Transactions on electron Devices, 1996, **43**, 10, 1717 – 1731
doi.org/10.1109/16.536818
132. S. I. Long, F. S. Lee, R. Zucca, B. M. Welch, and R. C. Eden, *MSI high-speed low-power GaAs integrated circuits using Schottky diode FET logic*, IEEE Transactions on Microwave Theory and Techniques, 1980, **28**, 5, 466 – 472 **doi.org/10.1109/TMTT.1980.1130102**
133. R. Singh, J. A. Cooper, M. R. Melloch, T. P. Chow, and J. W. Palmour, *SiC power Schottky and PiN diodes*, IEEE Transactions on Electron Devices, 2002, **49**, 4, 665 – 672
doi.org/10.1109/16.992877
134. L. Lorenz, G. Deboy, and I. Zverev, *Matched pair of Cool MOS transistor with SiC-Schottky diode-advantages in application*, IEEE Transactions on Industry Applications, 2004, **40**, 5, 1265 – 1272
doi.org/10.1109/TIA.2004.834017

135. E. R. Mueller, and A. J. DeMaria, *Broad bandwidth communication/data links using terahertz sources and Schottky diode modulators/detectors*, Terahertz and Gigahertz Electronics and Photonics IV, 2005, **5727**
doi.org/10.1117/12.590686
136. A. K. Singh, A. D. D. Dwivedi, P. Chakrabarti, and R. Prakash, *Electronic and optical properties of electrochemically polymerized polycarbazole/aluminum Schottky diodes*, Journal of Applied Physics, 2009, **105**, 11, 114506
doi.org/10.1063/1.3139277
137. O. Savadogo, and K. C. Mandal, *Low Cost Schottky Barrier Solar Cells Fabricated on CdSe and Sb₂S₃ Films Chemically Deposited with Silicotungstic Acid*, Journal of The Electrochemical Society, 1994, **141**, 2871
doi.org/10.1149/1.2059248
138. X. Li, H. Zhu, K. Wang, A. Cao, J. Wei, C. Li, Y. Jia, Z. Li, X. Li, and D. Wu, *Graphene-on-silicon Schottky junction solar cells*, Advanced materials, 2010, **22**, 25, 2743-2748
doi.org/10.1002/adma.200904383
139. H. S. Kong, J. W. Palmour, J. T. Glass, and R. F. Davis, *Temperature dependence of the current-voltage characteristics of metal-semiconductor field-effect transistors in n-type β -SiC grown via chemical vapor deposition*, Applied physics letters, 1987, **51**, 6, 442–444
doi.org/10.1063/1.98416
140. M. A. Khan, J. N. Kuznia, A. R. Bhattarai, and D. T. Olson, *Metal semiconductor field effect transistor based on single crystal GaN*, Applied Physics Letters, 1993, **62**, 15, 1786–1787
doi.org/10.1063/1.109549
141. H. Frenzel, A. Lajn, H. V. Wenckstern, and M. Grundmann, *Ultrathin gate-contacts for metal-semiconductor field-effect transistor devices: An alternative approach in transparent electronics*, Journal of Applied Physics, 2010, **107**, 11, 114515
doi.org/10.1063/1.3430988
142. H. Frenzel, A. Lajn, M. Brandt, H. Wenckstern, G. Biehne, H. Hochmuth, M. Lorenz, and M. Grundmann, *ZnO metal-semiconductor field-effect transistors with Ag-Schottky gates*, Applied Physics Letters, 2008, **92**, 19, 192108
doi.org/10.1063/1.2926684
143. S. Lee, J. H. Park, K. Jeon, S. Kim, Y. Jeon, D. H. Kim, D. M. Kim, J. C. Park, and C. J. Kim, *Modeling and characterization of metal-*

semiconductor-metal-based source-drain contacts in amorphous InGaZnO thin film transistors, Applied Physics Letters, 2010, **96**, 11, 113506

doi.org/10.1063/1.3364134

144. S. M. Sze, M. P. Lepselter, and R. W. MacDonald, *Metal-semiconductor Impatt diode*, Solid-State Electronics, 1969, **12**, 2, 107-109

doi.org/10.1016/0038-1101(69)90118-X

145. D. J. Coleman Jr, *Transit-Time Oscillations in BARITT Diodes*, Journal of Applied Physics, 1972, **43**, 4, 1812–1818

doi.org/10.1063/1.1661400

146. O.W. Richardson, *The Emission of Electricity from Hot Bodies*, Longmans Green, Harlow, Essex, 1921.

147. R. H. Fowler, *The analysis of photoelectric sensitivity curves for clean metals at various temperatures*, Phys. Rev, 1931, **38**, 45-56.

Chapter 2

Synthesis and Characterization Techniques of nanomaterial

2.1. *Introduction:*

Synthesis and characterization of nanoparticle is an important area of material Science and nanotechnology. The United States and Japan conducted the first comprehensive foundational investigations with nanoparticles in the 1970s and 1980s [1, 2]. Low cost, easy, efficient process of synthesis is more adaptable nowadays. Also, depending upon synthesis procedure and condition, different properties of nanomaterial can be tuned. Nucleation and growth are two vital stages of nanoparticle synthesis. The size and shape of the nanoparticles are significantly influenced by their initial nucleus. Starting nucleation processes also influence long-term stability [3]. If nucleation proceeds quickly, many crystals may form concurrently, resulting in a more monodisperse product. On the other hand, a polydisperse population of crystals of different sizes can form at sluggish nucleation rates. The control of nanoparticle phase, dispersity, and size is possible through the regulation of nucleation. In other words, the properties of a nanoparticle are strongly affected by its nucleation stages during synthesis. So, it is also very significant to characterize the synthesized nanoparticle properly. A variety of properties can be studied to characterise a nanomaterial, including its shape, size, and surface area, aspect ratio, agglomeration/aggregation state between individual particle, size distribution, surface morphology (also called topography), detail structure with degree of crystallinity and defects, structural formula (also called molecular structure), composition of the nanomaterial (with percentage of purity, presence of any known impurities or additives), phase identity, absorption, transmission, reflection, and light emission, magnetism, conductivity etc.

2.2. Synthesis Procedures of Nano Materials:

Several potential techniques have been used for synthesis of nanomaterials in material science researches. The two main categories of nanoparticle synthesis methods are top-down and bottom-up. Physical participation techniques including lithography, physical vapour deposition (PVD), mechanical machining (Ball Milling), and thermal evaporation pyrolysis are all part of the top-down technique [4]. Biological and chemical techniques are examples of bottom-up approaches. The bottom-up chemical procedures include the use of sol-gel, chemical vapour deposition (CVD), chemical co-precipitation, micro-emulsions, hydrothermal method, sono-chemical method, and microwave methods [5]. Among them, during this course of experiments, two methods are adopted which are illustrated in lucid way as follows:

2.2.1. Co-precipitation method:

Coprecipitation is the precipitation of one or multiple compounds simultaneously from a solution. It is the most practical and cost-effective method for preparing nanomaterials. This technique, which begins with a solution of dissolved precursor i.e., parental materials in a suitable common solvent and then addition of a precipitating agent in such a way that a homogeneous, single-phase inorganic solid is obtained at final stage. Co-precipitation holds the necessary cations close together for formulating the desired material in the reaction medium and reduces the decomposition temperature. It involves the occurrence of nucleation, growth, coarsening, and/or agglomeration processes simultaneously. Under conditions of high supersaturation, a large number of insoluble species (micro/nano particles) are produced. It has an easy control of particle size and

composition. It allows numerous opportunities to alter the particle surface condition and overall homogeneity.

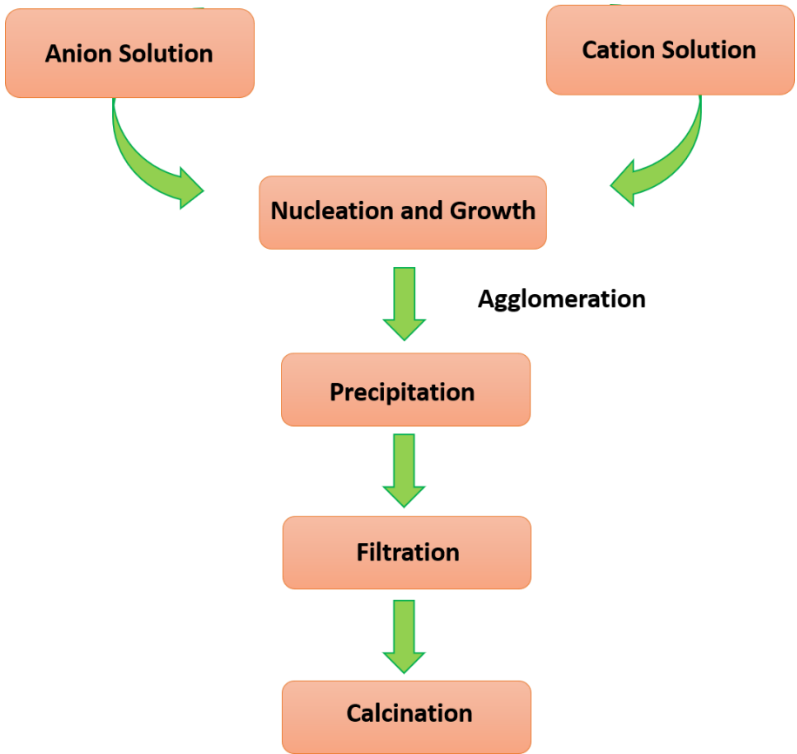


Figure 2.1: Flowchart of coprecipitation method

2.2.2. *Hydrothermal/ Solvothermal method:*

Hydrothermal and solvothermal synthesis is the synthesis procedure of materials in a solvent under at a constant and controlled temperature (typically from 100°C to 1000°C) and pressure (typically between 1 MPa and 100 MPa) helped by a specific route of chemical reaction. Condition of the synthesis like maintaining temperature, mother solution, time etc can vary the morphology of the nanomaterial. The high reactivity of the reactants at elevated temperatures and pressures helps in the synthesis of inorganic nanomaterials at significantly lower temperatures compared to solid-state reactions. Nucleation rates and particle size distribution can be accomplished at a satisfactory level by tuning reaction parameters such as pressure, temperature, time, reactant concentration, reaction cell fill volume and pH. A large number of inorganic materials belonging to

different classes have been prepared by the hydrothermal or solvothermal synthesis such as metals, oxides, chalcogenides, pnictides and many other materials.

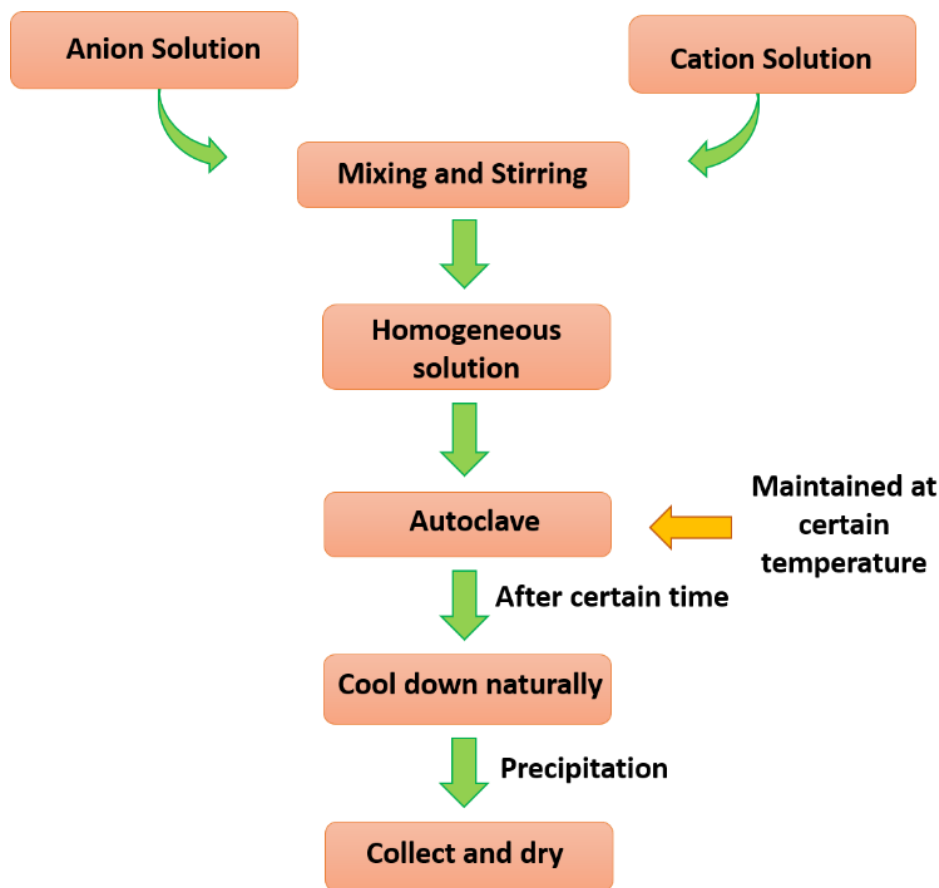


Figure 2.2: Flowchart of hydrothermal method

2.3. *Characterization techniques:*

Characterization is the process of measuring and investigating a material's attributes (such as composition, morphological, physical, optical, electrical, magnetic, mechanical, thermal, and phase changes); this process is known as characterization methodology. Techniques, those are very useful and adopted in material characterizations are introduced as follows:

2.3.1. X-Ray Diffraction (XRD) Technique & Data Analysis:

Mechanism of X-ray diffraction is basically based on constructive interference of monochromatic X-ray radiations with the radiation through a crystalline material. Cathode ray tubes are used to create these X-rays, which are then monochromatically filtered, collimated, and focused before being projected on the sample. Crystallographic structure can be determined in materials science by X-ray diffraction analysis (XRD). X-ray diffraction (XRD) involves exposing a sample to incident X-rays and then measuring the emitted X-rays' intensity and scattering angle [6]. X-ray diffraction (XRD) analysis is primarily employed in the determination of a material's identity via diffraction pattern. In addition to identifying phases, XRD can reveal how the structure actually differs from the ideal one due to internal tensions and flaws. Atoms in a crystal are arranged in regular arrays, and X-rays can be thought of as electromagnetic radiation waves. In a crystal, incoming X rays are scattered mostly because of the atoms' electrons. This effect is known as elastic scattering where electrons act as the scatterer. When scatterers are arranged in a grid, the resulting spherical waves also have a regular appearance. Destructive interference causes these waves to cancel out in most directions, but in a small number of directions, as defined by Bragg's law, they actually add:

$$2d\sin\theta = n\lambda \quad (2.1)$$

Where d , the interplanar spacing, is defined by the distance between diffracting planes, θ is the incident angle of X-ray on crystal, n is an integer, and λ is the beam wavelength (for Cu- $k\alpha$ source it is about 0.154 nm). A perfect crystal would stretch indefinitely in all directions; because to their finite size, no crystals are perfect. This variation from perfect crystallinity causes the diffraction peaks to broaden. Crystallite size and lattice strain are the two principal parameters acquired using diffraction peak width analysis. Crystallite size is a measurement of the size of domains that diffract coherently. Due to the creation of

polycrystalline aggregates, the crystallite size of particles is not often the same as their particle size [7]. The distribution of lattice constants caused by crystal defects, such as lattice dislocations, is quantified by lattice strain [8]. The triple junction found in grain boundary, contact or sinter stresses, stacking faults inside the crystal, and coherency stresses are other sources of strain.

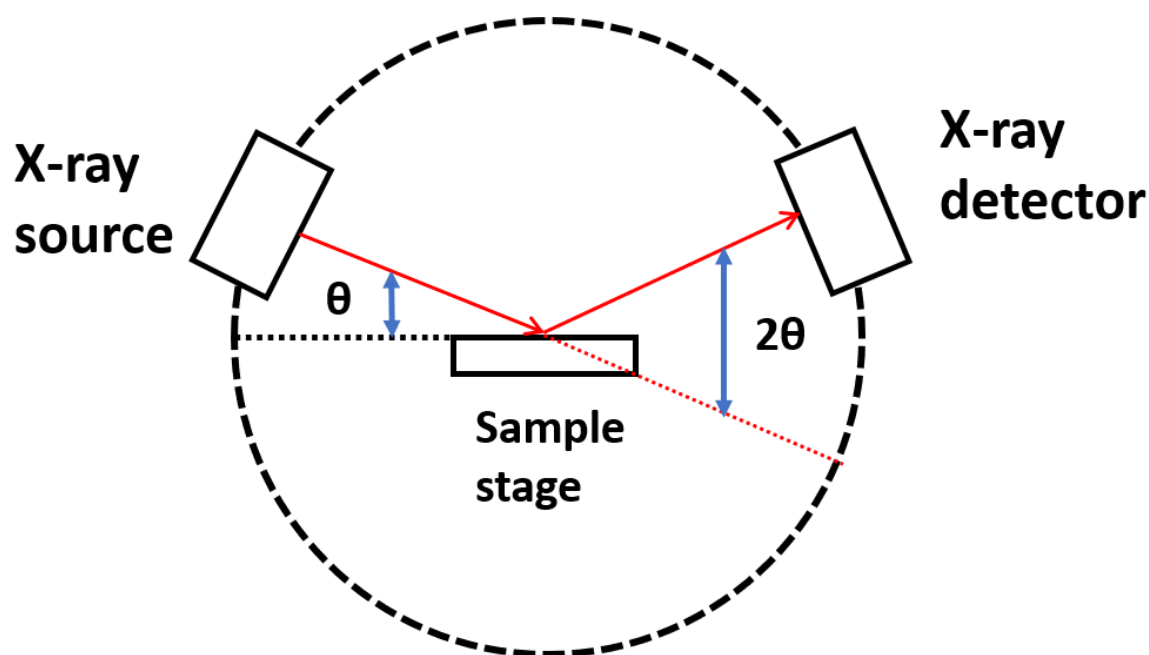


Figure 2.3: Schematic diagram of x-ray diffraction

2.3.2. *Field Emission Scanning Electron Microscopy (FESEM)*

Technique & Data Analysis:

The FE-SEM analysis helps us better understand the surface morphology of the synthesized nanomaterial. The FESEM is an example of a microscope that uses negatively charged electrons in place of light. A field emission source frees these electrons. The electrons scan the item in a zigzag motion. Imaging the microstructure of materials, field emission scanning electron microscopy (FE-SEM) is a cutting-edge technique. Due to the tendency of gas molecules to disrupt the electron beam and the necessity of generated secondary as well as backscattered electrons for imaging, FE-SEM is normally carried out in a high

vacuum. Field emission sources release electrons, that are accelerated by a strong electric field gradient. The primary electrons are concentrated and deflected by electronic lenses to create a narrow scan beam within the high vacuum column, which is then utilised to bombard the item resulting, emission of secondary electrons from each place on the item. The surface structure of an object is reflected in the angle and speed of these secondary electrons. The secondary electrons are trapped by a detector, which results in generation of an electric current. Amplification and digitization bring this signal into view on a screen or as a data-rich digital image [9].

Also increase in grain size provokes the electrical conductivity increment [10].

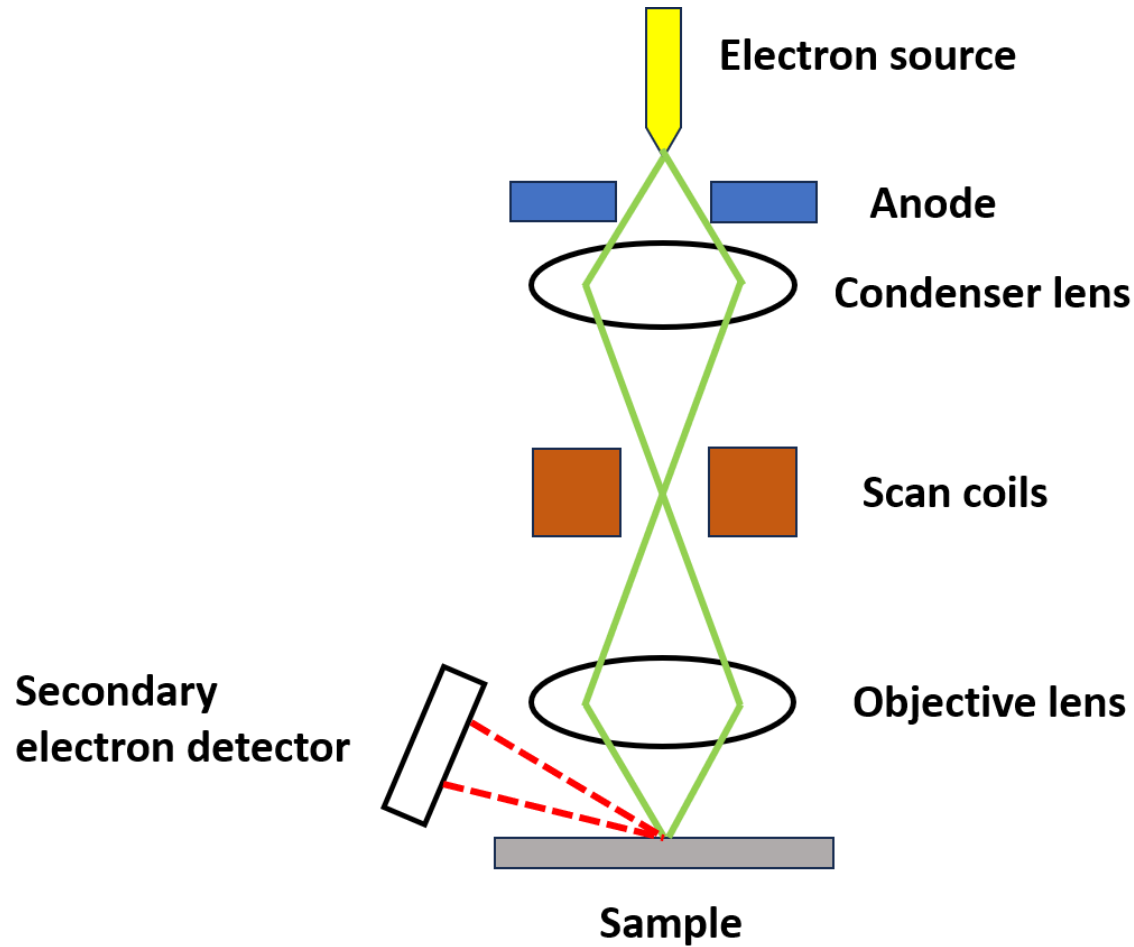


Figure 2.4: Schematic diagram of field effect scanning electron microscopy

2.3.3. Energy Dispersive X-Ray Spectroscopy (EDS) Technique and Elemental Mapping:

Chemical characterization and elemental analysis of materials are made possible by energy-dispersive X-ray spectroscopy (EDS, abbr. EDX or XEDS), an analytical technique. Excited by an external energy source (such as the electron beam of an electron microscope), a sample releases a core-shell electron to dissipate some of the absorbed energy. After this, an outer-shell electron with a higher energy takes its place, releasing the excess in the form of X-rays with a unique spectrum for each atom. This enables for the compositional examination of a certain sample volume that has been excited by the energy source. The element may be determined by looking at where the peaks in the spectrum appear, while the concentration can be determined by looking at how strong the signal is. It has already been mentioned that an electron beam has enough energy to expel core-shell electrons, leading to X-ray emission. When an EDS detector is attached to an electron microscope, atomic-level compositional details become available. As the electron probe is scanned across the sample, characteristic X-rays are generated and analysed; each recorded EDS spectra is assigned to a specific spot on the sample. Signal strength and spectrum cleanliness are two factors that affect the reliability of the findings. Trace element detection and dosage minimization (which permits faster recording and artifact-free findings) are especially reliant on a high signal-to-noise ratio. The number of spurious peaks observed is related to how clean the electron column is, which is a result of the electron column's constituent materials.

2.3.4. Raman Spectroscopy Technique & Data Analysis:

Raman spectroscopy, a non-destructive chemical analysis method, has the ability to disclose information about a substance's molecular interactions, crystallinity, phase, and polymorphism. It is based upon the interaction of light

with the chemical bonds within a substance where scattered light is utilised to determine the vibrational energy modes of a sample. According to the Raman effect, which forms the basis of Raman spectroscopy, excited tissue molecules will reflect light of a different wavelength when exposed to incoming light (750-850 nm).

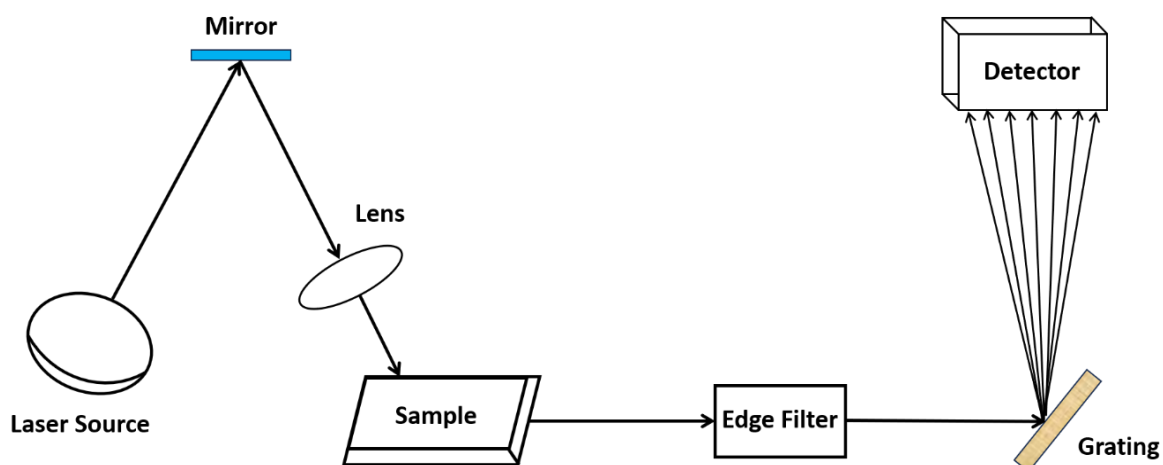


Figure 2.5: Schematic diagram of Raman spectroscopy

2.3.5. X-Ray Photoelectron Spectroscopy (XPS) Technique & Data Analysis:

X-ray photoelectron spectroscopy (XPS), one of the spectroscopic techniques that is a quantitative method, and sensible to the surface of the material. It uses the photoelectric effect to determine the elements present within or on the surface of a material (elemental composition), along with their chemical state, and the overall electronic structure and the electronic state density of the material. X-ray photoelectron spectroscopy (XPS) is a powerful method of measurement since it reveals not only the presence but also the bonding relationships of individual components. By exciting inner orbital and bonding electrons with a focused X-ray beam, X-ray photoelectron spectroscopy (XPS)

can be utilised to assess the elemental composition and oxidation states of elements on the surface of particles.

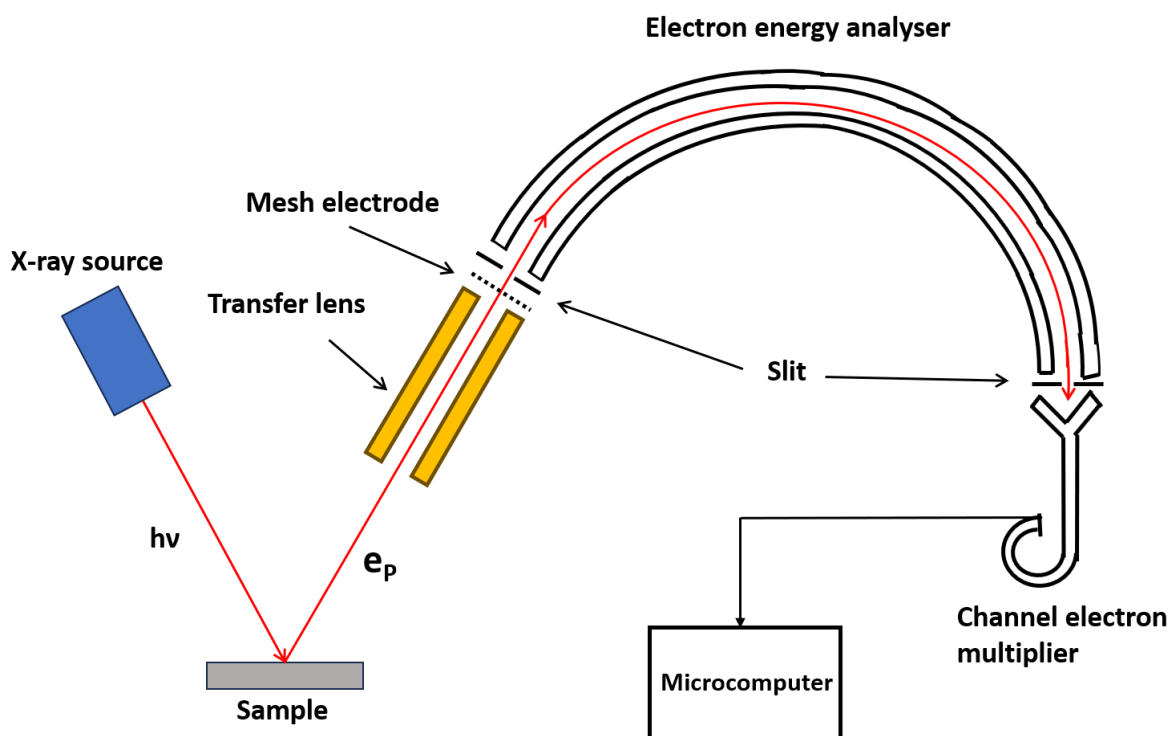


Figure 2.6: Schematic diagram of x-ray photoelectron spectrometer

2.3.6. Brunauer–Emmett–Teller (BET) Technique:

BET analysis is an analytical technique used to determine specific surface areas and pore size distributions of solid materials through the gas adsorption process. BET theory is applicable to multilayer adsorption systems and is typically used to assess specific surface area using probing gases that do not chemically react with material surfaces as adsorbates. The idea was published by Edward Teller, Paul Hugh Emmett, and Stephen Brunauer in the Journal of the American Chemical Society in 1938 [11].

2.3.6.1. Importance of surface of semiconductor:

Owing to the fact that semiconductor devices are constructed on or near the semiconductor surface, crystal plane alignments and their characteristics at

the surface are significant. Semiconductor surfaces are inherently unstable, both chemically and electrically. Passivation of compound semiconductor surfaces is a major issue because of the significant impact that surface features have great effect on the performance of semiconductor devices. Chemical reactivity of the dangling bonds is one source of electrical passivation; nevertheless, interfacial charge is commonly present, which Coulombically repels minority carriers and so limits recombination [12]. Due to their relatively delocalized bonding, metals' density of states exhibits smoother corrugations than those of semiconductor surfaces [13]. Radiative recombination is triggered by the merging of conduction-band electrons with valence-band holes. Dangling bonds are formed when the surface of a semiconductor contains defects like vacancies. The vacancies' energies are centred around the bandgap's midpoint. These energy levels, known as trap states, are actively involved in electron-hole recombination. This recombination is called non-radiative recombination and have severe consequences for the functionality and lifetime of the semiconductor device [14]. The injected carrier lifetime in the semiconductor is a structure-dependent characteristic. This occurs because flaws in the semiconductor serves as a channel for the recombination process. For a semiconductor that has many surface states, the Fermi level is said to be “pinned” at almost the mid-gap of the semiconductor. For over twenty years, researchers have been trying to find a solution to the issue of Fermi-level pinning at semiconductor surfaces and interfaces. A semiconductor surface or interface that contains numerous dangling bonds can be removed by chemical treatment; a method known as surface passivation. It was demonstrated that the Fermi level could be unpinned using a number of different passivation techniques.

2.3.6.2. *About the Technique:*

The method relies on the physical adsorption of an inert gas, like nitrogen, onto the sample's solid surface. The measured specific surface area is given in m^2

/ g. BET analysis is mostly used for analysing study of nanomaterials, improvement of cement and concrete fineness, characterisation of catalysts, adsorption efficiency of gas purifiers, and so on. Physisorption of an inert gas, commonly nitrogen, argon, or krypton, on the surface of the BET sample is used to calculate the specific surface area of the sample. Surface area measurements should be made in an isothermal environment, where the temperature is held constant throughout. The ideal temperature is determined by the inert gas being utilised (for instance, liquid nitrogen requires a temperature of 77 K). The sample's characteristics determine which inert gas is most suited for the analysis. The tiny gas molecules attract themselves to the surface of the solid sample forming a porous structure generating a monolayer of adsorbed gas. The sample is heated in an environment other than nitrogen once the gaseous monolayer of molecules has been produced. Adsorbed nitrogen gas molecules can be released from the sample's surface in this way. Once the number of gas molecules emitted is known, the sample's surface area and porosity may be computed.

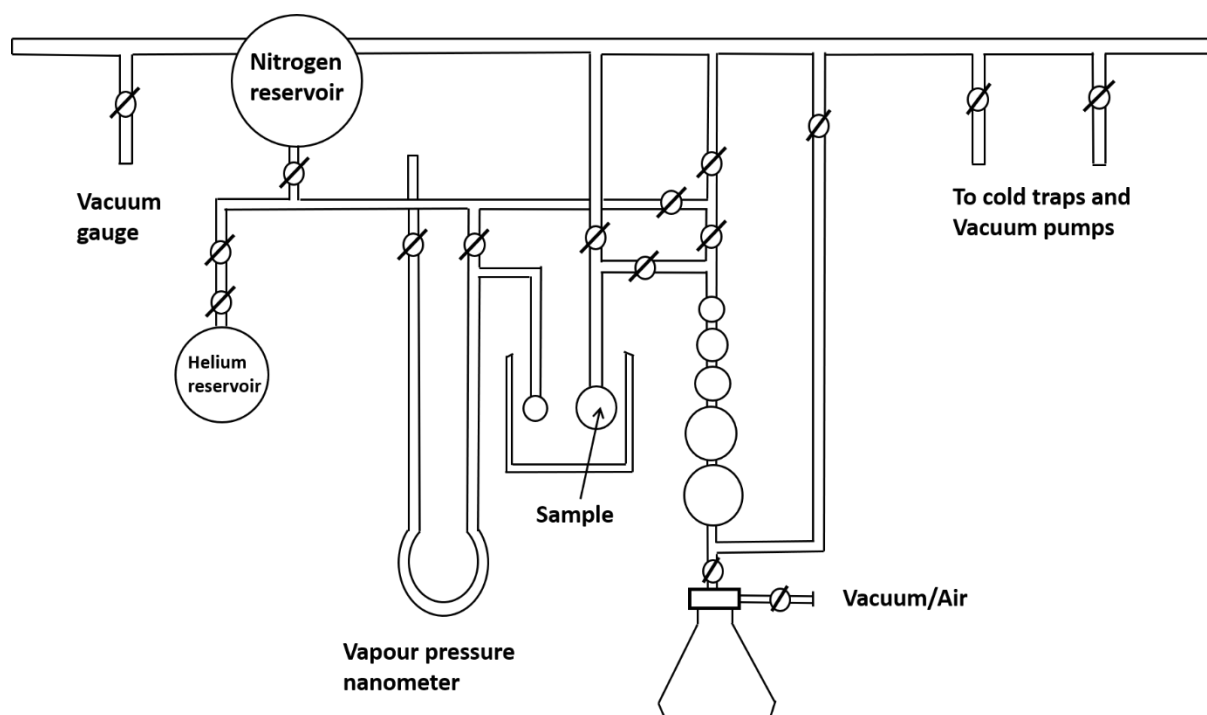


Figure 2.7: Schematic diagram of BET instrument

2.3.6.3. Effect of Surface in nano dimension:

Large surface-to-volume ratios are offered by all nanomaterials, making their surfaces the dominant factor in a variety of physical and chemical processes. Due to the low concentration of surface atoms in a bulk solid, broken chemical bonds on the outside have a negligible effect on the material's properties. However, the surface-to-volume ratio scales inversely with linear dimensions for all substances. As size decreases, the role of the surface grows and eventually becomes dominating. Surfaces at the nanoscale can substantially alter some qualities and generate entirely new phenomena. Smaller particle size leads the fraction of the atoms to become larger at the surface which causes the average binding energy per atom to be higher. The surface-to-volume ratio scales with the size inversely, and for this inverse relation other properties like temperature of phase transition and solubility of the material in any medium also obey the same scaling law.

2.3.7. Ultraviolet-visible (UV-VIS) Analysis:

Absorption or reflectance spectroscopy in the ultraviolet and the whole, neighbouring visible parts of the electromagnetic spectrum is referred to as UV-Vis spectroscopy, also known as UV-Visible spectrophotometry (UV-Vis or UV/Vis). This method is frequently used in both practical and theoretical settings due to its low cost and straightforward implementation.

2.3.7.1. Bandgap Measurement:

There is a prohibited energy range in which there is no allowed state for any semiconductor. Above and below this energy gap are permissible energy regions or energy bands. The upper bands are known as the conduction bands, while the lower bands are referred to as the valance bands. The difference in energy between the lowest of conduction band and the highest of valence band is

known as the bandgap or energy gap, and it is one of the most crucial parameters in semiconductor physics. Unlike metal the conduction band and valance band of a typical semiconductor doesn't overlay but there is an energy gap between 0-5 eV. The most important method for determining the band structures of semiconductors is optical measurement. It is possible for photon-induced electronic transitions to occur between different bands, thereby determining the energy bandgap. The absorption coefficient of semiconductors is a significant parameter which is a function of wavelength or the photon energy. The absorption coefficient can be expressed as $\alpha \propto (h\nu - E_g)^n$ where 'hν' is the photon energy and 'n' is a constant. For direct bandgap materials, transitions mostly occur between two bands of the same 'k' (extinction coefficient) value. For indirect transitions, phonons are involved in order to conserve momentum. By alloying or doping multiple compounds, some of the semiconductor materials are tuneable, e.g., in band gap or lattice constant.

2.3.7.2. Theoretical overview:

Absorption in the UV-Vis range by the material is all that is needed. These materials are called as chromophore. In addition to the wavelength, other important parameters include absorbance (A), transmittance (%T), and reflectance (%R). An excited state is produced when an electron in the chromophore is boosted into a higher energy molecular orbital by the absorbed photon. While solutions are the most typical medium for spectroscopic examination, solids and gases can also be examined. According to the Beer-Lambert law [15, 16, 17]

$$I = I_0 e^{-\alpha x} \quad (2.2)$$

Where x is the pathlength travelled by light i.e., thickness of the solution (width of the cuvette), α is the absorption coefficient, ' I ' is the final intensity of the light

after passing through the solution and ' I_0 ' is the primary intensity of light incident upon the solution.

If thickness of the cuvette is ' l ' then the above equation can be written as

$$I = I_0 e^{-\alpha l} \quad (2.3)$$

Or,

$$\frac{I}{I_0} = e^{-\alpha l} \quad (2.4)$$

Taking logarithm in both sides of the equation,

$$\log\left(\frac{I}{I_0}\right) = \log(e^{-\alpha l}) = -\alpha l * \log(e) \quad (2.5)$$

Or,

$$\log\left(\frac{I_0}{I}\right) = \alpha l * \log(e) \quad (2.6)$$

The value of $\log(e)$ is 0.4343

The absorbance value recorded by the spectrophotometer is

$$A = \log\left(\frac{I_0}{I}\right) \quad (2.7)$$

So,

$$\alpha = 2.303 * A * \frac{1}{l} \quad (2.8)$$

As width of the cuvette is 1cm one can easily calculate the value of α .

The absorption coefficient characterises the dimming of light as it travels through a substance.

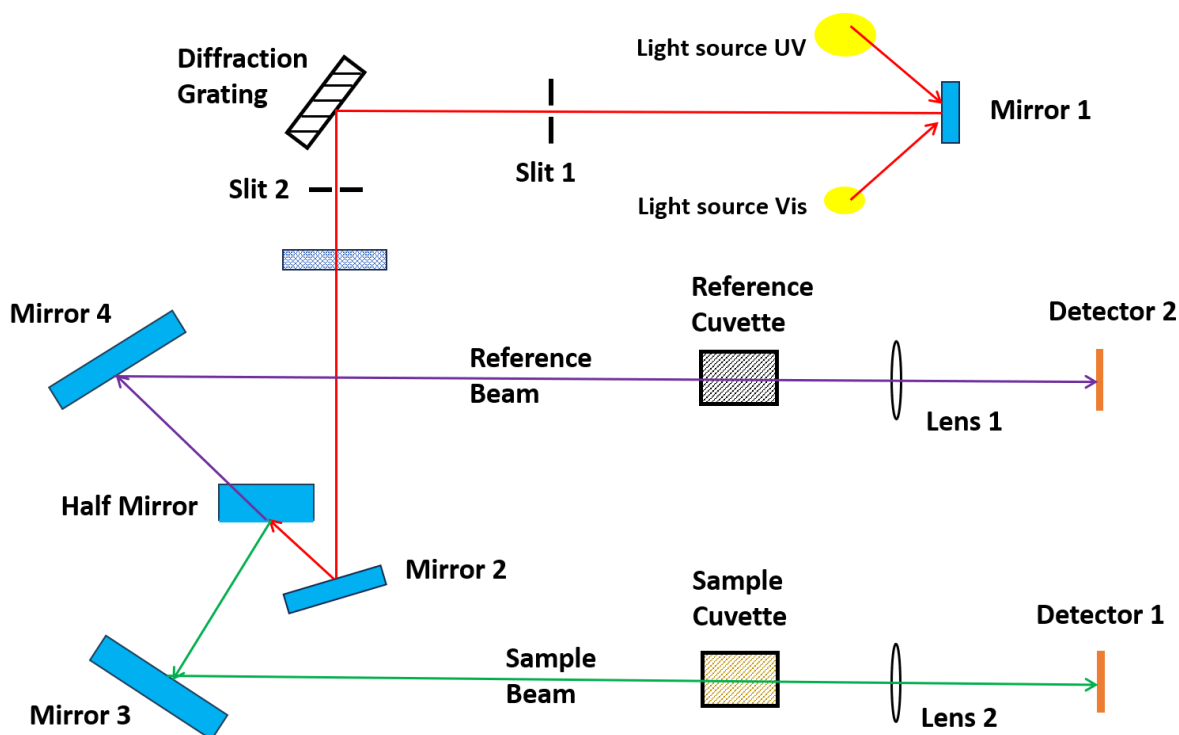


Figure 2.8: Schematic diagram of UV-Visible spectrophotometer

For an optical process, it can be thought of as the sum of the absorption cross sections per unit volume of the substance. The greater the coefficient, the shorter the wavelength of light, that can be transmitted through a material before it is absorbed.

2.3.8. Fourier transformed infrared Spectroscopy Technique and & Data Analysis:

The term "Fourier transform infrared" (FTIR) refers to the most popular kind of infrared spectroscopy. High-resolution data are collected over a wide spectral range by an FTIR spectrometer. All infrared spectroscopies operate under the premise that some IR energy is absorbed when it passes through a material. The radiation that passes through the sample is recorded.

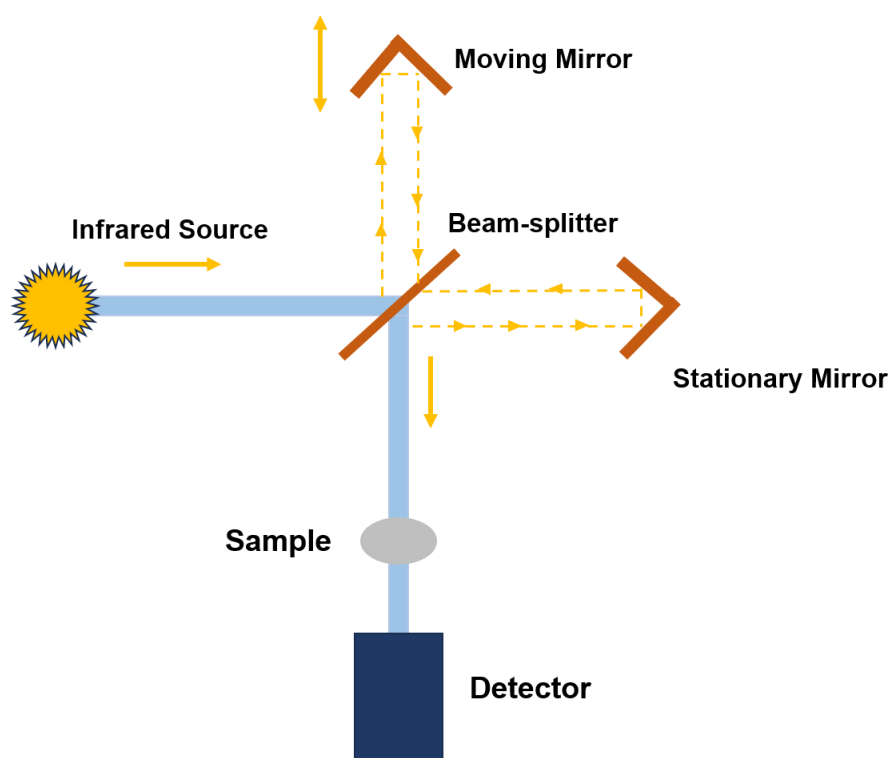


Figure 2.9: Schematic diagram of FTIR

With this method, a beam of light with multiple frequencies is directed at the sample simultaneously, and the amount of that beam that is absorbed by the sample is measured. A second data point is then obtained by altering the beam to comprise a different mix of frequencies. Over a short period of time, this procedure is quickly repeated numerous times.

FTIR is used to investigate various nanomaterials. With the aid of FTIR, the bond characteristics associated with different organic and inorganic nanomaterials may be identified, and their quantitative study can be carried out. When used to identify mixtures of chemicals, FTIR is only really useful for validating the identity of pure substances. The method is based on locating functional groups in molecules that vibrate when exposed to particular light wavelengths (either through stretching or bending in different ways). The intensity of these vibrations (% transmission) is mapped against the light

frequency (cm^{-1}) incident on the sample to generate an FTIR spectrum. FTIR spectra have fingerprint sections that are unique to the tested chemical.

The fixed-point microregion analysis of solid, gas, and liquid, quantitative analysis of the chemical characteristics, and the identification of organic compounds, daughter minerals, and solid components in the inclusions are some characteristics of the FTIR method.

It is easy to maintain and operate, has a high data collection speed, excellent spectrum quality, and good reproducibility of data. However, the composition of monoatomic (ion) compounds or uncommon gases cannot be determined using either method.

2.3.9. Cyclic Voltammetry& Data Analysis:

Catalysis is an example of a chemical reaction that begins with the transfer of an electron, and CV is a useful technique for studying such reactions. Cyclic voltammetry is a sophisticated potentiometric and voltametric method. The chemical undergoes either oxidation (electrons lost) or reduction (electrons gained) during the scanning process. The direction of the rising potential will determine this. Cyclic voltammetry (CV), an electrochemical potentio-dynamic experiment, is a type of voltammetry which is used for detail analysis of redox properties of compounds and their interfacial structures. Analysis of a cyclic voltammogram data through graphical aspect gives the peak positions, also known as redox peaks, i.e., peaks generated for reduction and oxidation of the material, foretelling the capacitive behaviour of the electrode. Hence, the electrode potential of the point at which the material gets itself oxidized or reduced may be established.

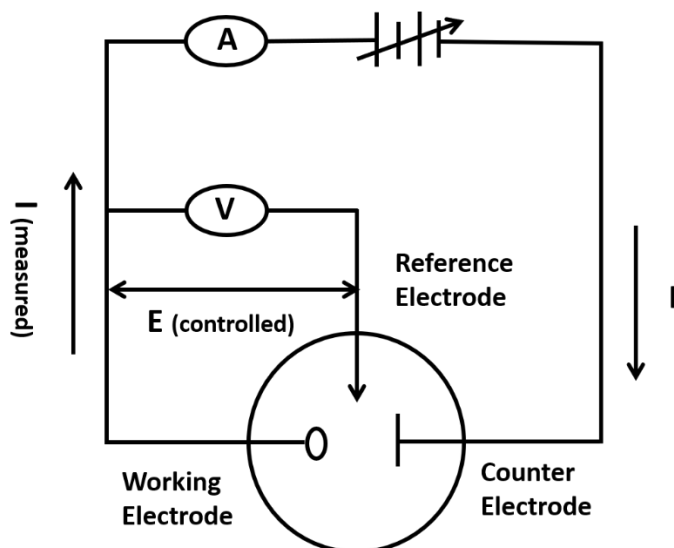


Figure 2.10: Schematic diagram of cyclic voltammetry

2.3.10. Thermogravimetric (TGA) & Data Analysis:

Thermogravimetric analysis (TGA), another analytical technique, is needed for determining a material's thermal stability. It is also used to determine the fraction of volatile components remain inside the material by monitoring the weight change that occurs as the material is being heated.

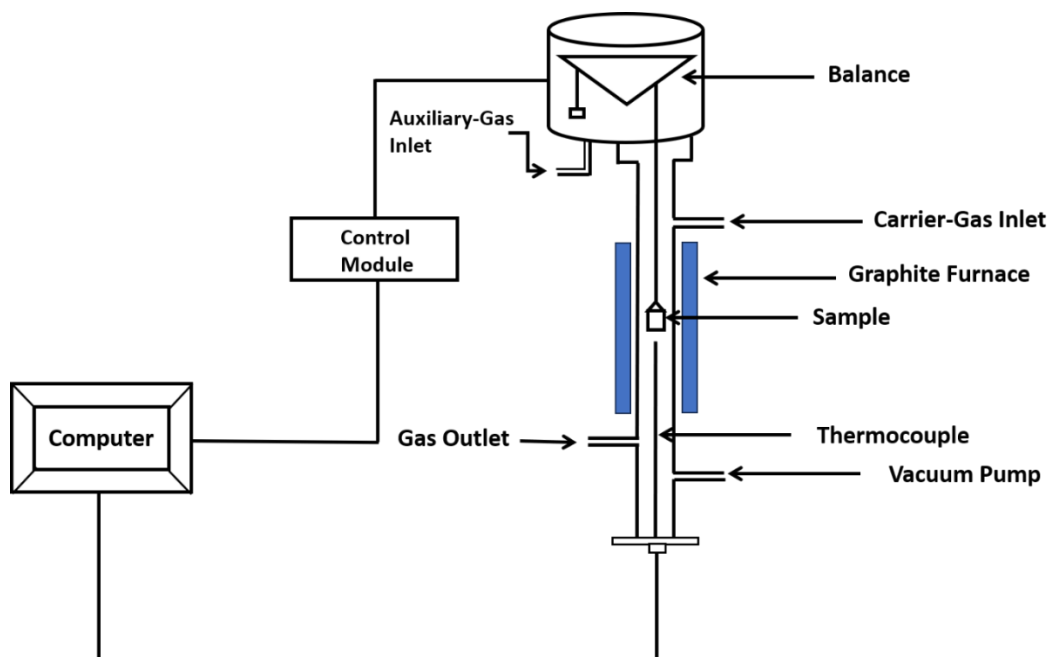


Figure 2.11: Schematic diagram of TGA instrument

2.3.11. *Vibrating-Sample Magnetometer (VSM) Technique & Analysis:*

Vibrating Sample Magnetometer is a versatile magnetic property measurement instrument. It is commonly used to study magnetic phases, the Curie point, the ratio of different magnetic phases, and the spin re-orientation point, among other phenomena. The magnetization is measured by vibrating the sample in the presence of a static magnetic field. The principle resides in the technique for detecting the variation in magnetic flux. The sample is positioned between two coils. When the sample vibrates, the change in flux within the coils generates an electromotive force (emf) within the pickup coils. A Lock-In Amplifier is used to detect signals from coils. A VSM includes a vibrator, DC magnet (typically superconducting), magnetic power supply, cooling device, temperature controller, and Lock-In Amplifier. Figure provides an example of a VSM diagram. The VSM is utilised to determine the change of the magnetic properties of a material with variable temperature, magnetic field, and time. In VSM, one can also conduct measurements dependent on the angle. By measuring time-dependent magnetization, it is also possible to calculate magnetic relaxation.

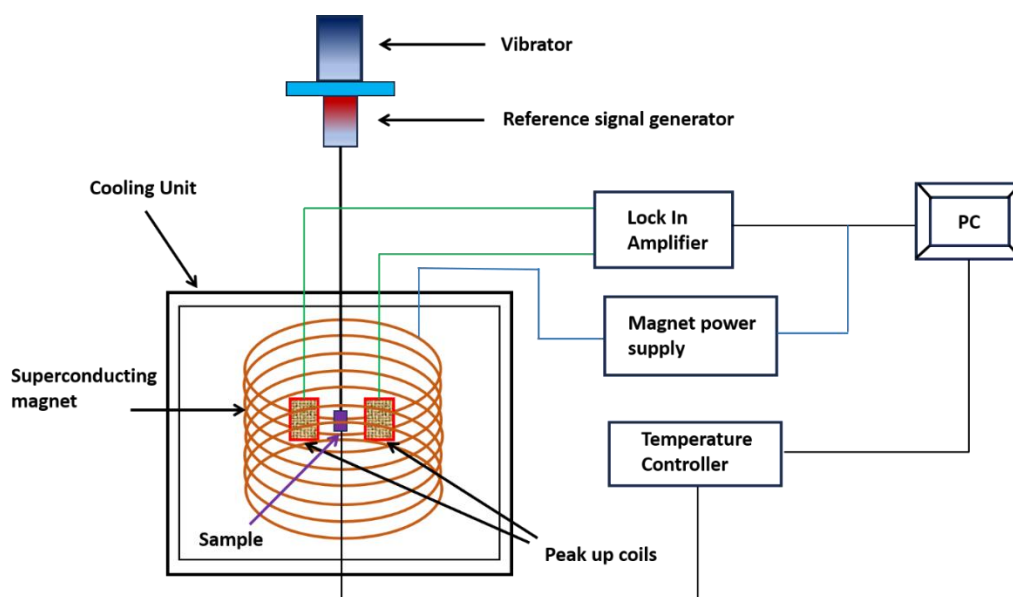


Figure 2.12: Schematic diagram of VSM instrument

2.4. Device fabrication:

For the device fabrication i.e., for make an MS junction it is necessary to choose a suitable metal for the metal portion. For n-type semiconductor aluminium (Al) or platinum (Pt) are mostly preferable to form a rectifying contact. Although silver (Ag) is an excellent electrical conductor, it is rarely employed in metal semiconductor junction due to its susceptibility to oxidation and tarnish when exposed to air.

For the thin film applications indium tin oxide (ITO) coated glass can be used as conducting layer and can operate at high temperatures also.

2.4.1. Aluminium in Device fabrication:

Aluminium, the most common metal on Earth, is also one of the most malleable, ductile, and lightweight metals available. It is relatively soft among many other metals. It's a decent electrical and thermal conductor with reasonable resistance to corrosion. In addition, it is surprisingly harmless and can be recycled without losing any of its natural properties. On the other hand, platinum is high pricing metal and also much heavier. Also, the work function of Al is 4.2 eV which is low compared to that of platinum (5.65 eV).

2.4.2. Indium Tin Oxide (ITO) coated glass-substrate:

ITO is a ternary compound made up of indium (In), tin (Sn), and oxygen (O) [74% In, 18% Sn, and 8% O]. Because of its electrical conductivity, optical transparency, ease of deposition as a thin layer, and chemical resistance to moisture, indium tin oxide is one of the most extensively used transparent conducting oxides. Thin films of indium tin oxide are most commonly deposited on glass surfaces by physical vapor deposition. Its optical transmittance for a thin film can be greater than 80%, and its electrical resistivity is only $10^{-4} \Omega\text{-cm}$ [18].

2.4.3. Fabrication Procedure:

The metal semiconductor junctions are fabricated in a vertical sandwich configuration like Al/synthesized material/ITO which is an easier method of junction fabrication. Prior to all well cleaning of ITO is required for this purpose. With this intention, first, the ITO coated glass substrates are cleaned successively by ultrasonication with mild basic water (by adding small amount of purified sodium hydroxide in distilled water), acetone, ethanol, and distilled water. Then the samples are well dispersed/dissolved in suitable medium under ultrasonication and spin coated on to the pre-cleaned ITO substrate at a certain rpm for few times. The films are then dried inside a vacuum chamber for few hours. Thickness of the deposited thin films are measured at about 1 μm by surface profiler. Then aluminium metal is deposited on the thin film of the material by thermal evaporation using an electron gun in a vacuum coating unit of HIND-HIVAC under much low pressure of 10^{-6} m-barr to get the required metal–semiconductor interface. The effective junctional area is maintained as $7.065 \times 10^{-6} \text{ m}^2$ using a shadow mask upon the film during metal deposition. The schematic device structure is given in Figure.

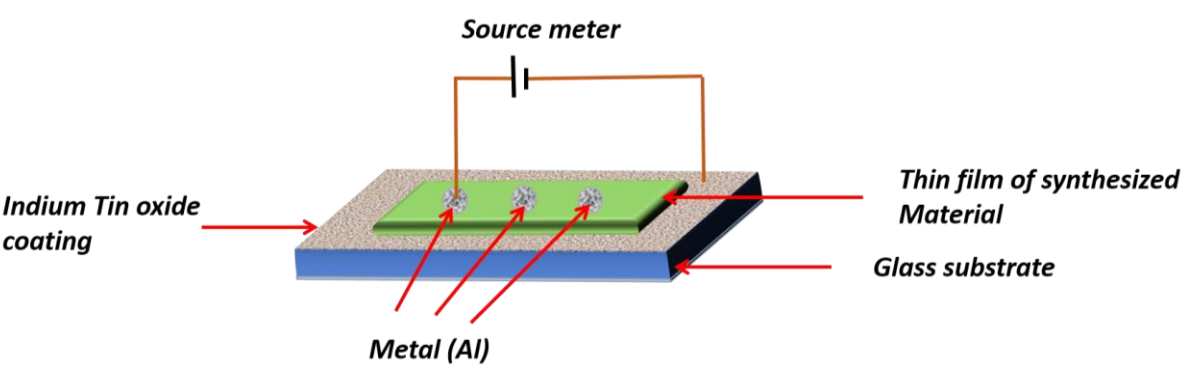


Figure 2.13: Schematic diagram of fabricated metal-semiconductor junction

References:

1. C. Granqvist, R. Buhrman, J. Wyns, and A. Sievers, *Far-Infrared Absorption in Ultrafine Al Particles*, Physical Review Letters, 1976, **37**, 10, 625-629
doi:10.1103/PhysRevLett.37.625
2. C. Hayashi, R. Uyeda, and A. Tasaki, *Ultra-fine particles: exploratory science and technology*, Noyes Publications, 1997 Translation of the Japan report of the related ERATO Project 1981-86
3. C. J. Gommers, *Ostwald ripening of confined nanoparticles: Chemomechanical coupling in nanopores*, Nanoscale, 2019, **11**, 15, 7386–7393
doi:10.1039/C9NR01349K. PMID 30938749. S2CID 91189669
4. A. Baptista, F. Silva, J. Porteiro, J. Míguez, and G. Pinto, *Sputtering physical vapour deposition (PVD) coatings: A critical review on process improvement and market trend demands*, Coatings, 2018, **8**, 402
doi.org/10.3390/coatings8110402
5. M. A. Shah, M. A. Bhat, and J. P. Davim, *Nanotechnology Applications for Improvements in Energy Efficiency and Environmental Management*, IGI Global, Hershey, PA, USA, 2015, Nanomaterials, novel preparation routes, and characterizations, 1–40.
6. **www.jove.com/science-education/10446/x-ray-diffraction**
7. K. Ramakanth, *Basic of Diffraction and Its Application*, I.K. International Publishing House Pvt. Ltd, New Dehli, 2007
8. J. Zhang, Y. Zhang, K.W. Xu, and V. Ji, *General compliance transformation relation and applications for anisotropic hexagonal metals*, Solid State Communications, 2006, **139**, 3, 87-91
doi.org/10.1016/j.ssc.2006.05.026
9. D. Semnani, *Geometrical characterization of electrospun nanofibers*, Electrospun nanofibers, 2017, 151-180
doi.org/10.1016/B978-0-08-100907-9.00007-6
10. X. Tong, H. Zhang, and D. Y. Li, *Effect of annealing treatment on mechanical properties of nanocrystalline α -iron: an atomistic study*, Scientific reports, 2015, 5, 8459
doi.org/10.1038/srep08459
11. S. Brunauer, P. H. Emmett, and E. Teller, *Adsorption of Gases in Multimolecular Layers*, Journal of the American Chemical Society, 1938, **60**, 2, 309–319
doi:10.1021/ja01269a023. ISSN 0002-7863

12. M. Chen, J. Hack, A. Iyer, X. Lin, and R. L. Opila, *Chemical and Electrical Passivation of Semiconductor Surfaces*, 2018, 547-552
doi.org/10.1016/B978-0-12-409547-2.13127-0
13. C. J. Roberts, M. C. Davies, S. J. B. Tendler, and P. Williams, *Scanning Probe Microscopy, Applications*, 1999
doi.org/10.1006/rwsp.2000.0271
14. AK Viswanath, *Surface and interfacial recombination in semiconductors*, Handbook of surfaces and interfaces of materials, 2001, chapter 3
doi.org/10.1016/B978-012513910-6/50010-4
15. P. Bouguer, *Essai d'optique sur la gradation de la lumière*, Paris, France, Claude Jombert, 1729, 16–22
16. J. H. Lambert, *Photometria sive de mensura et gradibus luminis*, colorum et umbrae, Augsburg, Germany, Eberhardt Klett, 1760
17. Beer, *Bestimmung der Absorption des rothen Lichts in farbigen Flüssigkeiten*, Annalen der Physik und Chemie, 1852, **162**, 5, 78–88
18. Chen, and Zhangxian, *Fabrication of Highly Transparent and Conductive Indium–Tin Oxide Thin Films with a High Figure of Merit via Solution Processing*, Langmuir, 2013, **29**, 45, 13836–13842
doi.org/10.1021/la4033282. PMID 24117323

Chapter 3

Outline of the thesis

It is evident from the preceding sections that inorganic compound semiconducting nanomaterials have great potential to lead the way in nanoscience in the future. Also, rGO as a graphene substitute makes a strong place to improve the performance of a nanomaterial. On the other hand, metal semiconductor junction plays a crucial role in nanotechnology as well because they are commonly found in a wide range of electronic devices, including transistors, photodetectors, and solar cells. Thus, evaluation of different inorganic compound semiconductors and the creation of rGO-inorganic nanocomposites, accurate and thorough characterization of them, performance in MS junction, and details analysis of the devices could be highly beneficial for the development of next-generation technologies. Researchers are also interested in these materials' charge transfer characteristics. During this research project, various inorganic compound semiconducting nanomaterials have been synthesized, characterised, and their device application has been thoroughly examined. Below is a quick summary of the upcoming chapters.

Chapter 4 describes the synthesis of rGO (reduced graphene oxide)-SnO₂ nanocomposite via hydrothermal of GO and Tin tetra chloride pentahydrate (SnCl₄·5H₂O) and its application in a photo-sensitive Schottky diode (Photodiode). Charge carrier transport mechanism is also studied with the help of space charge limited current theory.

Chapter 5 demonstrates the temperature dependent performance of the rGO-SnO₂ based Schottky device. Theoretical and experimental values of the Richardson constant are calculated and compared. Assuming a Gaussian distribution of the barrier heights resulting from barrier height inhomogeneities at the metal-semiconductor interface provides a precise explanation for the deviation in two values and modified value has also been calculated.

Chapter 6 reports the Schottky behaviour of another MS junction fabricated by two different shaped ZnO nanomaterial obtained by different synthesis method. The variation of shape dependent properties is also explained. Al/ZnO interface is studied by current-voltage, impedance spectroscopy and capacitance voltage measurements. Use of the interface as photodiode is also analysed.

In Chapter 7, the annealing effect after synthesis of cobalt sulfide on its structural, optical, magnetic properties and Al/CoS₂ interface are studied. Charge carrier mobility, life time and carrier diffusion length are extracted from impedance analysis and current-voltage characteristics.

Chapter 8 demonstrates the effect of maintained temperature during solvothermal synthesis of MoSe₂ on its properties and device performance is explained. Two different methods of Schottky parameters extraction are also reported.

Chapter 9 presents a brief summary and conclusion of the entire work.

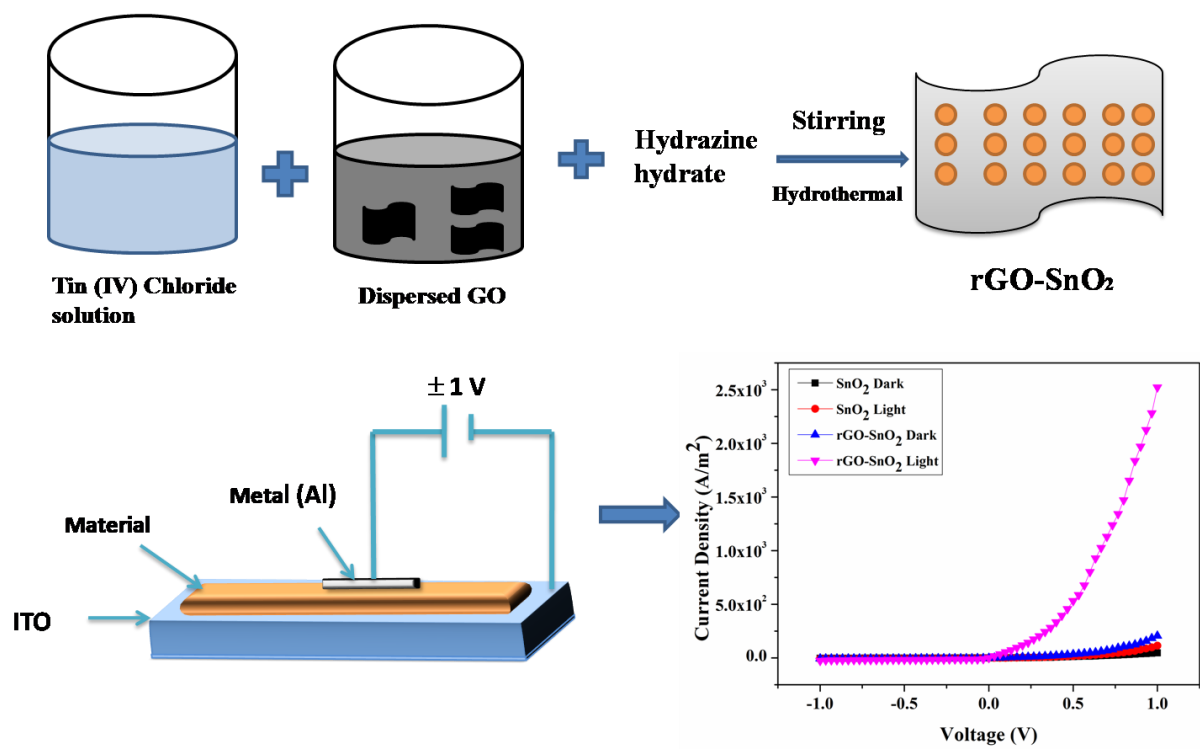
Chapter 4

Improved charge transport properties
of graphene incorporated tin oxide
based Schottky diode over pure one

Abstract

Graphene and its nanocomposites with different semiconductor materials have attracted significant research interest in the last decade due to their improved performance in various fields. In this report, SnO_2 and a reduced graphene oxide (rGO)- SnO_2 composite is synthesized via hydrothermal method. Structural, optical and electrical characterization of the material is performed. Incorporation of rGO increases the light absorption and reduces the band gap of SnO_2 . Schottky barrier formation at metal-semiconductor junction is important for various applications. Here, we describe the performance of SnO_2 and rGO- SnO_2 based Schottky diode. Important diode parameters like rectification ratio, ideality factor, barrier height and series resistances are calculated from forward Current density-voltage (J-V) characteristics. rGO- SnO_2 shows much better performance compared to SnO_2 . Analysis of Photoresponse behaviour reveals that rGO- SnO_2 shows photosensitivity of about 9.95 which is higher than that of SnO_2 (2.42). After incorporation of rGO, other diode parameters and transport properties were also improved. To gain better insight on charge transport properties, space charge limited current theory has been utilized. In rGO- SnO_2 , carrier mobility is increased by 62% compared to SnO_2 , implying that rGO- SnO_2 has better charge transport due to enhanced electron hole separation which is attribute to the presence of graphene.

Graphical Abstract



4.1. *Introduction:*

Graphene is a two-dimensional material with monolayer honeycomb nanostructure composed of sp^2 hybridized carbon atoms [1]. It has very large surface area ($2630 \text{ m}^2/\text{g}$) which facilitates higher absorption of light and greater interfacial contact [2]. It is a very thin but strong material with high carrier mobility and possesses optical transparency of wide wavelength range [3]. Nowadays, with these excellent properties, graphene has become good candidates for uses in different applications such as optoelectronic devices, photosensors, supercapacitors, solar cell etc [4, 5]. Graphene has already been used in numerous applications of Schottky diodes which is a key part of many electronic devices [6]. Higher rate of recombination, interface quality, cost and toxicity of the used materials are the issues for Schottky barrier diode (SBD) [7]. To overcome these problems, a number of semiconductor materials have been explored. Graphene based nanocomposite materials are especially attractive choice for improved performance.

Nowadays, metal oxide-based semiconductors are of great interest due to their versatile properties. They are applied frequently in field effect transistor, chemical sensors and memory application [8]. Among them SnO_2 is used widely for its low resistivity, excellent electron mobility, non-toxicity, good stability, low cost and availability [9]. It has application as gas sensors, anode in lithium-ion batteries etc. [10] SnO_2 is an n-type wide band gap semiconductor (bandgap of bulk SnO_2 is 3.6 eV) [11]. So, it is only sensitive to lower light wavelength. Also, it has higher recombination rate. If its bandgap and recombination rate can be reduced, we can use it for photovoltaic application and other optoelectronic devices. It has been shown that if graphene is incorporated in the SnO_2 , the light absorption range of SnO_2 can be increased.

According to earlier reports, graphene-SnO₂ composite is promising for its effective changes in dielectric properties, gas sensing, supercapacitor, and field emission study [12]. But investigation of Schottky diode properties through graphene-SnO₂/metal junction has gained rare notice. It motivated us to investigate graphene-SnO₂ based Schottky barrier diode compared to the Schottky barrier diode fabricated with pure SnO₂, which can be beneficial to understand the effect of graphene on device performance and charge transport properties of the material. As pure graphene is hard to achieve, reduced graphene oxide was used. Graphene oxide (GO) can be produced using a modified Hummers' method and after that followed by a reduction procedure GO can be achieved [13].

In this work, we compare the performance of rGO-SnO₂ Schottky diode to SnO₂ based Schottky diode. Structural, optical and morphological characterization was done for both samples. Schottky devices with the sandwich configuration of metal/sample/ITO (indium tin oxide) were fabricated for the synthesized materials. Important parameters such as rectification ratio, ideality factor, barrier height and series resistance were calculated from current density-voltage measurement. Charge transport parameters were obtained using space charge limited current (SCLC) theory. Device performance has also been observed under light irradiation to get idea about photo response of the nanocomposite over pure one.

4.2. Materials and method:

All the precursors are purchased from Merck and pure up to 99%.

4.2.1. Synthesis of tin (IV) oxide (SnO₂):

In a typical synthesis procedure, SnO₂ was obtained from SnCl₄·5H₂O. All the reagents were of analytical grade and used without further purification. At

first 0.76 g of $\text{SnCl}_4 \cdot 5\text{H}_2\text{O}$ was added to 60 mL distilled water and stirred for 30 min to get a concentration of 50 mmol/L. Then 425 μL Hydrazine hydrate ($\text{N}_2\text{H}_4 \cdot \text{H}_2\text{O}$) was added drop by drop to the solution under continuous stirring. After 10 min of stirring, the whole solution was shifted into an autoclave of 100 mL and sealed. The autoclave temperature was maintained at 160°C for 12hr and then cooled down naturally to room temperature. The final product was rinsed with alcohol and distilled water for few times and dried at 60°C for 1 hr under vacuum. After drying we get a white powder.

4.2.2. *Synthesis of rGO-SnO₂ nanocomposite:*

The graphene oxide (GO) was synthesized using modified Hummers' method [13]. According to this method 3 ml of phosphoric acid (H_3PO_4) was added to 27 mL of sulfuric acid (H_2SO_4) and stirred for 10 min. Then 0.226 g of graphite powder was poured into the acid mixture under continuous stirring. 1.34 g of potassium permanganate (KMnO_4) was then directly added to the mixture and stirred for several hours until the mixture began to be dark green. To get rid of excess KMnO_4 , 675 μL hydrogen peroxide (H_2O_2) was added dropwise and stirred for another 10 min. Final product was washed several times with hydrochloric acid (HCl) and distilled water. Then obtained GO solution was dried at 90°C for 24 h and black coloured GO powder was produced. Typically, 0.15 g (0.07 mmol) of GO and 0.76 g (3 mmol) of $\text{SnCl}_4 \cdot 5\text{H}_2\text{O}$ were added to 60 mL of distilled water followed by 1 h ultrasonication. Then 486 μL of hydrazine hydrate was poured dropwise into the solution and stirred for 30 min. Then the whole solution was transferred to an autoclave of 100 mL and the reaction was carried out at 160°C for 12 h. After reaction completion the autoclave was allowed to cool down naturally. The final output was rinsed with ethanol and distilled water and dried at 60°C for 1 h under vacuum. A blackish powder was obtained as final product.

4.3. Result and discussions:

4.3.1. Structural characterizations:

The powder x-ray diffraction patterns of GO and rGO-SnO₂ were recorded using diffractometer in the range of 10°-70° [SnO₂ PXRD scan is started from 20°]. The PXRD spectra of synthesized samples are represented in **Figure 4.1**. As per PXRD pattern, a peak at around $2\theta = 14.44^\circ$ is seen for GO, corresponding to characteristics plane (001) of the GO nanosheet. Interplanar distance (d) of the characteristic plane is measured as 0.61 nm which means higher oxidation of graphite [14]. For SnO₂, diffraction peaks have been recorded at 2θ of 26.12°, 33.78°, 37.74°, 51.23° corresponding to (110), (101), (200) and (211) Bragg's plane respectively. All the PXRD peaks of SnO₂ exhibit tetragonal rutile structure (JCPDS No. 77-0452). Also, rGO-SnO₂ exhibits same rutile structure. This implies that the prepared composite material holds on to its SnO₂ structure. Peaks of rGO were not detected in the PXRD spectrum of the composite due to small amount of rGO.

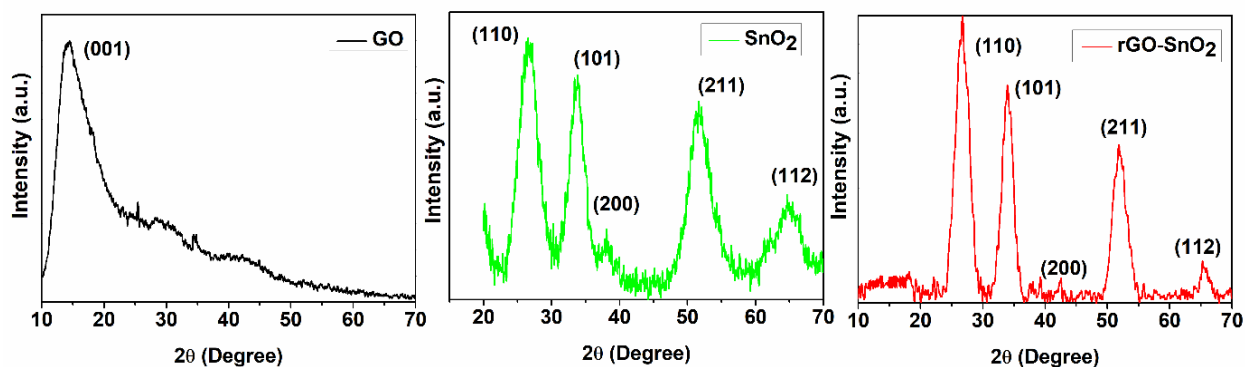


Figure 4.1: PXRD spectra of GO, SnO₂, and rGO-SnO₂

To study morphological structure and composition of SnO₂ and rGO-SnO₂, FESEM images of the materials were captured. **Figure 4.2 (a)** exhibits that SnO₂ particles are sphere-like with an average particle size of 28–54 nm and **Figure 4.2 (b)** shows that SnO₂ particles are nicely grafted onto graphene sheets.

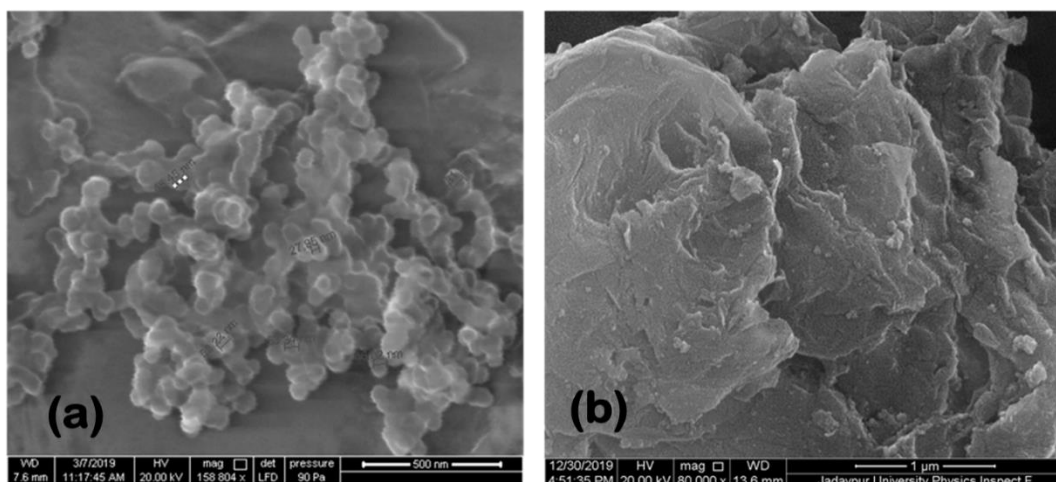


Figure 4.2: FESEM image of (a) SnO₂ and (b) rGO-SnO₂

Further characterization of the synthesized GO and rGO-SnO₂ composite was done by Raman spectroscopy. **Figure 4.3** shows Raman spectra of GO and rGO-SnO₂. In Raman spectra of GO, D and G band can be seen at 1357 cm⁻¹ and at 1611 cm⁻¹, respectively [14]. Raman lines for A_{1g} and B_{1g} modes related to SnO₂ phase are observed in rGO-SnO₂ composite. The characteristics D band is corresponding to defects and disorder states; and G band is for grain size. The value of I_D/I_G for rGO-SnO₂ (1.10) is higher than that for GO (1.02). This implies reduction of GO to rGO, as size of rGO is small and large number of defects are present here [14]. So, from the Raman spectra it can be concluded that GO is reduced to rGO and incorporated with SnO₂.

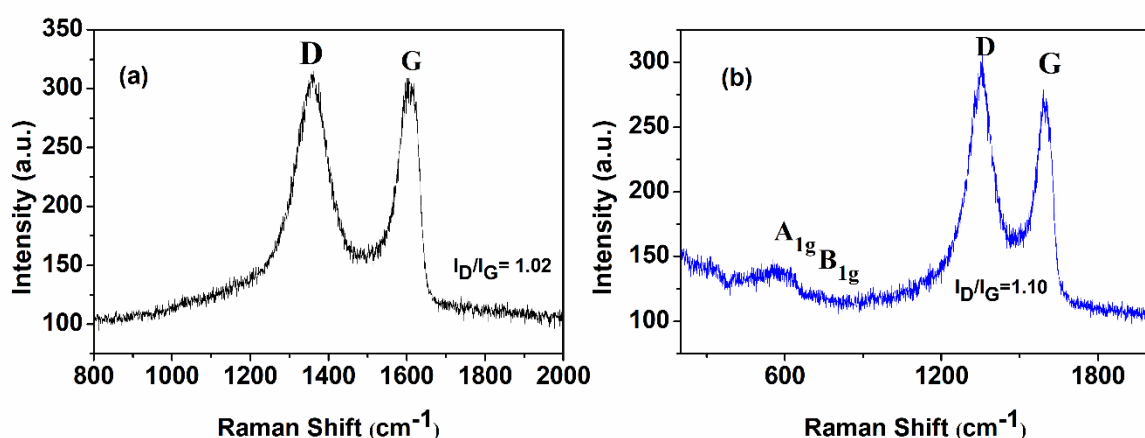


Figure 4.3: Raman spectrum of (a) GO and (b) rGO-SnO₂

Then XPS analysis was performed to analyse chemical composition of surface and chemical states of the as-prepared samples. **Figure 4.4 (a)** represents full scan spectrum of rGO-SnO₂ which shows peaks of only carbon, oxygen, and tin elements. In high resolution of Sn 3d spectrum (**Figure 4.4 b**), two peaks at 487.5 eV and 495.9 eV can be seen. These peaks correspond to Sn 3d^{5/2} and Sn 3d^{3/2} [15] with a splitting width of 8.4 eV. This confirms the presence of SnO₂ nanoparticles in the composite. Fig. 3.4 (c) and (d) show high resolution spectra of C 1s for GO and rGO-SnO₂. Deconvoluted spectrum of C 1s for GO shows peaks at 284.2 eV, 284.8 eV, 286.3 eV and 288.7 eV corresponding to C–C, C–O, C–O and O–C–O bond of carbon [16]. In Fig. 3.4(d), there is a decrement in intensity of all the peaks related to oxygen containing functional groups which indicates reduction of GO. So, XPS results confirm the successful synthesis of rGO-SnO₂.

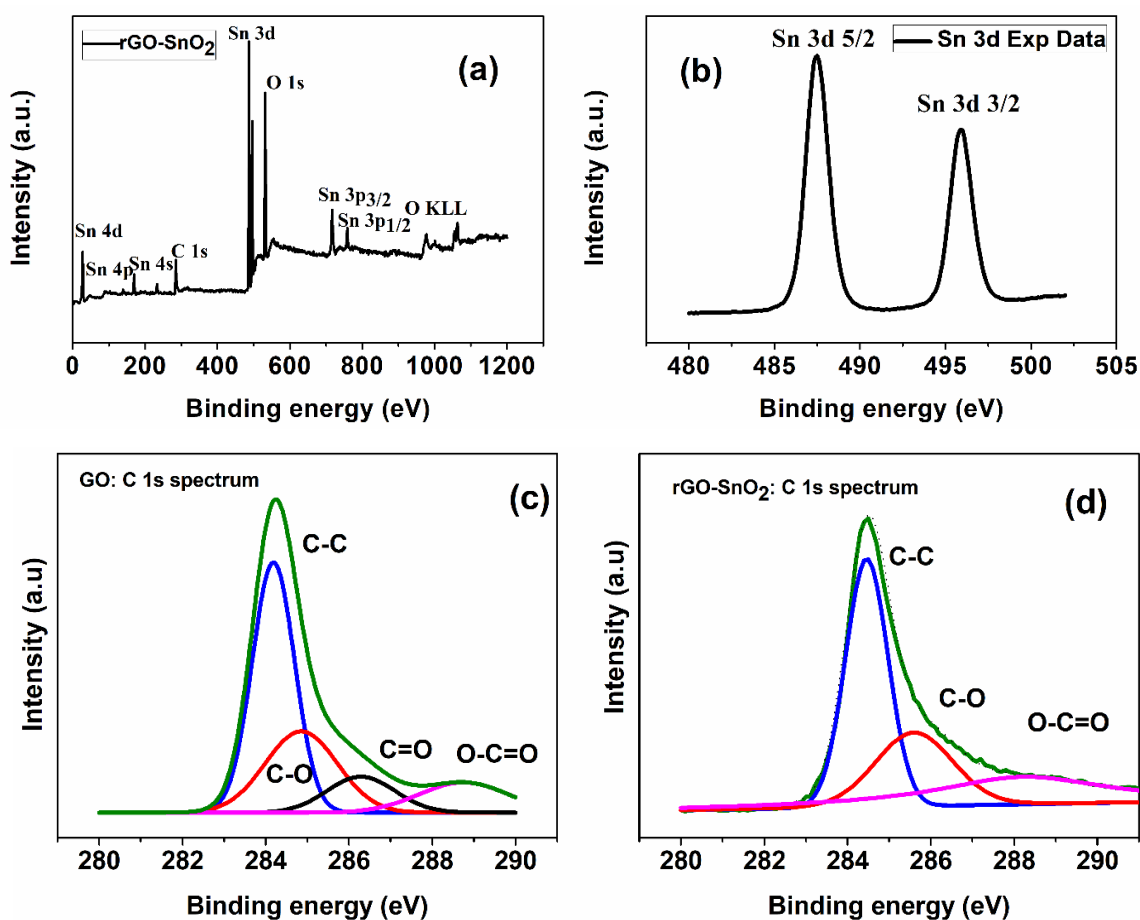


Figure 4.4: (a) XPS survey spectra of rGO-SnO₂, (b) Sn 3d spectrum of rGO-SnO₂, C 1s spectrum of (c) GO and (d) rGO-SnO₂

4.3.2. Optical characterization:

To reveal the light absorption properties of synthesized materials, the UV–Vis absorption spectra of the synthesized materials were recorded within the wavelength range of 250 nm–600 nm. From **Figure 4.5**, the absorption edge was found at 302 nm for SnO₂ which shifted to 361 nm for rGO-SnO₂. Presence of rGO in the composite is responsible for this shifting and increased light absorption range. Bandgap of the materials can be calculated using the equation [17],

$$E_{bg} = \frac{hc}{\lambda} \text{ (eV)} \quad (4.1)$$

where, E_{bg} is the optical bandgap energy, c is the velocity of light and λ is the onset wavelength corresponding to the absorption edge. The obtained bandgaps for SnO₂ and rGO-SnO₂ are 4.11 eV and 3.43 eV. Above values indicate that successful incorporation of graphene in SnO₂ has led to significant lowering of the bandgap, which should result in better photo-response for the fabricated device.

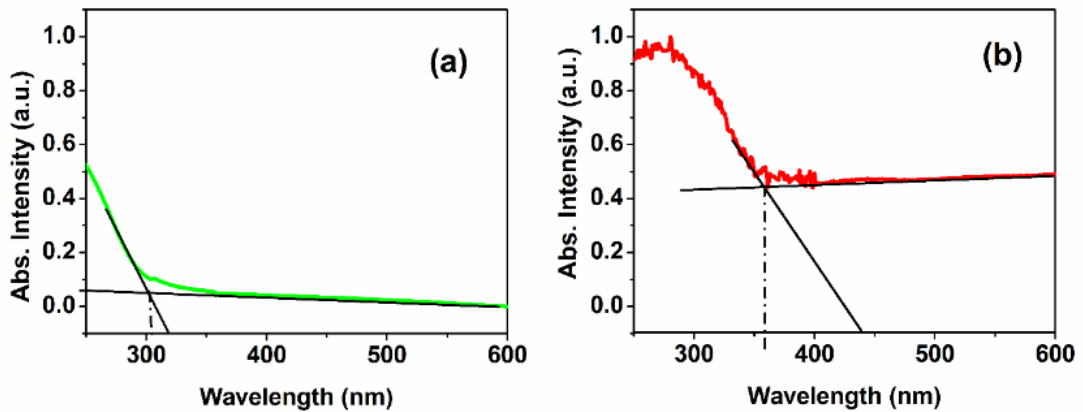


Figure 4.5: Absorption spectra for (a) SnO₂ (b) rGO-SnO₂

4.3.3. Electrical analysis:

For electrical characterization, a bias voltage from -1 V to +1 V was applied to the devices under dark and light conditions. White light of intensity of 1000

W/m² has been used for measuring J-V under illumination. The characteristics J-V curve is shown in **Figure 4.6**. Non-linear behaviour of J-V curves for both devices indicate Schottky barrier formation at metal-semiconductor junction.

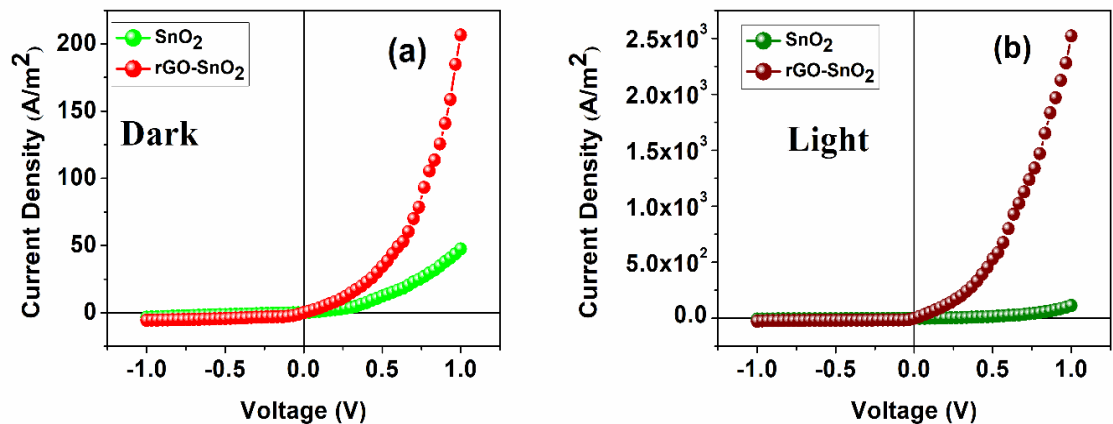


Figure 4.6: J-V curve for SnO₂ and rGO-SnO₂ under (a) dark (b) light illumination condition

Figure 4.6 illustrates that both devices show good rectifying behaviour under dark and light condition. A higher value of dark current density was recorded for rGO-SnO₂ device than SnO₂ based device. The rectification current ratio for SnO₂ diode was 14 at dark and 20 at light illumination condition whereas these values increased to 37 and 82 for rGO-SnO₂ diode. So, rGO-SnO₂ shows a better rectifying behaviour than pure SnO₂.

The conductivity of SnO₂ diode at room temperature was found to be $1.16 \times 10^{-5} \text{ S m}^{-1}$ and $1.95 \times 10^{-5} \text{ S m}^{-1}$ under dark and light conditions respectively. For the rGO-SnO₂ based device the conductivity increased to $4.41 \times 10^{-5} \text{ S m}^{-1}$ and $6.09 \times 10^{-4} \text{ S m}^{-1}$. The above values clearly show enhanced conductivity of the nanocomposite which is attributed to greater conductance of graphene and its intimate contact with SnO₂ nanoparticle. Due to chemical bonding between rGO and SnO₂, SnO₂ transfers electrons to the conduction band of rGO under biasing condition. rGO behaves like an electron collector and transporter which reduce possibility of recombination. As a result, the conductivity of the composite increased compared to the pure SnO₂.

The photo-sensitivities (S) of the devices were also calculated using the equation:

$$S = \frac{J_{ph}}{J_D} \quad (4.2)$$

where J_{ph} = photocurrent density = $J_{Light} - J_{Dark}$ and J_D = dark current density. Photosensitivity of rGO-SnO₂ based device was found to be 9.95 which is remarkably 4 times higher than the value of 2.42 shown by its counterpart. So, light irradiation influences electron conduction for composite even better due to enhanced electron transfer.

Photoresponsivity and specific detectivity explains the performance of Schottky diode as photodetector. The measure of electrical response to light i.e., photoresponsivity

$$R = \frac{J_{ph}}{P_{in}} \quad (4.3)$$

where P_{in} is the incident optical power. These values were 0.07 AW⁻¹ and 2.32 AW⁻¹ for SnO₂ and rGO-SnO₂ respectively. Photo-response of rGO-SnO₂ is increased by 33 times due to incorporation of rGO.

The specific detectivity D^* can be expressed as [18]:

$$D^* = \frac{R}{(2qAJ_D)^{\frac{1}{2}}} \quad (4.4)$$

where q = electronic charge. The specific detectivity were 2.14×10^9 Jones and 1.07×10^{11} Jones for SnO₂ and rGO-SnO₂ respectively. The conclusion of these results is that rGO-SnO₂ based Schottky diode is much superior than pure one in application of photodetector.

For further characterization, Current density-voltage relation of Schottky diode evaluated from *equation 1.11* and *1.12* (as $J = I/A$) is given by [19],

$$J = J_0 \left[\exp\left(\frac{qV}{\eta kT}\right) - 1 \right] \quad (4.5)$$

And

$$J_0 = A^* T^2 \exp\left(\frac{-q\phi_b}{kT}\right) \quad (4.6)$$

where J_0 is the saturation current density, q is the charge of electron, V is the bias voltage, n is the ideality factor, k is Boltzmann constant, T is absolute temperature, ϕ_b is the barrier height and A^* is effective Richardson constant. The effective Richardson constant is considered as $7 \times 10^5 \text{ AK}^{-2}\text{m}^{-2}$ [20].

By analysing the $\ln J$ - $\ln V$ curve, shown in **Figure 4.7(a)** and **(b)** Schottky current mechanism for entire range can be divided. From $\ln J$ vs $\ln V$ graph, two regions with distinct slope can be seen, which points to different current transport mechanisms. At low bias (region I), the current follows ohm's law i.e., current is directly proportional to applied voltage, after that it is ruled by space charge limited current theory corresponding to exponential trap distribution (region II). In the region II, the current is proportional to V^2 , which is indicative of trap free SCLC mechanism.

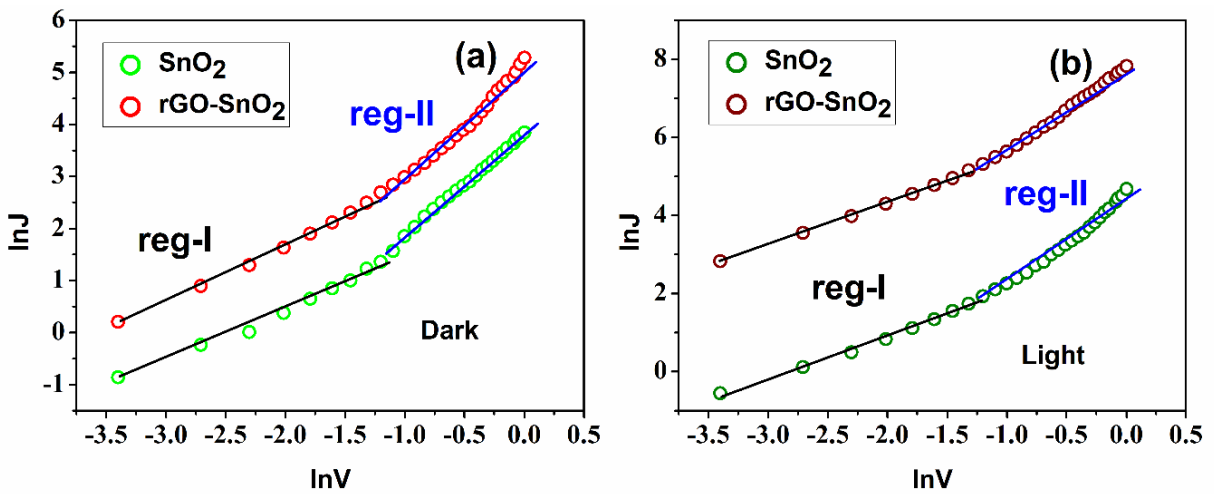


Figure 4.7: $\ln J$ vs $\ln V$ plot under (a) dark and (b) light condition

At low bias voltage, linearity of current is noticed. When bias voltage is higher, then the deviation from linearity is mainly due to the series resistance of diode. The ideality factor (n) and series resistance (R_s) for the fabricated device can be derived using Cheung's equation [21, 22]:

$$\frac{dV}{d\ln(J)} = \frac{nkT}{q} + JAR_s \quad (4.7)$$

The ideality factor and series resistance are calculated using the intercept and slope from linearly fitted $dV/d\ln J$ versus J curve. The $dV/d\ln J$ vs J graphs for dark and light condition are shown in **Figure 4.8**.

The acquired values of ideality factors show deviation from ideal behaviour, which may be due to several reasons like the presence of structural defects and interface states, tunneling current, existence of inhomogeneities in Schottky barrier and series resistance [23]. After light illumination, the values come closer to 1 for both devices. Upon light irradiation, trapping states of the device and generation of the recombination centers reduces and hence improves ideality factor.

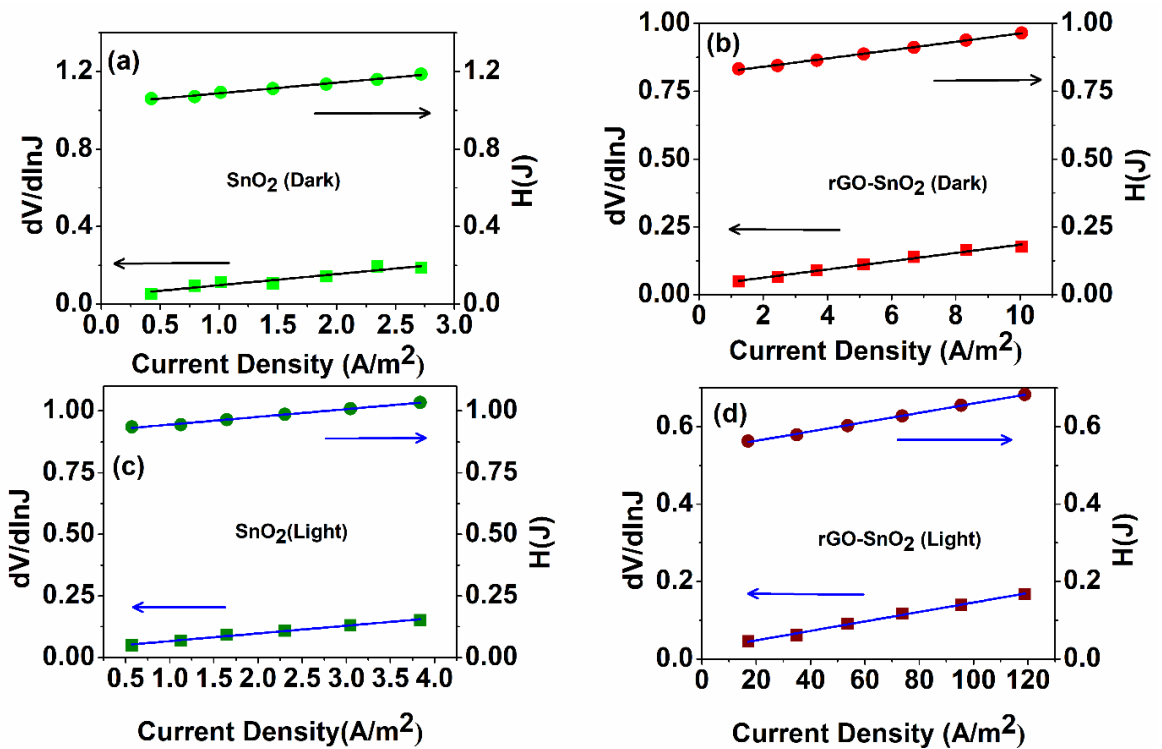


Figure 4.8: $dV/d\ln J$ vs J and $H(J)$ vs J curve for SnO_2 and rGO-SnO_2 under (a and b) dark (c and d) light condition

Also, according to the Cheung model, the current density-dependent function $H(J)$ can be expressed as [21],

$$H(J) = V - \left(\frac{nkT}{q}\right) \ln\left(\frac{J}{A^*T^2}\right) = R_s AJ + n\phi_b \quad (4.8)$$

From the above equation, we can calculate the barrier height of Schottky diode from the intercept of linear $H(J)$ vs J plots (**Figure 4.8**).

As shown in **Table 4.1**, the series resistance values estimated from two different approaches i.e., from $dV/d\ln J$ vs J and $H(J)$ vs J graph is nearly same. The value of series resistance is reduced for rGO-SnO₂ diode compared to other one. This explains the higher current exhibited for the rGO-SnO₂ device.

Table 4.1: Schottky diode parameters

Device	Condition	Rectification ratio	Conductivity (S m ⁻¹)	S	LF (η)	R _s (dV/dlnJ) (kΩ)	R _s (H) (kΩ)	Φ _b (eV) (Cheung method)	Φ _b (eV) (Norde method)
SnO ₂	Dark	14	1.16×10 ⁻⁵	2.42	1.53	8.14	7.78	0.68	0.70
	Light	20	1.95×10 ⁻⁵		1.36	4.41	4.48	0.66	0.68
rGO-SnO ₂	Dark	37	4.41×10 ⁻⁵	9.95	1.24	2.15	2.17	0.65	0.66
	Light	82	6.09×10 ⁻⁴		0.92	0.17	0.16	0.59	0.59

Uncertainty determination in linear fits is required to get an idea about the accuracy of the measurement of internal series resistance, barrier height, ideality factor etc. Uncertainties in linear fits using Cheung’s method are given in **Figure 4.9**. Average uncertainties for different linear fits are given in **Table 4.2**.

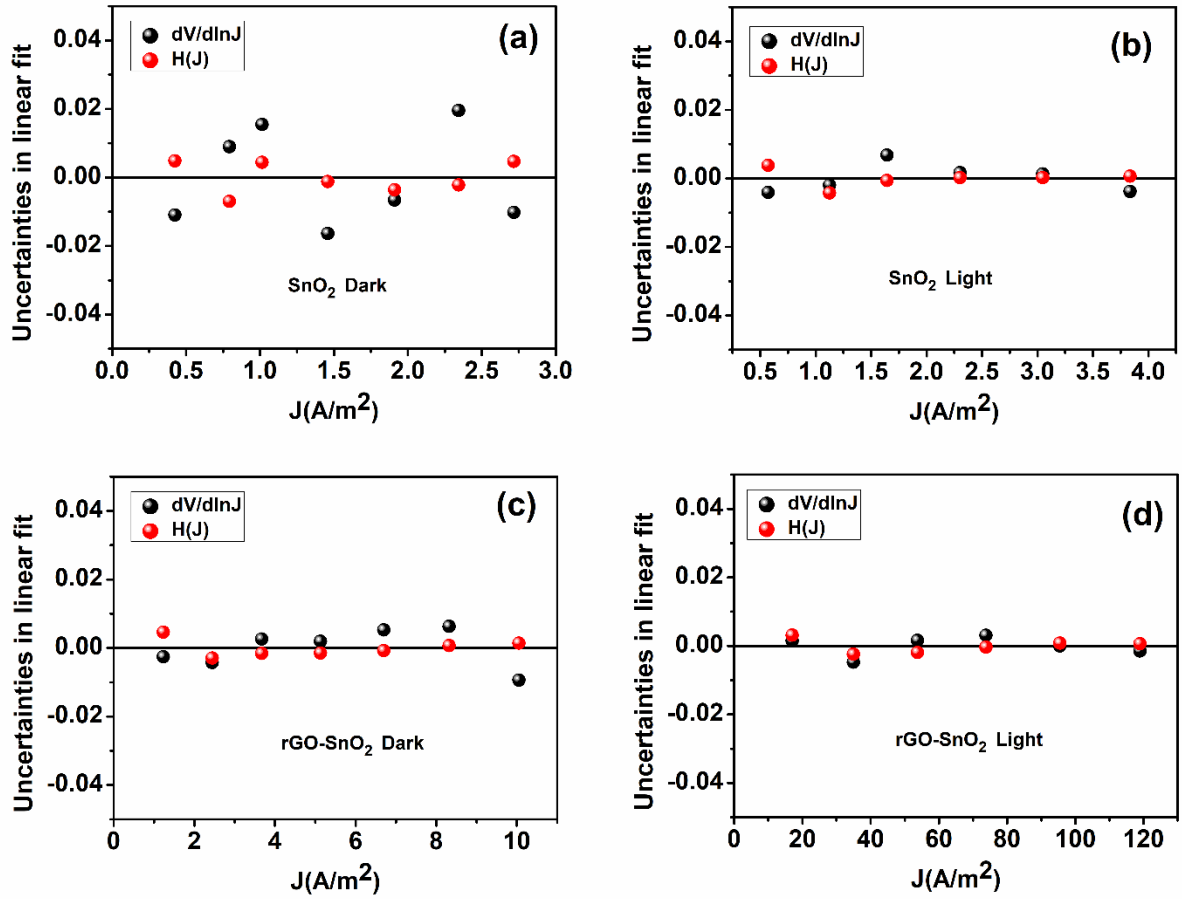


Figure 4.9: Uncertainties from the linear fits of Cheung's method for (a) SnO₂ Dark (b) SnO₂ Light (c) rGO-SnO₂ Dark and (d) rGO-SnO₂ Light respectively.

Table 4.2: Average uncertainties in linear fits

Sample	Condition	Average uncertainties in linear fit of	
		dV/dlnJ	H(J)
SnO ₂	<i>Dark</i>	0.0126	0.0039
	<i>Light</i>	0.0033	0.0016
rGO-SnO ₂	<i>Dark</i>	0.0046	0.0019
	<i>Light</i>	0.0021	0.0015

For a second verification of the result obtained from Cheung's equation, we also used a different method to calculate barrier height of the devices. According to Norde, the generalized Norde function can be expressed as [24]:

$$F(V) = \frac{V}{\alpha} - \left(\frac{kT}{q}\right) \ln\left(\frac{J}{A^*T^2}\right) \quad (4.9)$$

where α is an arbitrary constant which is greater than ideality factor n and other notations remain same. Barrier height values can be calculated from the following equation [24],

$$\Phi_b = F_{min}(V) + \left(\frac{\alpha-n}{n}\right) \left(\frac{V_{min}}{\alpha} - \frac{kT}{q}\right) \quad (4.10)$$

where $F_{min}(V)$ and V_{min} represent minimum Norde function obtained from graph and its corresponding voltage respectively. $F(V)$ versus V plot is presented in *Figure 4.10*.

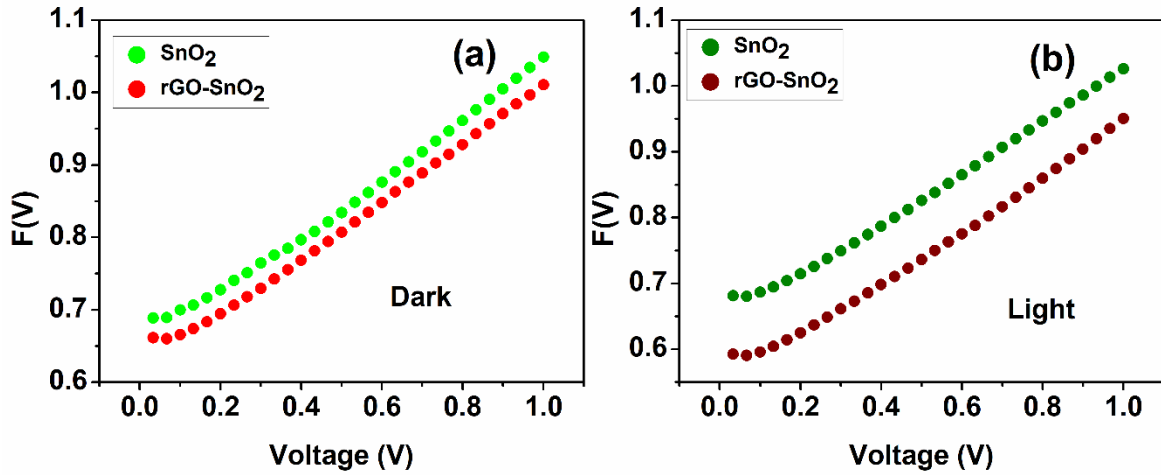


Figure 4.10: $F(V)$ versus Voltage plot for SnO_2 and rGO-SnO_2 under (a) dark (b) light condition

The barrier height obtained from two different methods was also in close agreement with each other. The barrier height values show same trends for both the samples. Under light condition, values of barrier height for both the materials reduces compared to dark condition, possibly due to Fermi level pinning [24]. Barrier height of the rGO-SnO_2 nanocomposite is lower than that of the pure SnO_2 .

All the Schottky diode parameters obtained from Cheung's method and Norde method, along with the on/off ratio, conductivity, photosensitivity of the fabricated device is given in **Table 4.1**. Above values imply that introduction of graphene to the SnO₂ matrix has resulted in reduced turn on voltage of the device. So, the rGO-SnO₂ is supposed to be a better material for fast switching device applications. Under light condition for rGO-SnO₂, the values of Schottky diode parameters are even better than dark condition.

For an extremely high electron mobility of 15,000 cm²V⁻¹s⁻¹ of graphene at room temperature, it is presumed that the electron fetch and electron-hole pair separation will enhance in the presence of graphene.

To gain better insight into charge transport properties, carrier mobility and transit time of carriers are evaluated with the help of standard SCLC theory for the SCLC region.

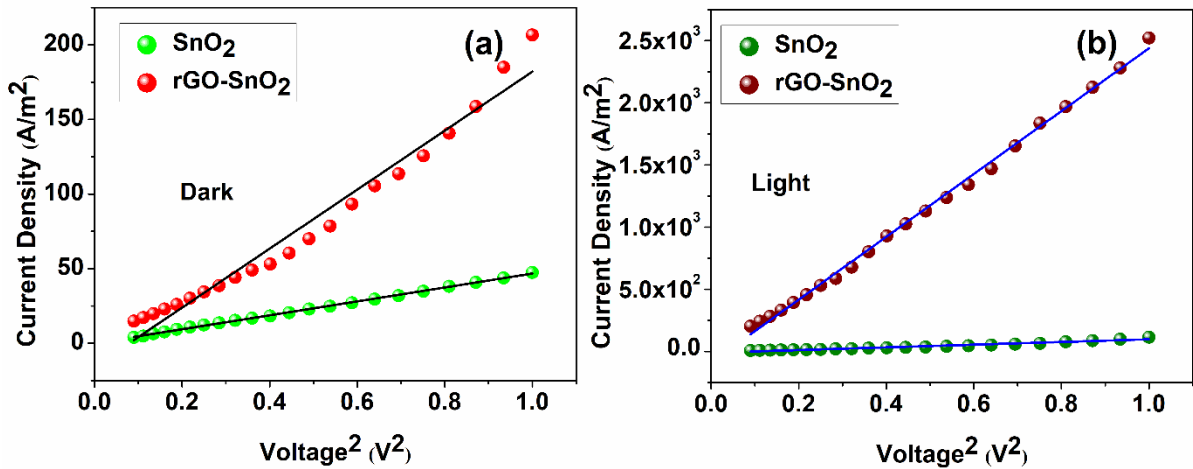


Figure 4.11: J vs V² plot under (a) dark and (b) light condition

So, the effective mobility is derived from J versus V² plot (**Figure 4.11a** and **b**) for the SCLC region from Mott-Gurney equation [23, 25]:

$$J = \frac{9\mu_{eff}\epsilon_0\epsilon_r}{8} \left(\frac{V^2}{d^3} \right) \quad (4.11)$$

where J is the current density, ϵ_0 is the permittivity of the free space, ϵ_r is the dielectric constant of the prepared material and μ_{eff} is the effective mobility. The dielectric constants were derived as 0.29 and 0.64 for SnO_2 and rGO-SnO_2 nanocomposite respectively.

The relative dielectric constant of SnO_2 and rGO-SnO_2 are derived from the following equation:

$$\epsilon_r = \frac{1}{\epsilon_0} \cdot \frac{C \cdot l}{A} \quad (4.12)$$

Where C is the capacitance at saturation, ' l ' is the thickness of the film, ϵ_0 is the free space permittivity and A is the effective area.

Saturation capacitance value is determined from capacitance versus logarithm of frequency graphs at a constant bias voltage (**Figure 4.12**).

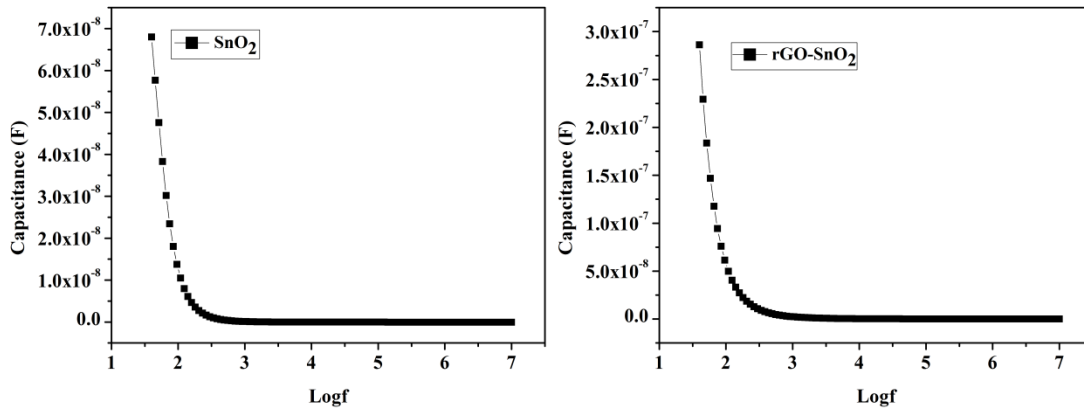


Figure 4.12: Capacitance versus logf graph

The following equation was used to determine transit time of the charge carriers [26],

$$\tau = \frac{9\epsilon_0\epsilon_r}{8d} \left(\frac{V}{J} \right) \quad (4.13)$$

The density of states (N_F) near the Fermi level is evaluated using the den-Boer method from the SCLC J-V characteristics. The equation for density of states can be expressed as [27].

$$N_F = \frac{2\varepsilon_0\varepsilon_r(V_2-V_1)}{d^2\Delta E_F} \quad (4.14)$$

Here ΔE_F represents the shift in quasi-Fermi level and is measured from the following equation [27],

$$\Delta E_F = kT \ln \left(\frac{J_2 V_1}{J_1 V_2} \right) \quad (4.15)$$

V_1 and V_2 are two forward bias voltage taken from SCLC region and J_1 , J_2 are their corresponding current density.

Under dark condition the density of states for SnO_2 and rGO-SnO_2 were $1.47 \times 10^{21} \text{ m}^{-3}$ and $9.68 \times 10^{20} \text{ m}^{-3}$. The low density of states for rGO-SnO_2 indicates the presence of a smaller number of defects and traps in the forbidden gap which eventually increase the dark current density.

Table 4.3: Charge transport parameters

Sample	Condition	Mobility $\times 10^{-4}(\text{m}^2\text{V}^{-1}\text{S}^{-1})$	Transit time (ns)	$\mu_{\text{eff}}\tau \times 10^{-13}(\text{m}^2\text{V}^{-1})$
SnO₂	Dark	0.16	49	7.87
	Light	0.32	25	8.22
rGO-SnO₂	Dark	0.26	34	8.65
	Light	3.76	2.5	9.43

Evaluated values of effective mobility, carrier transit time and mobility-transit time product are given in **Table 4.3**. From **Table 4.3**, mobility of rGO-SnO_2 is almost 62% higher than pure SnO_2 . And under light illumination, mobility increases about 12-fold for rGO-SnO_2 compared to its counterpart. This is due to higher photo-response of the composite. Clearly the high electron generation, faster transportation of charge carrier and lower recombination under light influence these results.

Finally, to further investigate the role of rGO in electron transfer through MS junction, impedance spectroscopy (IS) measurement was done at a bias voltage of 500 mV. **Figure 4.13** shows Nyquist plot of the devices. The diameter of the semi-circular arc represents resistance of the MS junction. There is a noteworthy decrease in the diameter for rGOSnO₂ diode which implies reduction in charge recombination and decrement in resistance. Thus, rGO incorporation leads to better charge transport in the composite device.

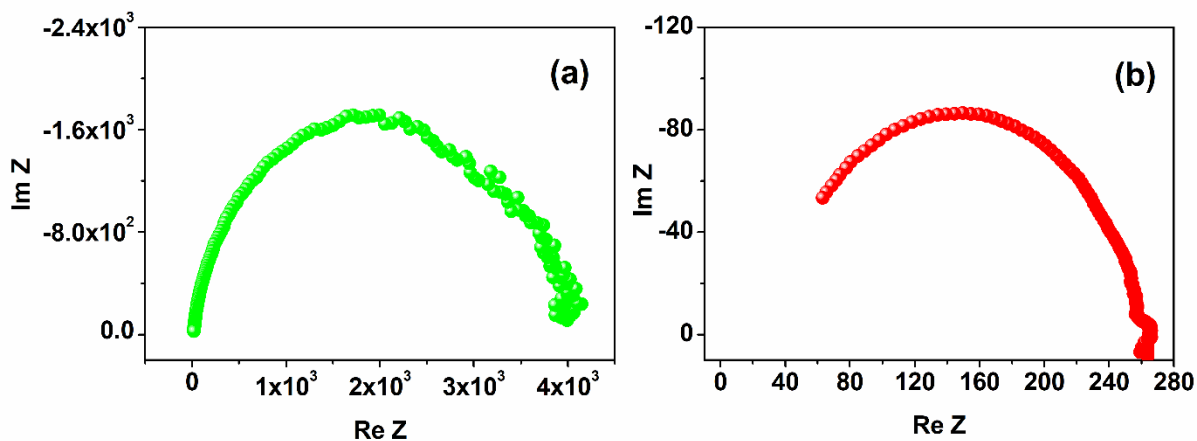


Figure 4.13: Nyquist plots for (a) SnO₂ and (b) rGO-SnO₂

4.4. Conclusion:

In conclusion, SnO₂ and rGO-SnO₂ were synthesized successfully using hydrothermal method and detail characterizations were performed. Comparative studies revealed that rGO-SnO₂ based Schottky diode exhibited far better performance than pure SnO₂ based Schottky diode. rGO-SnO₂ based Schottky diode shows better rectification, lower turn on voltage and a 4 times higher photosensitivity. SCLC theory was employed to calculate carrier mobility and transit time. rGO-SnO₂ based diode shows superior charge transport phenomena with a sharp rise of 62% in carrier mobility. Finally, from the different results we got, we can conclude that rGO-SnO₂ is promising material as an upgrade on SnO₂ for better rectifying, fast switching and photosensitive device.

References:

1. Z. Yin, J. Zhu, Q. He, X. Cao, C. Tan, H. Chen, Q. Yan and H. Zhang, *Graphene-Based Materials for Solar Cell Applications*, Advance Energy Materials, 2014, **4**, 1300574
doi.org/10.1002/aenm.201300574
2. V. H. Luan, H. N. Tien, L. T. Hoa, N. T. M. Hien, E-S Oh, J. Chung, E. J. Kim, and W. M. Choi, B-S Kong and S. H. Hur, *Synthesis of a highly conductive and large surface area graphene oxide hydrogel and its use in a supercapacitor*, Journal of Materials Chemistry A, 2013, **1**, 2, 208-211
doi.org/10.1039/C2TA00444E
3. M. Das, J. Datta, A. Dey, R. Jana, A. Layek, S. Middya, and P. P. Ray, One step hydrothermal synthesis of a rGO–TiO₂ nanocomposite and its application on a Schottky diode: improvement in device performance and transport properties, RSC Advances, 2015, **5**, 101582-101592
doi.org/10.1039/C5RA17795B
4. S. Sun, L. Gaoand, and Y. Liu, *Enhanced dye-sensitized solar cell using graphene-TiO₂ photoanode prepared by heterogeneous coagulation*, Applied physics letters, 2010, **96**, 8, 083113
doi.org/10.1063/1.3318466
5. S. Liu, Q. Liao, S. Lu, Z. Zhang, G. Zhang, and Y. Zhang, *Strain Modulation in Graphene/ZnO Nanorod Film Schottky Junction for Enhanced Photosensing Performance*, Advance Function Materials, 2016, **26**, 9, 1347–1353
doi.org/10.1002/adfm.201503905
6. A. A. Noroozi and Y. Abdi, *A graphene/Si Schottky diode for the highly sensitive detection of protein*, RSC Advances, 2019, **9**, 19613-19619
doi.org/10.1039/C9RA03765A
7. J. Vobecký, P. Hazdra, V. Záhřava, A. Mihaila, and M. Berthou, *ON-state characteristics of proton irradiated 4H–SiC Schottky diode: The calibration of model parameters for device simulation*, Solid-State Electronics, 2014, **94**, 32-38
doi.org/10.1016/j.sse.2014.02.004
8. P. D. Ye, G. D. Wilk, B. Yang, J. Kwo, S. N. G. Chu, S. Nakahara, H.-J. L. Gossman, J. P. Mannaerts, M. Hong, K. K. Ng, and J. Bude, *GaAs metal–oxide–semiconductor field-effect transistor with nanometer-thin dielectric grown by atomic layer deposition*, Applied Physics Letters, 2003, **83**, 1, 180
doi.org/10.1063/1.1590743

9. J. Xie, K. Huang, X. Yu, Z. Yang, K. Xiao, Y. Qiang, X. Zhu, L. Xu, P. Wang, C. Cui and D. Yang, *Enhanced Electronic Properties of SnO₂ via Electron Transfer from Graphene Quantum Dots for Efficient Perovskite Solar Cells*, ACS Nano, 2017, **11**, 9, 9176-9182
doi.org/10.1021/acsnano.7b04070
10. M. Ippommatsu, H. Sasaki, and H. Yanagida, *Sensing mechanism of SnO₂ gas sensors*, Journal of Materials Science, 1990, **25**, 259-262
doi.org/10.1007/BF00544217
11. A. M. Ganose and D. O. Scanlon, *Band gap and work function tailoring of SnO₂ for improved transparent conducting ability in photovoltaics*, Journal of Materials Chemistry C, 2016, **4**, 1467-1475
doi.org/10.1039/C5TC04089B
12. S. P. Lim, N. M. Huang and H. N. Lim, *Solvothermal synthesis of SnO₂/graphene nanocomposites for supercapacitor application*, Ceramics International, 2013, **39**, 6, 6647-6655
doi.org/10.1016/j.ceramint.2013.01.102
13. N. I. Zaaba, K. L. Foo, U. Hashim, S. J. Tan, W-W. Liu, and C. H. Voon, *Synthesis of Graphene Oxide using Modified Hummers Method: Solvent Influence*, Procedia Engineering, 2017, **184**, 469-477
doi.org/10.1016/j.proeng.2017.04.118
14. A. Ahmed, M. N. Siddique, T. Ali, and P. Tripathi, *Influence of reduced graphene oxide on structural, optical, thermal and dielectric properties of SnO₂ nanoparticles*, Advanced Powder Technology, 2018, **29**, 12, 3415-3426
doi.org/10.1016/j.appt.2018.09.026
15. L. Liu, M. An, P. Yang and J. Zhang, *Superior cycle performance and high reversible capacity of SnO₂/graphene composite as an anode material for lithium-ion batteries*, Scientific Reports, 2015, **5**, 9055
doi.org/10.1038/srep09055
16. Y. Wang, H. Zhang, D. Yao, J. Pu, Y. Zhang, X. Gao and Y. Sun, *Direct electrochemistry of hemoglobin on graphene/Fe₃O₄ nanocomposite-modified glass carbon electrode and its sensitive detection for hydrogen peroxide*, Journal of Solid-State Electrochemistry, 2013, **17**, 3, 881-887
doi.org/10.1007/s10008-012-1939-5
17. M. R. Hasan, S. B. A. Hamid, W. J. Basirun, Z. Z. Chowdhury, A. E. Kandjanib, and S. K. Bhargavab, *Ga doped RGO-TiO₂ composite on an ITO surface electrode for investigation of photoelectrocatalytic activity under visible light irradiation*, New Journal of Chemistry, 2015, **39**, 369-376
doi.org/10.1039/C4NJ01048E

18. Z. Chen, W. Li, R. Li, Y. Zhang, G. Xu and H. Cheng, *Fabrication of Highly Transparent and Conductive Indium–Tin Oxide Thin Films with a High Figure of Merit via Solution Processing*, ACS publications, Langmuir, 2013, **29**, 45, 13836-13842
doi.org/10.1021/la4033282
19. L. Dou, Y. M. Yang, J. You, Z. Hong, W-H. Chang, G. Li and Y. Yang, *Solution-processed hybrid perovskite photodetectors with high detectivity*, Nature Communications, 2014, **5**, 1, 1-6
doi.org/10.1038/ncomms4942
20. J. Datta, A. Dey, S. K. Neogi, M.Das, S. Middya, R. Jana, S. Bandyopadhyaya, A. Layek and P. P. Ray, *Application Possibility of $Mn_{0.04}Cu_{0.05}Zn_{0.91}O$ in Electronic and Magnetic Devices*, IEEE Transactions on Electron Devices, 2018, **64**, 11, 4724–4730
doi.org/10.1109/TED.2017.2754190
21. C. A. Amorim, E. P. Bernardo, E. R. Leiteand, and A. J. Chiquito, *Effect of inhomogeneous Schottky barrier height of SnO_2 nanowires device*, Semiconductor Science and Technology, 2018, **33**, 5, 055003
doi.org/10.1088/1361-6641/aab69e
22. S. K. Cheung, and N. W. Cheung, *Extraction of Schottky diode parameters from forward current-voltage characteristics*, Applied Physics Letters, 1986, **49**, 2, 85-87
doi.org/10.1063/1.97359
23. R. Jana, S. Sil, A. Dey, J. Datta, and P. P. Ray, *Analysis of temperature dependent electrical performance of Al/CuO/ITO Schottky barrier diode and explanation of inhomogeneous barrier heights by double Gaussian distribution*, AIP Advances, 2018, **8**, 12, 125104
doi.org/10.1063/1.5066258
24. S. Halder, B. Pal, A. Dey, S. Sil, P. Das, A. Biswas, and P. P. Ray, *Effect of graphene on improved photosensitivity of MoS_2 -graphene composite based Schottky diode*, Material Research Bulletin, 2019, **118**, 110507
doi.org/10.1016/j.materresbull.2019.110507
25. A. Dey, S. Middya, R. Jana, M. Das, J. Datta, A. Layek, and P. P. Ray, *Light induced charge transport property analysis of nanostructured ZnS based Schottky diode*, Journal of Materials Science: Materials in Electronics, 2016, **27**, 6325-6335
doi.org/10.1007/s10854-016-4567-5
26. M. Das, J. Datta, R. Jana, S. Sil, S. Halder, and P. P. Ray, *Synthesis of $rGO-Zn_{0.8}Cd_{0.2}S$ via in situ reduction of GO for the realization of a Schottky diode with low barrier height and highly enhanced photoresponsivity*, New Journal of Chemistry, 2017, **41**, 5476-5486
doi.org/10.1039/C7NJ00428A

27. S. Sil, A. Dey, J. Datta, M. Das, R. Jana, S. Halder, J. Dhar, D. Sanyal, and P. P. Ray, *Analysis of interfaces in Bornite (Cu_5FeS_4) fabricated Schottky diode using impedance spectroscopy method and its photosensitive behavior*, Materials Research Bulletin, 2018, **106**, 337-345
doi.org/10.1016/j.materresbull.2018.06.016
28. J. Datta, M. Das, S. Sil, S. Kumar, A. Dey, R. Jana, S. Bandyopadhyay, and P. P. Ray, *Improvement of charge transport for hydrothermally synthesized $\text{Cd}_{0.8}\text{Fe}_{0.2}\text{S}$ over co-precipitation method: A comparative study of structural, optical and magnetic properties*, Material Science in Semiconductor Processing, 2019, **91**, 133-145
doi.org/10.1016/j.mssp.2018.11.010

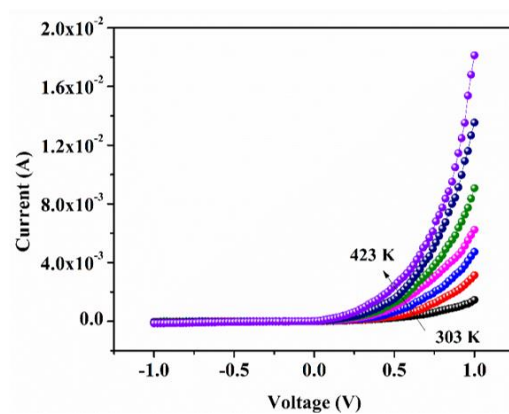
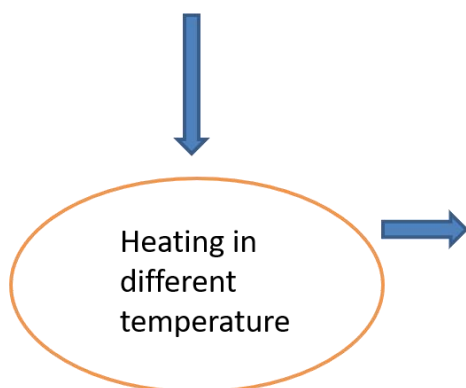
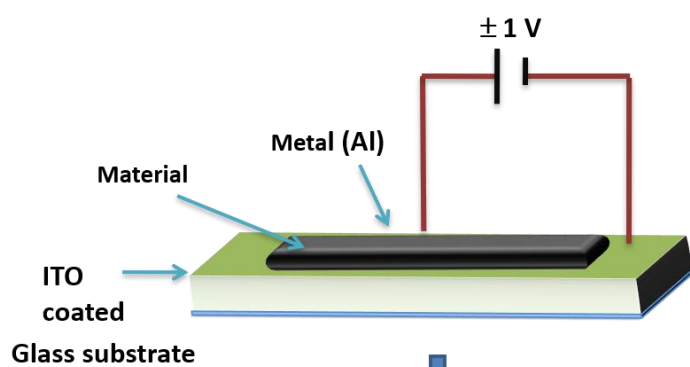
Chapter 5

Findings of inhomogeneity in barrier height of Schottky junction Al/rGO-SnO₂ having anomaly in theoretical and experimental value of Richardson constant: A Gaussian approach

Abstract

In this research, the temperature dependent dynamical behaviour of Schottky junction Al/rGO-SnO₂ has been investigated with thermionic emission (TE) theory within the temperature regime 303 K to 423 K at interval 20 K. During analysis of electrical charge transport behaviour an anomalous change is observed in the value of ideality factor and barrier height with rising temperature for the junction. Experimentally derived Richardson constant (of the order 10^{-5} A/m²K²) using TE theory is exceptionally substandard to the theoretical (of the order 10^6 A/m²K²) values. The beauty of this work is to find out the underline physics for this discrepancy in measurement of Richardson constant (might arose due to inhomogeneity in barrier of metal-semiconductor junction) by assuming the Gaussian distribution of the barrier height with TE theory at the junction. It is obvious that the occurrence of barrier inhomogeneity across the junction leading charge transport phenomena which mostly impacting upon the parameters of Schottky diodes and its nature because of intrinsic formation of ripples and ridges. In this study, it is found that the charge transport mechanism is highly follows the single Gaussian distribution.

Graphical Abstract



5.1. *Introduction:*

Thin film-based Metal-Semiconductor (MS) Schottky Barrier Diode (SBD)s [1] have attracted huge attention for its wide range of applications, especially in the micro-electronic devices such as optoelectronic [2], bipolar integrated circuits [3] and high frequency device applications [4]. Several current transport mechanisms such as thermionic emission (TE), barrier tunnelling and carrier generation-recombination at space charge region have been studied to explain various MS junction. Moreover, for the unique features like high conductivity, wide optical transparency and great compatibility for thin film fabrication, graphene composite has proven itself as an important candidate for application in Schottky barrier diodes (SBDs) [5].

As various defects in the crystalline structure effect on material's characteristics under the impact of different environments, having high grain boundary density graphene composites can be influenced by the operating environment [6]. The current conduction mechanism of SBDs depends upon numerous parameters like the operating temperature of the device, barrier height inhomogeneities at MS junction, internal series resistance, functional bias voltage, process of diode preparation [7].

Moreover, there has been growing interest towards rGO-SnO₂ nanocomposite in bio sensors [8], Schottky diodes etc. [9]. The reported band gap value of rGO-SnO₂ is nearly 3.1 eV for the rutile structured SnO₂ decorated in rGO layers [10].

The performance and reliability of rGO-SnO₂ based SBD is dominated by ideality factor, Schottky barrier height (SBH), active metal semiconductor interface, density of interface states and internal series resistance at the metal–semiconductor (MS) junction [11]. For an ideal SBD, ideality factor is 1 and the barrier height is measured simply by the difference between the work function of

the metal and the electron affinity of the semiconductor [12]. Barrier height (BH) influences depletion layer width as well as charge transport mechanism through the MS junction. Usually, the electrical characteristics of SBD is highly influenced by the quality of interface. The room temperature conductivity and barrier height are not sufficient to understand the whole underlying mechanism. Many efforts have been made to comprehend the barrier height characteristics of rGO-SnO₂ based SBDs as well as the conduction process at room temperature.

A number of theories are reported there to explain some of experimental facts [13], [14]. At higher temperatures, metal contact may worsen due to diffusion into semiconductor and prepares a weakened MS junction. The operation at high temperature of SBDs with nanocomposite is often essential in application field. The increasing temperature can perturb the device parameters as well as the performance [12]. Different types of Gaussian distribution models are used to clarify the effectuality of barrier height with temperature. To the best of our knowledge, however, the performance of the Al/rGO-SnO₂/ITO SBD at different temperatures has not yet been documented.

The performance of Al/rGO-SnO₂/ITO SBD with varying temperature from 303 K to 423 K have been studied and reported accordingly. In this analysis, an anomalous dependency of barrier height and ideality factor on temperature is observed. This anomalous behaviour is clarified and demonstrated with a double Gaussian distribution (GD) of the BHs around a mean value for this device structure.

5.2. Result and discussion:

5.2.1. Powder XRD analysis:

The powder XRD is a common and useful technique to characterize nanoscale material. The change in dislocation density due to the change in crystallite size on thermal treatment of the nanocomposite material can also be

determined from XRD data using Scherrer equation [15]. **Figure 5.1** shows powder XRD patterns of rGO-SnO₂ nanocomposite before and after heat treatment. The pattern obtained after heat treatment is broadened followed by decrease in peak intensity of the material that might have occurred due to the change in crystallites' size and hence effective surface area. Using the Scherrer equation, the crystallite size (D) and dislocation density (δ) of rGO-SnO₂ nanocomposite for each hkl plane (fitted with JCPDS 77-0452 of SnO₂) before and after heat treatment are estimated and given in **Table 5.1**:

$$D = \frac{k\lambda}{\beta \cos \theta} \quad (5.1)$$

Here, β is the full width half maxima of peaks in radian and k is shape factor usually taken as 0.89.

And

$$\delta = \frac{1}{D^2} \quad (5.2)$$

Increase in dislocation density for each hkl plane after heat treatment assures defects increment in material [16]. This increment might impact upon the optical absorption of the derived material.

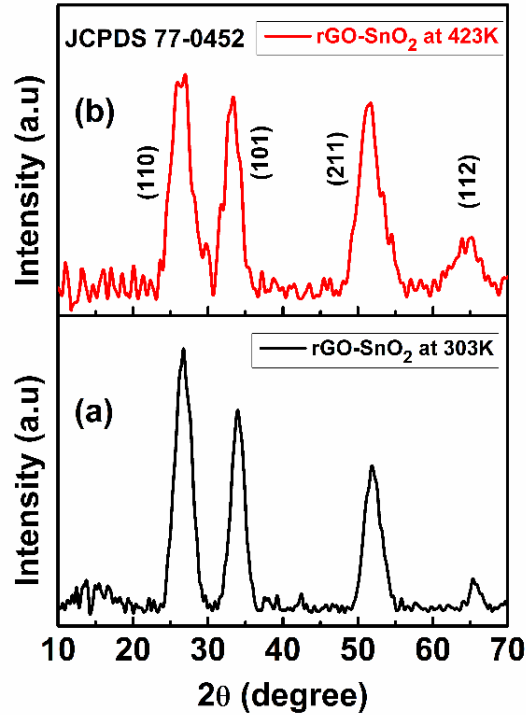


Figure 5.1: PXRD patterns of as-prepared rGO-SnO₂ before and after heat treatment

Table 5.1: *Crystallite size and dislocation density*

Material	Heat Treatment	Plane (hkl)	$\beta\cos\theta$	Crystallite size (D) (nm)	Dislocation density (δ) (nm ⁻²)
rGO-SnO ₂	<i>Before</i> (at 303K)	1 1 0	0.0434	3.19	0.098
		1 0 1	0.0348	3.98	0.063
		2 1 1	0.0399	3.47	0.083
		1 1 2	0.0205	6.76	0.022
	<i>After</i> (at 423K)	1 1 0	0.0533	2.60	0.148
		1 0 1	0.0411	3.37	0.088
		2 1 1	0.0551	2.51	0.159
		1 1 2	0.0242	5.73	0.030

5.2.2. UV–Visible spectroscopy analysis:

The optical absorbance spectra are recorded within wavelength range of 230–600 nm. **Figure 5.2(a & b)** represent that the absorption edge is shifted from higher UV region to lower one after heat treatment of the sample. The optical band gap of the rGO-SnO₂ composite at 303 K and 423 K are determined as 2.9 eV and 3.5 eV with the help of Tauc plot [**Figure 5.2(c & d)**] respectively.

Tauc's equation related to these plots is as follows [17]:

$$\alpha h\nu = C(h\nu - E_{bg})^n \quad , \quad (5.3)$$

where, α is the absorption coefficient, and C is a constant. Here, n was taken as 1/2 for direct transition.

These optical band gaps (E_{bg}) are calculated by extrapolating the linear portion of the plot of $(\alpha h\nu)^2$ vs $h\nu$ [**Figure 5.2(c & d)**] on the energy axis. Increase in optical bandgap rather a rigorous change in absorption edge indicates decrease in particle size and hence increase in surface area, which might lead to change in pore size/porosity or occurrence of various interstitial defect states. These

interstitial defects impact upon the carrier transport mechanism whenever the sample is introduced within the device.

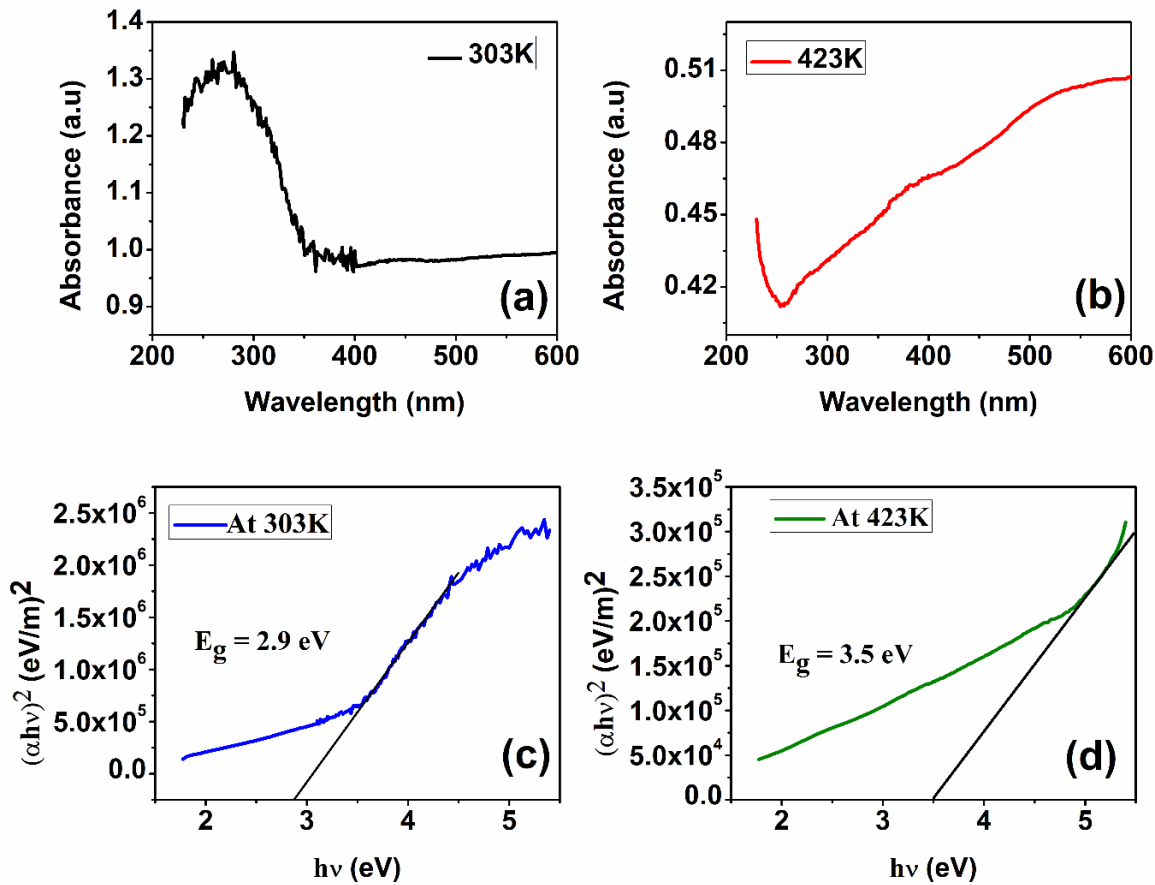


Figure 5.2: UV-Visible absorbance spectra and Tauc plot of rGO-SnO₂ at 303K (a, c) and (b, d) 423K

5.2.3. BET characterization:

Electrical conductivity is related to pore-size and porosity of the nanomaterial. The influence on charge conduction mechanism because of defects, arising due to change in specific surface area during formation of interface [18] within device affects the electrical conductivity. To find out pore size, BET is performed for the composite. **Figure 5.3(a&b)** illustrate the hysteresis loops of the nitrogen adsorption/desorption isotherms of the samples collected at 303 K and 423 K respectively through a relative pressure range of 0.1–1. The graphs correspond to the type I isotherm with a type H₂ hysteresis loop. A type H₂

hysteresis loop is frequently linked with ink-bottle pores with random size distributions of cavities and neck. **Figure 5.3(c & d)** represents $1/[V(P_0/P)-1]$ vs P/P_0 plots, determined using the BET equation in relative pressure range of $0.05 < P/P_0 < 0.35$. The emergence of an ultra-microporous or nano-porous structure with a high surface area of $205.37 \text{ m}^2/\text{g}$ (for 303 K) and $357.09 \text{ m}^2/\text{g}$ (for 423 K) are confirmed by this sort of isotherm, which are accompanied by 0.7713 nm and 0.7049 nm pore size with pore volume 0.144 cc/g and 0.235 cc/g respectively. The results depict that after high (423 K) temperature treatment, the pore size decreases with increasing pore volume and specific surface area accordingly [19]. The increase in specific surface area produces large number of defects at interface [20].

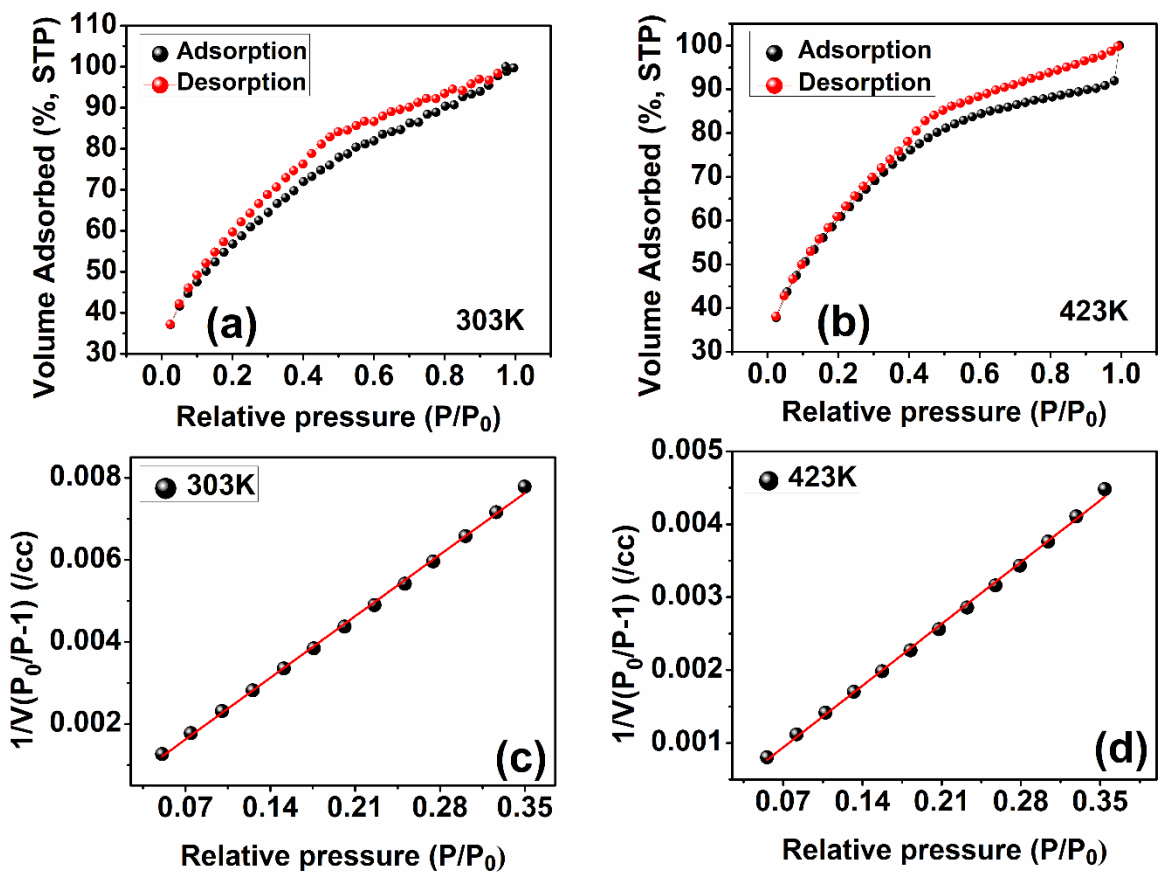


Figure 5.3: (a, b) N₂ adsorption–desorption isotherm for rGO-SnO₂ (c, d) $1/V(P_0/P-1)$ variation with relative pressure

5.2.4. Thermogravimetric analysis:

As discussed earlier the purpose of this measurement is to determine the purity percentage of rGO in the rGO-SnO₂ composite and to analyse its stability with temperature. **The Figure 5.4** depicts TGA curves in the temperature range from 30°C to 800°C. There are two distinct weight loss pathways for rGO-SnO₂. The dislodgement of absorbed water causes 5 % weight loss in the range of room temperature to 110°C [21]. The breakdown of oxygen-containing groups causes 4 % mass loss from 110°C to 425°C. The weight loss (3.5 %) is attributable to the degradation of the carbon skeleton at high temperatures, between 425°C and 600°C. This decomposition process results in considerable weight reduction, showing that the samples are devoid of rGO. So, the weight percentage of rGO in composite is 7.5 %. From the analysis, it is concluded that thermal stability of composite is high enough compared to the operating temperature (303 K–423 K) of the device and there is no degradation of composite during the experimental procedure.

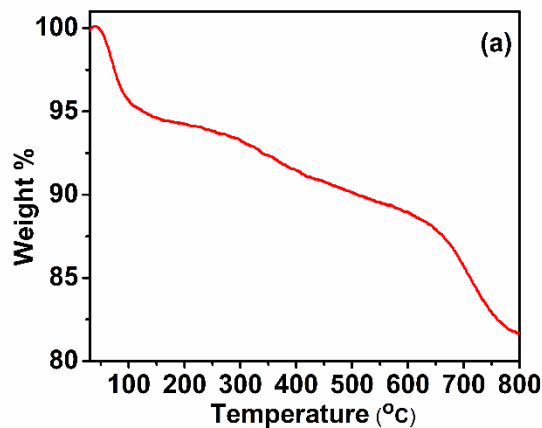


Figure 5.4: Thermogravimetric curve for rGO-SnO₂

5.2.5. Electrical characterization:

To intervene into the change in charge transport phenomena of the material at different ambient temperature the current voltage characteristics is recorded for

the fabricated device of sandwich structure ITO/rGO-SnO₂/Al. **Figure 5.5a** shows current–voltage (I-V) characteristics of ITO/rGO-SnO₂/Al for the temperature range of 303 K-423 K with an interval of 20 K, which depict rectifying nature implying formation of Schottky barrier diode (SBD). **Figure 5.5b** exhibits Semi-logarithmic I-V characteristics. Supported by thermionic emission (TE) theory the rectification nature of SBD can be analysed for a forward bias voltage $V (\geq 3kT/q)$.

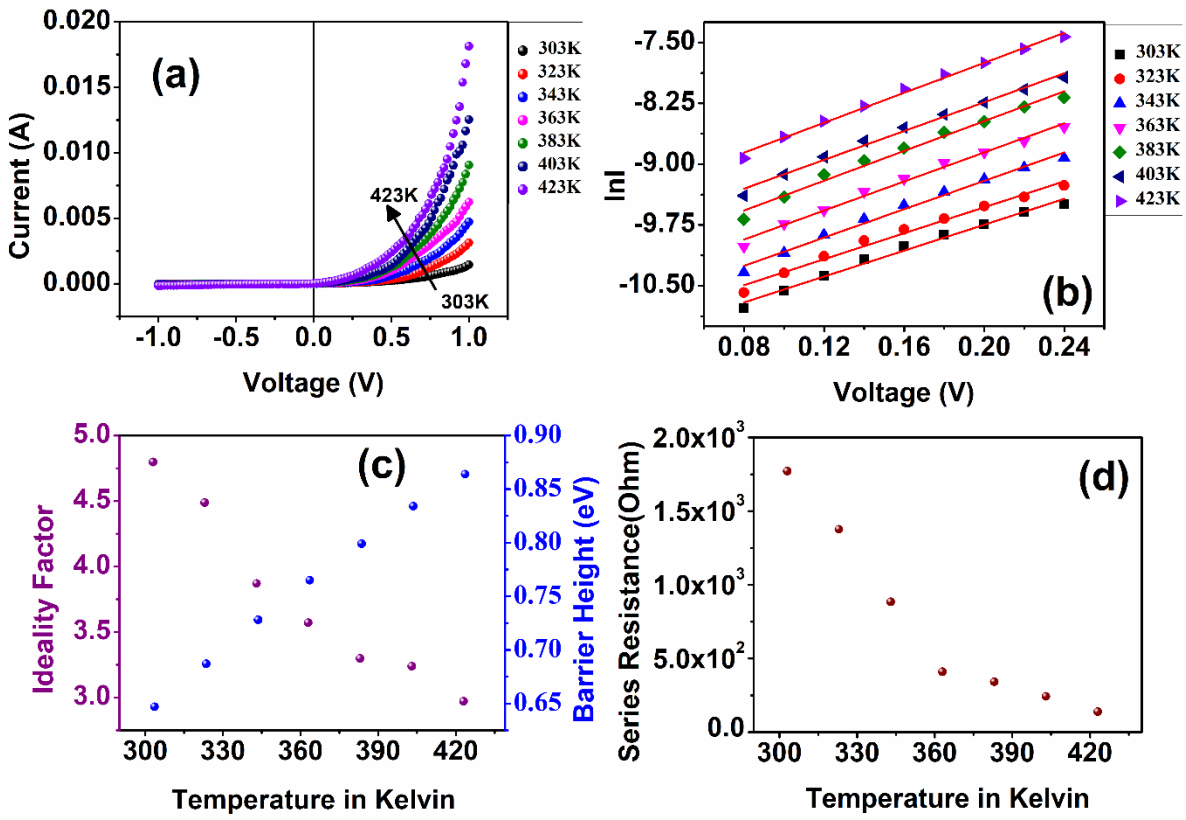


Figure 5.5: Temperature variation of (a) I-V characteristics (b) $\ln I$ vs V graph (c) ideality factor and barrier height (c) series resistance of Al/rGO-SnO₂/ITO configuration

The ideality factor can be measured at each temperature from the slope of forward $\ln I$ -V (**Figure 5.5b**) plot using the following equation [22, 23],

$$\eta = \frac{q}{kT} \left(\frac{dV}{d \ln I} \right) \quad (4.4)$$

From extrapolation of this plot to $V = 0$, one can evaluate reverse saturation current. From the value of reverse saturation current, effective BH can be easily estimated by rearranging *equation 1.12* as *equation 5.5* [11],

$$\phi_{b0} = \frac{kT}{q} \ln \left(\frac{AA^*T^2}{I_0} \right) \quad (5.5)$$

At higher bias voltage, I-V curve shows deviation from linearity due to interface states and series resistance (R_s). This series resistance is a current limiting factor which differs due to both the bias voltage and applied temperature. The R_s values for different temperature are estimated from I to V characteristics curve (*Figure 5.5a*) by using Mikhelashvili method [24], listed in *Table 5.2*. Mikhelashvili function $\alpha(V)$ is represented by the following equation [25],

$$\alpha(V) = d(\ln I)/d(\ln V) \quad (5.6)$$

Value of R_s according to Mikhelashvili,

$$R_s = \frac{V_{max}}{\alpha_{max}^2 I_{max}} \quad (5.7)$$

Where, I_{max} is the respective current of V_{max} where V_{max} is the voltage of the maximum point of $\alpha(V)$ versus V graph.

$\alpha(V)$ versus V graphs are shown in *Figure 5.6*.

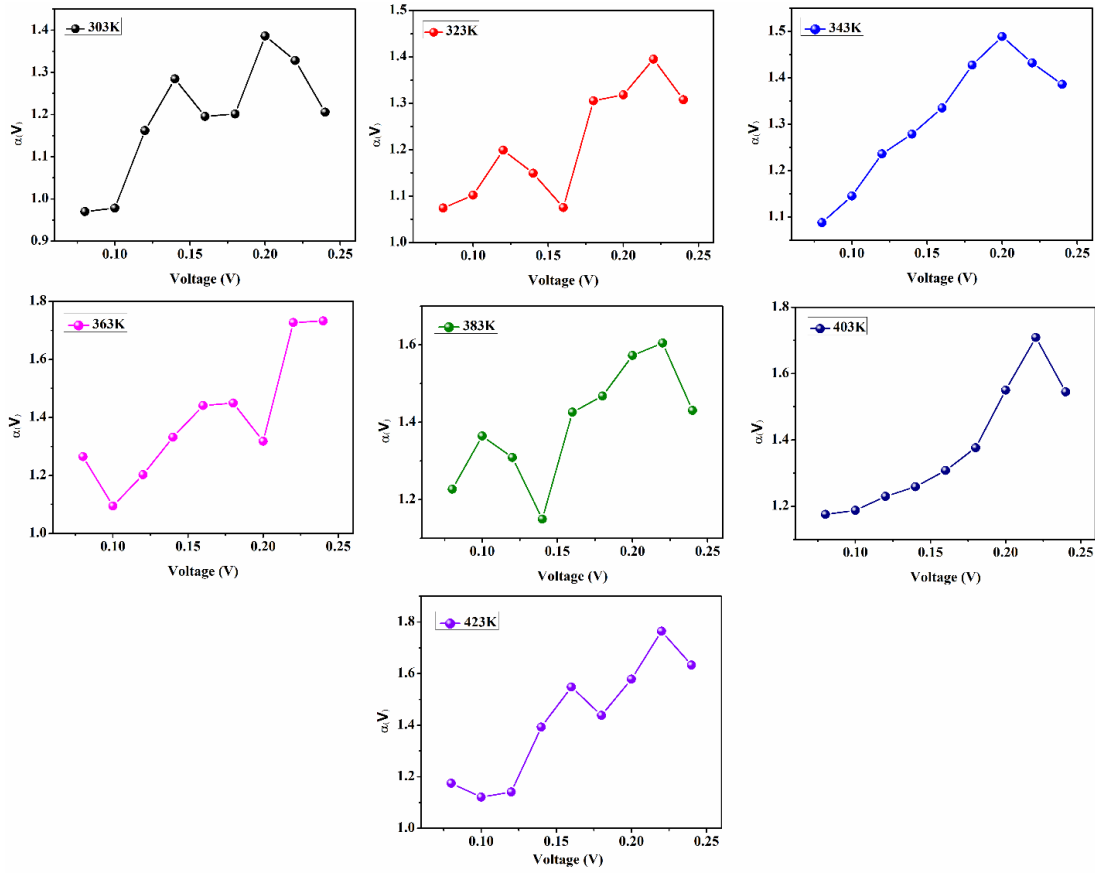


Figure 5.6: $\alpha(V)$ versus Voltage plot in different temperature for rGO-SnO₂

The derived values of ideality factor, reverse saturation current and barrier height are enlisted in **Table 5.2**. In this consequence the Richardson constant is estimated from theoretical approach as illustrated below.

The value of effective mass (m_e^*) of rGO-SnO₂ at 303 K and 423 K, are obtained ($0.88m_e$ and $0.9m_e$) from the following equation [7],

$$m_e^* = m^* m_e$$

Where,

$$\frac{1}{m^*} = 1 + \frac{p^2}{2m_e E_g} \quad (5.8)$$

where m_e ($= 9.1 \times 10^{-31}$ kg) is the free electron mass, E_g represents the optical bandgap of rGO-SnO₂ (obtained from optical data) differs with temperature (2.9 eV and 3.5 eV respectively) and momentum $p = \hbar G \approx \hbar/a$ (G is the smallest

reciprocal lattice vector and 'a' is the highest lattice constant). The value of 'a' is found to be 0.3199 nm from the JCPDS data which are same for material at temperature 303 K and 423K. The estimated effective Richardson constant at 303 K and 423 K are $1.057 \times 10^6 \text{ A/m}^2\text{K}^2$ and $1.081 \times 10^6 \text{ A/m}^2\text{K}^2$ respectively derived from the equation.

$$A^* = \frac{4\pi m_e^* k^2 q}{h^3} \quad (5.9)$$

where, h is Planck constant.

The change in barrier height and ideality factor with temperature, represented in **Figure 5.5(c)** indicates an increment of barrier height and a decrement of ideality factor with increasing temperature. **Figure 5.5(d)** exhibits decrease in internal series resistance along with temperature. The formation mechanism of barrier height depending upon the thermal treatment could be understood with the help of band diagram (schematic presentation) as indicated below:

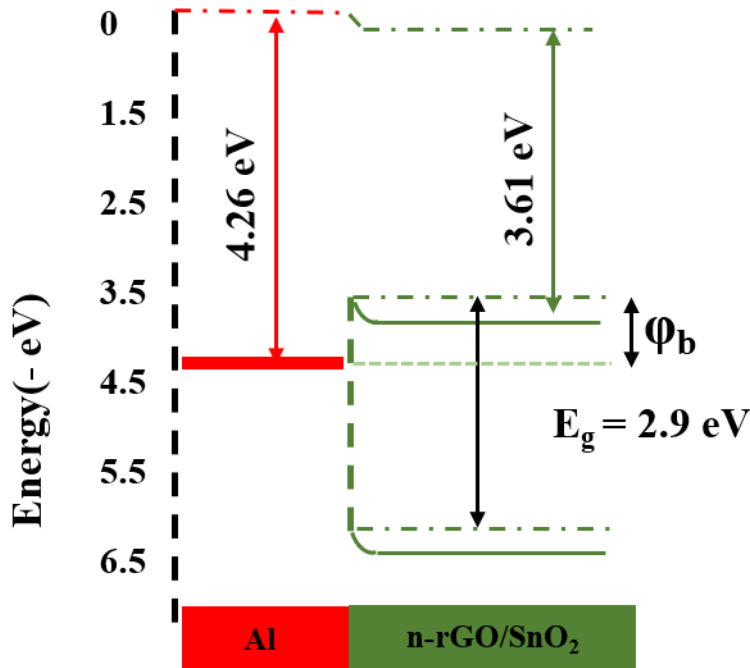


Figure 5.7: Schematic Energy band diagram of the MS device

Figure 5.7 represents certain barrier height, formed in the device at room temperature. With the increase of the temperature, band gap increases i.e., the bands of the semiconductor probably shifted from their previous position creating a high barrier height [26] (given in **Table 5.2**).

The high values of ideality factor (**Table 5.2**) indicate spatial barrier inhomogeneities and occurrence of interface states at MS junction. The large value of ideality factor (I.F), highly depends on current transportation mechanism that will be dominated by the electrons impinging through the SBH [27]. In a practical Schottky diode, SBH may not be exactly same over the entire interface area due to a variation in thickness of contact layer, composition of the junction layer and non-uniformity of interfacial charges etc [28]. As conduction of carriers is influenced quite a bit by temperature, at low temperature the conduction electrons can overcome the lower barriers through tunnelling [29]. With an increase of temperature, the charge carriers get adequate kinetic energy to overcome the patches of higher barriers through thermionic emission [30, 31]. In this study, the barrier height increases with increasing bias voltage and temperature, those attributed to deviation from ideal thermionic emission theory [32, 33].

Table 5.2: *SBD parameters in different temperature*

T(K)	$I_0 \times 10^{-5}$ (A)	η (IF)	ϕ_{b0} (eV)	R_s (Ω)
303	1.183	4.797	0.647	1771.48
323	1.461	4.488	0.687	1376.07
343	1.747	3.870	0.728	884.29
363	2.377	3.571	0.765	409.55
383	3.337	3.298	0.799	341.57
403	4.476	3.239	0.834	242.89
423	6.787	2.971	0.864	138.44

One should check whether this deviation might influence the value of Richardson constant. For this very purpose, **equation 1.15** is taken into consideration.

The activation energy plot i.e., $\ln(I_0/T^2)$ against q/kT is plotted with the help of **equation 1.15**. This plot implies a bowing trend rather than a straight line (while Schottky barrier is independent of temperature). A^* can also be evaluated from the intercept (**Figure 5.8**). **Figure 5.8** shows two linear temperature regions, one from 303 K to 363 K (referred as section I) and other from 383 K to 423 K (referred as section II). These A^* s ($6.211 \times 10^{-5} \text{ A/m}^2\text{K}^2$ for section I and $4.034 \times 10^{-3} \text{ A/m}^2\text{K}^2$ for section II) are much lesser than theoretical values as obtained earlier. The deviation in experimental value of A^* is probably due to the existence of charged surface states, metal induced gap states, material defects [34], barrier potential fluctuation of junction [35] etc.

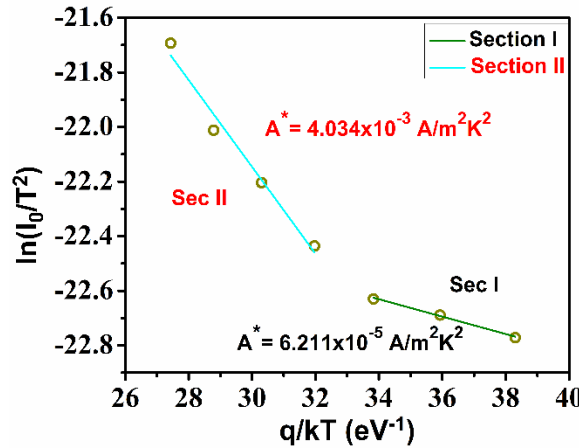


Figure 5.8: $\ln(I_0/T^2)$ versus q/kT plot for Al/rGO-SnO₂/ITO configuration

To intervene into the barrier inhomogeneity, ϕ_{b0} vs η (IF) is plotted and treated by Tung's theoretical approach, a linear relation between ϕ_{b0} and η (IF) [36]. **Figure 5.9** interprets the above indicated correlation curve which implies two different linear regions (Reg-I and Reg-II) of different slope. Lateral inhomogeneities of the barrier height may be the cause of occurrence of these two regimes. Considering $\eta = 1$, ϕ_{b0} are determined as 0.973 eV and 1.199 eV respectively from these plots.

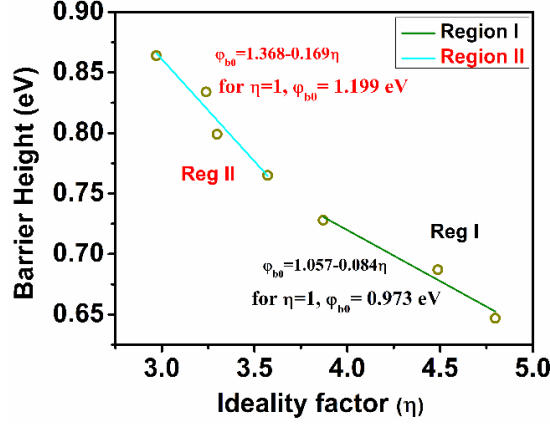


Figure 5.9: Barrier height vs Ideality factor for temperature range 303K to 423K

In *Figure 5.8* for region-I the charge transport mechanism is ruled by TE mechanism whereas for region-II is ruled by thermionic field emission theory [30]. These two linear regions could be best fitted to two Gaussian distributions (GD) plots, GD-I (Reg-I) and GD-II (Reg-II) [35]. Here, the GD model is implied to explain the junctional inhomogeneities. This model of inhomogeneous Schottky barrier follows a GD relation [37].

$$P(\phi_{ap}) = \frac{1}{\sigma_s \sqrt{2\pi}} \exp\left(-\frac{\phi_{ap} - \overline{\phi_{bo}}}{2\sigma_s^2}\right) \quad (5.10)$$

and the related current $I(V)$ is

$$I(V) = \int_{-\infty}^{\infty} I(\phi_{ap}, V) P(\phi_{ap}) d\phi_{ap} \quad (5.11)$$

where ϕ_{ap} denotes experimentally measured apparent barrier height and $\frac{1}{\sigma_s \sqrt{2\pi}}$ is the normalization constant of the Gaussian distribution where σ_s is standard deviation.

$I(\phi_{ap}, V)$ indicates current flow at a bias voltage V according to ideal TED theory and $P(\phi_{ap})$ is the accuracy probability for BH [38]. In this model ϕ_{ap} is related to ϕ_{b0} as [39],

$$\phi_{ap} = \phi_{b0}(T = 0) - \frac{q\sigma_s^2}{2kT} \quad (5.12)$$

To get insight of the best fitted GD (of the type: single or double or multiple) of BH, the plot of ϕ_{ap} against $q/2kT$ is drawn. **Figure 5.10a** represents two distinct regions within the curve, with two different slopes approving double Gaussian distribution. The slope of each straight line yields the standard deviation whereas intercept gives the barrier potential. Here the value of ϕ_{b0} is 1.465 eV and 1.339 eV and value of σ_s is 0.19 V and 0.209 V for region-I and region-II, respectively. Generally lower value of σ_s indicates lower barrier inhomogeneity. As the slopes seemed quite closer in magnitude, there is every possibility to explain the phenomena by using single GD method. By implying single GD method (**equation 5.12**), the parameters ϕ_{b0} and σ_s related with barrier inhomogeneity are estimated as 1.41 eV and 0.2 V (**Figure 5.10b**).

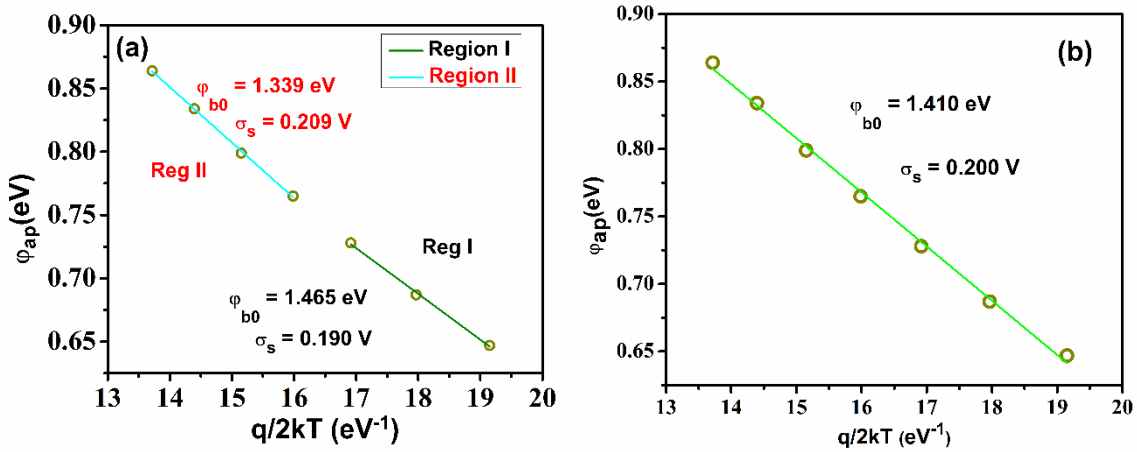


Figure 5.10: ϕ_{ap} against $q/2kT$ plot to check (a) double and (b) single Gaussian

To estimate the modified value of A^* with above approach, the Arrhenius equation (**equation 1.15**) of the form,

$$\ln\left(\frac{I_0}{T^2}\right) - \left(\frac{q^2\sigma_s^2}{2k^2T^2}\right) = \ln(AA^*) - \frac{q\phi_{b0}}{kT} \quad (5.13)$$

is considered. Considering the intercept of the extrapolated curve of $\ln(I_0/T^2) - q^2\sigma_s^2/2k^2T^2$ against q/kT (**Figure 5.11**) the value of A^* is calculated as 1.169×10^6 A/m²K² which is close to the theoretical value.

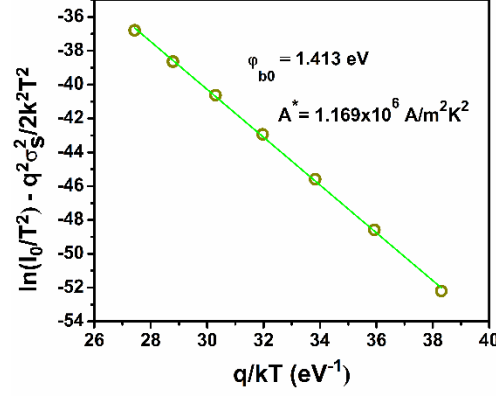


Figure 5.11: Modified Arrhenius plot for single Gaussian

5.3. Conclusion:

In this research work the temperature dependent current–voltage relation of Al/rGO-SnO₂/ITO Schottky diode are measured within the temperature range of 303 K-423 K at interval 20 K. While the curves are analysed to intervene into the charge transport mechanism, an incongruity is observed in the value of ideality factor and barrier height with rising temperature. The value of Richardson constant (of the order 10⁻⁵ A/m²K²) derived from experimental data by using TE theory is remarkably substandard to the theoretical (of the order 10⁶ A/m²K²) value. The discrepancy for barrier inhomogeneity is shorted out in **Figure 5.8**. ln(I₀/T²) versus q/kT plot for Al/rGO-SnO₂/ITO configuration. illustrated by adopting the Gaussian distribution (of kind single and double) analysis. The theoretical model of single Gaussian distribution of barrier inhomogeneity approves our approach and is sufficient to provide satisfactory insights of the leading parameters of charge transportation through junction. From the modified Richardson plot, it is confirmed that the evaluated values of Richardson constants are in close agreement to the theoretical values. Thus, it can be concluded that the temperature dependent current–voltage (I-V) characteristics of Al/rGO-SnO₂ Schottky junction can be successfully explained based on TE theory assuming a single Gaussian distribution of the barrier height.

References:

1. H. Guo, X. Lang, X. Tian, W. Jiang, and G. Wang, *Tunable Schottky barrier in Janus- XGa_2Y /graphene ($X/Y = S, Se, Te; X \neq Y$) van der Waals heterostructures*, Nanotechnology, 2022, **33**, 42, 425704
doi.org/10.1088/1361-6528/ac800d
2. B. S. Sannakashappanavar, A. B. Yadav, C. R. Byraredy, and N. V. L. Narasimha Murty, *Fabrication and characterization of Schottky diode on ultrathin ZnO film and its application for UV detection*, Materials Research Express, 2019, **6**, 116445
doi.org/10.1088/2053-1591/ab4cba
3. S. Singh, and J. A. Cooper, *Bipolar integrated circuits in 4H-SiC*, IEEE Transactions on Electron Devices, 2011, **58**, 4, 1084-1090
doi.org/10.1109/TED.2011.2107576
4. H. M. Manohara, E. W. Wong, E. Schlecht, B. D. Hunt, and P. H. Siegel, *Carbon nanotube Schottky diodes using Ti-Schottky and Pt-ohmic contacts for high frequency applications*, Nano Letters, 2005, **5**, 7, 1469-1474
doi.org/10.1021/nl050829h
5. M. Das, J. Datta, A. Dey, R. Jana, A. Layek, S. Middya, and P. P. Ray, *One step hydrothermal synthesis of a rGO-TiO₂ nanocomposite and its application on a Schottky diode: improvement in device performance and transport properties*, RSC Advances, 2015, **5**, 123, 101582-101592
doi.org/10.1039/C5RA17795B
6. V.-M. Hiltunen, P. Koskinen, K. K. Mentel, J. Manninen, P. Myllyperkiö, M. Pettersson, and A. Johansson, *Ultrastiff graphene*, npj 2D Materials and Applications, 2021, **5**, 49
doi.org/10.1038/s41699-021-00232-1
7. S. Sil, R. Jana, A. Biswas, D. Das, A. Dey, J. Datta, D. Sanyal, and P. P. Ray, *Elucidation of inhomogeneous heterojunction performance of Al/Cu₅FeS₄ Schottky diode with a gaussian distribution of barrier heights*, IEEE Transactions on Electron Devices, 2020, **67**, 5, 2082-2087
doi.org/10.1109/TED.2020.2983489
8. M. Gijare, S. Danane, M. Modak, and A. Garje, *Synthesis and characterization of rGO + SnO₂ composite for bio sensor application*, 2019 JETIR May 2019, **6**, 5, 17-22

9. P. Das, B. Pal, J. Datta, M. Das, S. Sil, and P. P. Ray, Improved charge transport properties of graphene incorporated tin oxide based Schottky diode over pure one, *Journal of Physics and Chemistry of Solids*, 2021, **148**, 109706
doi.org/10.1016/j.jpcs.2020.109706
10. P. Van Tuan, H. B. Tuong, V. T. Tan, L. H. Thu, N. D. Khoang, and T. N. Khiem, *SnO₂/reduced graphene oxide nanocomposites for highly efficient photocatalytic degradation of methylene blue*, *Optical Materials*, 2022, **123**, 111916
doi.org/10.1016/j.optmat.2021.111916
11. A. Dey, R. Jana, J. Dhar, P. Das, and P. P. Ray, *Gaussian distribution of inhomogeneous barrier height of Al/ZnS/ITO Schottky barrier diodes*, *Materials Today: Proceedings*, 2018, **5**, 3, 9958-9964
doi.org/10.1016/j.matpr.2017.10.193
12. Ö.F. Yüksel, N. Tuğluoğlu, B. Güleveren, H. Şafak, and M. Kuş, *Electrical properties of Au/perylene-monoimide/p-Si Schottky diode*, *Journal of Alloys and Compounds*, 2013, **577**, 15, 30-36
doi.org/10.1016/j.jallcom.2013.04.157
13. R. F. Schmitsdorf, T. U. Kampen, and W. Mönch, *Explanation of the linear correlation between barrier heights and ideality factors of real metal-semiconductor contacts by laterally nonuniform Schottky barriers*, *Journal of Vacuum Science & Technology B*, 1997, **15**, 4, 1221-1226
doi.org/10.1116/1.589442
14. C. H. Belgacem, and A. A. El-Amine, *Theoretical models for anomalously high ideality factor in a Au/SnO₂-Si(n)/Al solar cell*, *Silicon*, 2018, **10**, 1063-1066
doi.org/10.1007/s12633-017-9572-7
15. A. Monshi, M. R. Foroughi, and M. R. Monshi, *Modified Scherrer equation to estimate more accurately nano-crystallite size using XRD*, *World journal of nano science and engineering*, 2012, **2**, 3, 154-160
doi.org/10.4236/wjnse.2012.23020
16. M. Gomathi, P.V. Rajkumar, and A. Prakasam, *Study of dislocation density (defects such as Ag vacancies and interstitials) of silver nanoparticles, green-synthesized using Barleria cristata leaf extract and the impact of defects on the antibacterial activity*, in *Results Physics*, 2018, **10**, 858-864
doi.org/10.1016/j.rinp.2018.08.011

17. P. Tyagi, A. Sharma, M. Tomar, and V. Gupta, *A comparative study of RGO-SnO₂ and MWCNT-SnO₂ nanocomposites based SO₂ gas sensors*, Sensors and Actuators B: Chemical, 2017, **248**, 980-986
doi.org/10.1016/j.snb.2017.02.147
18. M. Hakamada, T. Kuromura, Y. Chen, H. Kusuda, and M. Mabuchi, *Influence of porosity and pore size on electrical resistivity of porous aluminum produced by spacer method*, Materials Transactions, 2007, **48**, 1, 32-36
doi.org/10.2320/matertrans.48.32
19. D. Liu, W. Zhou, J. Wu, W. Zhou, and W. Jiang, *CuO-CeO₂/ZSM-5 composites for reactive adsorption of hydrogen sulphide at high temperature*, The Canadian Journal of Chemical Engineering, 2016, **94**, 12, 2276-2281
doi.org/10.1002/cjce.22613
20. M. Ilka, S. Bera, and S. H. Kwon, *Influence of Surface Defects and Size on Photochemical Properties of SnO₂ Nanoparticles*, Materials (Basel, Switzerland), 2018, **11**, 6, 904
doi.org/10.3390/ma11060904
21. C. Aydın, *Synthesis of SnO₂: rGO nanocomposites by the microwave-assisted hydrothermal method and change of the morphology, structural, optical and electrical properties*, Journal of Alloys and Compounds, 2019, **771**, 964-972
doi.org/10.1016/j.jallcom.2018.08.298
22. D. Tomer, S. Rajput, and L. Li, *Spatial inhomogeneity in Schottky barrier height at graphene/MoS₂ Schottky junctions*, Journal of Physics D: Applied Physics, 2017, **50**, 16, 165301
doi.org/10.1088/1361-6463/aa61d9
23. M. Sağlam, B. Güzeldir, A. Türüt, and D. Ekinci, *Role of Reduced Graphene Oxide-Gold Nanoparticle Composites on Au/Au-RGO/p-Si/Al Structure Depending on Sample Temperature*, Journal of Electronic Materials, 2021, **50**, 4752-4761
doi.org/10.1007/s11664-021-09017-0
24. V. Mikhelashvili, G. Eisenstein, V. Garber, S. Fainleib, G. Bahir, D. Ritter, M. Orenstein, and A. Peer, *On the extraction of linear and nonlinear physical parameters in nonideal diodes*, Journal of Applied Physics, 1999, **85**, 9, 6873-6883
doi.org/10.1063/1.370206

25. O. Ya. Olikh, *Review and test of methods for determination of the Schottky diode parameters*, Journal of Applied Physics, 2015, **118**, 2, 024502
doi.org/10.1063/1.4926420
26. A. Baltakesmez, M. Sevim, B. Güzeldir, C. Aykaç, and M. Biber, *Interface application of NiPt alloy nanoparticles decorated rGO nanocomposite to eliminate of contact problem between metal and inorganic/organic semiconductor*, Journal of Alloys and Compounds, 2021, **867**, 158802
doi.org/10.1016/j.jallcom.2021.158802
27. S. Alialy, Ş. Altındal, E. E. Tanrikulu, and D. E. Yıldız, *Analysis of temperature dependent current-conduction mechanisms in Au/TiO₂/n-4H-SiC (metal/insulator/semiconductor) type Schottky barrier diodes*, Journal of Applied Physics, 2014, **116**, 8, 083709
doi.org/10.1063/1.4893970
28. S. Zeyrekli, M. M. Bülbül, Ş. Altındal, M. C. Baykul, and H. Yüzer, *The double gaussian distribution of inhomogeneous barrier heights in Al/GaN/p-GaAs (MIS) schottky diodes in wide temperature range*, Brazilian Journal of Physics, 2008, **38**, 4
doi.org/10.1590/S0103-97332008000500011
29. A. Turut, *On current-voltage and capacitance-voltage characteristics of metal-semiconductor contacts*, Turkish Journal of Physics, 2020, **44**, 4, 1
doi.org/10.3906/fiz-2007-11
30. H. Saghrouni, A. Missaoui, R. Hannachi, and L. Beji, *Investigation of the optical and electrical properties of p-type porous GaAs structure*, Superlattices and Microstructure, 2013, **64**, 507-517
doi.org/10.1016/j.spmi.2013.10.007
31. A. Gümüş, A. Türüt, and N. Yalçın, *Temperature dependent barrier characteristics of CrNiCo alloy Schottky contacts on n-type molecular-beam epitaxy GaAs*, Journal of Applied Physics, 2002, **91**, 1, 245-250
doi.org/10.1063/1.1424054
32. Ç.Ş. Güçlü, A.F. Özdemir, and Ş. Altındal, *Double exponential I-V characteristics and double Gaussian distribution of barrier heights in (Au/Ti)/Al₂O₃/n-GaAs (MIS)-type Schottky barrier diodes in wide temperature range*, Applied Physics A, 2016, **122**, 1032
doi.org/10.1007/s00339-016-0558-x
33. H. Cetin, and E. Ayyildiz, *Temperature dependence of electrical parameters of the Au/n-InP Schottky barrier diodes*, Semiconductor Science and Technology, 2005, **20**, 6, 625
doi.org/10.1088/0268-1242/20/6/025

34. F. Iucolano, F. Roccaforte, F. Giannazzo, and V. Raineri, *Temperature behavior of inhomogeneous Pt/GaN Schottky contacts*, Applied Physics Letters, 2007, **90**, 9, 092119
doi.org/10.1063/1.2710770
35. M. Das, J. Datta, A. Dey, S. Halder, S. Sil, and P. P. Ray, *Temperature dependent properties of Al/rGO-ZnCdS Schottky diode and analysis of barrier inhomogeneities by double Gaussian distribution*, Materials Letters, 2017, **204**, 184-187
doi.org/10.1016/j.matlet.2017.06.006
36. O. Pakma, N. Serin, T. Serin, and Ş. Altındal, *The double Gaussian distribution of barrier heights in Al/TiO₂/p-Si (metal-insulator-semiconductor) structures at low temperatures*, Journal of Applied Physics, 2008, **104**, 1, 014501
doi.org/10.1063/1.2952028
37. M. A. Laurent, G. Gupta, D. J. Suntrup, S. P. DenBaars, and U.K. Mishra, *Barrier height inhomogeneity and its impact on (Al, In, Ga) N Schottky diodes*, Journal of Applied Physics, 2016, **119**, 6, 064501
doi.org/10.1063/1.4941531
38. Z. Ouennoughi, S. Toumi, and R. Weiss, *Study of barrier inhomogeneities using I-V-T characteristics of Mo/4H-SiC Schottky diode*, Physica B: Condensed Matter, 2015, **456**, 176-181
doi.org/10.1016/j.physb.2014.08.031
39. Ş. Aydoğan, M. Sağlam, and A. Türüt, *On the barrier inhomogeneities of polyaniline/p-Si/Al structure at low temperature*, Applied Surface Science, 2005, **250**, (1-4), 43-49
doi.org/10.1016/j.apsusc.2004.12.020

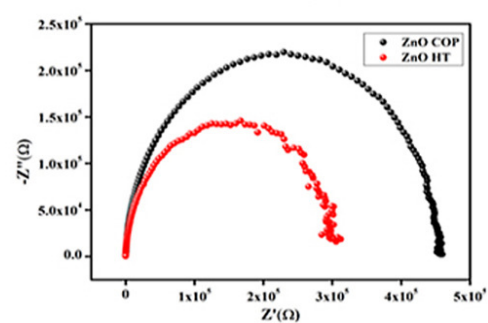
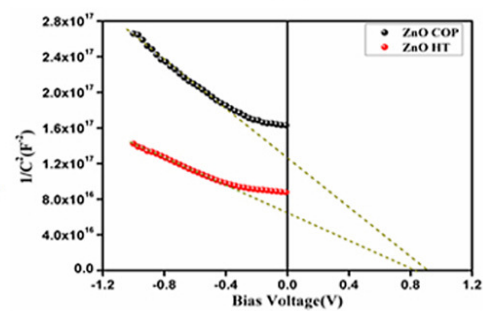
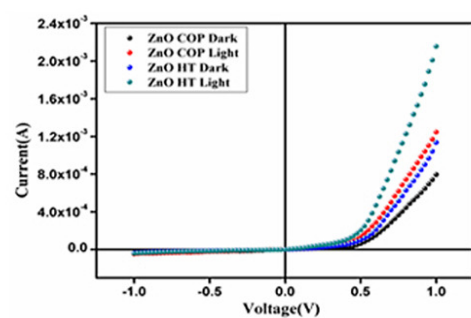
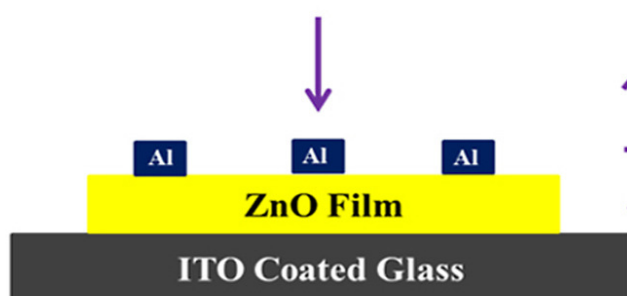
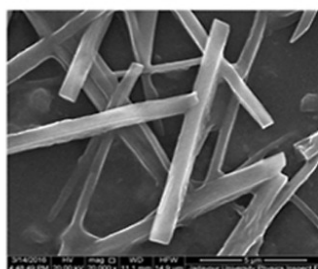
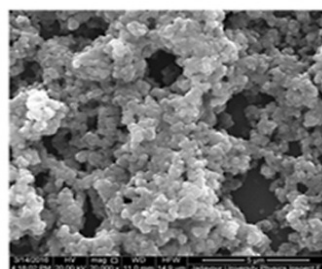
Chapter 6

Improved device performance of rod
like ZnO in a Schottky type
photosensor compared to particle like
ZnO: Analysis of charge transport

Abstract

In this work, we report two different synthesis process of semiconducting ZnO which modifies the morphology of the ZnO materials and its impact in photosensing Schottky diode. Hydrothermal and co-precipitation method were used to synthesize ZnO which gave rise to rod like (ZnO HT) and particle like ZnO (ZnO COP), respectively. From UV–Vis analysis, ZnO HT exhibited greater optical absorption. Al/ZnO (HT and COP)/ITO Schottky diodes were fabricated and the photo-response as well as diode parameters were investigated by current-voltage and capacitance voltage measurements. Then charge transport properties were determined by space charge limited current theory and impedance spectroscopy. The results showed that the ZnO HT based SBD delivered a responsivity of 0.144 A/W which is 121% higher than the responsivity showed by ZnO COP based SBD (0.065 A/W). The specific detectivity of ZnO HT was measured at 7.54×10^9 Jones, a noticeable improvement from the 4.10×10^9 Jones of ZnO COP. The carrier mobility, lifetime and diffusion length of the ZnO HT based device were found to be $0.0014 \text{ cm}^2 \text{ V}^{-1}\text{s}^{-1}$, 72.35 μs and 72.37 μm respectively which are again superior to its counterpart. The faster and better charge transport is facilitated by the rod like morphology of the former. The study demonstrates improved device performance of rod like ZnO based Schottky diode and provides detail analysis of the Al/ZnO interface which can be beneficial for future research on metal-semiconductor junction.

Graphical Abstract



6.1. *Introduction:*

For a long time, zinc oxide (ZnO) has been the centre of intensive research and it continues to be so due to its optical transparency, non-toxic environment friendly nature, simple cost- effective synthesis procedure and promising applications. Due to hexagonal wurtzite crystal structure and noncentro symmetry of the oxygen atom in tetrahedral coordination geometry, ZnO exhibits exciting properties [1, 2]. Equipped with these favourable attributes, ZnO has been extensively used for electronic, optoelectronic, and electrochemical applications such as Schottky diodes, lasers, thin-film transistors, piezoelectric devices, light-emitting diode, photovoltaic cell and gas sensors [[3], [4], [5], [6], [7], [8], [9], [10], [11], [12], [13], [14], [15], [16], [17], [18]].

Among them, metal-semiconductor Schottky barrier diodes (SBDs) are one of the most important devices for radio frequency (RF) electronics, optoelectronics, and fast switching device application. Not only that, they offer an interesting platform for material characterization [[19], [20], [21]]. The performance of a Schottky diode is influenced by the material properties and especially, by the morphology of the materials. Over the past decade, application of rod like structures of ZnO has received widespread attention due to a large surface-to-volume ratio with reduced dimension [2]. Significant time and effort are being devoted for high-quality ZnO-based Schottky diode fabrication and their characterization using a variety of techniques [[22], [23], [24], [25], [26], [27]]. The morphology of ZnO can change depending upon the synthesis technique and that change can affect its performance in a Schottky device.

To have a good understanding of the metal-semiconductor interface, along with current-voltage (I–V) characteristics, capacitance-voltage (C–V) and impedance spectroscopy measurements can play a pivotal role. In addition, the

analysis of charge transport from I–V and impedance spectroscopy is very important.

So, in this paper, we report the synthesis of ZnO with particle (ZnO COP) and rod like (ZnO HT) morphology by coprecipitation and hydrothermal method, respectively. Thereafter Al/ZnO SBD are fabricated and their photoresponse is compared. To investigate the Al/ZnO interface, different diode parameters are analyzed from I–V and C–V measurements. Finally, the charge transport parameters are extracted from space charge limited current theory and impedance spectroscopy analysis for further understanding of the metal-semiconductor junction.

6.2. *Materials and methods:*

To synthesize ZnO nanomaterial of different morphology, coprecipitation and hydrothermal process was utilized. In two separate beakers, 0.1 M $\text{Zn}(\text{CH}_3\text{COO})_2$ and 0.1 M NaOH aqueous solution was prepared. After that, the $\text{Zn}(\text{CH}_3\text{COO})_2$ solution was divided into two equal volumes and kept in separate beakers. For the synthesis of ZnO COP, NaOH was added dropwise to one of the $\text{Zn}(\text{CH}_3\text{COO})_2$ solution and the mixture was vigorously stirred for 12 h. The product that ensued was washed thoroughly with distilled water and ethanol. The resultant was vacuum dried at 60°C to achieve the final product in white powder form. To synthesize ZnO HT, a similar process was carried out until the stirring. Once the stirring was done; the solution was transferred to a Teflon lined autoclave and kept at 160°C for 24 h. After that heating was stopped and the solution was kept at same state to age for 1 day. After washing the resultant solution thoroughly with distilled water and ethanol, it was dried in vacuum at 60°C. A white powder was obtained as final product.

6.3. Results and discussion:

6.3.1. XRD analysis:

Figure 6.1 shows the XRD patterns of ZnO COP and ZnO HT. The XRD was performed to confirm the phase purity of the samples. The XRD pattern of both the ZnO samples i.e., ZnO COP and ZnO HT showed the peaks at $2\theta = 31.69^\circ$, 34.38° , 36.16° , 47.51° , 56.55° , 62.86° , 66.50° , 67.99° and 69.06° corresponding to the planes (100), (002), (101), (102), (110), (103), (200), (112) and (201) of ZnO in a hexagonal wurtzite lattice (supported by JPCDS card no. 36–1451) [28, 29]. Presence of these peaks for both the materials and the peak positions confirms successful synthesis of ZnO. The peaks of the ZnO COP were broader than the peaks of ZnO HT, which suggests smaller crystallite size for the synthesized ZnO COP compared to ZnO HT, a fact supported by **Table 6.1**. However, the absence of any secondary phase confirms the synthesis of pure and single phase ZnO.

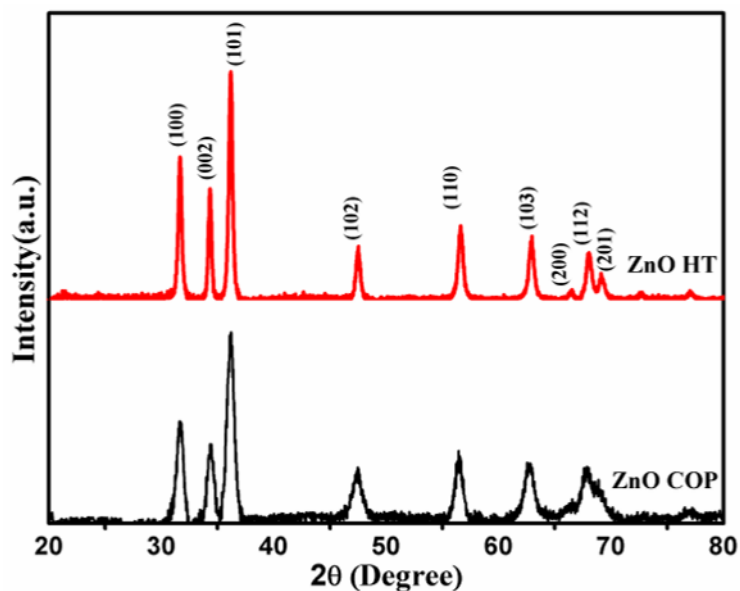


Figure 6.1: XRD images of ZnO HT and ZnO COP

The interplanar spacing is calculated from the Bragg's law (*equation 2.1*). The crystalline sizes of the ZnO samples are also calculated from Williamson-

Hall plot (**Figure 6.2a** and **b**). These plots are drawn using the equation below [30, 31]:

$$\beta \cos \theta = \frac{K\lambda}{D} + \mu \sin \theta \tag{6.1}$$

The average crystallite sizes are determined to be 51.16 nm and 20.24 nm for the ZnO HT and ZnO COP samples, respectively.

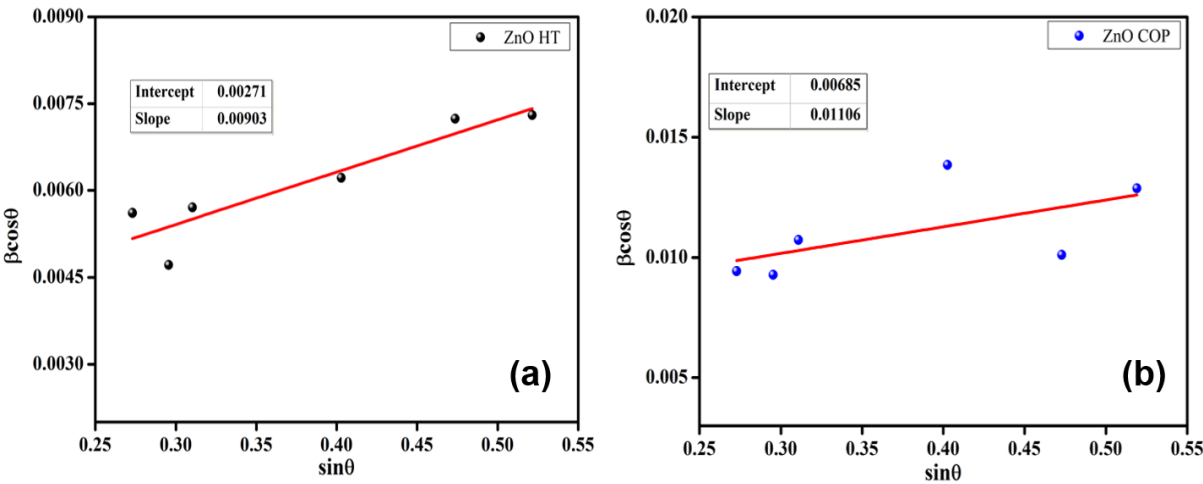


Figure 6.2: Williamson-Hall plot for (a) ZnO HT and (b) ZnO COP

Table 6.1: XRD parameters of different planes

Peak position [2θ (degree)]		Interplanar spacing [d (Å)]		Miller indices (hkl)
ZnO HT	ZnO COP	ZnO HT	ZnO COP	
31.69	31.67	2.82124	2.82298	(100)
34.38	34.34	2.60640	2.60935	(002)
36.16	36.21	2.48208	2.47877	(101)
47.51	47.48	1.91224	1.91337	(102)
56.55	56.44	1.62612	1.62903	(110)
62.86	62.54	1.47721	1.48399	(103)
66.50	66.59	1.40491	1.40322	(200)
67.99	67.85	1.37770	1.38020	(112)
69.06	69.01	1.35894	1.35981	(201)

The lattice parameters *a* and *c*, found from the equation for hexagonal lattice parameter, are enlisted in **Table 6.2**:

$$\frac{1}{d_{hkl}^2} = \frac{4}{3} \frac{h^2 + hk + k^2}{a^2} + \frac{l^2}{c^2} \tag{6.2}$$

Table 6.2: *lattice parameter of ZnO HT and ZnO COP*

	Lattice parameters	
	a=b (Å)	c (Å)
ZnO HT	3.25626	5.21281
ZnO COP	3.25969	5.21870

6.3.2. SEM analysis:

The morphology of the samples can play a decisive role in their device performance. So, SEM was done to analyze the morphology of the synthesized materials. The SEM images of the synthesized ZnO COPs and ZnO HTs are presented in **Figure 6.3(a)** and **(b)**, respectively. In **Figure 6.3(a)**, some agglomeration was seen for the ZnO COP.

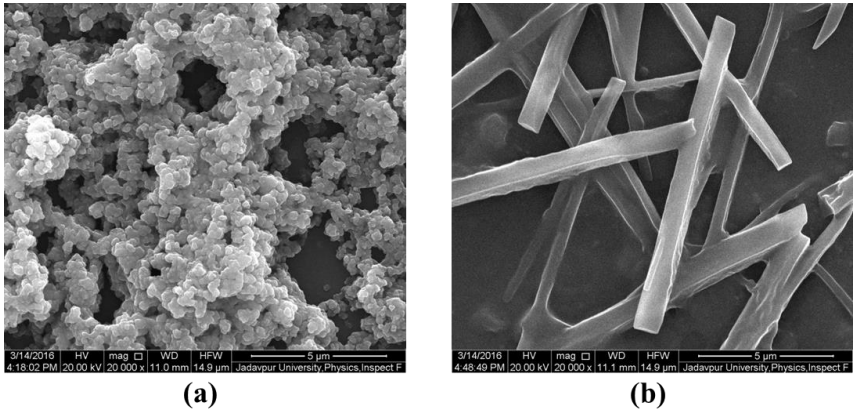


Figure 6.3: SEM images of synthesized (a) ZnO COP and (b) ZnO HT materials

The morphology of ZnO COP particles was found to be spherical and the particle size was around 500 nm. Fig. 5.3(b) reveals the morphology of the ZnO HT particles. In the ZnO HT, no such agglomeration like ZnO COP was seen. The figure shows that the morphology of ZnO HT is rod like while the length of the

rods is around 10 μm and the width is in the range of 400–800 nm. So, it is seen that the synthesis process has affected the morphology of the synthesized ZnO materials.

6.3.3. FTIR Analysis:

Fourier transform infrared (FTIR) spectroscopy experiment was carried out for the synthesized ZnO materials to find out the functional groups in the samples and the obtained spectra is given in **Figure 6.4**. The FTIR peak positions for both the samples were same.

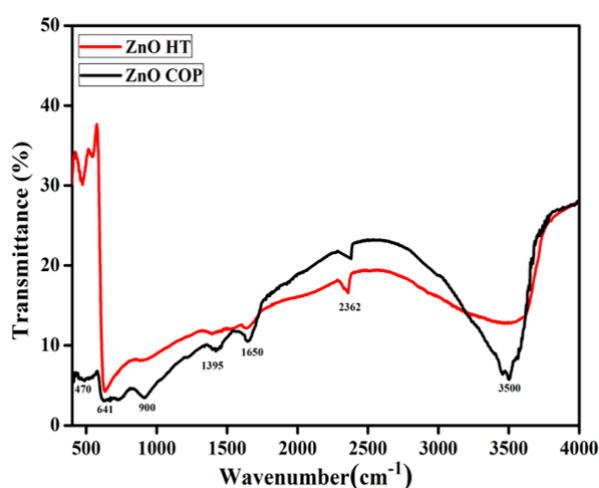


Figure 6.4: FTIR spectra of ZnO HT and ZnO COP

The broad band centred around 3500 cm^{-1} region is ascribed to the O–H stretching vibrations of the hydroxyl groups and the peaks around 2362 cm^{-1} are due to the presence of oxygen [32, 33, 34]. There is another small peak at 1395 cm^{-1} which corresponds to an O–H bending vibration [32, 33]. The peaks at 900 cm^{-1} , 641 cm^{-1} , 470 cm^{-1} has been allotted to Zn–O stretching vibration [32]. At 1650 cm^{-1} , another peak was observed, and attributed to the first overtone of the crucial stretching mode of OH [35]. There is a sudden change between the transmittance of ZnO HT and ZnO COP near 600 cm^{-1} . This can be due to few probable reasons. One probable reason is that, this is due to difference of concentration and thickness or path length through the samples. Another reason

may be the difference in amount of that particular Zn–O bond present in the different samples. Scattering in the samples may also affect their transmittance. However, most importantly, the FTIR analysis shows presence of peaks related to the Zn–O bonding in both the samples which confirm the successful synthesis of ZnO HT and ZnO COP.

6.3.4. UV–vis absorption analysis:

To explore the optical absorption property of the synthesized materials, UV–Vis absorption spectroscopy was performed. The obtained absorption spectra are given in **Figure 6.5(a)** for the wavelength range between 300 nm and 800 nm. The figure shows enhanced light absorption for the ZnO HT compared to ZnO COP, especially in the visible wavelength region. Further, to find out the optical band gap of the materials Tauc's equation (**equation 5.3**) was employed.

To find out the band gap from Tauc's plot [given in **Figure 6.5(b)**], a line was extrapolated from the linear region of the graphs to the X-axis. The band gap of ZnO HT and ZnO COP was found to be 3.22 eV and 3.25 eV from the plot. The lower band gap and higher light absorption of ZnO HT implies that it should show higher photo-response in the fabricated Schottky diode.

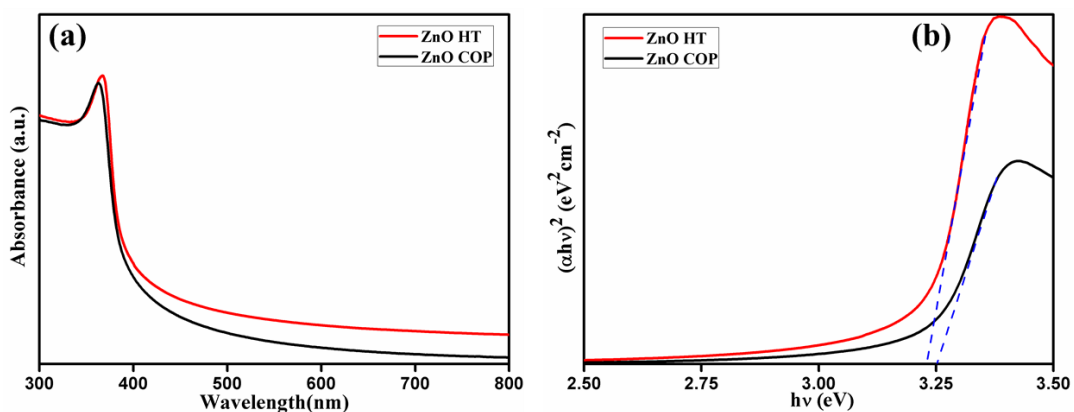


Figure 6.5: (a) UV–Visible spectra and (b) Tauc's Plot of ZnO HT and ZnO COP

6.3.5. Current-voltage (I–V) measurements:

To analyse the electrical properties of MS junction formed between the synthesized ZnO of different morphology and aluminium, current-voltage (I–V) measurement of the fabricated devices are performed in the voltage range -1 V to +1 V. The experiment is first carried out under dark and then under white light illumination to have a glimpse of the photosensitivity. The I–V characteristics curves for dark and light conditions are given in **Figure 6.6**. The I–V graph with current in log scale (y-axis) is also provided in the inset of **Figure 6.6**. All the I–V graphs showed rectifying nature with rectification ratio of 25 and 35 for ZnO COP and ZnO HT respectively, under dark condition. For both the devices, there was slight improvement in rectification under light. The rectifying nature of the curves points towards a Schottky barrier formation. The ZnO our experiment and showed higher current and rectification.

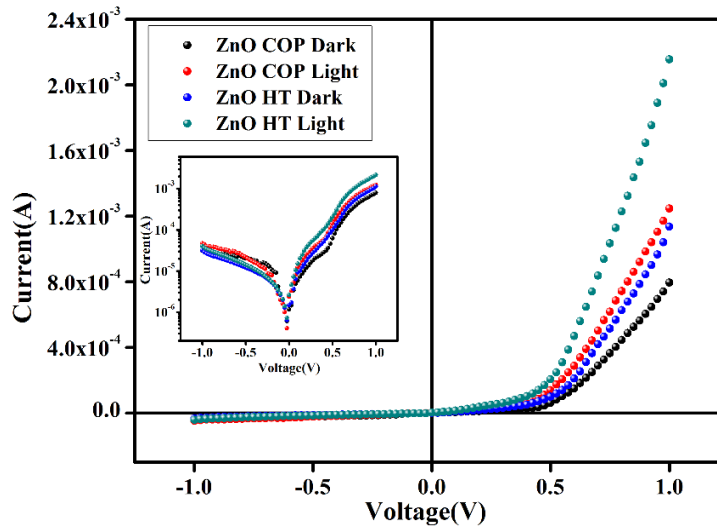


Figure 6.6: Current-voltage (I–V) characteristics graph for all the devices under dark and light (Inset: Current-voltage graph with current presented in log scale (y axis))

It is important to also assess the photo-response of the devices for potential optoelectronic application. So, I–V measurement was done under a white light illumination of 100 mW/cm² intensity. Parameters such as photosensitivity (S),

responsivity (R) and specific detectivity (D) are necessary to analyse the merit of a photo-sensing device. These are calculated by using *equation 4.2, 4.3 and 4.4*.

The results obtained are given in *Table-6.3*. The results show better photoresponse in the devices fabricated with ZnO HT compared to the device fabricated with ZnO COP. Especially, the responsivity of ZnO HT based SBD was 0.144 A/W which is 121% higher than that of the ZnO COP.

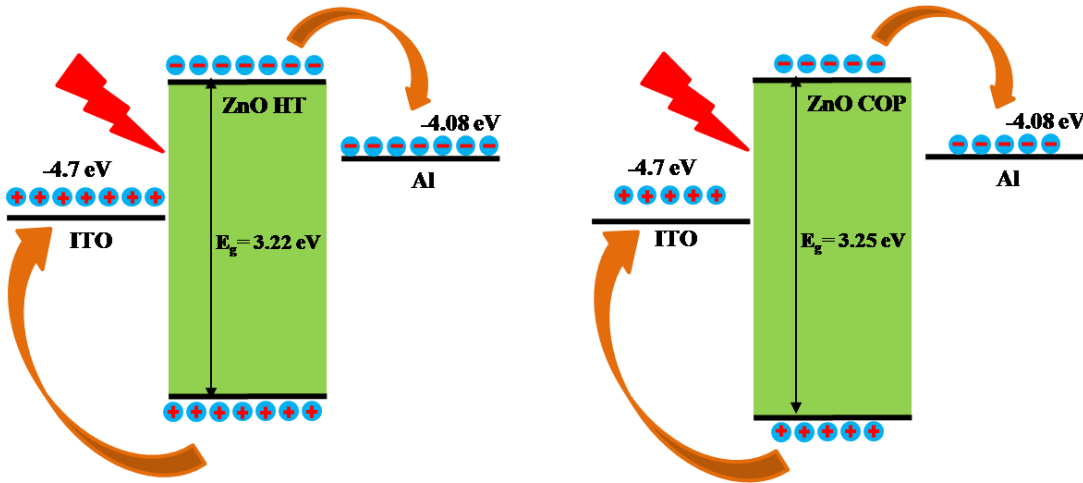


Figure 6.7: Schematic diagram for working mechanism of photoresponse in Al/ZnO HT/ITO and Al/ZnO COP/ITO SBDs

The better photosensing performance of ZnO HT has been demonstrated by energy band diagrams in *Figure 6.7*. The UV–Vis analysis revealed that the band gap of ZnO HT is less than that of ZnO COP. Upon light illumination, more photoinduced charge carriers are generated in ZnO HT. On top of that, the lower energy of band gap of ZnO HT ensures that higher number of electrons can reach the conduction band of ZnO HT compared to the number of electrons that reaches the conduction band in ZnO COP. Therefore, finally more electrons can reach the electrode in ZnO HT, thus resulting in more photocurrent. The photosensitivity and specific detectivity also improved for ZnO HT. This is due to the enhanced light absorption of the ZnO HT material as is evident from the UV–Vis absorption

analysis. As can be seen from the **Table-6.3**, the responsivity and specific detectivity values of our devices were comparable or better than some of the reported values for ZnO based Schottky type photodetectors [36, 37]. *Tian et al.* reported with 0.028 A/W responsivity for ZnO based UV photodetector whereas *Wang et al.* reported a responsivity of 0.00125 A/W for ZnO/Ag Schottky junction. So clearly our devices, specially the one based on ZnO HT performed quite well in this regard and have potential for photodetector application.

For the purpose of extracting Schottky parameters, I–V curve in log-log scale is presented in **Figure 6.8**, where three regions are noticed appertaining to different conduction mechanisms. In the first region, the current is dominated by tunnelling of bulk generated electrons and the slope is around 1 [38, 39]. The charge conduction is modified by presence of traps at the MS interface.

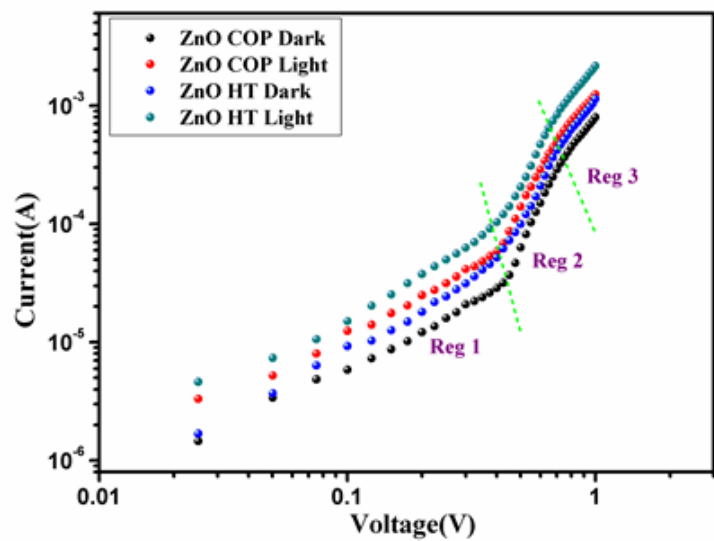


Figure 6.8: I–V graph in log-log scale

Implying Cheungs’ equation (**equation 4.7** and **4.8**) and considering Richardson constant as $32 \text{ A K}^{-2}\text{m}^{-2}$ in this case ideality factor, barrier height and series resistance are calculated to further analyse the devices.

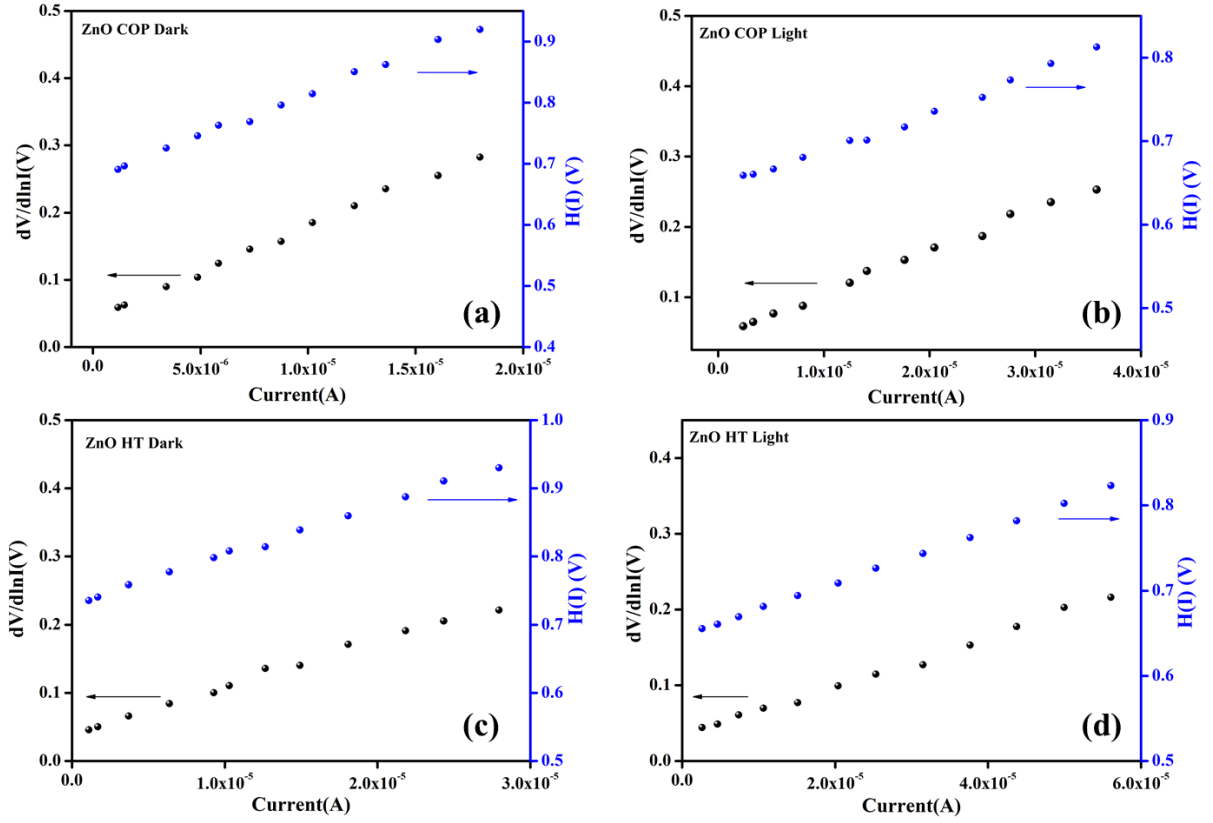


Figure 6.9: $dV/d\ln I$ vs I and $H(I)$ vs I graph under dark ((a) and (c)) and light ((b) and (d)) for Al/ZnO COP/ITO and Al/ZnO HT/ITO Schottky diodes

The $dV/d\ln I$ vs I graph, shown in **Figure 6.9** for both dark and light condition, can provide the ideality factor and series resistance from the y axis intercept and slope of the graph, respectively. Barrier heights and a second approximation of series resistance were obtained from the $H(I)$ vs I graph (**Figure 6.9**). The values of series resistances were calculated from the slope of the graphs and the barrier height values were extracted from the y axis intercept. First and second approximation of R_s from $dV/d\ln I$ vs I and $H(I)$ vs I gave us almost similar results, thus authenticating the consistency of this method. The series resistance of the ZnO HT based SBD is significantly lower than ZnO COP based SBD as shown in **Table-6.3**. This is indicative of better device performance of the ZnO HT. However, the diodes didn't show ideal junction behaviour with ideality factors being larger than 1 for all the cases, probably caused by the presence of a thin oxide layer at the Al/ZnO junction or barrier electron tunnelling. Carrier

recombination process within the depletion region may have played a part, too. The ideal factor of ZnO HT based SBD is slightly closer to 1, which implies a better junction behaviour. However, there is not much difference in the barrier heights of the devices. The ideality factor and barrier height for both the devices are given in **Table-6.3**.

Table 6.3: *SBD parameters from I–V*

SBD	Cond ⁿ	Rectification ratio	S (%)	R (A/W)	D* (Jones) ×10 ⁹	R _s (dV/dlnI) kΩ	R _s (H) kΩ	Ideality Factor	Barrier Height (eV)
Al/ ZnO COP/ ITO	Dark	25	58	0.065	4.10	0.54	0.53	1.76	0.60
	Light	27				0.33	0.38	1.75	0.58
Al/ ZnO HT/ ITO	Dark	35	89	0.144	7.54	0.44	0.48	1.74	0.57
	Light	53				0.21	0.24	1.70	0.57

6.3.6. Capacitance-voltage measurements:

To further characterize the diodes, capacitance (C) versus voltage (V) measurements was performed. This method also can be used to determine barrier height, along with built in potential and depletion layer width. 1/C² vs voltage graph for the SBDs is shown in Fig. 5.10, at 1 MHz frequency with 50 mV oscillatory voltages.

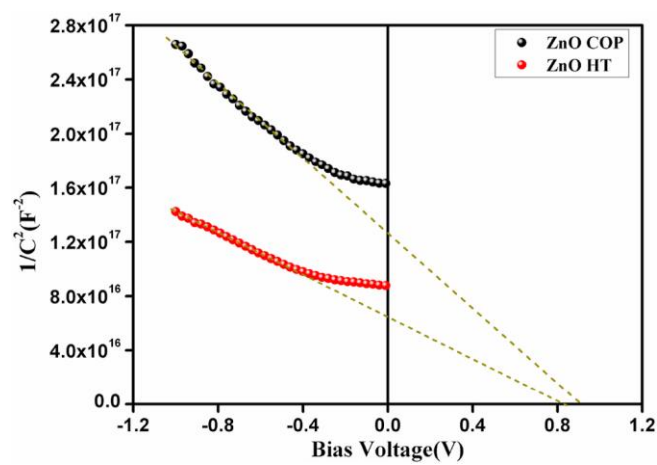


Figure 5.10: 1/C² vs V graph for the Al/ZnO HT/ITO and Al/ZnO COP/ITO SBDs

The linear portion of the graph was extrapolated to obtain the built-in potential (V_{bi}) of the SBD from X-axis intercept following the equation [40, 41] derived from *equation 1.16*:

$$C^{-2} = \frac{2(V_{bi}+V)}{q\epsilon_r\epsilon_0 A^2 N_D} \quad (6.3)$$

The relative dielectric constant for this equation is measured from capacitance vs frequency plot of the film at a constant bias potential, presented in *Figure 6.11* by employing *equation 4.12*.

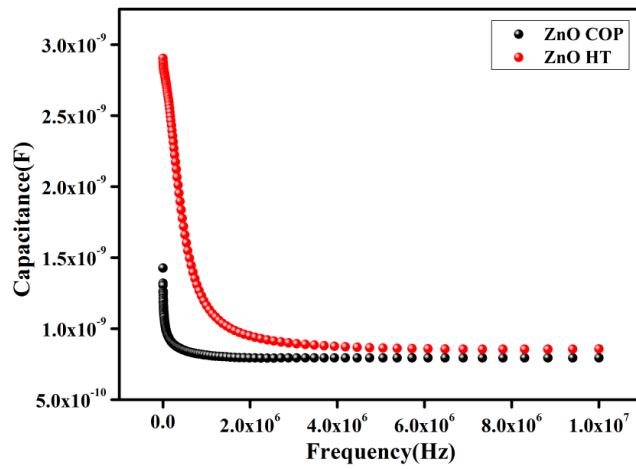


Figure 6.11: Capacitance vs Frequency graph for ZnO COP and ZnO HT

N_D is derived from the slope of $1/C^2-V$ plot. The graph shows that the slope of the linear portion is higher for ZnO COP than the slope for ZnO HT which indicates higher N_D value for ZnO HT, as that is inversely proportional to the slope. The X-axis intercept denotes higher built in potential for ZnO COP based SBD. The built-in potential of ZnO COP based SBD was 0.90 V and that of ZnO HT based SBD was 0.85 V. Depletion layer width of a diode is indicative of its performance. So, the depletion layer width (W_D) was also extracted from [40, 41]:

$$W_D = \left(\frac{2\epsilon_r\epsilon_0 V_{bi}}{qN_D} \right)^{\frac{1}{2}} \quad (6.4)$$

Thereafter, another determination of the barrier height (ϕ_b) is done by using the equation [40, 41]:

$$\phi_b = V_{bi} + \frac{(E_C - E_F)}{q} = V_{bi} + \left(\frac{kT}{q}\right) \left[\ln \frac{N_C}{N_D}\right] \quad (6.5)$$

where E_C and E_F are the conduction band edge energy and the Fermi level energy respectively, and N_C is density of states of conduction band-

$$N_C = 2 \left(\frac{2\pi m_e^* k_B T}{h^2}\right)^{3/2} \quad (6.6)$$

The values of V_{bi} , N_D , W_D and ϕ_b are given in **Table-6.4**. The ZnO HT has higher value of N_D than the ZnO COP, which explains the higher current in ZnO HT SBD from I–V curve. A lower depletion layer width in ZnO HT based SBD was found which imply its better performance and better charge transport. The barrier heights of the devices were 0.95 eV and 0.89 eV. There is a deviation from the values obtained from I–V graphs. It has been seen that, in general C–V curves give higher barrier height value than that derived from I–V graphs. This is due to different methods of measurement technique. In the metal-semiconductor junction, barriers are not uniform and ideal. This distribution of BHs due to the inhomogeneties may also have played a part in different values of BHs obtained from the two techniques.

Table-6.4: SBD parameters from C–V

Device	Built-in potential (V_{bi}) (Volt)	Donor Concentration (N_D) (m^{-3}) $\times 10^{22}$	W_D (nm)	Barrier Height (ϕ_b) (eV)
Al/ZnO COP/ITO	0.90	1.58	284	0.95
Al/ZnO HT/ITO	0.85	2.21	243	0.89

Apart from that, notably the C–V method produces the flat band barrier height whereas the I–V method yields the zero-bias barrier height, presented in **Table-6.4**. The reports have also shown similar or greater mismatch in barrier

heights obtained from I–V (Cheung’s method) and C–V method. *Semple et al.* reported significant deviation in barrier heights obtained from Cheung’s method (0.54 eV) and C–V method (0.89 eV) in an Au/ZnO/Al Schottky diode [42]. *Varma et al.* also reported a barrier height of 0.21 eV from Cheung’s method and 0.68 eV from C–V method in Au/ZnO Schottky diode which is an even greater mismatch than ours [43]. They attributed this phenomenon to barrier inhomogeneities and interface defect states present at the Schottky junction.

6.3.7. Charge transport analysis from I–V:

A very essential aspect of device performance that is to be taken into account is analysis of the charge transport properties of the materials. The slope in **Figure 6.8** increases sharply after region I to about 4–5. This increase in region II is due to the traps being filled by the electrons. When the voltage increases, the traps begin to fill quickly with high number of electrons and hence the dramatic increase in current takes place. This region is trap filling region. After a certain voltage, when majority or all the traps have been filled, the movement of electron slows down resulting in decline of the slope. The slope here (region III) becomes around 2 that is current follows the relation $I \propto V^2$. This is indicative of space charge limited current (SCLC) mechanism [38, 39]. SCLC theory has been an effective tool to estimate the transport properties. So, this region is taken into consideration for further analysis.

The effective carrier mobility of materials by employing Mott-Gurney space-charge limited-current (SCLC) *equation 4.11*.

Following the equation, effective carrier mobility (μ_{eff}) was calculated as $0.0011 \text{ cm}^2 \text{ V}^{-1} \text{ s}^{-1}$ for ZnO COP and $0.0014 \text{ cm}^2 \text{ V}^{-1} \text{ s}^{-1}$ for ZnO HT from the I vs V^2 graph (**Figure 6.12**). So, charge transport in ZnO HT was faster leading to higher current.

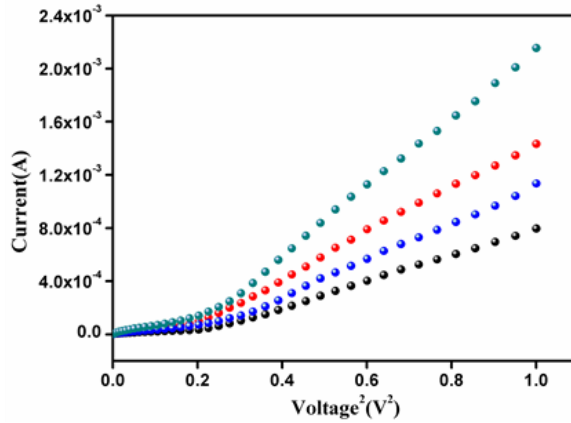


Figure 6.12: $I-V^2$ graph for the Al/ZnO HT/ITO and Al/ZnO COP/ITO SBDs under dark and light

Then transit time (τ_t) of charge carriers is also derived from the *equation 4.13* in Chapter 4. The transit time of charge carriers in ZnO HT was lower than that in ZnO COP which is indicative of faster charge transfer from one electrode to the other. This helped to produce higher current in the ZnO HT based SBD.

6.3.8. Charge transport analysis from impedance spectroscopy:

Apart from the $I-V$ characteristics, impedance spectroscopy (IS) analysis can give an idea about the charge transport properties of the devices. The IS was performed at a bias voltage of 200 mV and the resulting Nyquist plots are shown in **Figure 6.13(a)**, which shows the graphs to be distorted semicircle. The Nyquist plots reveal that the diameter of the semicircle of ZnO HT based device is significantly smaller than the semicircle for its opposite number. The smaller semicircle implies lesser charge recombination and lower charge transfer resistance in ZnO HT. As a result, faster charge transfer was possible in the ZnO HT thin film. While Nyquist plot gives an idea about charge transfer resistance, the Bode phase plot can deliver us the lifetime of charge carriers. **Figure 6.13(b)** presents the corresponding Bode phase plot, which shows that the characteristic frequency peak for ZnO HT based SBD occurs at a lower value compared to its counterpart. From this frequency peak (f_{peak}), the lifetime (τ_L) of charge carriers

can be obtained by using: $\tau_L = 1/2\pi f_{\text{peak}}$ [44]. The charge carrier lifetime of ZnO HT and ZnO COP were 72.3 μs and 53.8 μs respectively.

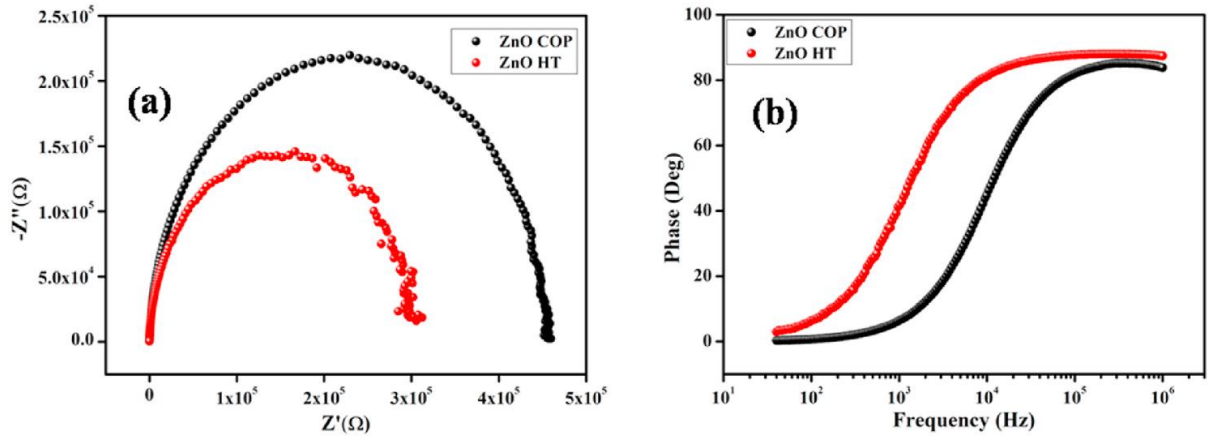


Figure 6.13: (a) Nyquist Plot and (b) Bode phase plot for the Al/ZnO COP/ITO and Al/ZnO HT/ITO Schottky barrier diodes

So, the charge carrier lifetime in the ZnO HT were higher which is another factor contributing to its better performance. Here, we want to further emphasize that the charge carrier lifetime of the materials should be higher than their respective transit times for efficient transfer of charge carriers to opposite electrodes. However, while the carrier lifetime of ZnO COP was just a little bit higher than its carrier transit time; for ZnO HT, the carrier lifetime was significantly higher than its carrier transit time which subsequently ensured its better device performance. It is important to know about diffusion length of charge carriers for understanding their efficient transfer from one electrode to the opposite electrode across the thin film. Diffusion length (L_D) of carriers was estimated by employing [38, 39]:

$$L_D = \sqrt{2D\tau_L} \quad (6.7)$$

where, D is the diffusion coefficient. The diffusion coefficient was calculated by using the Einstein-Smoluchowski equation [34, 39]:

$$\mu_{eff} = \frac{qD}{kT} \quad (6.8)$$

All the derived charge transport parameters are given in **Table-6.5**. It is clearly seen, the diffusion lengths of the charge carriers were greater than the thickness of the film, which is essential for an efficient device performance. Moreover, the average diffusion length of the ZnO HT was about 31% higher than that of ZnO COP which led to better performance in the ZnO HT based device.

Table 6.5: *Charge transport parameters*

SBD configuration	Condⁿ	Mobility (cm²V⁻¹s⁻¹)	Transit time (μs)	Life time (μs)	Diffusion Length (μm)
Al/ZnOCOP/ITO	Dark	0.0011	51.92	53.81	55.28
	Light	0.0018	36.01		
Al/ZnO HT/ ITO	Dark	0.0014	43.10	72.35	72.37
	Light	0.0026	23.12		

Finally, the overall better performance of ZnO HT can be attributed to its enhanced light absorption capacity and faster charge transport properties. The faster charge transport in ZnO HT is attributed to the rod like structure of the synthesized material. In a particle system like that of ZnO COP, often carrier scattering happens between the particles. But, the rod like structure in the ZnO HT provided a direct path for excited electrons and suppressed this carrier scattering. Also, the improved performance of rod like ZnO may be explained on the basis of aspect ratio of ZnO rod morphology. It has been shown in previous reports that the device performance of a photosensor improves with higher aspect ratio of the particles or rods in the synthesized materials [45, 46]. In this case, the ZnO COP sample is particle type and their morphology is nearly spherical while the ZnO HT sample is rod like. So, the aspect ratio of rod like ZnO is higher than that of particle like ZnO. That is why the rod like ZnO device delivered better performance than particle like ZnO. The better photoresponse of the ZnO HT

based SBD can be explained by looking into the energy band gap of the two synthesized materials. Moreover, the donor concentration was also found to be higher in ZnO HT leading to better photo-sensing performance of ZnO HT based SBD.

6.4. Conclusion:

ZnO with particle like (ZnO COP) and rod like morphology (ZnO HT) was synthesized by co-precipitation and hydrothermal method respectively; and thin film Schottky barrier diodes were fabricated based on the materials. The device performance was analyzed by I–V and C–V measurements. The photo-response of the devices were also investigated. Notably, ZnO HT based SBD exhibited a huge 121% higher responsivity compared to ZnO COP, implying its better potential for optoelectronic applications. The charge transfer kinetics for the ZnO HT based diode was much faster with significantly higher carrier mobility, carrier lifetime and diffusion lengths compared to its counterpart. The better performance of ZnO HT is attributed to its rod like structure which resulted in suppressed carrier scattering and efficient charge transport compared to the particle like ZnO COP. To conclude, the study shows that synthesis of the active material can drastically alter the morphology, which in turn can play a pivotal role to elevate photo-response and charge transport of the device. In our study, hydrothermal synthesis and the resulting rod like ZnO proved to be better candidate for device application compared to co-precipitation method. Furthermore, the detail insight provided into the interface properties of Al/ZnO Schottky diode can be fruitful for future studies on metal-semiconductor Schottky junctions.

References:

1. Z. L. Wang, and Z. C. Kang, *Functional and Smart Materials: Structural Evolution and Structure Analysis*, (first ed.), Plenum Press, NY (1998)
2. S. Xu, and Z. L. Wang, *One-dimensional ZnO nanostructures: solution growth and functional properties*, Nano Research, 2011, **4**, 1013-1098
doi.org/10.1007/s12274-011-0160-7
3. C. L. Hsu, and S. J. Chang, *Doped ZnO 1D nanostructures: synthesis, properties, and photodetector application*, Small, 2014, **10**, 4562-4585
doi.org/10.1002/sml.201401580
4. L. Sang, M. Liao, and M. Sumiya, *A comprehensive review of semiconductor ultraviolet photodetectors: from thin film to one-dimensional nanostructures*, Sensors, 2013, **13**, 8, 10482-10518
doi.org/10.3390/s130810482
5. A. Yadav, A. Pandey, D. Somvanshi, and S. Jit, *Sol-gel-based highly sensitive Pd/n-ZnO thin film/n-Si Schottky ultraviolet photodiodes*, IEEE Transactions on Electronic Devices, 2015, **62**, 6, 1879-1884
doi.org/10.1109/TED.2015.2423322
6. B. Lee, C. Kim, Y. Lee, S. Lee, and D. Y. Kim, *Dependence of photocurrent on UV wavelength in ZnO/Pt bottom-contact Schottky diode*, Current Applied Physics, 2015, **15**, 1, 29-33
doi.org/10.1016/j.cap.2014.10.024
7. N. Nasiri, R. Bo, F. Wang, L. Fu, and A. Tricoli, *Ultraporous electron-depleted ZnO nanoparticle networks for highly sensitive portable visible-blind UV photodetectors*, Advanced Materials, 2015, **27**, 29, 4336-4343
doi.org/10.1002/adma.201501517
8. D. Vanmaekelbergh, and L. van Vugt, *ZnO nanowire lasers*, Nanoscale, 2011, **3**, 7, 2783-27800
doi.org/10.1039/C1NR00013F
9. Y. Lin, H. Faber, K. Zhao, Q. Wang, A. Amassian, M. McLachlan, and T. D. Anthopoulos, *High-performance ZnO transistors processed via an aqueous carbon-free metal oxide precursor route at temperatures between 80–180 °C*, Advanced Materials, 2013, **25**, 31, 4340-4346
doi.org/10.1002/adma.201301622

10. Z. L. Wang, and J. Song, *Piezoelectric nanogenerators based on zinc oxide nanowire arrays*, Science, 2006, **312**, 5771, 242-246
doi.org/10.1126/science.1124005
11. S. Xu, Y. Qin, C. Xu, Y. Wei, R. Yang, and Z. L. Wang, *Self- powered nanowire devices*, Nature Nanotechnology, 2010, **5**, 366-373
doi.org/10.1038/nnano.2010.46
12. H. Gullapalli, V. S. M. Vemuru, A. Kumar, A. Botello-Mendez, R. Vajtai, M. Terrones, S. Nagarajaiah, and P. M. Ajayan, *Flexible piezoelectric ZnO–Paper nanocomposite strain sensor*, Small, 2010, **6**, 15, 1641-1646
doi.org/10.1002/sml.201000254
13. Y. S. Choi, J. W. Kang, D. K. Hwang, and S. J. Park, *Recent advances in ZnO-based light-emitting diodes*, IEEE Transactions on Electronic Devices, 2010, **57**, 1, 26-41
doi.org/10.1109/TED.2009.2033769
14. D.-K. Hwang, S.-H. Kang, J.-H. Lim, E.-J. Yang, J.-Y. Oh, J.-H. Yang, and S.-J. Park, *p-ZnO/n-GaN heterostructure ZnO light- emitting diodes*, Applied Physics Letters, 2005, **86**, 22, 222101
doi.org/10.1063/1.1940736
15. M. Law, L. E. Greene, J. C. Johnson, R. Saykally, and P. Yang, *Nanowire dye-sensitized solar cells*, Nature Materials, 2005, **4**, 455-459
doi.org/10.1038/nmat1387
16. V. Kobrinsky, E. Fradkin, V. Lumelsky, A. Rothschild, Y. Komem, and Y. Lifshitz, *Tunable gas sensing properties of p- and n-doped ZnO thin films*, Sensors and Actuators B: Chemical, 2010, **148**, 2, 379-387
doi.org/10.1016/j.snb.2010.05.025
17. C. C. Li, Z. F. Du, L. M. Li, H. C. Yu, Q. Wan, and T. H. Wang, *Surface-depletion controlled gas sensing of ZnO nanorods grown at room temperature*, Applied Physics Letters, 2007, **91**, 3, 032101
doi.org/10.1063/1.2752541
18. M. R. Mourya, V. Toutam, and D. Haranath, *Comparative study of photoresponse from vertically grown ZnO nanorod and nanoflake films*, ACS Omega, 2017, **2**, 9, 5538-5544
doi.org/10.1021/acsomega.7b00914

19. R. Singh, J. A. Cooper, M. R. Melloch, T. P. Chow, and J. W. Palmour, *SiC power Schottky and PiN diodes*, IEEE Transactions on Electronic Devices, 2002, **49**, 4, 665-672
doi.org/10.1109/16.992877
20. F. Yakuphanoglu, E. Basaran, B. F. Şenkal, and E. Sezer, *Electrical and optical properties of an organic semiconductor based on polyaniline prepared by emulsion polymerization and fabrication of Ag/Polyaniline/n-Si Schottky diode*, Journal of Physical Chemistry B, 2006, **110**, 34, 16908-16913
doi.org/10.1021/jp060445v
21. A. Maestrini, B. Thomas, H. Wang, C. Jung, J. Treuttel, Y. Jin, G. Chattopadhyay, I. Mehdi, and G. Beaudin, *Schottky diode-based terahertz frequency multipliers and mixers*, Comptes Rendus Physique, 2010, **11**, 7-8, 480-495
doi.org/10.1016/j.crhy.2010.05.002
22. K.V. Chandekar, M. Shkir, B. M. Al-Shehri, S. AlFaify, R. G. Halor, A. Khan, K. S. Al-Namshah, and M. S. Hamdy, *Visible light sensitive Cu doped ZnO: facile synthesis, characterization and high photocatalytic response*, Materials Characterization, 2020, **165**, 110387
doi.org/10.1016/j.matchar.2020.110387
23. N. Hernandez-Como, M. Lopez-Castillo, F.J. Hernandez-Cuevas, H. Baez-Medina, R. Baca-Arroyo, and M. Aleman, *Flexible PEDOT: PSS/ZnO Schottky diodes on polyimide substrates*, Microelectronic Engineering, 2019, **216**, 111060
doi.org/10.1016/j.mee.2019.111060
24. Y. Li, Y. Li, J. Zhang, X. Zou, and Y. Wang, *Analysis on the temperature dependent electrical properties of graphene/Al-ZnO Schottky contact*, Current Applied Physics, 2019, **19**, 10, 1063-1067
doi.org/10.1016/j.cap.2019.06.007
25. Y. Li, Y. Li, and J. Zhang, *Analysis of the carrier transport mechanism and barrier height formation of graphene/Zr-ZnO Schottky contact by I-V-T*, Material Science in Semiconductor Processing, 2020, **106**, 104793
doi.org/10.1016/j.mssp.2019.104793
26. V. S. Rana, J. K. Rajput, T. K. Pathak, and L. P. Purohit, *Cu sputtered Cu/ZnO Schottky diodes on fluorine doped tin oxide substrate for optoelectronic applications*, Thin Solid Films, 2019, **679**, 79-85
doi.org/10.1016/j.tsf.2019.04.019

27. R. Yatskiv, S. Tiagulskyi, and J. Grym, *Characterization of graphite/ZnO Schottky barriers formed on polar and nonpolar ZnO surfaces*, Physica Status Solidi, 2018, **216**, 2, 1800734
doi.org/10.1002/pssa.201800734
28. Z. Zhan, L. Zheng, Y. Pan, G. Sun, and L. Li, *Self-powered, visible-light photodetector based on thermally reduced graphene oxide–ZnO (rGO–ZnO) hybrid nanostructure*, Journal of Materials Chemistry, 2012, **22**, 2589-2595
doi.org/10.1039/C1JM13920G
29. J. C. Tinoco, S. A. Hernández, O. Rodríguez-Bernal, A. G. Vega-Poot, G. Rodríguez-Gattorno, M. de la L Olvera, and A. G. Martinez-Lopez, *Fabrication of Schottky barrier diodes based on ZnO for flexible electronics*, Journal of Materials Science: Materials in Electronics, 2020, **31**, 7373-7377
doi.org/10.1007/s10854-019-02736-5
30. A. Khorsand Zak, W. H. Abd. Majid, M. E. Abrishami, and R. Yousefi, *X-ray analysis of ZnO nanoparticles by Williamson–Hall and size–strain plot methods*, Solid State Sciences, 2011, **13**, 1, 251-256
doi.org/10.1016/j.solidstatesciences.2010.11.024
31. D. Kumar, A. Kumar, R. Prakash, and A. K. Singh, *X-ray diffraction analysis of Cu²⁺ doped Zn_{1-x}Cu_xFe₂O₄ spinel nanoparticles using Williamson-Hall plot method*, AIP Conference Proceedings, 2019, 2142, 1, 070018
doi.org/10.1063/1.5122410
32. R. Sharma, F. Alam, A. K. Sharma, V. Dutta, and S. K. Dhawan, *ZnO anchored graphene hydrophobic nanocomposite-based bulk heterojunction solar cells showing enhanced short-circuit current*, Journal of Materials Chemistry C, 2014, **2**, 8142-8151
doi.org/10.1039/C4TC01056F
33. X. Pan, Y. Zhao, S. Liu, C.L. Korzeniewski, S. Wang, and Z. Fan, *Comparing graphene-TiO₂ nanowire and graphene-TiO₂ nanoparticle composite photocatalysts*, ACS Applied Materials & Interfaces, 2012, **4**, 8, 3944-3950
doi.org/10.1021/am300772t

34. S. Middya, A. Layek, A. Dey, P. P. Ray, *Morphological impact of ZnO nanoparticle on MEHPPV: ZnO based hybrid solar cell*, Journal of Materials Science: Materials in Electronics, 2013, **24**, 11, 4621-4629
doi.org/10.1007/s10854-013-1453-2
35. J. Singh, P. Kumar, K. S. Hui, K. N. Hui, K. Ramam, R. S. Tiwaria, and O. N. Srivastava, *Synthesis, band-gap tuning, structural and optical investigations of Mg doped ZnO nanowires*, CrystEngComm, 2012, **14**, 5898-5904
doi.org/10.1039/C2CE06650E
36. J. Yu, and N. Tian, *High spectrum selectivity and enhanced responsivity of a ZnO ultraviolet photodetector realized by the addition of ZnO nanoparticles layer*, Physical Chemistry Chemical Physics, 2016, **18**, 24129-24133
doi.org/10.1039/C6CP03504C
37. Y. Wang, L. Zhu, Y. Feng, Z. Wang, and Z. L. Wang, *Comprehensive pyro-phototronic effect enhanced ultraviolet detector with ZnO/Ag Schottky junction*, Advanced Functional Materials, 2019, **29**, 5, 1807111
doi.org/10.1002/adfm.201807111
38. M. Das, J. Datta, R. Jana, S. Sil, S. Halder, and P. P. Ray, *Synthesis of rGO–Zn_{0.8}Cd_{0.2}S via in situ reduction of GO for the realization of a Schottky diode with low barrier height and highly enhanced photoresponsivity*, New Journal of Chemistry, 2017, **41**, 5476-5486
doi.org/10.1039/C7NJ00428A
39. M. Das, J. Datta, A. Dey, R. Jana, A. Layek, S. Middya, and P. P. Ray, *One step hydrothermal synthesis of a rGO–TiO₂ nanocomposite and its application on a Schottky diode: improvement in device performance and transport properties*, RSC Advances, 2015, **5**, 101582-101592
doi.org/10.1039/C5RA17795B
40. M. Das, J. Datta, S. Sil, A. Dey, R. Jana, S. Halder, and P. P. Ray, *Equivalent circuit analysis of Al/rGO–TiO₂ metal-semiconductor interface via impedance spectroscopy: graphene induced improvement in carrier mobility and lifetime*, Materials Science in Semiconductor Processing, 2018, **82**, 104-111
doi.org/10.1016/j.mssp.2018.03.039

41. J. Datta, M. Das, A. Dey, S. Halder, S. Sil, and P. P. Ray, *Network analysis of semiconducting $Zn_{1-x}Cd_xS$ based photosensitive device using impedance spectroscopy and current-voltage measurement*, Applied Surface Science, 2017, **420**, 566-578
doi.org/10.1016/j.apsusc.2017.05.192
42. J. Semple, S. Rossbauer, and T. D. Anthopoulos, *Analysis of Schottky contact formation in coplanar Au/ZnO/Al nanogap radio frequency diodes processed from solution at low temperature*, ACS Applied Materials & Interfaces, 2016, **8**, 35, 23167-23174
doi.org/10.1021/acsami.6b07099
43. T. Varma, C. Periasamy, and D. Boolchandani, *Performance analyses of Schottky diodes with Au/Pd contacts on n-ZnO thin films as UV detectors*, Superlattices and Microstructures, 2017, **112**, 151-163
doi.org/10.1016/j.spmi.2017.08.060
44. L. P. Wu, Y. L. Zhang, L. Z. Long, C. P. Cen, and X. J. Li, *Effect of ZnS buffer layers in ZnO/ZnS/CdS nanorod array photoelectrode on the photoelectrochemical performance*, RSC advances, 2014, **4**, 20716-20721
doi.org/10.1039/C4RA00005F
45. F. Ahmed, N. Arshi, M. S. Anwar, R. Danish, and B. H. Koo, *Morphological evolution of ZnO nanostructures and their aspect ratio-induced enhancement in photocatalytic properties*, RSC advances, 2014, **4**, 29249-29263
doi.org/10.1039/C4RA02470B
46. T. Park, K. E. Lee, N. Kim, Y. Oh, J.-K. Yoo, and M.-K. Um, *Aspect ratio-controlled ZnO nanorods for highly sensitive wireless ultraviolet sensor applications*, Journal of Materials Chemistry C, 2017, **5**, 12256-12263
doi.org/10.1039/C7TC04671E

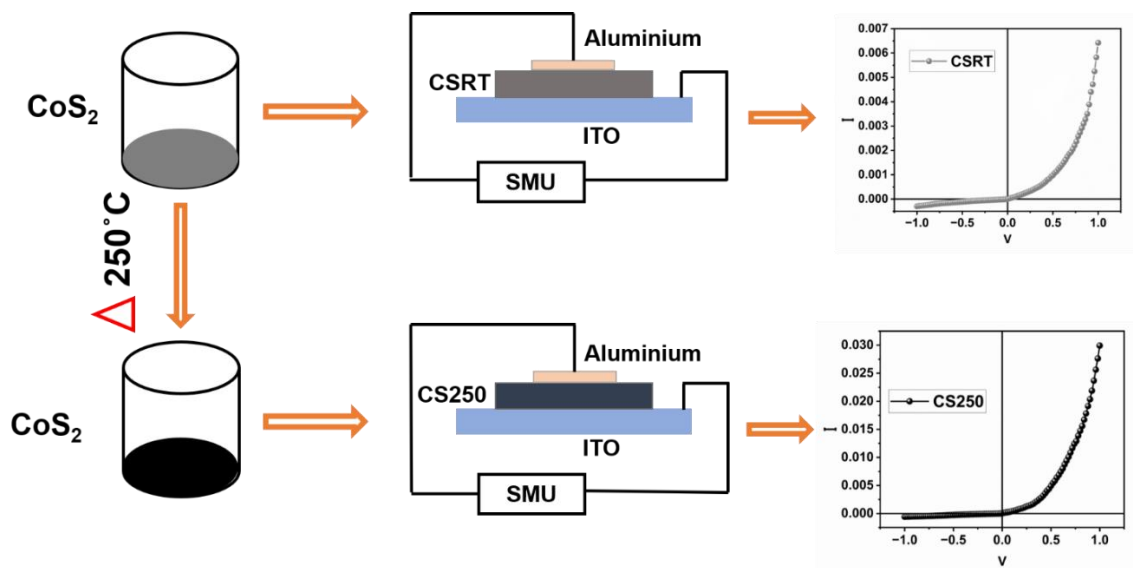
Chapter 7

Potential impact of annealed Cobalt-Sulfide on current rectification of ITO/CoS₂/Al Schottky device: Structural, Optical, Electrical and Magnetic characterizations

Abstract

In this report the annealing effect on structural, optical and semiconducting properties of hydrothermally derived CoS_2 nanoparticles are explored. The structural and optical properties are also studied. Possibility of semiconductor behaviour is found from the analysis which helps to grow interest upon semiconducting device formation. The metal-semiconductor (MS) junctions have been fabricated using these CoS_2 along with aluminium (Al) as interfacing metal. Here the study of charge transport behaviour within CoS_2/Al interface is confirmed from the analysis of current-voltage characteristics. The charge transport phenomenon is examined by thermionic emission theory and related parameters are estimated by employing space charge limited conduction (SCLC) mechanism. The occurrence of free carriers give rise the ferromagnetic behaviour, which has also been studied for these derived materials. It is an approach to study the relation between magnetic spin and electronic behaviour of CoS_2 nanoparticles. The observation of intrinsic ferromagnetism and the magnetic behaviour with respect to temperature and magnetic field exhibits the suitability for spin based electronic application. Finally, the potential behaviour of annealed (at 250°C) CoS_2 has been established in context to fabrication of $\text{ITO}/\text{CoS}_2/\text{Al}$ structured device.

Graphical Abstract



7.1. Introduction:

*M*etallic chalcogenide semiconductors have attracted much attention due to their uniqueness in optical, catalytic and photovoltaic properties [1]. The potential use of these chalcogenides in application of photovoltaic devices, gas sensors, optical devices and biological imaging [2-8] are reported so far. Among them Cobalt sulfide (CoS_2) is peculiar because of its strong intrinsic absorption coupled with surface morphology, hence provides a better catalytic for solar cell applications [9-14]. CoS_2 with pyrite type structure is well studied for its electrical and magnetic properties. In addition to its use as electro-catalytic for clean hydrogen fuel [15], as well as an alternate anode material for lithium-ion batteries [16]. Recent studies on CoS_2 showing high electrical conductivity and high capacitance are reported very aptly. However, due to its poor cyclability the material has still a lot to be improved to be useful [17, 18]. Multiple attempts have been made in synthesis procedures and thereby overcome deficiencies like poor cyclability. The annealing treatment improves the material's structural properties by reducing dislocation and can also improve material's ductility through strengthening grain boundaries' resistance to inter granular cracks [19]. It also plays an important role in microstructure, morphology and magnetic properties, consequently it may affect the performance of semiconductor characteristics [20, 21]. This seems to affect optical, electrical and magnetic properties which leads to growing interest in cultivating the entire work. There have been reports of the effect of annealing in different physical properties. Yong Shi already showed effective change in properties of chalcopyrite CuInSe_2 due to annealing [22]. In a report *Fadl et. al.* has shown that the optical and electrical properties changed significantly in copper selenides. [23]. On a similar report *Hilal et al.* have shown that the photoelectrochemical (PEC) properties change significantly with annealing at different temperatures [24]. However, no such studies have been

done there in the context of metal semiconductor (MS) junction formed with CoS₂ and aluminium.

In any electronic device a metal semiconductor junction plays a predominant role. MS junctions show either non-rectifying (Ohmic) or rectifying (Schottky) behaviour depending upon the work function of the metal and the semiconductor. At the interface of the metal and semiconductor junction a barrier, often called Schottky barrier is formed, which controls the width of the depletion region and the current conduction mechanism. CoS₂ is a wide bandgap material with energy $E_g \sim 3.1$ eV. From environmental perspective CoS₂ is non-toxic and ecofriendly. Also, it's easier synthesis and large-scale applicability is appreciable. The morphological changes in size and shape have significant effect on the absorption capacity of a material, which is why an immense effort has been devoted to the growth/synthesis process of CoS₂ nanomaterials and control its morphology.

In this work, pure CoS₂ has been synthesized by hydrothermal process and annealed at different temperatures. The characteristic change in structural, magnetic and optical properties before and after annealing have been studied. Apart from these basic characteristics, a Metal-Semiconductor (MS) junction-based device has been fabricated using these CoS₂s. The successful formation of Schottky barrier in the MS junction has been confirmed by its nonlinear current-voltage characteristics and extraction of the various impacting parameters on the basis of thermionic emission theory, has been explored well. All these parameters like barrier height, ideality factor, diffusion coefficient etc. are enlisted to get a reasonable view. Apart from I-V analysis impedance spectroscopy (IS) has also been used to describe the electrical behaviour of interfaces as well as the conduction mechanism within the junction. Moreover, to get any significant change in its magnetic behaviour or specifically on spin, which can assure its potential spintronic behaviour within the device, upon implementation of

magnetic field or with temperature the zero-field cooled (ZFC) and field cooled (FC) data are analysed aptly.

7.2. Experimental:

7.2.1. Materials and Methods:

All the chemicals used in the synthesis process are purchased commercially from Merck and no further purification has been done before synthesis. CoS_2 microstructures are prepared by conventional one-step hydrothermal process. A 40 ml solution of deionized water and ethylene glycol is prepared with a 3:1 volume ratio. After ultra-sonication stoichiometric amount of hydrated cobalt chloride $\text{CoCl}_2 \cdot 6\text{H}_2\text{O}$ are mixed with 80 mg of L-Cysteine. The mixture is stirred with magnetic stirrer at room temperature for an hour, then transferred to a Teflon autoclave, tightly sealed and heated in an oven for 6 hours at temperature 180°C . After cooling down naturally, the sample is collected and washed alternately with ethanol and water three times each by centrifuged technique and dried at room-temperature for overnight. The powder sample is divided into three equal parts. The first part is marked as CSRT (e.g., Cobalt Sulfide at Room-Temperature). The other two parts are annealed at 200°C and 250°C respectively and are assigned as CS200 and CS250 respectively.

7.2.2. Result and discussions:

7.2.2.1. Structural Characterizations:

Figure 7.1 represents the images of CoS_2 particles as collected from FESEM data. The figures illustrate that the particles are nano in dimension with coagulations. No significant change has been observed for the sample after heat treatment at all.

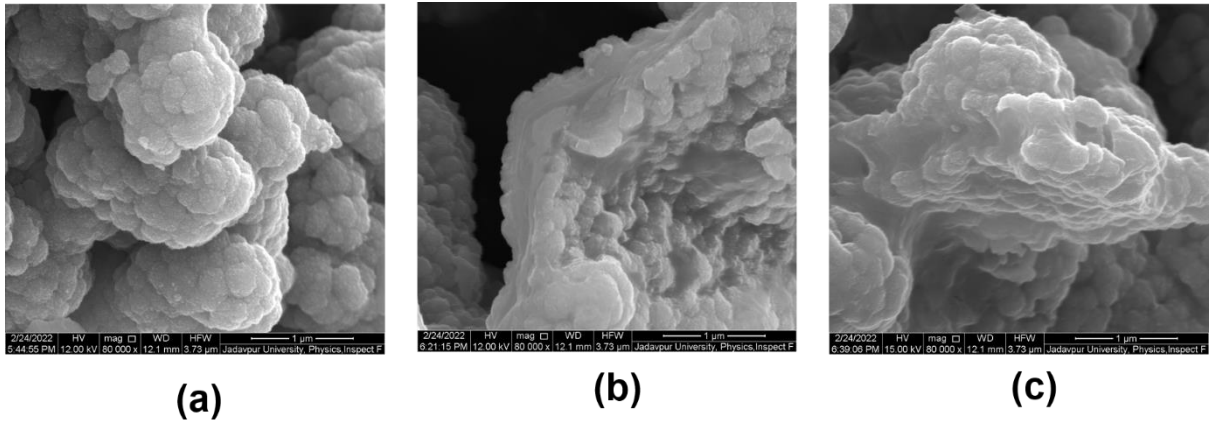


Figure 7.1: Surface morphology of CoS_2 , before and after annealing at two different temperatures (a) RT (b) 200 °C (c) 250 °C

The powder X-ray diffraction (PXRD) spectra of the individual sample is represented in Figure 2. PXRD patterns of as prepared sample at room temperature (CSRT) and annealed samples (CS200 and CS250) are recorded within Bragg's diffraction angle at 20° to 70° . The figure (**Figure 7.2**) illustrates distinct peaks at Bragg's angles (2θ) of 32.19° , 36.18° , 39.58° , 46.41° , 54.93° , 60.07° with support of JCPDS data card No. 41-1471 for corresponding Bragg's plane (200), (210), (211), (220), (311) and (230) respectively. The variation of intensity and stretching of these peaks may be due to the changes in microstructural parameters like particle size, interplanar distance, lattice parameter, dislocation density etc. However, all the samples exhibit cubic lattice structure individually (JCPDS Card No. 41-1471). The peaks intensity goes higher after annealing and most of peaks becomes sharpest after annealed at 250°C which implies better crystallinity. As crystallinity mostly affects the electron transport, it is assumed that the annealed sample at 250°C could have better impact within MS junction. [25].

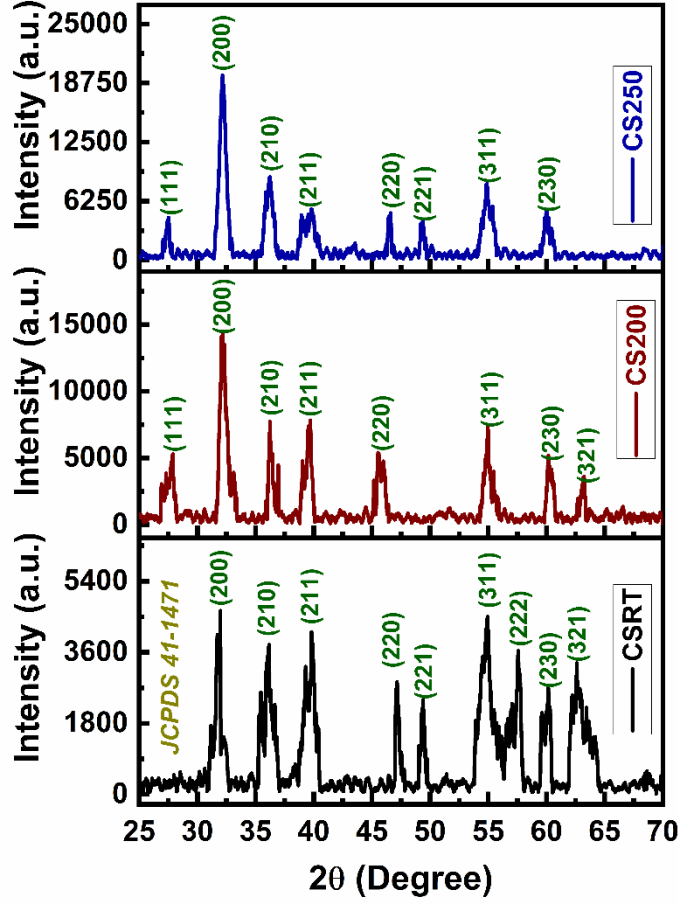


Figure 7.2: PXRD spectra of CoS₂, before and after annealing at two different temperatures

The inter planar distances (d) are measured (enlisted in Table-1) employing Bragg's *equation 2.1*.

Lattice constants (a) are derived for each (hkl) plane by using the equation:

$$\frac{1}{d^2} = \frac{(h^2 + k^2 + l^2)}{a^2} \quad (7.1)$$

for cubic system and are tabulated accordingly (*Table-7.1*).

The crystallite size (D), and dislocation density (δ) for corresponding (hkl) plane are estimated (listed on *Table 7.1*) using *equations 5.1* and *5.2* [26, 27, 28].

And the microstructural strain (ϵ) is

$$\epsilon = \frac{\beta}{4 \tan \theta} \quad (7.2)$$

The average size of crystallites is estimated as 12.35 nm, 14.35 nm and 13.82 nm respectively. In general, for larger crystallite sizes the sheet resistance becomes low, due to possible quantum confinement and edge effects in the individual crystallites. On the other hand, reducing the dislocation density, the dislocations are more randomly arranged, resulting in a decrease in the electrical conductivity [25]. So, analysing the average crystallite size and dislocation density for CSRT, CS200 and CS250, and considering the above fact it can be concluded that in respect to CSRT and CS200, CS250 sample may shows moderate impact in electronic device application.

Generally, a decrease in magnitude in lattice constant value means the electrons are more tightly bound to the atom, and hence require more energy to remove, leading to an increased electronic band gap. From **Table-7.1** average lattice constants for all the samples have nearly same values of lattice constant. Lattice strain increases with increasing crystallite-size while a highly strained nanomaterial has more randomly oriented grains, and thus, the evolution of texture changes.

The crystallographic orientation and overall quality of the boundaries between grains are also strongly influence energy gap sizes. The deterioration of boundary quality thus not only lowers boundary conductivity but also creates edge effects which could have a negative influence on within-grain conductivity at room temperature [25].

The information of a particular plane concerned by the preferential crystallite orientation determined from the texture coefficient. The texture coefficient for each (*hkl*) plane can be extracted using the following equation:

$$TC(hkl) = \frac{I(hkl)/I_0(hkl)}{\frac{1}{n} \sum_n I(hkl)/I_0(hkl)} \times 100\% \quad (7.3)$$

Here $I(hkl)$ and $I_0(hkl)$ denote measured value of intensity and standard intensity taken from JCPDS card data respectively. ‘n’ is the total no of peaks [29].

The preferred orientation for the material mainly towards (230) plane before and after annealing (*Table-7.2*).

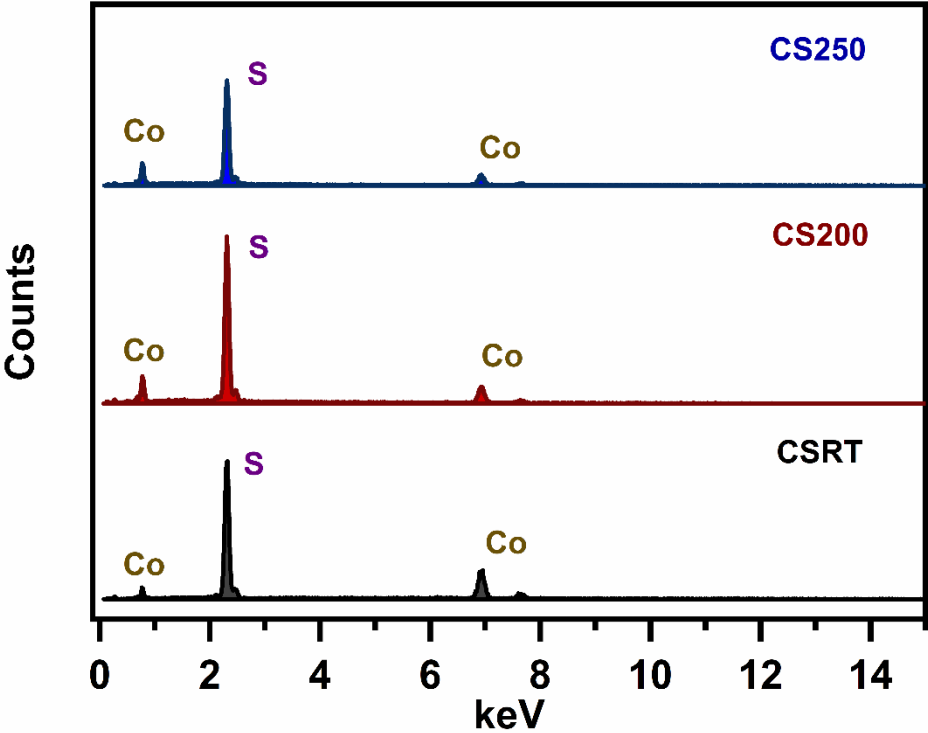


Figure 7.3: EDX spectra of CoS₂ after annealing at different temperatures

Figure 7.3 shows the energy dispersion X-ray (EDX) spectra of the samples. The experimental values of atomic percentage (at%) and weight percentage (wt%) are illustrated in *Table 7.3*. It can be concluded from this analysis that the prepared samples all are pure with identical chemical composition.

7.2.2.2. Optical characterization:

To reveal the optical response of the synthesized materials, UV absorption spectra [*Figure 7.4(a)*] are recorded within the wavelength range of 250 nm to

800 nm. **Figure 7.4(b)** shows corresponding Tauc's plots for each sample by employing Tauc's equation (equation 5.3) [30, 31].

The estimated bandgaps for the samples CSRT, CS200 and CS250 are 3.12 eV (Inset of **Figure 7.4(b)**), 3.54 eV and 3.29 eV respectively. It can be noted that the samples are wide bandgap material in nature, which is especially crucial for devices to operate at significantly higher temperatures, higher frequency and at higher voltage regimes [32].

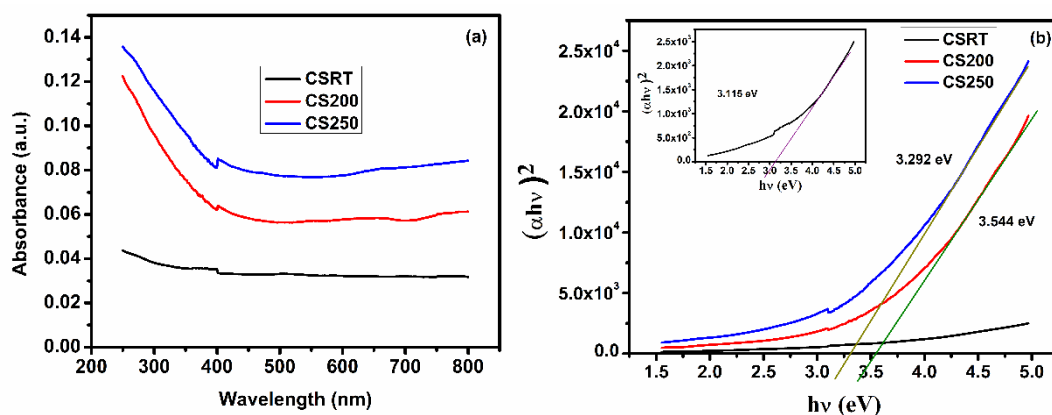


Figure 7.4: (a) UV-Visible spectra and corresponding (b) Tauc's plots of the samples. The inset in figure (b) shows the Tauc's plot of the sample CSRT.

7.2.2.3. Magnetic characterization:

Magnetic properties of CoS₂ nanoparticles are extracted from the zero-field cooled and field cooled (ZFC/FC) data. **Figure 7.5** shows the temperature dependent behaviour of ZFC, and FC protocols measured in magnetic field strength of 200 Oe for all these three samples. At lower temperatures, the magnetization value obtained for FC is much higher than the ZFC curve. This low temperature character indicates a ferromagnetic like behaviour which can be attributed to surface spins frozen in the magnetic field direction. As the temperature increases FC starts decreasing and near the peak, it merges with the ZFC. This is an indication of the superparamagnetic behaviour of CoS₂ nanoparticles at high temperatures [33]. As one can see the ZFC and FC merge at

higher temperature and becomes almost zero. It is because thermal fluctuations become dominant over the magnetic moments at high temperatures.

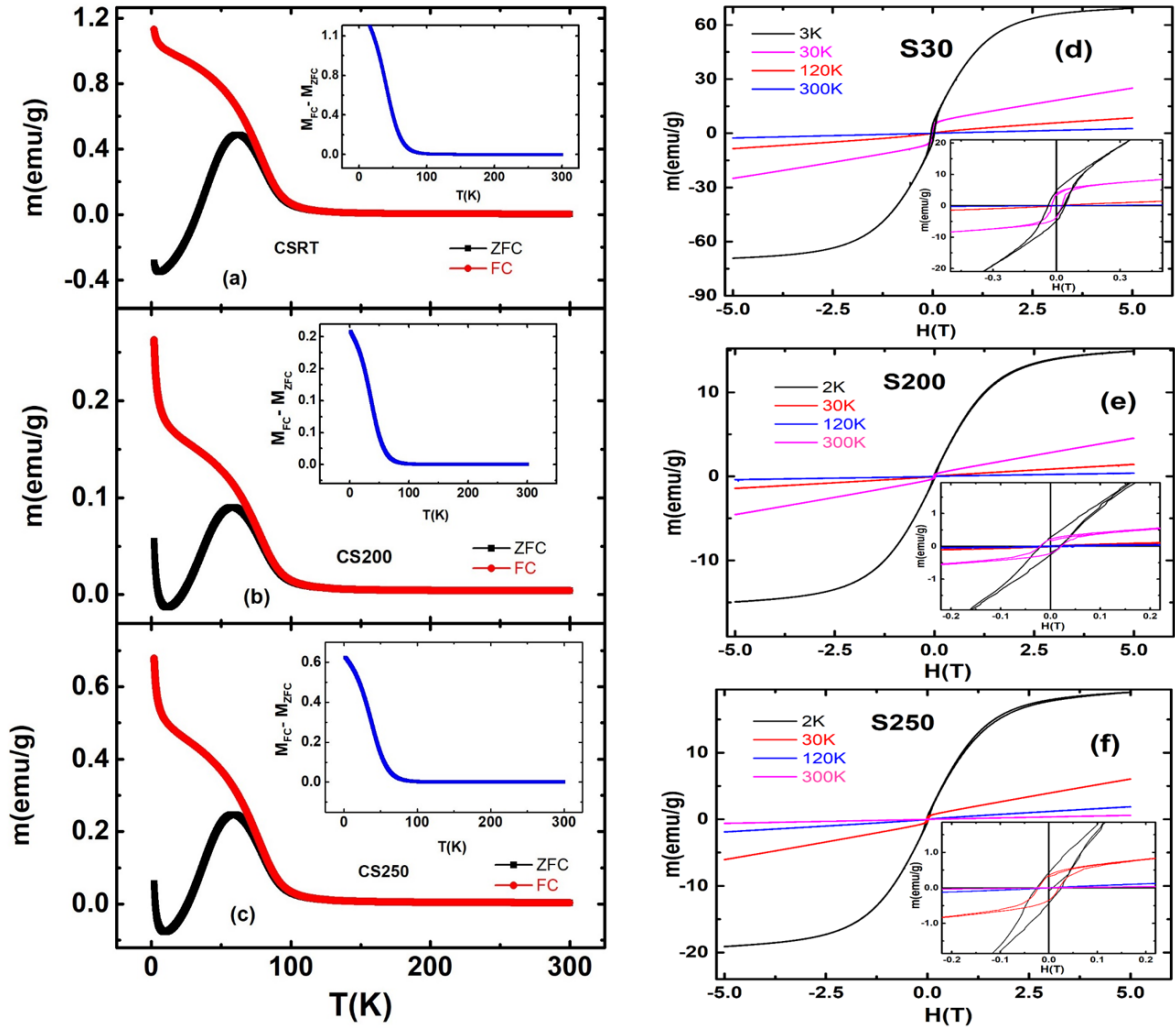


Figure 7.5: (a)-(c) magnetization ZFC & FC as a function of temperature of the three samples. (d)-(f) MH loop at different temperatures for the three samples. Insets in each MH graph show the zoomed in portion near zero field. The color-coding w.r.t temperatures are the same for each of the MH curves.

The insets in figures illustrate the difference between ZFC and FC curves with respect to temperature. It can be clearly seen that the difference between ZFC and FC is getting more prominent at low temperature regime ($2 \text{ K} \leq T \leq 90 \text{ K}$). The high temperature region shows the difference $M_{zfc} - M_{fc}$ almost equal to zero, which indicates the single-phase nature of the sample. Hence the weak

ferromagnetic ordering seems to be intrinsic and no secondary phase is involved for this ferromagnetism.

Figure 7.6 (a-c) exhibit the inverse magnetic susceptibility with respect to temperature, derived from M_{FC} at a magnetic field of 200Oe.

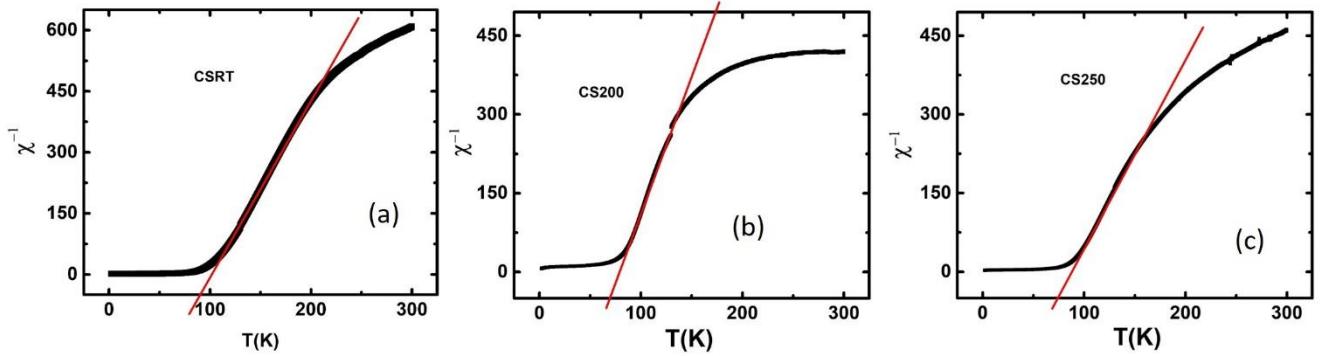


Figure 7.6: inverse magnetic susceptibility with respect to temperature for (a) CSRT; (b) CS200 and (c) CS250

The inverse magnetic susceptibility $\chi^{-1} = (T-\theta)/C$ is plotted against temperature within range 0K to 300K. Where C is Curie constant and θ is Curie Weiss temperature. The straight line represents the Curie Weiss Fit of the data in the linear region, which is around 100K-200K. The slope of $1/\chi$ vs T curve gives the value of $1/C$ and the intercept on x-axis gives the value θ . The positive intercept indicates ferromagnetic ordering. For all the samples the θ is around 69 K to 89 K and effective magnetic moments were calculated from C , are found to be $1.3 - 1.5 \mu_B$. The theoretical value of the effective magnetic moment corresponding to Co^{2+} ion per formula unit comes around $3.85 \mu_B$. It is interesting to note that the ZFC curves goes to negative value below 10 K. This negative magnetization can be attributed to the trapped field of the superconducting magnets [34]. To further clarify the magnetic behavior, magnetic hysteresis loops were recorded at various temperatures. **Figure 7.5(d)** depicts the hysteresis loop at 2K, 30K, 120K and 300K for CS250 sample. At room temperature there is hardly any visible hysteresis, it looks like strait line indicating the paramagnetic

nature. As the temperature goes lower the hysteresis gets bigger and wider which clearly verifies the ferromagnetic nature of CoS₂ nanoparticles. The inset shows enlarged picture in the field region of ± 0.2 T. The materials get fully saturated at a very high field of around 4T. For the MH loop recorded at the lowest temperature 4K MH, the saturation magnetization Ms and coercive field Hc is found to be 19.1 emu/g and 257.5 Oe respectively for the sample CS250. Table 4 shows the different values of Hc and Ms of all the samples at low temperature ~ 4 K. The results are comparable to the values shown in earlier reports [33]. From the estimated magnetic result, it is clear that after high temperature annealing the coercivity decreases indicating increase of material's softness. Although there is some increment in coercivity in CS250 material, it doesn't show much difference from CS200, whereas saturation magnetization does not show much variations. **Table 7.4** shows values of Hc, Ms and remanent magnetization (M_R) of different samples. The high coercivity combined with low value of Ms and M_R indicates a weak but irreversible nature of ferromagnetism. The exchange interaction between free delocalized electrons and holes are responsible for the magnetic ordering. Hence the presence of free carriers is essential condition for appearance of ferromagnetism [35].

From the above analysis, these synthesized CSs having such semiconductor nature and magnetic ordering could have the potential to be applicable in electronic devices. This motivates to study the carrier transport phenomena under applied electric field through metal-semiconductor interface for large scale device application. In this regards a device has been fabricated of configuration ITO/CoS₂/Al.

7.2.2.4. Electrical Analysis:

Intending for electrical characterization, bias voltage from -1 V to +1 V is applied to ITO/CoS₂/Al based devices (schematic diagram) under dark conditions. The nonlinear characteristic I-V [**Figure 7.7(a)**] illustrates that the

devices show good rectifying behaviour. These non-linear behaviours of I-V curve for each device indicates Schottky barrier formation at aluminium-CoS₂ interface. For the annealed sample CS200 and CS250, the current of respective device is found to become higher at same potential value. The rectification ratios (On/Off ratio at $\pm 1\text{V}$) for the diodes are enlisted in **Table 7.5**. According to these results, much better rectification is observed for CS250 sample based device. The better crystallinity of CS250 might be the cause for better junction formation with aluminium resulting better electron transport in the particular device and hence increases rectification ratio [36]. The conductivities of respective diodes at room temperature are measured as $2.144 \times 10^{-4} \text{ S m}^{-1}$, $6.709 \times 10^{-4} \text{ S m}^{-1}$ and $1.278 \times 10^{-3} \text{ S m}^{-1}$. More grain growth in CS250 after annealing would be the possible reason for enhancement of conductivity [31, 32].

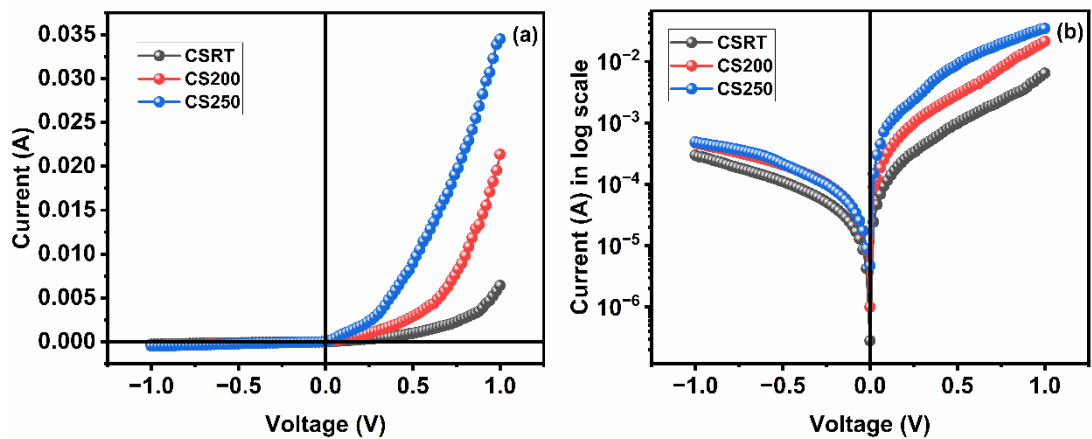


Figure 7.7: I-V Characteristics curve for the fabricated structures in (a) linear and (b) log scale.

To intervene into the mechanism of carrier transport within the device $\ln I$ vs $\ln V$ graph (**Figure 7.8**) are plotted. **Figure 7.8** illustrates two distinct regions with different slopes, pointing out different current transport mechanisms. At low bias (Region- I), the current follows ohm's law i.e., current is directly proportional to applied voltage, after that it is ruled by space charge limited

current theory corresponding to exponential trap distribution up to some extend (Region-II) and follows $I \propto V^2$ dynamics.

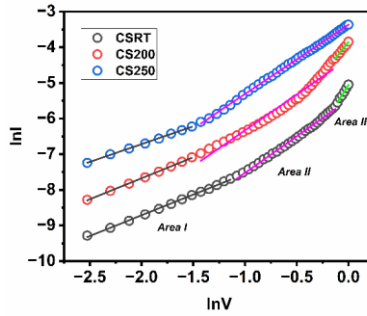


Figure 7.8: $\ln I$ - $\ln V$ graph for the fabricated structures to determine type of current transport mechanism.

Thus, for further investigation, thermionic emission theory for Schottky diode has been employed on I-V data. Current-voltage behaviour of Schottky junction can be illustrated follow by *equation 1.13* [37]

The effective value of Richardson constant is considered as $1.206 \times 10^6 \text{ AK}^{-2} \text{m}^{-2}$ [35]. At low voltage region, linear variation of current is noticed. When bias voltage is higher, it deviates from its linear behaviour. The deviation from linearity is mainly due to the occurrence of series resistance of diode. The ideality factor (η) and series resistance (R_s) for Schottky device are derived using Cheungs' equation (*equation 4.7 and 4.8*) [38],

The ideality factor and series resistance are calculated using the intercept and slope from linearly fitted $dV/d(\ln I)$ versus I curve.

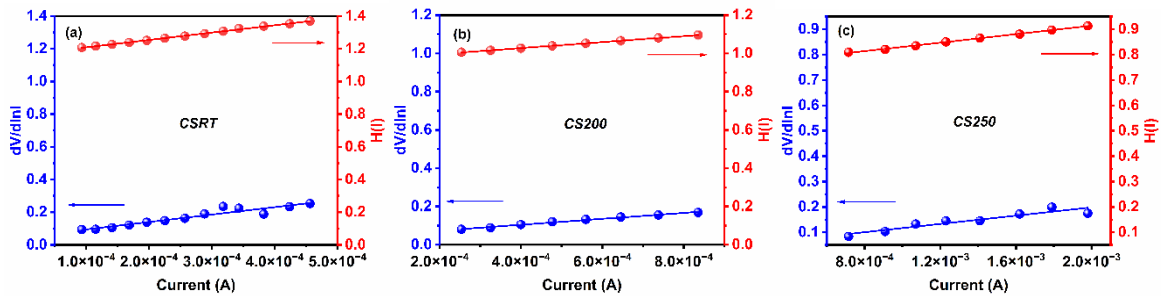


Figure 7.9: $dV/d\ln I$ vs I and $H(I)$ vs I curves for the corresponding devices.

From *equation 4.8*, the barrier height of Schottky diode can be estimated. **Figure 7.9** shows $dV/d\ln I$ vs I graph and $H(I)$ vs I plot for these three devices, which are linear in nature. From the intercepts at the y-axis of these $H(I)$ vs I plots, the barrier heights are estimated. The measured values of ideality factors and barrier heights are enlisted in tabular form in **Table 7.5**. All these characteristics show deviation from ideal behaviour of the device as expected. This deviation from ideal behaviour is may be due to a tunnelling current, induced by structural defects or the existence of inhomogeneities in the Schottky barrier [39]. The series resistance values estimated (**Table-7.5**) from two different aspects are nearly equal. **Table 7.5** illustrates that the value of series resistance is reduced significantly for the sample after annealing depending upon the increase of passivation of grain boundary [40]. This also explains the reason behind higher current rectification, exhibited by CS250 based device.

The results also depict that the barrier height decreases as annealing temperature increases, implying reduction of turn on voltage. This reduction is a result of reduction of fermi energy difference between aluminium and synthesized CSs. As early report, if annealing temperature increases then carrier concentration also increases in the semiconducting material [41] and fermi energy depends upon carrier concentration such that if carrier concentration increases fermi energy also increases.

The annealing of sample has also a distinguishable effect on carrier mobility [42, 43]. The carrier mobility and transit time of carriers are evaluated analysing I-V curve by standard SCLC theory.

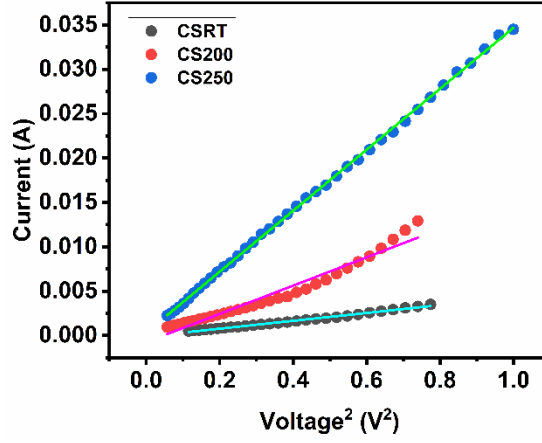


Figure 7.10: Current versus square of voltage graph for different fabricated devices

The effective mobility is derived from I vs V^2 plot (**Figure 7.10**) employing Mott-Gurney equation (**equation 4.11**) [44].

The relative dielectric constants are derived as 0.73, 1.55 and 1.77 for samples CSRT, CS200 and CS250 respectively by **equation 4.12** [45]:

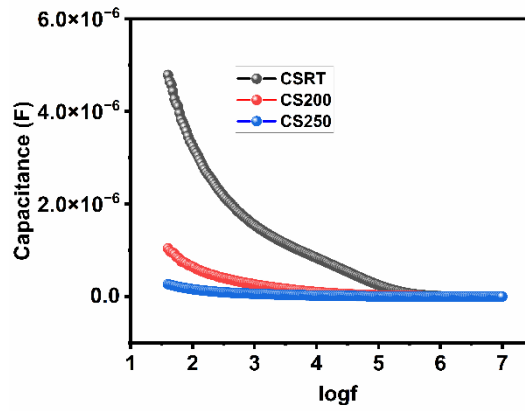


Figure 7.11: Capacitance versus log of frequency graph for each device

To estimate Capacitance ‘C’, here the saturated value of capacitance is considered from the Capacitance versus logarithm of frequency graphs (**Figure 7.11**).

Equation 4.13, **6.7** and **6.8** are used to determine transit time (τ) and diffusion length (L_D) of the charge carriers [46].

To calculate the value of diffusion length, carrier lifetime is needed and can be obtained from the described bode plot. When compared to the peak for CoS₂-based MS junction in the Bode-phase plot (**Figure 7.12**), the characteristic frequency peak for CS250-based diode is displaced to a lower frequency, which suggests a more rapid electron transport in device. Since the characteristic frequency is inversely correlated with the free electron lifetime (τ_L) one can calculate the value using the equation.

$$\tau_L = \frac{1}{2\pi f_{peak}} \tag{7.4}$$

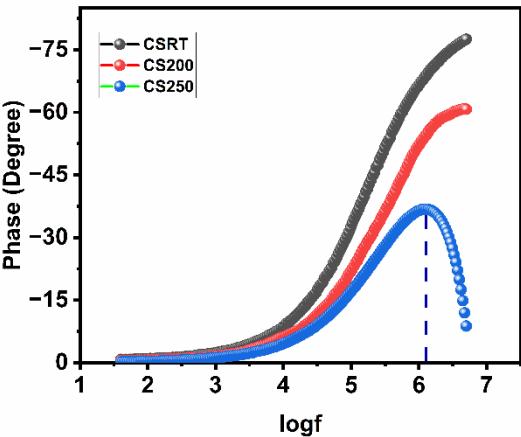


Figure 7.12: Bode plot representation of respective devices

Thus, the electrons in CS250 have a longer free carrier lifetime and a higher diffusion length that enables carriers to enter more likely in electrical conduction.

Evaluated values of effective mobility, carrier transit time, lifetime and diffusion length are represented in tabular form (**Table 7.6**), which exhibits the carrier mobility of CS250 is quite high compared to other two.

Moreover, to clarify the dynamics of electron transfer through MS junction, subject to carrier recombination and interface resistance, impedance spectroscopy (IS) measurement is performed at a voltage of 100 mV. The recorded data is analysed with EIS analyser software. **Figure 7.13** shows the corresponding Nyquist plot of the IS spectrum for different devices. The diameter of the

semicircular arc (**Figure 7.13**) represents effective resistance of the MS junction. There is a noteworthy decrease in the diameter for CS250-based diode which implies reduction in charge recombination and decrement in interface resistance. All the parameters extracted from the EIS analyser are tabulated at **Table 7.7**. It clearly shows that the effective series resistances in the circuits, are somehow similar as obtained from the results derived from Cheung's method. These above overall results illustrate the potential behaviour of derived CoS_2 in fabrication of Schottky diode and its annealed state is highly appreciable for device application.

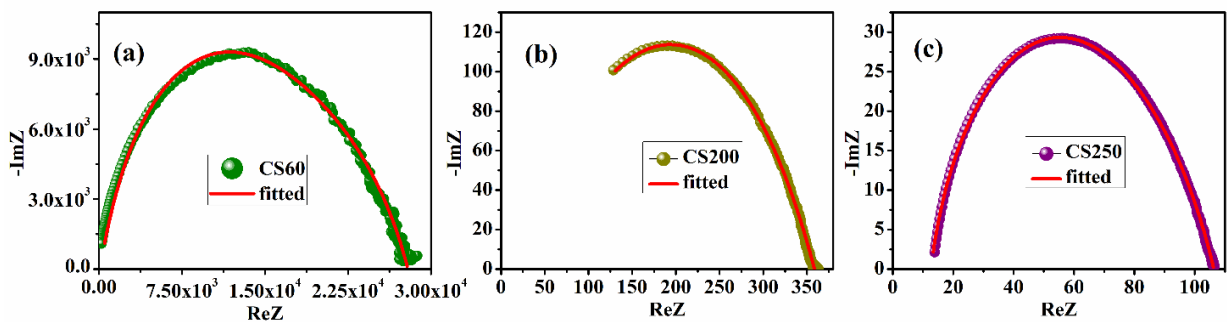


Figure 7.13: Experimental Nyquist plot and fitted plot using EIS analyser for each SBD

Nevertheless, for realistic theoretical view the equivalent circuit of Nyquist plot for a typical Schottky barrier are illustrated through schematic diagram in **Figure 7.14(a)**. In the equivalent circuit, the series resistance is represented by R_s , the inductance by L , the contact's depletion layer capacitance is shown by the capacitance component (C_p), and a shunt resistance is linked to the parallel resistance component (R_p). The semicircles representing Nyquist plot in Figure 12 of devices are not quite perfect, which indicates possibility of occurrence of more than one RC parallel network within the diode. The contact areas of layer or the interfaces may be the cause behind this imperfect semicircle, and they produce extra capacitive component within the device.

Here fitted semicircles are assisted by the modified equivalent circuit (**Figure 7.14 (b)**) bearing two RC parallel networks in series, and they are also connected linearly with R_s and a parasitic inductance (L) in series. R_1C and

$R_2(\text{CPE})$ are mostly related to the Al- CoS_2 and CoS_2 -ITO interfaces sequentially. CPE denotes constant phase element that can have any capacitance value within a limiting value.

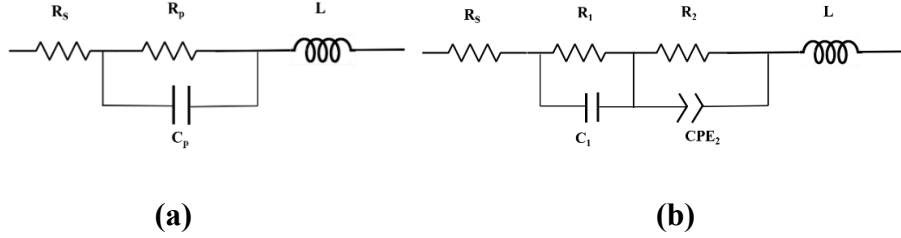


Fig. 7.14: (a) Typical equivalent circuit model (b) Extended/modified equivalent circuit model for the SBDs

In general, the ac impedance of a diode is given by [47],

$$Z(\omega) = Z'(\omega) - jZ''(\omega) \quad (7.5)$$

Where ω is the angular frequency, Z' and Z'' are magnitudes of the real and imaginary parts of the impedance respectively. For theoretical analysis of the equivalent circuit as shown in schematic diagram [Figure 7.14(b)],

$$Z'(\omega) = \frac{R_1}{1+(\omega R_1 C)^2} + \frac{R_2}{1+(\omega R_2 (\text{CPE}))^2} + R_s \quad (7.6)$$

And

$$Z''(\omega) = \frac{\omega R_1^2 C}{1+(\omega R_1 C)^2} + \frac{\omega R_2^2 (\text{CPE})}{1+(\omega R_2 (\text{CPE}))^2} - \omega L \quad (7.7)$$

must be considered for comprehensive mathematical modelling [48].

7.3. Conclusions:

In conclusion, CoS_2 nanoparticles are successfully synthesized using hydrothermal process and the crystal phases are not changed after annealing is found. The structural, optical and magnetic properties are studied for derived materials. Magnetic characterizations explore a ferromagnetic ordering at low

temperature and paramagnetic at high temperature for all the samples. All these characterizations approve the potential applicability of the derived materials within metal-semiconductor based Schottky barrier diode. The approach of formation of Schottky diode for each sample is confirmed by measuring non-linear behaviour of current – voltage (I-V) characteristics after fabrication sandwich like ITO/CoS₂/Al device. The I-V of all the devices, made by replacing intermediate main active layer with annealed samples, are recorded aptly. To get further inside the device the I-V characteristics are investigated thoroughly following diode equation. The material collected after annealing the sample at 250 °C improved device performance. The underneath mechanism of electrical performance is also explored by impedance spectroscopy. These overall analyses illustrate the potential behaviour of derived CoS₂ in fabrication of Schottky diode and its annealed state (at 250⁰C) is highly appreciable for efficient device application. Combined with magnetic and transport properties CoS₂ can be considered as a material of interest for the application of magnetic spin based electronic devices in near future.

All Tables

Table 7.1: *Parameter from XRD analysis of common peaks*

Annealing Temperature (in °C)	Plane (hkl)	Peak position (2θ in degree)	FWHM (β in degree)	Crystallite size (D in nm)	Average crystallite size (nm)	Dislocation density (δ in nm ⁻²)	Average dislocation density (nm ⁻²)	Micro-strain (ε)	Average micro-strain	Interplanar distance (d in Å)	Lattice constant (a=b=c in Å)	Average lattice constant (Å)
-	200	31.79	0.7651	11.27	12.35	0.00787	0.0116	0.01172	0.01018	2.811	5.622	5.535
	210	36.08	1.1686	7.46		0.01797		0.01565		2.486	5.559	
	211	39.66	1.1353	7.77		0.01656		0.01374		2.269	5.558	
	220	47.89	0.3278	27.70		0.00130		0.00322		1.898	5.368	
	311	54.82	1.3265	7.04		0.02018		0.01116		1.673	5.549	
	230	60.01	0.7424	12.90		0.00601		0.00561		1.540	5.552	
200	200	32.23	0.6790	12.71	14.35	0.00619	0.0054	0.01025	0.00721	2.774	5.548	5.433
	210	36.30	0.4477	19.49		0.00263		0.00596		2.472	5.528	
	211	39.54	0.7009	12.58		0.00632		0.00851		1.983	4.857	
	220	45.76	0.7599	11.85		0.00712		0.00785		1.981	5.603	
	311	54.95	0.7673	12.18		0.00674		0.00644		1.669	5.535	
	230	60.30	0.5639	17.01		0.00346		0.00424		1.533	5.527	
250	200	32.19	0.6798	12.70	13.82	0.00620	0.0087	0.01028	0.00878	2.778	5.556	5.545
	210	36.18	0.7651	11.40		0.00769		0.01022		2.480	5.545	
	211	39.58	1.2948	6.81		0.02156		0.01570		2.274	5.570	
	220	46.52	0.3205	28.20		0.00126		0.00325		1.951	5.518	
	311	54.93	0.9743	9.59		0.01087		0.00818		1.669	5.535	
	230	60.07	0.6729	14.24		0.00493		0.00508		1.538	5.545	

Table 7.2: *Texture Coefficient (TC) of different peaks*

(hkl) plane	TC for CSRT (%)	TC for CS200 (%)	TC for CS250 (%)
111	—	11.25	11.59
200	2.82	4.48	7.34
210	6.17	6.70	8.94
211	10.80	10.80	9.18
220	8.09	8.06	11.09
311	8.54	7.21	9.62
230	33.11	32.08	42.23
321	33.42	19.4	—

Table 7.3: *Experimental data from EDX*

Sample Name	Element	Atomic percentage (at%)	Normalized weight percentage (wt%)	Error (3 Sigma) in wt%
CSRT	Sulfur	58.65	43.56	3.70
	Cobalt	41.35	56.44	3.87
CS200	Sulfur	61.98	47	3.65
	Cobalt	38.02	53	3.99
CS250	Sulfur	64.53	49.75	3.87
	Cobalt	35.47	50.25	4.11

Table 7.4: *Magnetic parameters for different samples*

Sample	H _c (Oe)	M _R (emu/g)	M _s (emu/g)	C	θ (K)	μ _{eff} (μ _B)
CSRT	390	1.25	18	0.2306	89	1.36
CS200	202	0.27	15	0.191	69	1.24
CS250	257	0.44	19	0.277	75	1.49

Table 7.5: *Estimated Schottky diode parameters*

Sample	Rectification ratio	Conductivity (S m ⁻¹)	I.F	R _s (dV/dlnI) (Ω)	R _s (H) (Ω)	Φ _b (eV)
CSRT	21.57	2.144×10 ⁻⁴	1.89	453.75	449.75	0.618
CS200	45.51	6.709×10 ⁻⁴	1.62	154.73	156.01	0.596
CS250	70.61	1.278×10 ⁻³	1.34	81.66	83.66	0.557

Table 7.6: *Charge transport parameters as estimated*

Sample	Mobility (m ² V ⁻¹ S ⁻¹) ×10 ⁻⁴	Transit time (ns)	Carrier Concentration (m ⁻³)	Density of State (eV ⁻¹ m ⁻³)	Diffusion coefficient×10 ⁻⁶ (m ² /s)	Lifetime (ns)	Diffusion length (μm)
CSRT	0.865	9.55	5.679 × 10 ¹⁹	1.667 × 10 ²¹	2.261	—	—
CS200	1.460	6.40	1.169 × 10 ²⁰	3.061 × 10 ²¹	3.817	—	—
CS250	2.760	2.92	1.357 × 10 ²⁰	4.385 × 10 ²¹	7.216	123.83	1.337

Table 7.7: Parameters value from EIS analyser

Parameters	Determined from EIS Analyzer for					
	CSRT-based device		CS200-based device		CS250-based device	
	Value	Errors (%)	Value	Errors (%)	Value	Errors (%)
Series Resistance (Ω)	10.69	297.28	1.0052	22.997	4.5773	0.9211
Resistance arose from Al-CoS ₂ interface (Ω)	8980	0.77751	85.093	0.29091	8.6103	0.57045
Capacitance arose from Al-CoS ₂ interface (F)	9.258×10^{-11}	3.2154	7.9981×10^{-10}	1.4779	4.7902×10^{-8}	2.4409
Resistance arose from CoS ₂ -ITO interface (Ω)	18925	0.44731	272.57	0.09697	93.166	0.059586
Capacitance arose from CoS ₂ -ITO interface (F)	8.7413×10^{-9}	1.6741	7.2654×10^{-8}	0.59914	1.0136×10^{-6}	0.252
Constant Phase Value	0.67688	0.18806	0.64175	0.058212	0.6423	0.027084
Series Inductance (H)	1×10^{-6}	527.02	1.8951×10^{-7}	18.481	2.9186×10^{-7}	2.1694

References:

1. F. Soofivand, M. Sabet, H. Seyghalkar, and M. Salavati-Niasari, *Using the [Co(oct)2] as a New Precursor for Simple Synthesis of CoS₂ Nanoparticles and Kinetics Studies on Photocatalytic Activities Under UV Irradiation*, Journal of Nanostructures, 2018, **8**, 1, 75-81
doi.org/10.22052/JNS.2018.01.009
2. Q. Xiong, G. Chen, J. D. Acord, X. Liu, J. J. Zengel, H. R. Gutierrez, J. M. Redwing, L. C. Lew Yan Voon, B. Lassen, and P. C. Eklund, *Optical Properties of Rectangular Cross-sectional ZnS Nanowires*, Nano Letters, 2004, **4**, 9, 1663-1668
doi.org/10.1021/nl049169r
3. H. Safardoust-Hojaghan, M. Shakouri-Arani, and M. Salavati-Niasari, *Structural and spectroscopic characterization of HgS nanoparticles prepared via simple microwave approach in presence of novel sulfuring agent*, Transactions of Nonferrous Metals Society of China, 2016, **26**, 3, 759-766
doi.org/10.1016/S1003-6326(16)64166-3
4. Z.-G. Chen, J. Zou, G. Liu, H. F. Lu, F. Li, G. Q. Lu, and H. M. Cheng, *Silicon-induced oriented ZnS nanobelts for hydrogen sensitivity*, Nanotechnology, 2008, **19**, 5, 055710
doi.org/ 10.1088/0957-4484/19/05/055710
5. YG Liu, P Feng, XY Xue, SL Shi, XQ Fu, C Wang, and T. H. Wang, *Room-temperature oxygen sensitivity of ZnS nanobelts*, Applied Physics Letters, 2007, **90**, 4, 042109
doi.org/10.1063/1.2432278
6. J. S. Hu, L. L. Ren, Y. G. Guo, H. P. Liang, A. M. Cao, L. J. Wan, and C. L. Bai, *Mass Production and High Photocatalytic Activity of ZnS Nanoporous Nanoparticles*, Angewandte chemie, 2005, **117**, 8, 1295- 1299
doi.org/10.1002/ange.200462057
7. L. X. Shao, K. H. Chang, and H. L. Hwang, *Zinc sulfide thin films deposited by RF reactive sputtering for photovoltaic applications*, Applied Surface Science, 2003, **212-213**, 305-310
doi.org/10.1016/S0169-4332(03)00085-0

8. L. Wang, Y.-S. Liu, X. Jiang, D.-H. Qin, and Y. Cao, *Enhancement of Photovoltaic Characteristics Using a Suitable Solvent in Hybrid Polymer/Multiarmed CdS Nanorods Solar Cells*, The Journal of Physical Chemistry C, 2007, **111**, 26, 9538-9542
doi.org/10.1021/jp0715777
9. R. C. Hoodless, R. B. Moyes, and P. B. Wells, *D-tracer study of butadiene hydrogenation and tertahydrothiophen hydrodesulphurization catalysed by Co₉S₈*, Catalysis Today 2006, **114**, 4, 377–382
doi.org/10.1016/j.cattod.2006.02.078
10. S. A. Patil, D. V. Shinde, I. Lim, K. Cho, S. S. Bhande, R. S. Mane, N. K. Shrestha, J. K. Lee, T. H. Yoon, and S.-H. Han, *Anion exchange mediated shape preserving strategy for constructing 1-D arrays of porous CoS_{1.0365} nanorods for electrocatalytic reduction of triiodide*, Journal of Materials Chemistry A, 2015, **3**, 7900–7909
doi.org/10.1039/C5TA00494B
11. L.-J. Sun, Y. Bai, and K.-N. Sun, *Organic molecule-controlled synthesis of three- dimensional rhododendron-like cobalt sulfide Hier architectures as counter electrodes for dye-sensitized solar cells*, RSC Advances, 2014, **4**, 42087–42091
doi.org/10.1039/C4RA04729J
12. M. Congiu, L. G. S. Albano, F. Decker, and C. F. O. Graeff, *Single precursor route to efficient sulphide counter electrodes for dye sensitized solar cells*, Electrochimica Acta, 2015, **151**, 517–524
doi.org/10.1016/j.electacta.2014.11.001
13. Y.-D. Luo, J. Shen, R. Cheng, X.-H. Chen, Y.-W. Chen, Z. Sun, and S.-M. Huang, *Facile synthesis of mixed-phase cobalt sulfide counter electrodes for efficient dye sensitized solar cells*, Journal of Materials Science: Materials in Electronics, 2015, **26**, 42–48
doi.org/10.1007/s10854-014-2360-x
14. G. B. Smith, A. Ignatiev, and G. Zajac, *Solar selective black cobalt: preparation, structure, and thermal stability*, Journal of Applied Physics, 1980, **51**, 4186
doi.org/10.1063/1.328276
15. S. Peng, L. Li, X. Han, W. Sun, M. Srinivasan, S. G. Mhaisalkar, F. Cheng, Q. Yan, J. Chen and S. Ramakrishna, *Cobalt Sulfide Nanosheet/Graphene/Carbon Nanotube Nanocomposites as Flexible Electrodes for Hydrogen Evolution*, Angewandte Chemie, 2014, **126**, 46, 12802–12807
doi.org/10.1002/ange.201408876

16. M. Armand and J. M. Tarascon, *Building better batteries*, Nature, 2008, **451**, 652–657
doi.org/10.1038/451652a
17. L. Fang, Y. Zhang, Y. Guan, H. Zhang, S. Wang and Y. Wang, *Specific synthesis of CoS₂ nanoparticles embedded in porous Al₂O₃ nanosheets for efficient hydrogen evolution and enhanced lithium storage*, Journal of Materials Chemistry A, 2017, **5**, 2861
doi.org/10.1039/C6TA10700A
18. Y. Wang, J. Wu, Y. Tang, X. L^ü, C. Yang, M. Qin, F. Huang, X. Li and X. Zhang, *Phase-Controlled Synthesis of Cobalt Sulfides for Lithium-Ion Batteries*, ACS ACS Applied Materials & Interfaces, 2012, **4**, 8, 4246–4250
doi.org/10.1021/am300951f
19. X. Tong, H. Zhang and D. Y. Li, *Effect of Annealing Treatment on Mechanical Properties of Nanocrystalline α -iron: an Atomistic Study*, Scientific reports, 2015, **5**, 8459
doi.org/10.1038/srep08459
20. J. Würfl, and B. Janke, *Technology towards GaAs MESFET-based IC for high temperature applications*, Materials Science and Engineering: B, 1997, **46**, 1-3, 52-56
doi.org/10.1016/S0921-5107(96)01930-7
21. W.-S. Lee and T.-Y. Liu, *The effect of annealing temperature on the microstructure of nano-indented Au/Cr/Si thin films*, Nanotechnology, 2007, **18**, 33, 335701
doi.org/10.1088/0957-4484/18/33/335701
22. Y. Shi, Z. Jin, C. Li, H. An, and J. Qiu, *Effects of post-heat treatment on the characteristics of chalcopyrite CuInSe₂ film deposited by successive ionic layer absorption and reaction method*, Thin Solid Films, 2007, **515**, 7-8, 3339–3343
doi.org/10.1016/j.tsf.2006.09.015
23. A. Abu EL-Fadl, M. M. Hafiz, M. M. Wakaad, and A. S. Aashour, *Annealing effects on the optical parameters of Cu₁₀Se₉₀ and Cu₂₀Se₈₀ films deposited by evaporation technique*, Physica B: Condensed Matter, 2006, **382**, 1-2, 110–117
doi.org/10.1016/j.physb.2006.02.004
24. H. S. Hilal, A. Zyoud, M. H. S. Helal, H. Bsharat, H. H. Helal, and C. Ali, *Effects of annealing temperature and cooling rate on photo-electrochemical*

performance of pristine polycrystalline metal-chalcogenide film electrodes, Solar energy, 2019, **183**, 704-715

doi.org/10.1016/j.solener.2019.03.028

25. M. Flygare, and K. Svensson, *Influence of crystallinity on the electrical conductivity of individual carbon nanotubes*, Carbon Trends, 2021, **5**, 100125

doi.org/10.1016/j.cartre.2021.100125

26. P. Scherrer, *Estimation of the size and internal structure of colloidal particles by means of r.ovrddot.ontgen rays*, Nachr. Ges. Wiss. Gottingen, 1918, 96-100

27. A. R. Stokes, and A. J. C. Wilson, *The diffraction of X rays by distorted crystal aggregates – I*, Proceedings of the physical society, 1944, **56**, 174 - 181

doi.org/10.1088/0959-5309/56/3/303

28. K. Maniammal, G. Madhu, and V. Biju, *X-ray diffraction line profile analysis of anostructured nickel oxide: Shape factor and convolution of crystallite size and microstrain contributions*, Physica E: Low-dimensional Systems and Nanostructures, 2017, **85**, 214-222

doi.org/10.1016/j.physe.2016.08.035

29. D. Aryanto, P. Marwoto, T. Sudiro, A. S. Wismogroho and Sugianto, *Growth of a-axis-oriented Al-doped ZnO thin film on glass substrate using unbalanced DC magnetron sputtering*, Journal of Physics: Conference Series, 2019, **1191**, 012031

doi.org/10.1088/1742-6596/1191/1/012031

30. J. Tauc, R. Grigorovici, and A. Vancu, *Optical properties and electronic structure of amorphous germanium*, Physica status solidi (b), 1966, **15**, 2, 627-637

doi.org/10.1002/pssb.19660150224

31. J. Tauc, *Optical properties and electronic structure of amorphous Ge and Si*, Materials research bulletin, 1968, **3**, 1, 37-46

doi.org/10.1016/0025-5408(68)90023-8

32. P. G. Neudeck, R. S. Okojie and L.-Y. Chen, *High-temperature electronics - a role for wide bandgap semiconductors*, in Proceedings of the IEEE, 2002, **90**, 6, 1065-1076

doi.org/10.1109/JPROC.2002.1021571

33. B. Liu, F. Wang, D. Zheng, X. Liu, X. Sun, S. Hou, and Y. Xing, *Hydrothermal synthesis and magnetic properties of CoS₂ nano-octahedrons*, Materials Letters, 2011, **65**, 17–18, 2804-2807
doi.org/10.1016/j.matlet.2011.05.064
34. X. Xie, H. Che, H. Wang, G. Lin, and H. Zhu, *Negative Zero-Field-Cooled Magnetization in YMn_{0.5}Cr_{0.5}O₃ due to Giant Coercivity and Trapped Field*, Inorganic chemistry, 2018, **57**, 1, 175–180
doi.org/10.1021/acs.inorgchem.7b02365
35. J. Datta, A. Dey, S. K. Neogi, M. Das, S. Middya, R. Jana, S. Bandyopadhyay, A. Layek, and P. P. Ray, *Application Possibility of Mn_{0.04}Cu_{0.05}Zn_{0.91}O in Electronic and Magnetic Devices*, IEEE Transactions on Electron Devices, **64**, 11, 2017
doi.org/10.1109/TED.2017.2754190
36. J. D. Hwang and K. S. Lee, *A high rectification ratio nanocrystalline p–n junction diode prepared by metal-induced lateral crystallization for solar cell applications*, Journal of The Electrochemical Society, 2008, **155**, 4, H259
doi.org/10.1149/1.2840618
37. E. H. Rhoderick and R. H. Williams, *Metal Semiconductor Contacts*, 2nd ed. (Clarendon Press, Oxford, 1988)
38. S. K. Cheung, and N. W. Cheung, *Extraction of Schottky diode parameters from forward current-voltage characteristics*, Applied physics letters, 1986, **49**, 2, 85-87
doi.org/10.1063/1.97359
39. P. Das, B. Pal, J. Datta, M. Das, S. Sil, and P. P. Ray, *Improved charge transport properties of graphene incorporated tin oxide based Schottky diode over pure one*, Journal of Physics and Chemistry of Solids, 2021, **148**, 109706
doi.org/10.1016/j.jpcs.2020.109706
40. K. Yim, H. W. Kim and C. Lee, *Effects of annealing on structure, resistivity and transmittance of Ga doped ZnO films*, Materials Science and Technology, 2007, **23**, 1, 108-112
doi.org/10.1179/174328407X158514
41. M. Asghar, K. Mahmood, I. T. Ferguson, M. Y. A. Raja, Y. H. Xie, R. Tsu, and M. A. Hasan, *Investigation of VO–Zni native donor complex in MBE grown bulk ZnO*, Semiconductor science and technology, 2013, **28**, 105019
doi.org/10.1088/0268-1242/28/10/105019

42. L. V. Duong, N. N. Anh, T. B. Trung, L. D. Chung, N. Q. Huan, D. T. Nhung, M. T. Phuong, P. N. Minh, D. D. Phuong, and P. V. Trinh, *Effect of annealing temperature on electrical and thermal property of cold-rolled multi-walled carbon nanotubes reinforced copper composites*, Diamond and Related Materials, 2020, **108**, 107980
doi.org/10.1016/j.diamond.2020.107980
43. D.-chuan Zhu, K. Tang, M.-zhao Song, and M.-jing Tu, *Effects of annealing process on electrical conductivity and mechanical property of Cu-Te alloys*, Transactions of Nonferrous Metals Society of China, 2006, **16**, 2, 459-462
doi.org/10.1016/S1003-6326(06)60078-2
44. E. H. Rhoderick, *Metal-semiconductor contacts*, IEE Proceedings I Communications, Speech and Vision 129 (1982)
45. P. Das, B. Pal, M. Das, S. Sil, D. Das, A. Layek, and P. P. Ray, *Findings of inhomogeneity in barrier height of Schottky junction Al/rGO-SnO₂ having anomaly in theoretical and experimental value of Richardson constant: A Gaussian approach*, Results in Physics, 2022, **42**, 105996
doi.org/10.1016/j.rinp.2022.105996
46. M. Das, P. Das, J. Datta, D. Das, S. Acharya, and P. P. Ray, *Improved device performance of rod like ZnO in a Schottky type photosensor compared to particle like ZnO: Analysis of charge transport*, Materials Science in Semiconductor Processing, 2021, **130**, 105799
doi.org/10.1016/j.mssp.2021.105799
47. J. R. Macdonald, and W. B. Johnson, *Fundamentals of Impedance Spectroscopy*. In Impedance Spectroscopy (eds E. Barsoukov and J.R. Macdonald), 3rd edition, 2018
doi.org/10.1002/0471716243.ch1
48. J. Datta, M. Das, A. Dey, S. Halder, S. Sil, and P. P. Ray, *Network analysis of semiconducting Zn_{1-x}Cd_xS based photosensitive device using impedance spectroscopy and current-voltage measurement*, Applied Surface Science, 2017, **420**, 566-578
doi.org/10.1016/j.apsusc.2017.05.192

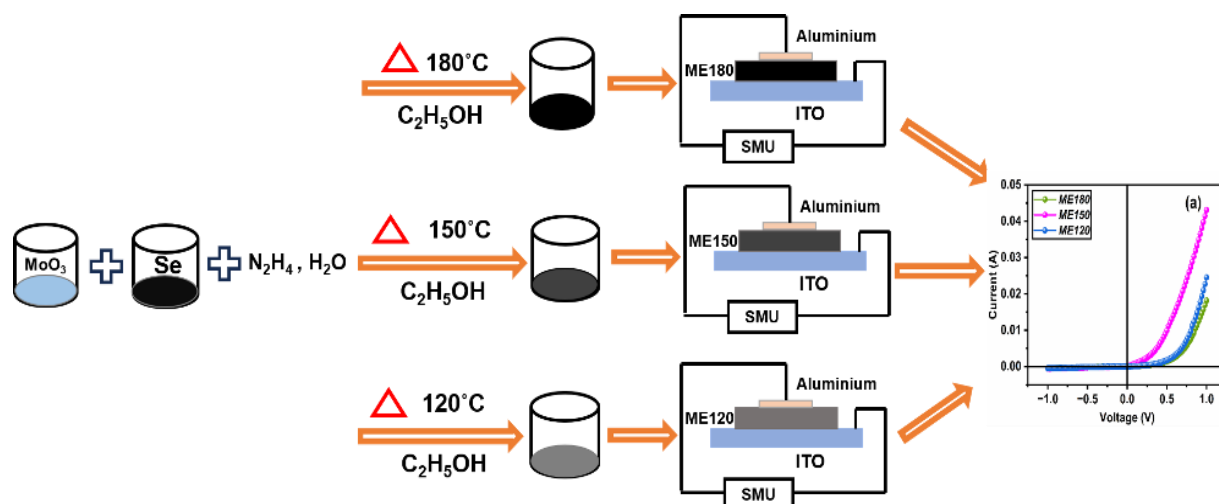
Chapter 8

Low temperature solvothermal
synthesis of Molybdenum di-selenide
from MoO_3 , their comparative study
in different properties and device
application

Abstract

In this section the effect of synthesis temperature in solvothermal synthesis of MoSe_2 is elaborately discussed. Also, synthesis procedure of the nanomaterial from MoO_3 in a very low temperature about 120°C is also successfully established. Dependence of various properties of synthesized nanoparticle on solvothermal temperature are analysed in details. Possibility of semiconducting behaviour leads to semiconducting device fabrication. The metal-semiconductor (MS) junctions, fabricated using these MoSe_2 obtained using different temperature along with aluminium (Al) as interfacing metal are studied and formation of Schottky junctions are clearly indicated. Extraction of different Schottky parameters using two different method of extraction is compared. The study of charge transport behaviour within MoSe_2/Al interface is done from the analysis of current-voltage characteristics as well as impedance spectroscopy.

Graphical Abstract



8.1. *Introduction:*

Transition metal dichalcogenides (TMDs) have recently gained great attention due to their narrow band gap, which enables a wide range of applications in fields such as electronics, optoelectronics, and energy conversion [1, 2, 3]. Studies indicate that the less-studied selenides may be preferable to sulfides in several ways, including a lower band gap (1.5 eV in MoSe₂ vs. 1.9 eV in MoS₂), a 10-fold narrower line width, and tuneable excitonic charging effects [4]. Molybdenum di-selenide (MoSe₂) has a "three-layer" structure consisting of Se layers on the top and bottom with Mo layers in between [5]. In multilayer arrangements, layers are piled with Se atoms interacting via weak van der Waals forces. The band structure of MoSe₂ changes from indirect (as in a bulk crystal) to direct (as in a monolayer) when the thickness decreases, while the band gap increases from 1.1 to 1.5 eV [6]. MoSe₂ is a suitable material for different electrical and optical applications due to its tuneable features.

Hydrothermal/solvothermal synthesis of nanomaterial and properties of resulting nanomaterial depends upon the conditions for the synthesis i.e., type of solvent, maintained temperature, duration of synthesis etc.

In 2001, Chen and Fan [7] used sodium selenite and sodium molybdate as the raw ingredients in an aqueous solution at 150 °C to successfully synthesize MoSe₂ nanocrystalline. There is number of papers for hydrothermal/solvothermal synthesis of MoSe₂ reported previously using sodium molybdate [8, 9, 10, 11]. But molybdenum trioxide (MoO₃) as a precursor for hydrothermal/solvothermal synthesis of MoSe₂ is rarely reported [12]. Influenced by the things, the low temperature solvothermal synthesis using MoO₃ and selenium powder is reported in this work. A thorough comparison between different properties of material with varying synthesis temperature is discussed. Further study of MS device application of them is also analysed.

8.2. Experimental:

8.2.1. Materials and methods:

All the chemicals used in the synthesis process have been purchased commercially from Loba Chemicals and no further purification was done before synthesis.

MoSe₂ nanostructures have been prepared by conventional one-step hydrothermal process. Prior to all 1mmol of molybdenum tri oxide (MoO₃) is added to a beaker already having 40 ml ethanol and stirred until a homogeneous white solution (Solution I) is obtained. In another beaker 2 mmol selenium (Se) powder is taken and about 10 ml hydrazine hydrate (NH₄.H₂O) with 80% purity is dropped slowly onto the powder. Also, a magnetic stirrer is used in this time to maintain a continuous stirring and hence perform a well mixing of Se in NH₄.H₂O solution. Now, after quite well mixing, 10 ml ethanol is added to this mixture without putting an end to stirring. After getting a dark brown solution (Solution II), Solution II is poured slowly to the beaker containing Solution I and the mixture of these two solutions is stirred for 4 hr. Then final solution is transferred to a Teflon autoclave, then tightly sealed and heated in an oven for 16 hours at temperature 120°C. After cooling down naturally, the sample is collected and washed alternately with ethanol and water three times each by centrifuged technique and dried at room-temperature under vacuum desiccator for overnight. The collected powder is named ME120. The above procedure is repeated another two times only changing the temperature to 150°C and 180°C respectively and the final products are labelled as ME150 and ME180 respectively.

8.3. Result and discussions:

8.3.1. Structural Analysis:

The structures of MoSe₂ nanoparticles prepared in different hydrothermal temperature are characterized by field effect scanning electron microscopy (FESEM). FESEM images of different MoSe₂ nanoparticles in **Figure 8.1** suggests a roughly uniform nanostructure.

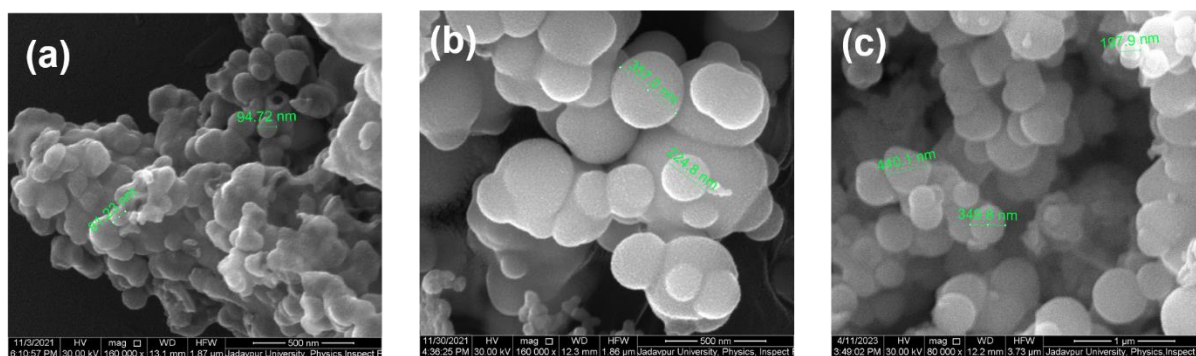


Figure 8.1: FESEM image for (a) ME180, (b) ME150 and (c) ME120

However, inside apparent spherical structure there is a possibility of internal hole (as seen in **Figure 8.1c**) in the synthesized materials. When the hydrothermal temperature is maintained as 180°C grain sizes reduce significantly, and also, agglomeration is clearly found which affects the conductivity of the material. As shown in SEM images grain sizes in ME180 are less than 100 nm where for ME150 it can be ranged from 150 nm to 400 nm approximately. When synthesis temperature goes to a lower value of 120°C the maximum grain size increases further.

Average grain sizes for the prepared materials are extracted using Image J software. Corresponding histograms are depicted in **Figure 8.2**. Average grain sizes for ME180, ME150 and ME120 are 92 nm, 246.5 nm and 353.5 nm respectively.

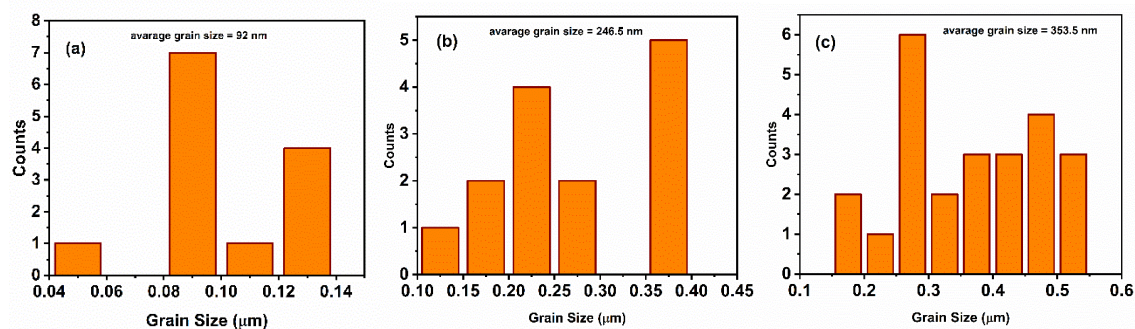


Figure 8.2: Histogram for (a) ME180, (b) ME150 and (c) ME120

From the analysis it can be concluded that upon reducing reaction temperature grain size for MoSe_2 increases significantly. Generally, ductility increases with grain size which means decreasing temperature make the material more suitable for device applications [13]. However, the increased grain boundary (GB) and high dislocation density may cause a drop of electrical conductivity [14].

The crystalline phase of a sample can be identified using PXRD. So, to analyze the phase and get an idea about the structure of all synthesized compounds, the PXRD pattern of the compound has been recorded and illustrated in *Figure 8.3*.

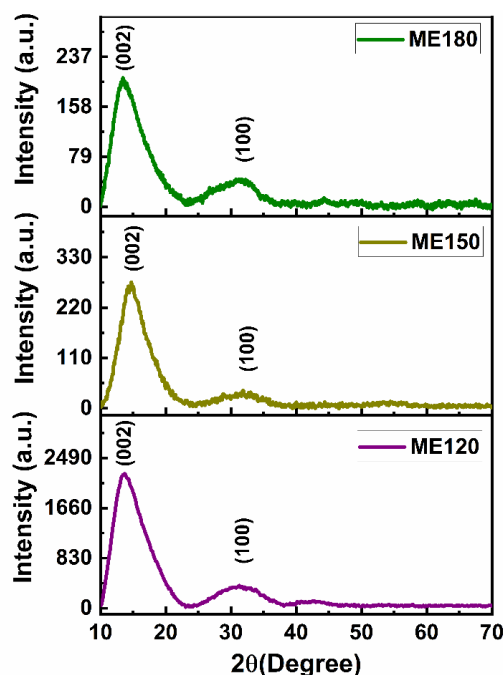


Figure 8.3: PXRD pattern of ME180, ME150, ME120

Observing and comparing the plot to JCPDS files the patterns show more similarity with JCPDS 15-0029, and the analysis proves the presence of hexagonal MoSe₂. As found in the above diffraction pattern, there are two well distinguishable peaks in each pattern of respective material. The highest intensity peaks relative to (002) plane at about $2\theta = 13.44^\circ$ is quite broad in nature relieving the possibility of smaller particle size in nanometer order. The growing sharpness of the peak of (002) plane for ME120 and ME150 reveals larger particle size of these material than ME180 which also supported by SEM. Also, it indicates towards increment in crystalline nature in material. Another peak in each pattern at about $2\theta = 31.65^\circ$ corresponds to Bragg's plane (100). As the peaks are shifted right from its actual position for ME150 the interplanar distance for ME150 reduces which signifies lattice contraction in ME150 material. As reported by Yong-Rong Sun and Xue Zhang, the lattice contraction can effectively increase the electrical conductivity [15].

The interplanar distance (d) can be obtained using the well-known Bragg's equation (eqⁿ 2.1) and listed in **Table-8.1**.

Parameters like crystallite size (D), and dislocation density (δ) for each material can be determined using **equation 5.1**, and **5.2**. As seen from **Table-8.1** average crystallite sizes are small enough which may be attributed as result of lattice defects and strain.

The micro-strains (ϵ) for the synthesized materials are therefore evaluated from **equation 7.2 (Table-8.1)**. Also, the induced lattice defects are calculated with following equation-

$$N_d = \frac{d}{D^3} \quad (8.1)$$

The calculated values of N_d (**Table-8.1**) suggest a relatively high defects present in ME150 which can affect the conductivity of the material.

Table 8.1: *Parameter from XRD analysis for highest intensity peak (002) and (100) peak*

Sample Name	Plane (hkl)	2θ (Degree)	β (radian)	D (nm)	Average D (nm)	δ (nm ⁻²)	Average δ (nm ⁻²)	ε	Average ε	d (Å)	N _d (/nm ²)	Average N _d (/nm ²)
ME180	002	13.44	0.0890	1.64	1.330	0.372	0.666	0.1889	0.156	6.58	0.149	0.207
	100	31.65	0.1398	1.02		0.961		0.1233		2.82	0.266	
ME150	002	14.75	0.0867	1.68	1.275	0.354	0.837	0.1675	0.155	6.00	0.126	0.276
	100	31.88	0.1630	0.87		1.321		0.1427		2.80	0.425	
ME120	002	13.71	0.0866	1.68	1.285	0.354	0.808	0.1801	0.161	6.45	0.136	0.271
	100	31.26	0.1590	0.89		1.262		0.1421		2.86	0.406	

Crystallinity refers to the degree of structural order in a solid. The variation from perfect crystallinity causes the diffraction peaks to broaden. It can be measured with crystallinity index (*Table -8.2*).

Crystallinity index (CI) [16]

$$CI = \frac{I_c}{I_c+I_a} \tag{8.2}$$

Because there is less lattice deformation in ME150 i.e., higher crystallinity, there is a larger charge carrier mobility, which leads to an increase in conductivity.

Lattice parameter is proportional to the distance between atoms (interatomic distance) in the crystal. That indicates for lower lattice parameters (as in ME150 in *Table-8.2*) there is higher number of atoms in the surface of the material. As a result, carrier concentration may increase affecting the conductivity of the material.

Lattice parameters for these hexagonal systems can be estimated using *equation 6.2*.

Table-8.2: Crystallinity index and lattice parameters

Name of Sample	Crystallinity index (%)	Lattice parameters	
		$a = b$ (Å)	c (Å)
ME180	85.21	3.256	12.90
ME150	87.24	3.233	12.00
ME120	88.05	3.302	13.16

7.3.2. Optical Analysis:

The absorption spectra for as synthesized materials are recorded within a range of 400-1100 nm wavelength i.e., in visible and near infrared range. Analysis of the recorded spectra as shown in **Figure 8.4** suggests that ME180 shows absorbance peak in Visible range and for ME150 absorption peak lies in near infrared region. The peaks of the mentioned absorbances found near 649.93 nm and 987.16 nm referring a band gap near 1.91 eV and 1.26 eV for ME180 and ME150 respectively. Possibility of getting peak at far infrared region for ME120 indicates relatively lower optical band gap. The above optical band gaps are calculated using *equation 4.1*.

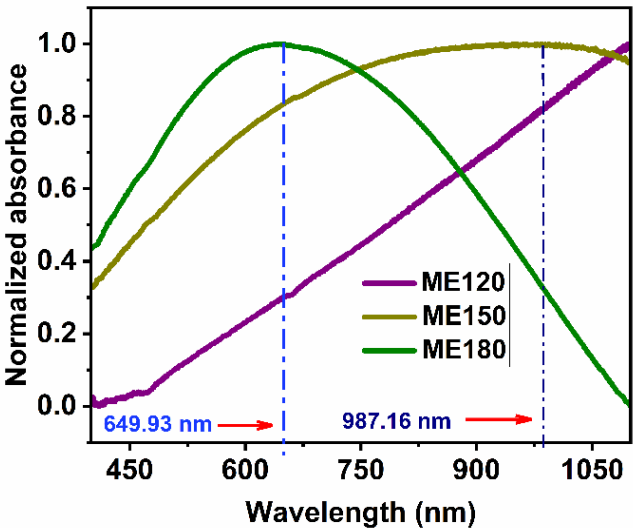


Figure 8.4: UV-Visible spectrophotometer response of ME180, ME150, ME120

8.3.3. Electrochemical Analysis:

Further cyclic voltammetry (CV) is done to investigate the reduction and oxidation processes of the materials. From the potential of reduction and oxidation, LUMO and HOMO energy level of a material can be extracted, additionally which can be used to calculate electrochemical band gap energy of corresponding material. **Figure 8.5** shows CV graph of ferrocene, ME180, ME150 and ME120 respectively.

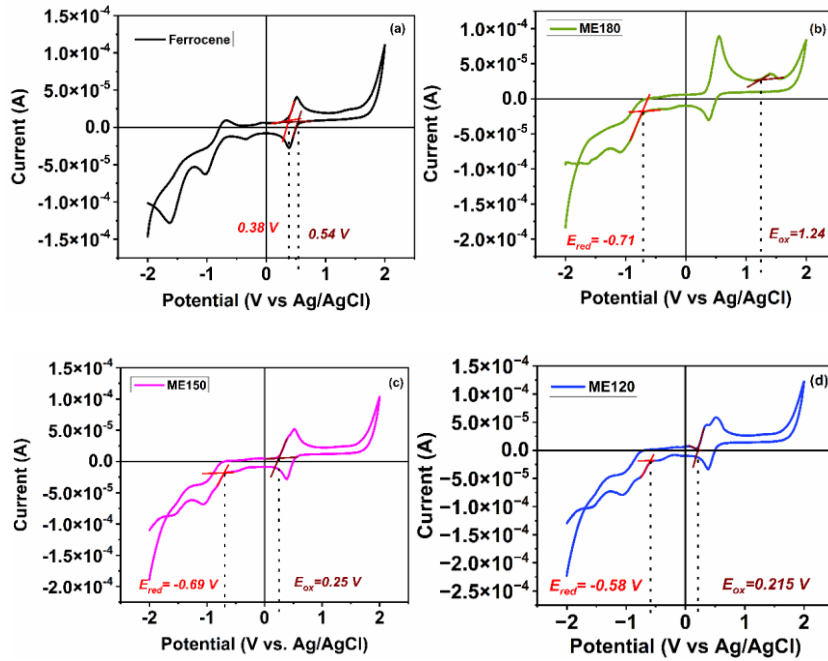


Figure 8.5: Cyclic voltammetry plot for (a) ferrocene, (b) ME180, (c) ME150 and (d) ME120

HOMO and LUMO energy level can be calculated using equations below [17, 18].

$$E_{HOMO} = - \left[\left(4.8 - E_{\frac{1}{2}ferro} \right) + E_{ox} \right] \text{ eV} \quad (8.3)$$

$$E_{LUMO} = - \left[\left(4.8 - E_{\frac{1}{2}ferro} \right) + E_{red} \right] \text{ eV} \quad (8.4)$$

$E_{1/2 \text{ ferro}}$ can be calculated using oxidation and reduction potential of ferrocene with help of the following equation [17, 18].

$$E_{\frac{1}{2}ferro} = \frac{E_{ox} + E_{red}}{2} \quad (8.5)$$

Voltammogram has recorded oxidation and reduction of ferrocene have started at 0.38V and 0.54V respectively. So, the value of $E_{1/2 \text{ ferro}}$ is obtained as 0.46V using **equation 8.5**. Oxidation process of synthesized materials has started at 1.24V, 0.25V and 0.22V respectively i.e., ionization of ME180 starts at much high potential level than other two. From CV, using **equation 8.3** and **8.4** the HOMO and LUMO positions of the materials are determined as -5.58 eV and -3.63 eV (ME180), -4.59 eV and -3.65 eV (ME150), and -4.56 eV and -3.76 (ME120) respectively. The electrochemical band gap energies (i.e., difference between LUMO and HOMO energy) are obtained as 1.95 eV, 0.94 eV and 0.8 eV for ME180, ME150 and ME120 respectively.

8.3.4. Stability Analysis:

Thermogravimetric analysis (TGA) is used to measure a material's thermal stability and its proportion of volatile components by observing the sample's weight change during continual heating. According to the TGA data recorded up to 800°C the graph of **Figure 8.6** has been obtained. As clearly seen in the figure, all respective graphs indicate an abrupt fall in weight percentage (wt%) near 350°C. The 1st reduction in wt% for all the depicted curves between 90°C to 110°C specifies evaporation of volatile impurities in samples [19]. The mentioned fall near 350°C refers starting of possible oxidation of samples and formation of molybdenum oxide (MoO_3) [19]. The compound mixture is stable up to 735°C. The complete deformation of whole compound happens after that.

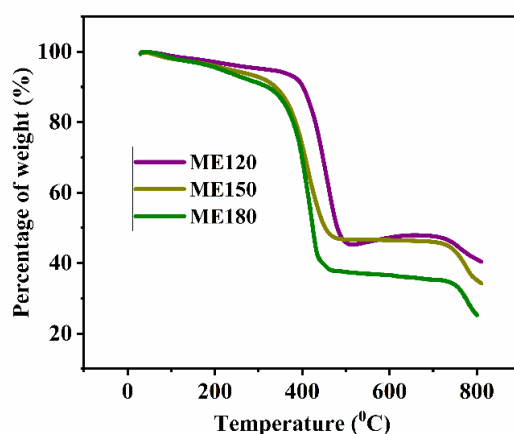


Figure 8.6: Thermogravimetric graph for respective material

8.3.4. Electrical Analysis:

The current-voltage characteristics of respective MS devices was also studied in an applied voltage range of ± 1 V. All the recorded data plotted in the X-Y plane (I-V) graph as shown in **Figure 8.7** indicates non-linearity in curves in forward bias regime. This nature of curve significantly justifies the formation of Schottky contact at the MS junction. However, the device made with ME150 shows better response than other two. Calculated rectification ratios listed in **Table 8.3** propose quite better rectifying nature of Al/ME150 junction.

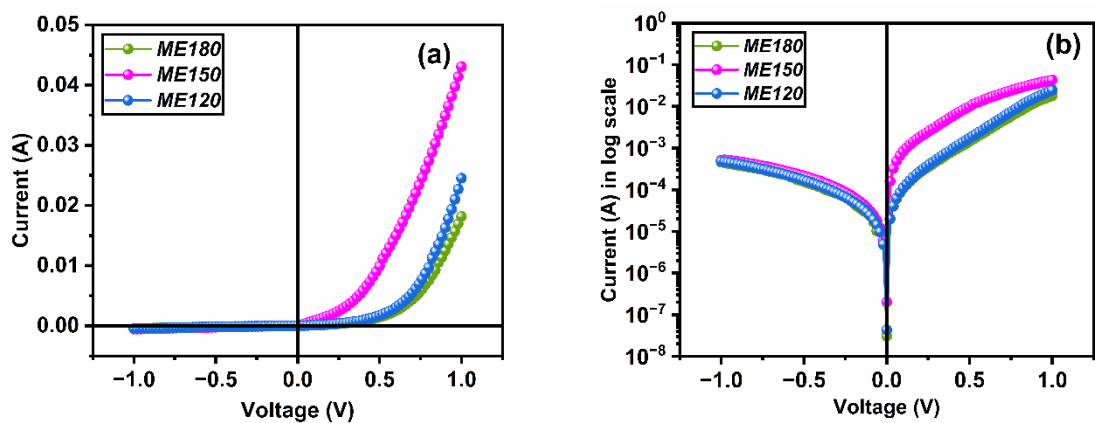


Figure 8.7: I-V Characteristics curve for the fabricated structures in (a) linear and (b) log scale.

The $\ln I$ - $\ln V$ graph in **Figure 8.8** has three distinguish region named as Region I, Region II and Region III.

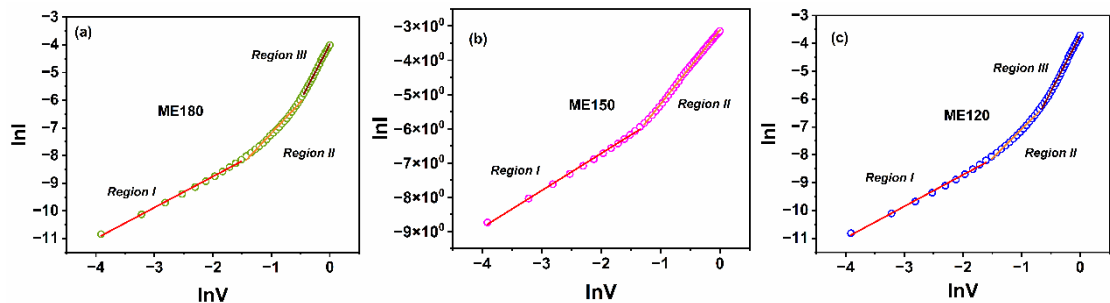


Figure 8.8: $\ln I$ - $\ln V$ graph for the fabricated structures using (a) ME180, (b) ME150 and (c) ME120 to determine type of current transport mechanism

For Region I slope values are nearly one for individual curves. In this region current value is directly proportional to the applied voltage i.e., it follows Ohm's law of conduction [20].

From Region I, Schottky parameters like ideality factor (I.F.), barrier height of the interface and series resistance associated with the junction can be calculated with the help of the renowned Cheung's method [Figure 8.9] using thermionic emission theory assuming the effect of series resistance [equation 1.13, 4.7 and 4.8].

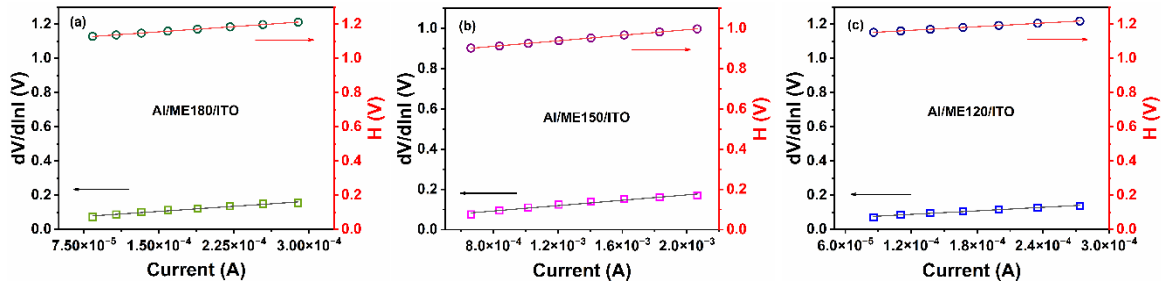


Figure 8.9: $dV/d\ln I$ vs I and $H(I)$ vs I curves for the corresponding SBDs

The trend of lowest barrier height and better ideality of Al/ME150 diode is supported by Mikhelashvilli method [Figure 8.10].

The equations for Mikhelashvilli method of Schottky parameter extraction are given bellow [21]:

$$\eta = \frac{qV_{max}(\alpha_{max}-1)}{\alpha_{max}^2 kT} \quad (8.6)$$

$$\phi_b = \frac{kT}{q} \left[\alpha_{max} + 1 - \ln \left(\frac{I_{max}}{AA^* T^2} \right) \right] \quad (8.7)$$

Where α (V) is Mikhelashvilli function, defined in Chapter 4.

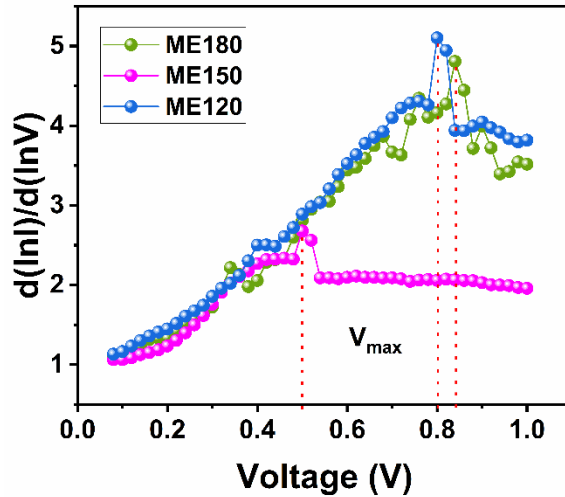


Figure 8.10: $d(\ln I)/d(\ln V)$ plot against biasing voltage for each device

Although the extracted values are slightly different for indicated methods, but the overall analysis of results suggests ME150 based device shows no doubt better performance than other two devices.

Table 8.3: Forward bias Schottky parameters

Device	Rectification ratio	Conductivity (S m^{-1}) $\times 10^{-4}$	From Cheungs' method				Mikhelasvilli	
			I.F.	Barrier height (eV)	R_s (Ohm)		I.F.	Barrier height (eV)
					From $dV/d\ln I$ (Ohm)	From $H(I)$ (Ohm)		
Al/ME180 /ITO	16.96	2.077	1.736	0.630	397.711	408.965	5.265	0.633
Al/ME150/ITO	28.65	15.319	1.496	0.572	66.692	68.766	4.451	0.575
Al/ME120/ITO	6.75	2.212	1.777	0.631	344.552	353.805	4.796	0.639

In **Figure 8.8**, region II having slope value nearly equal to 2 indicates the current follows $I \propto V^2$ rule. This region is known as space charge limited current (SCLC) region. The current in this region is mainly governed by the equilibrium charge-carrier density and the induced charge carriers resulting by an applied voltage. From this region using Mott-Gurney law (**equation 4.11**) carrier mobility for single current device can be easily extracted. According to this law, if the

voltage across a single-carrier device is high enough, the virtual electrode will line up with the actual electrode, and reduction in barrier height will be close to zero, leaving the current across the device to be controlled primarily by drift.

Relative permittivity of each MoSe₂ sample can be calculated using capacitance versus frequency measurement. Change in capacitance value with respect to logarithm of frequency is shown in the figure below (**Figure 8.11**).

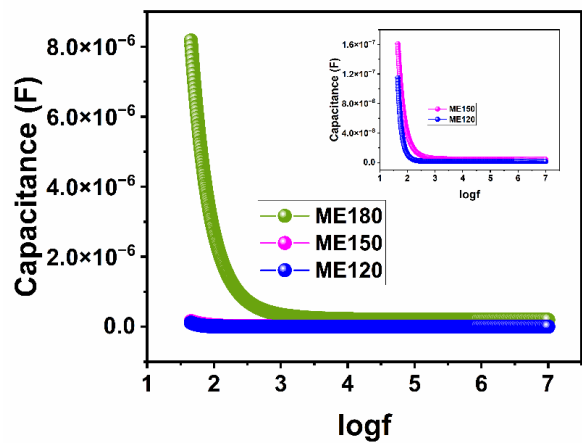


Figure 8.11: Capacitance versus logarithmic frequency graph for each sample

In *equation 4.12* using saturation value of frequency induced capacitance dielectric constant of the material can be calculated. The extracted values of dielectric constants are 22.08, 11.45 and 7.67 for ME180, ME150 and ME120 respectively.

Figure 8.12 shows I-V² graph of the fabricated configurations. The values of mobilities are enlisted in **Table 8.4** and suggest a better carrier mobility for Al/ME150/ITO device.

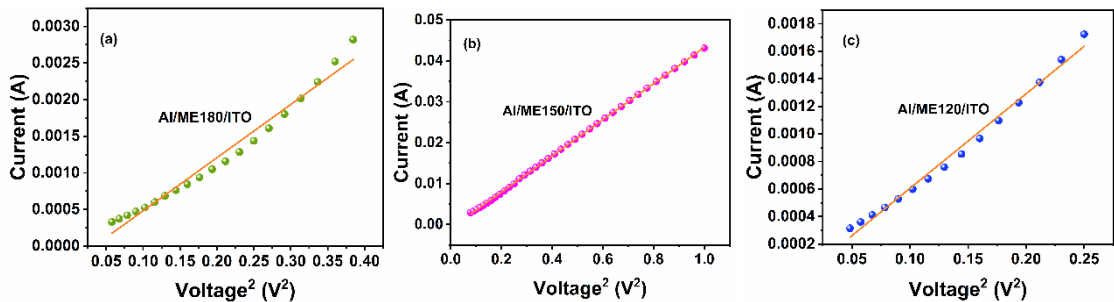


Figure 7.12: Plot for variation of current against square of voltage for (a) Al/ME180/ITO, (b) Al/ME150/ITO and (c) Al/ME120/ITO configuration

As discussed earlier, impedance spectroscopy (IS) analysis can also be a method of extracting the charge transport properties. The IS is performed with oscillatory voltage 50 mV and a frequency range of 40 Hz to 10 MHz. The resulting Nyquist plots at unbiased condition are shown in **Figure 8.13**, which shows the graphs to be distorted semicircle. The semicircle of the ME150-based device has a much lower diameter than the semicircles for other devices, according to the Nyquist plots. The ME150's shorter semicircle suggests that there is less charge recombination and charge transfer resistance.

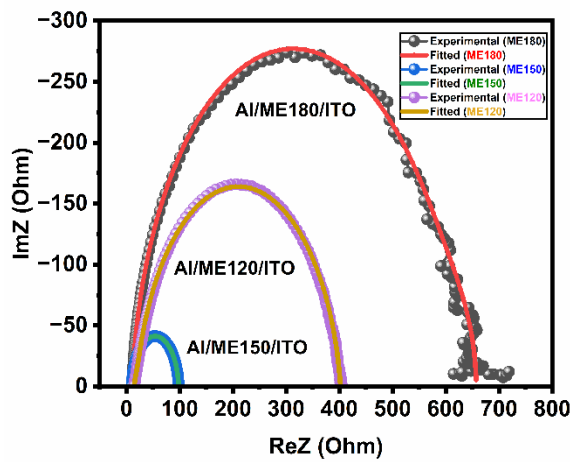


Figure 8.13: Nyquist plot for diode made with synthesized materials

Faster charge transfer is therefore feasible with the ME150 thin film. Whereas the Nyquist plot provides an insight regarding the impedance against charge transfer, the Bode phase diagram can provide us information about the lifespan of charge carriers. **Figure 8.14** represents the corresponding Bode phase plot, which clearly indicates that the characteristic peak for ME120 based SBD occurs at a higher value compared to others. Also, ME180 and ME150 based diode show their peaks at same frequency. Using this peak frequency (f_{peak}), the lifetime (τ_L) of charge carriers can be obtained. The charge carrier lifetime of both ME180, and ME150 is 419 ns and for ME120, this is 218 ns which is much lower.

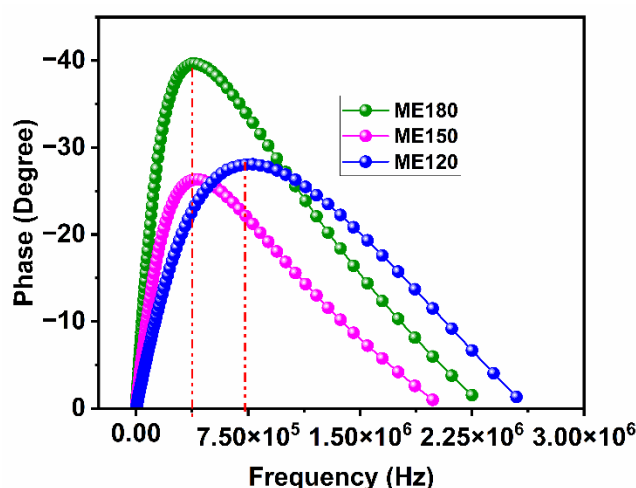


Figure 8.14: Bode phase plot for Schottky barrier diodes

So, the lifetime of the active charge carriers in the ME150 is higher which is another key factor contributing to its better performance. The fact that the charge carrier lifetime of the materials is required to be higher than their respective transit times for efficient charge transfer by the carriers to opposite electrodes, is emphasized here. However, comparing the carrier lifetime and carrier transit time for all the respective diode it is crystal clear that for ME150, its superior device performance can be attributed to the fact that its carrier lifespan is orders of magnitude greater than its carrier transit time. Understanding how charge carriers diffuse from one electrode to the other across a thin layer requires knowledge of the diffusion length of charge carriers. Diffusion length (L_D) of carriers can be evaluated by employing *equation 6.7* and *6.8*.

Table 8.4: Charge transport parameters

Sample Name	mobility	Transit time (ns)	Carrier concentration $\times 10^{20}$	Defect density $\times 10^{22}$	Life time (ns)	Diffusion length (μm)
ME180	5.748×10^{-6}	206	12.41	2.94	419	13.57
ME150	5.486×10^{-5}	14	8.99	2.44	419	41.93
ME120	1.272×10^{-5}	110	3.49	1.03	218	14.56

All the parameters related to charge transport, derived here, are given in **Table-8.4**. It is clearly seen, the diffusion lengths of the charge carriers are larger than the thickness of the film, which is also an essential criterion for an efficient device performance. The average diffusion length of ME150 is about 3 times larger than both ME180 and ME120 based devices which led to better performance in the ME150 based device.

However, the semicircular plots of **Figure 8.13**, demonstrates that the SBD's comparable circuit is made up of both resistive and capacitive networks [22]. As seen in **Figure 7.13 (a)**, the analogous circuit for a Schottky diode is often represented by an RC network that is connected in parallel and a series resistance that is connected to RC network serially. The simulated spectra from the conventional model are unable to accurately match the experimental impedance spectra for each device. Therefore, in order to see if it could fit the impedance spectra correctly, a more complicated equivalent circuit is created (**Figure 7.13b**). It is evident that the equivalent circuit resembles the behaviour of a diode in an alternating current by using two resistance-capacitance circuits, a parasitic inductance, and a series resistance.

Table 8.5: *Parameters value from EIS analyser*

From EIS analyzer for	Series Resistance (Ω)	Series Inductance (H)	Resistance arose from Al-MoSe ₂ interface (Ω)	Capacitance arose from Al-MoSe ₂ interface (F)	Resistance arose from MoSe ₂ -ITO interface (Ω)	Capacitance arose from MoSe ₂ -ITO interface (F)	Constant Phase Value
ME180-based device	11.13 ± 1.2324	$1.9257 \times 10^{-7} \pm 7.9874$	57.232 ± 10.272	$2.6461 \times 10^{-6} \pm 26.272$	589.3 ± 0.68306	$4.8519 \times 10^{-8} \pm 0.75935$	0.94705 ± 0.059891
ME150-based device	10.072 ± 0.34096	$1.93 \times 10^{-7} \pm 6.0744$	25.814 ± 0.16685	$9.1983 \times 10^{-8} \pm 0.62447$	62.18 ± 0.07164	$9.5335 \times 10^{-8} \pm 0.26817$	0.94697 ± 0.022049
ME120-based device	12.6 ± 2.3678	$1.6398 \times 10^{-7} \pm 18.911$	6.3746 ± 4.9384	$6.7803 \times 10^{-9} \pm 28.002$	383.44 ± 0.10674	$2.3689 \times 10^{-8} \pm 0.4084$	0.90082 ± 0.034714

For mathematical analysis of the model, *equation 7.4, 7.5 and 7.6* are taken into consideration.

The electric conductivity that is referred to as ac conductivity when the electric conductivity originates from a potential dependent on time.

The ac conductivity of the materials can be determined using the subsequent formula [23]:

$$\sigma_{ac} = \frac{Z'}{Z'^2 + Z''^2} \cdot \frac{d}{A} \quad (8.8)$$

Where d is the film thickness.

The graph illustrates that at low frequencies, σ_{ac} exhibits frequency independent behaviour, whereas at higher frequencies, a frequency dependent area takes precedence. The frequency at which curve's slope begins to change is known as “hopping frequency”. Jonschers’ power law [24] describes the behaviour of the obtained plot of σ_{ac} as follows.

$$\sigma_{ac} = \sigma_{dc} + S\omega^n \quad (8.9)$$

Where, σ_{dc} is the frequency independent dc conductivity, the temperature dependent constant is S, and the exponent n lies $0 < n < 1$. A translational motion is also engaged by hopping conduction when n is equal to or less than 1. However, localized hopping is involved for n values larger than 1.

The graph (*Figure 8.15*) indicates that as frequency increases, ac conductivity rises as well. From *Figure 8.15* extrapolating the frequency independent part of the curve to σ_{ac} axis the value of dc conductivity. Nonetheless, it is evident that ME150 has the highest dc conductivity values out of the three (ME180: $1.17 \times 10^{-4} \text{ Sm}^{-1}$, ME150: 0.00139 Sm^{-1} , and ME120: $3.22 \times 10^{-4} \text{ Sm}^{-1}$).

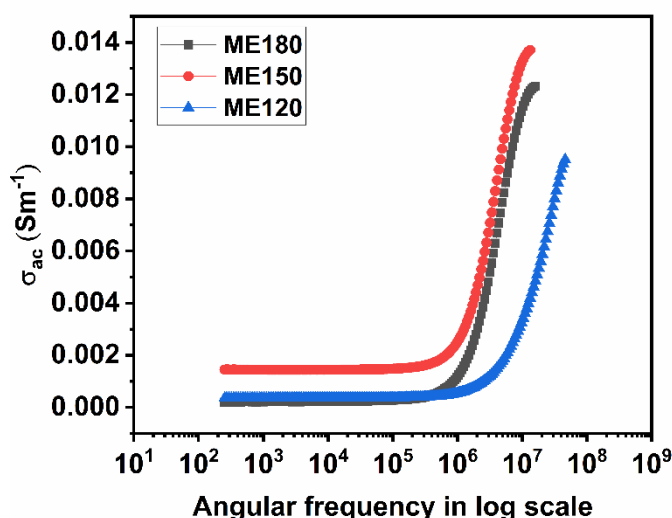


Figure 8.15: Frequency dependent conductivities for the synthesized materials

8.4. *Conclusions:*

In conclusion, MoSe₂ nanospheres are successfully synthesized using hydrothermal process even in a low temperature of 120°C. Different characteristic analysis indicates possibility of better performance of MoSe₂ synthesized at 150°C in electronic device applications. The potential applicability of the derived materials within metal-semiconductor based Schottky barrier diode is confirmed from non-linear behaviour of I-V characteristics of fabricated diodes. Schottky parameters reveals significantly lower turn on voltage that put ME150-based device forward than other two. The underneath mechanism of electrical performance is explored by charge transport analysis using both I-V data and IS measurements. These overall analyses illustrate the potential behaviour of low temperature derived MoSe₂ in fabrication of Schottky diode. At a quite low temperature (150°C) MoSe₂ is highly appreciable for efficient device application. However, for optical application ME180 may shows a better performance than other two as only it has absorbance in visible light range.

References:

1. H. Liu, A. T. Neal, and P. D. Ye, *Channel Length Scaling of MoS₂ MOSFETs*, ACS Nano, 2012, **6**, 10, 8563– 8569
doi.org/10.1021/nn303513c
2. G. Eda, and S. A. Maier, *Two-Dimensional Crystals: Managing Light for Optoelectronics*, ACS Nano, 2013, **7**, 7, 5660– 5665
doi.org/10.1021/nn403159y
3. S. Larentis, B. Fallahazad, and E. Tutuc, *Field-effect transistors and intrinsic mobility in ultra-thin MoSe₂ layers*, Applied Physics Letters, 2012, **101**, 22, 223104
doi.org/10.1063/1.4768218
4. JS Ross, S Wu, H Yu, NJ Ghimire, AM Jones, G Aivazian, J Yan, DG Mandrus, D Xiao, W. Yao, and X. Xu, *Electrical Control of Neutral and Charged Excitons in a Monolayer Semiconductor*, Nature communications, 2013, **4**, 1474
doi.org/10.1038/ncomms2498
5. Q. H. Wang, K. Kalantar-Zadeh, A. Kis, J. N. Coleman, and M. S. Strano, *Electronics and Optoelectronics of Two-Dimensional Transition Metal Dichalcogenides*, Nature nanotechnology, 2012, **7**, 699– 712
doi.org/10.1038/nnano.2012.193
6. S Tongay, J Zhou, C Ataca, K Lo, TS Matthews, J Li, J. C. Grossman, and J. Wu, *Thermally Driven Crossover from Indirect toward Direct Bandgap in 2D Semiconductors: MoSe₂ versus MoS₂*, Nano Letters, 2012, **12**, 11, 5576– 5580
doi.org/10.1021/nl302584w
7. X.H. Chen, and R. Fan, *Low-temperature hydrothermal synthesis of transition metal dichalcogenides*, Chemistry of Materials, 2001, **13**, 3, 802-805
doi.org/10.1021/cm000517+
8. X. Zhang, M. Xue, X. Yang, G. Luo, and F. Yang, *Hydrothermal synthesis and tribological properties of MoSe₂ nanoflowers*, Micro & Nano Letters, 2015, **10**, 7, 339-342
doi.org/10.1049/mnl.2015.0014
9. H. Tang, H. Huang, X. Wang, K. Wu, G. Tang, and C. Li, *Hydrothermal synthesis of 3D hierarchical flower-like MoSe₂ microspheres and their*

- adsorption performances for methyl orange*, Applied Surface Science, 2016, **379**, 296-303
doi.org/10.1016/j.apsusc.2016.04.086
10. X. Li, and K. Peng, *MoSe₂/Montmorillonite Composite Nanosheets: Hydrothermal Synthesis, Structural Characteristics, and Enhanced Photocatalytic Activity*, Minerals, 2018, **8**, 7, 268
doi.org/10.3390/min8070268
 11. H. Mittal, A. Kumar, and M. Khanuja, *In-situ oxidative polymerization of aniline on hydrothermally synthesized MoSe₂ for enhanced photocatalytic degradation of organic dyes*, Journal of Saudi Chemical Society, 2019, **23**, 7, 836-845
doi.org/10.1016/j.jscs.2019.02.004
 12. J. H. Zhan, Z. D. Zhang, X. F. Qian, C. W. Y. Xie, and Y. T. Qian, *Synthesis of MoSe₂ nanocrystallites by a solvothermal conversion from MoO₃*, Materials research bulletin, 1999, **34**, 4, 497-501
doi.org/10.1016/S0025-5408(99)00048-3
 13. C. C. Koch, D. G. Morris, K. Lu, and A. Inoue, *Ductility of nanostructured materials*, MRS Bulletin, 1999, **24**, 2, 54-58
doi:10.1557/S0883769400051551
 14. H. Bishara, S. Lee, T. Brink, M. Ghidelli, and G. Dehm, *Understanding grain boundary electrical resistivity in Cu: the effect of boundary structure*, ACS nano, 2021, **15**, 10, 16607–16615
doi.org/10.1021/acsnano.1c06367
 15. Y. R. Sun, X. Zhang, L. G. Wang, Z. K. Liu, N. Kang, N. Zhou, W.-L. You, J. Li, and X.-F. Yu, *Lattice contraction tailoring in perovskite oxides towards improvement of oxygen electrode catalytic activity*, Chemical Engineering Journal, 2021, **421**, 1, 129698
doi.org/10.1016/j.cej.2021.129698
 16. D. G. Chukhchin, A. V. Malkov, I. V. Tyshkunova, L. V. Mayer, and E. V. Novozhilov, *Diffraction method for determining the degree of crystallinity of materials*, Crystallography Reports, 2016, **61**, 371–375
doi.org/10.1134/S1063774516030081
 17. M. Kumada, and K. Tamao, *Aliphatic organopolysilanes*, Advances in organometallic chemistry, 1968, **6**, 19-117
doi.org/10.1016/S0065-3055(08)60587-0

18. J. Pommerehne, H. Vestweber, W. Guss, R. F. Mahrt, H. Bassler, M. Porsch and J. Daub, *Efficient two-layer leds on a polymer blend basis*, Advanced Materials, 1995, 7, 6, 551-554
doi.org/10.1002/adma.19950070608
19. H. Mittal, A. Kumar, and M. Khanuja, *MoSe₂-PANI Nanocomposite as Supercapacitor Electrode Material: Optimization, Mechanism and Electrochemical Performance*, Chemistry Select, 2022, 7, 27, e202201623
doi.org/10.1002/slct.202201623
20. B. Pal, P. Das, J. Datta, U. Gangopadhyay, and P. P. Ray, Materials Science in Semiconductor Processing, 2023, **162**, 107535
doi.org/10.1016/j.mssp.2023.107535
21. V. Mikhelashvili, G. Eisenstein, V. Garber, S. Fainleib, G. Bahir, D. Ritter, M. Orenstein, and A. Peer, *On the extraction of linear and nonlinear physical parameters in nonideal diodes*, Journal of Applied Physics, 1999, **85**, 9, 6873-6883
doi.org/10.1063/1.370206
22. C. Yim, N. McEvoy, H-Y. Kim, E. Rezvani and G. S. Duesberg, *Investigation of the Interfaces in Schottky Diodes Using Equivalent Circuit Models*, ACS Applied Materials & Interfaces, 2013, **5**, 15, 6951-6958
doi.org/10.1021/am400963x
23. S. Naaz, P. Das, S. Khan, B. Dutta, S. Maity, P. Ghosh, P. P. Ray, and M. H. Mir, *Fabrication of a halopyridine appended Co (II) based 1D coordination polymer for efficient charge transportation*, Polyhedron, 2021, **201**, 115159
doi.org/10.1016/j.poly.2021.115159
24. R. Kajal, A. Kandasami, B. Kataria, P. Solanki, and D. Mohan, *Structural, optical, and dielectric characteristics of pulsed laser deposited SnO₂-TiO₂ composite thin films*, Physica Scripta, 2023, **98**, 8, 085935
doi.org/10.1088/1402-4896/ace569

Chapter 9

Overall Summary and Future Outlook of the Work

Since its first discovery inorganic compound semiconductors have grabbed both the attention and interest of the researcher till the date. Different properties and corresponding different applications are discovered and yet to explore in future. The revolutionary advancement of electronics over the latter part of the 20th century has had a significant impact on our way of life and society. Science and technology have advanced their study and development, highlighting the significance of metal-semiconductor interfaces as the building blocks of all electronic devices.

Therefore, in this thesis, an overview of some inorganic compound semiconductor (SnO_2 , ZnO , CoS_2 , MoSe_2) has been drawn, and also, their properties and application in metal-semiconductor junction has been demonstrated elaborately. However, performance of SnO_2 composite with rGO has also been reported. As a better and easy synthesis procedure for nanomaterial synthesis mainly hydrothermal/solvothermal synthesis of each considered semiconductor has been reported here. Also, one example of co-precipitation method has been enlisted in this thesis. Different barrier height extraction method like current-voltage (I-V), capacitance-voltage (C-V) etc. and their successful implementation for the calculation of devices' barrier height are discussed precisely here.

SnO_2 being an important and huge studied inorganic semiconductor already proves its beneficial performance in the field of electronics. A brief comparison between SnO_2/Al junction with a metal semiconduction junction of aluminium and rGO- SnO_2 nanocomposite has been elaborated. A little incorporation of rGO has made a great improvement in junctional behaviour of fabricated device. Also, high photosensitivity has been reported which makes rGO- SnO_2 nanocomposite a promising material for photodiode and possible other optoelectronic devices.

An examination of the temperature-dependent performance of the manufactured SBDs has revealed a significant departure of the Richardson constant from the theoretically calculated value, suggesting the existence of barrier inhomogeneity. According to the research, the TE mechanism with a Gaussian distribution of the barrier heights best explains the temperature-dependent I-V characteristics of the produced SBD. This mechanism has also yielded a value of the Richardson constant that is extremely close to the theoretical value.

As, different synthesis procedures may affect different properties of synthesized nanomaterial, a comparison between ZnO nanomaterial obtained from two different synthesis method has been drawn and better performance of ZnO from hydrothermal method has been established through the analysis of I-V, C-V and IS characteristics.

Metal chalcogenides a recent development in semiconductor family is also taken into consideration and successful implementation of them in MS junction has been described.

Annealing of a nanomaterial has an obvious effect on the properties of material as recrystallization happens during annealing. It may have positive or negative impact on the performance of the devices made with the material. A positive impact of higher annealing temperature on the performance of CoS₂-based MS junction as a result of improved properties of annealed CoS₂ has been presented in this thesis. Magnetic moments of material before and after annealing also has been demonstrated.

Properties of obtained material from solvothermal synthesis depends on the conditions i.e., temperature, time, medium etc. of the synthesis. Using ethanol as the medium of a fruitful synthesis of MoSe₂ nanomaterial has been reported even in a very low temperature of 120°C. Among the all when synthesis temperature is

maintained for 150°C, obtained MoSe₂ gives its best performance as the device component of fabricated MS device.

Ultimately, the overall image that emerges from this thesis shows that inorganic compound semiconductors like metal oxides and chalcogenides are excellent material for electronic device applications because of their unique properties. Easy synthesis method for each material has been described. The study also has clarified a straightforward method of adding rGO to improve the inorganic semiconductors' device performance. Furthermore, a thorough examination of the charge transport characteristics and metal-semiconductor junction might aid in the basic comprehension of these interfaces. The research described here, which is based on the enhancement of properties and application of compound inorganic semiconductors as a device, could be useful in the future for the design of electronic devices such as photovoltaics, transistors, photodetectors and other different electronic devices. Tuning of different properties of nanomaterial is one of the most promising emerging technologies. This study provided evidence that properties and morphology of a material can be tuned by changing condition of the synthesis method and processes applied after synthesis. By further refining synthesis processes, device fabrication techniques, and other elements, the device performance may be further enhanced. It appears that inorganic compound nanomaterials could be the ultimate flagbearer, helping to shape nanotechnology's future like never before, thanks to the tireless efforts being made all across the world.

Continue...

List of Publications

Publications in International Journals:

1. **Pubali Das**, Baishakhi Pal, Mrinmay Das, Sayantan Sil, Dhananjoy Das, Animesh Layek, and Partha Pratim Ray, “*Findings of inhomogeneity in barrier height of Schottky junction Al/rGO-SnO₂ having anomaly in theoretical and experimental value of Richardson constant: A Gaussian approach*”, Results in Physics, 2022, 42, 105996
2. **Pubali Das**, Baishakhi Pal, Joydeep Datta, Mrinmay Das, Sayantan Sil, and Partha Pratim Ray, “*Improved charge transport properties of graphene incorporated tin oxide based Schottky diode over pure one*”, Journal of Physics and Chemistry of Solids, 2021, 148, 109706
3. **Pubali Das**, Santanu Majumdar, Arka Dey, Sourav Mandal, Atish Mondal, Sinchan Chakrabarty, Partha Pratim Ray, and Biswajit Dey, “*4, 4'-Bipyridine-based Ni (ii)-metallo gel for fabricating a photo-responsive Schottky barrier diode device*”, New Journal of Chemistry, 2023, 45, 35, 15920-15927
4. Samim Khan, **Pubali Das**, Sanobar Naaz, Paula Brandão, Aditya Choudhury, Raghavender Medishetty, Partha Pratim Ray and Mohammad Hedayetullah Mir, “*A dual-functional 2D coordination polymer exhibiting photomechanical and electrically conductive behaviours*”, Dalton Transactions, 2023, 52, 47, 17934-17941
5. Gurupada Bairy, **Pubali Das**, Basudeb Dutta, Saumitra Bhowmik, Partha Pratim Ray, and Chittaranjan Sinha, “*In Situ Oxidation of Pyridyl-Dihydrobenzoimidazoquinazoline and the Synthesis of a Highly Luminescent Cd (II) Coordination Polymer: A Promising Candidate for Mutagenic Nitroaromatic Detection and Device Fabrication*”, Inorganic Chemistry, 2023, 62, 32, 12773-12782

6. Baishakhi Pal, **Pubali Das**, Joydeep Datta, Utpal Gangopadhyay, and Partha Pratim Ray, “*Improvement of charge kinetics of MoS₂ nano-petal based Schottky device by incorporation of W: A comparative study of structural, optical, and electrical properties*”, Materials Science in Semiconductor Processing, 2023, 162, 107535
7. Sanobar Naaz, **Pubali Das**, Souvik Mukherjee, Samim Khan, Goutam Pramanik, Prasanta Ghosh, Antonio Frontera, Partha Pratim Ray, and Mohammad Hedayetullah Mir, “*Exploration of Cl⋯Cl and π ⋯ π stacking contacts along with the conductivity properties of a Cu-MOF featured with paddle-wheel SBUs*”, CrystEngComm, 2023, 25, 5, 813-821
8. Sudip Bhunia, **Pubali Das**, Snehasis Banerjee, Rosa M Gomila, Michael GB Drew, Antonio Frontera, Partha Pratim Ray, and Shouvik Chattopadhyay, “*Fabrication of Schottky barrier diodes utilizing carboxylate bridged trinuclear mixed valence cobalt (III/II/III) complexes of tetradentate N₂O₂ donor reduced Schiff base ligands*”, New Journal of Chemistry, 2023, 47, 30, 14202-14216
9. Manik Shit, **Pubali Das**, Sukanya Paul, Arnab Samnta, Sk Mohammad Aziz, Partha Pratim Ray, and Chittaranjan Sinha, “*In quest of New Energy Material: 3D Mn (II)-coordination Polymer, the Schottky Device and Theoretical Interpretation*”, ES Materials & Manufacturing, 2022, 19, 804
10. Sanobar Naaz, **Pubali Das**, Samim Khan, Basudeb Dutta, Sourav Roy, Antonio Frontera, Partha Pratim Ray, and Mohammad Hedayetullah Mir, “*Cu (II)-Based Molecular Hexagons Forming Honeycomb-like Networks Exhibit High Electrical Conductivity*”, Inorganic Chemistry, 2022, 61, 49, 19828-19837
11. Sanobar Naaz, **Pubali Das**, Antonio Frontera, Basudeb Dutta, Samim Khan, Partha Pratim Ray, and Mohammad Hedayetullah Mir, “*Halogen⋯Halogen and π -Hole Interactions in Supramolecular Aggregates and*

- Electrical Conductivity Properties of Cu (II)-Based 1D Coordination Polymers*”, Crystal Growth & Design, 2022, 22, 9, 5189-5197
12. Mrinmay Das, **Pubali Das**, Joydeep Datta, Dhananjay Das, Somobrata Acharya, and Partha Pratim Ray, “*Improved device performance of rod like ZnO in a Schottky type photosensor compared to particle like ZnO: Analysis of charge transport*”, Materials Science in Semiconductor Processing, 2021, 130, 105799
 13. Sanobar Naaz, **Pubali Das**, Samim Khan, Basudeb Dutta, Suwendu Maity, Prasanta Ghosh, Partha Pratim Ray, and Mohammad Hedayetullah Mir, “*Fabrication of a halopyridine appended Co (ii) based 1D coordination polymer for efficient charge transportation*”, Polyhedron, 2021, 201, 115159
 14. Sakhiul Islam, **Pubali Das**, Saswati Maiti, Samim Khan, Suwendu Maity, Prasanta Ghosh, Atish Dipankar Jana, Partha Pratim Ray, and Mohammad Hedayetullah Mir, “*Electrically conductive Cu (II)-based 1D coordination polymer with theoretical insight*”, Dalton Transactions, 2020, 49, 43, 15323-15331
 15. Akhtaruzzaman, **Pubali Das**, Samim Khan, Suwendu Maity, Sanobar Naaz, Sakhiul Islam, Prasanta Ghosh, Partha Pratim Ray, and Mohammad Hedayetullah Mir, “*Two zinc (ii)-based coordination polymers with flexible dicarboxylate and pyridine mixed ligands: effect of $\pi \cdots \pi$ interactions on electrical activity*”, New Journal of Chemistry, 2019, 43, 40, 16071-16077
 16. Sukanya Paul, Basudeb Dutta, **Pubali Das**, Satyajit Halder, Manik Shit, Partha Pratim Ray, Kuladip Jana, and Chittaranjan Sinha, “*Double advantages of 2D coordination polymer of coumarinyl-pyridyl Schiff base decorated Zn (II): The fabrication of Schottky device and Anti-*

- carcinogenic activity*”, Applied Organometallic Chemistry, 2023, 37, 8, e7160
17. Soumi Halder, Baishakhi Pal, Arka Dey, Sayantan Sil, **Pubali Das**, Animesh Biswas, and Partha Pratim Ray, “*Effect of graphene on improved photosensitivity of MoS₂-graphene composite based Schottky diode*”, Materials Research Bulletin, 2019, 118, 110507
 18. Rajkumar Jana, Arka Dey, Mrinmay Das, Joydeep Datta, **Pubali Das**, and Partha Pratim Ray, “*Improving performance of device made up of CuO nanoparticles synthesized by hydrothermal over the reflux method*”, Applied Surface Science, 2018, 452, 155-164
 19. Joydeep Datta, Mrinmay Das, Arka Dey, Sayantan Sil, Rajkumar Jana, Soumi Halder, **Pubali Das**, and Partha Pratim Ray, “*Experimental and theoretical overview on bias dependent Debye relaxation and conduction mechanism of Cd_{1-x}Zn_xS film and its significance in signal transport network*”, Materials Chemistry and Physics, 2018, 213, 23-34

Publication in Conference Proceedings:

Arka Dey, Rajkumar Jana, Joydeep Dhar, **Pubali Das**, and Partha Pratim Ray, “*Gaussian distribution of inhomogeneous barrier height of Al/ZnS/ITO Schottky barrier diodes*”, Materials Today: Proceedings, 2018, 5, 3, 9958-9964

List of Presentation/Participation in Conferences/Workshop:

1. Participation in “Advanced Materials for Environmental Sensors”, Department of Metallurgy Engineering, IIT Indore, India, 7th March-12th March, 2022
2. Oral presentation of a paper entitled “Effect of synthesis procedure on charge transport analysis of Zinc Oxide”, at the “3rd International

Conference on MATERIAL SCIENCE & NANOTECHNOLOGY”,
Lisbon, Portugal, 16th -17th August, 2021

3. Presentation of a paper entitled “Explanation of inhomogeneous barrier height of Al/rGO-SnO₂ Schottky barrier diode using double Gaussian Distribution”, in International Conference on “CURRENT TRENDS IN MATERIALS SCIENCE AND ENGINEERING (CTMSE 2021)”, Institute of Engineering & Management, Salt Lake, Kolkata, India, 11th-13th March, 2021
4. Participation in “Development of Low cost High efficiency Perovskite solar cells Energy Independence of Atmanirbhar Bharat”, IIT Roorkee, India, 20th November, 2020
5. Presentation of a poster entitled “Comparison of rGO-SnO₂-based Schottky diode with SnO₂-based Schottky diode”, in “XXth International Workshop on the PHYSICS OF SEMICONDUCTOR DEVICES”, Kolkata, India, 17th -20th December, 2019



Improved charge transport properties of graphene incorporated tin oxide based Schottky diode over pure one

Pubali Das, Baishakhi Pal, Joydeep Datta, Mrinmay Das, Sayantan Sil, Partha Pratim Ray^{*}

Department of Physics, Jadavpur University, Jadavpur, Kolkata, 700032, West Bengal, India

ARTICLE INFO

Keywords:
rGO-SnO₂
Carrier mobility
Schottky diode
Rectification ratio

ABSTRACT

Graphene and its nanocomposites with different semiconductor materials have attracted significant research interest in the last decade due to their improved performance in various fields. In this report, SnO₂ and a reduced graphene oxide (rGO)-SnO₂ composite is synthesized via hydrothermal method. Structural, optical and electrical characterization of the material is performed. Incorporation of rGO increases the light absorption and reduces the band gap of SnO₂. Schottky barrier formation at metal-semiconductor junction is important for various applications. Here, we describe the performance of SnO₂ and rGO-SnO₂ based Schottky diode. Important diode parameters like rectification ratio, ideality factor, barrier height and series resistances are calculated from forward Current density-voltage (J-V) characteristics. rGO-SnO₂ shows much better performance compared to SnO₂. Analysis of Photoresponse behavior reveals that rGO-SnO₂ shows photosensitivity of about 9.95 which is higher than that of SnO₂ (2.42). After incorporation of rGO, other diode parameters and transport properties were also improved. To gain better insight on charge transport properties, space charge limited current theory has been utilized. In rGO-SnO₂, carrier mobility is increased by 62% compared to SnO₂, implying that rGO-SnO₂ has better charge transport due to enhanced electron hole separation which is attribute to the presence of graphene.

1. Introduction

Graphene is a two dimensional material with monolayer honeycomb nanostructure composed of sp² hybridized carbon atoms [1]. It has very large surface area (2630 m²/g) which facilitates higher absorption of light and greater interfacial contact [2]. It is a very thin but strong material with high carrier mobility and possesses optical transparency of wide wavelength range [3]. Nowadays, with these excellent properties, graphene have become good candidates for uses in different applications such as optoelectronic devices, photosensors, supercapacitors, solar cell etc [4,5]. Graphene has already been used in numerous applications of Schottky diodes which is a key part of many electronic devices [6]. Higher rate of recombination, interface quality, cost and toxicity of the used materials are the issues for Schottky barrier diode (SBD) [7]. To overcome these problems, a number of semiconductor materials have been explored. Graphene based nanocomposite materials are especially attractive choice for improved performance. Nowadays, metal oxide based semiconductors are of great interest due to their versatile properties. They are applied frequently in field effect transistor, chemical sensors and memory application [8]. Among them SnO₂ is used widely

for its low resistivity, excellent electron mobility, non toxicity, good stability, low cost and availability [9]. It has application as gas sensors, anode in lithium ion batteries etc. [10] SnO₂ is an n-type wide band gap semiconductor (bandgap of bulk SnO₂ is 3.6 eV) [11]. So, it is only sensitive to lower light wavelength. Also it has higher recombination rate. If its bandgap and recombination rate can be reduced, we can use it for photovoltaic application and other optoelectronic devices. It has been shown that if graphene is incorporated in the SnO₂, the light absorption range of SnO₂ can be increased. According to earlier reports, graphene-SnO₂ composite is promising for its effective changes in dielectric properties, gas sensing, supercapacitor, and field emission study [12]. But investigation of Schottky diode properties through graphene-SnO₂/metal junction has gained rare notice. It motivated us to investigate graphene-SnO₂ based Schottky barrier diode compared to the Schottky barrier diode fabricated with pure SnO₂, which can be beneficial to understand the effect of graphene on device performance and charge transport properties of the material.

As pure graphene is hard to achieve, reduced graphene oxide was used. Graphene oxide (GO) can be produced using a modified Hummers' method and after that followed by a reduction procedure GO can be

^{*} Corresponding author. Department of Physics, Jadavpur University, Kolkata, 700032, India.
E-mail addresses: partha@phys.jdvu.ac.in, parthapray@yahoo.com (P.P. Ray).

<https://doi.org/10.1016/j.jpcs.2020.109706>

Received 29 April 2020; Received in revised form 27 July 2020; Accepted 9 August 2020

Available online 14 August 2020

0022-3697/© 2020 Elsevier Ltd. All rights reserved.



Findings of inhomogeneity in barrier height of Schottky junction Al/rGO-SnO₂ having anomaly in theoretical and experimental value of Richardson constant: A Gaussian approach

Pubali Das^a, Baishakhi Pal^a, Mrinmay Das^{a,b,c}, Sayantan Sil^{a,d}, Dhananjoy Das^a, Animesh Layek^a, Partha Pratim Ray^{a,*}

^a Department of Physics, Jadavpur University, Jadavpur, Kolkata 700032, West Bengal, India

^b School of Applied and Interdisciplinary Sciences, Indian Association for the Cultivation of Science, Jadavpur, Kolkata 700032, West Bengal, India

^c Department of Physics, Sister Nivedita University, New Town, Kolkata 700156, West Bengal, India

^d Department of Physics, University of Engineering and Management, University Area, Action Area III, B/5, Newtown, Kolkata 700160, West Bengal, India

ARTICLE INFO

Keywords:

rGO-SnO₂ nanocomposite
Defects
Schottky diode
Barrier height
Interface
Inhomogeneity
Gaussian distribution

ABSTRACT

In this research, the temperature dependent dynamical behavior of Schottky junction Al/rGO-SnO₂ has been investigated with thermionic emission (TE) theory within the temperature regime 303 K to 423 K at interval 20 K. During analysis of electrical charge transport behavior an anomalous change is observed in the value of ideality factor and barrier height with rising temperature for the junction. Experimentally derived Richardson constant (of the order $10^{-5} \text{ A/m}^2 \text{ K}^2$) using TE theory is exceptionally substandard to the theoretical (of the order $10^6 \text{ A/m}^2 \text{ K}^2$) values. The beauty of this work is to find out the underline physics for this discrepancy in measurement of Richardson constant (might arise due to inhomogeneity in barrier of metal-semiconductor junction) by assuming the Gaussian distribution of the barrier height with TE theory at the junction. It is obvious that the occurrence of barrier inhomogeneity across the junction leading charge transport phenomena which mostly impacting upon the parameters of Schottky diodes and its nature because of intrinsic formation of ripples and ridges. In this study, it is found that the charge transport mechanism is highly follows the single Gaussian distribution. The material characterization and its Schottky behavior in normal temperature had been published elsewhere.

Introduction

Thin film based Metal-Semiconductor (MS) Schottky Barrier Diode (SBDs) [1] have attracted huge attention for its wide range of applications, especially in the micro-electronic devices such as optoelectronic [2], bipolar integrated circuits [3] and high frequency device applications [4]. Several current transport mechanism such as thermionic emission (TE), barrier tunneling and carrier generation-recombination at space charge region have been studied to explain various MS junction. Moreover, for the unique features like high conductivity, wide optical transparency and great compatibility for thin film fabrication, graphene composite has proven itself as an important candidate for application in Schottky barrier diodes (SBDs) [5]. As various defects in the crystalline structure effect on material's characteristics under the impact of different environments, having high grain boundary density

graphene composites can be influenced by the operating environment [6]. The current conduction mechanism of SBDs depends upon numerous parameters like the operating temperature of the device, barrier height inhomogeneities at MS junction, internal series resistance, functional bias voltage, process of diode preparation [7]. Moreover, there has been growing interest towards rGO-SnO₂ nanocomposite in bio sensors [8], Schottky diodes etc. [9]. The reported band gap value of rGO-SnO₂ is nearly 3.1 eV for the rutile structured SnO₂ decorated in rGO layers [10]. The performance and reliability of rGO-SnO₂ based SBD is dominated by ideality factor, Schottky barrier height (SBH), active metal semiconductor interface, density of interface states and internal series resistance at the metal-semiconductor (MS) junction [11]. For an ideal SBD, ideality factor is 1 and the barrier height is measured simply by the difference between the work function of the metal and the electron affinity of the semiconductor [12]. Barrier height (BH) influences

* Corresponding author.

E-mail address: parthap.ray@jadavpuruniversity.in (P.P. Ray).

<https://doi.org/10.1016/j.rinp.2022.105996>

Received 18 July 2022; Received in revised form 11 September 2022; Accepted 15 September 2022

Available online 16 September 2022

2211-3797/© 2022 The Authors. Published by Elsevier B.V. This is an open access article under the CC BY-NC-ND license (<http://creativecommons.org/licenses/by-nc-nd/4.0/>).



Improved device performance of rod like ZnO in a Schottky type photosensor compared to particle like ZnO: Analysis of charge transport

Mrinmay Das^{a,b}, Pubali Das^b, Joydeep Datta^b, Dhananjay Das^b, Somabrata Acharya^a, Partha Pratim Ray^{b,*}

^a School of Applied and Interdisciplinary Sciences, Indian Association for the Cultivation of Science, Jadavpur, Kolkata, 700032, West Bengal, India

^b Department of Physics, Jadavpur University, Jadavpur, Kolkata, 700032, West Bengal, India

ARTICLE INFO

Keywords:
Morphology
Schottky
Metal-semiconductor interface
Photoresponse
Space charge limited current
Charge transport

ABSTRACT

In this work, we report two different synthesis process of semiconducting ZnO which modifies the morphology of the ZnO materials and its impact in photosensing Schottky diode. Hydrothermal and co-precipitation method were used to synthesize ZnO which gave rise to rod like (ZnO HT) and particle like ZnO (ZnO COP), respectively. From UV–Vis analysis, ZnO HT exhibited greater optical absorption. Al/ZnO (HT and COP)/ITO Schottky diodes were fabricated and the photoresponse as well as diode parameters were investigated by current-voltage and capacitance voltage measurements. Then charge transport properties were determined by space charge limited current theory and impedance spectroscopy. The results showed that the ZnO HT based SBD delivered a responsivity of 0.144 A/W which is 121% higher than the responsivity showed by ZnO COP based SBD (0.065 A/W). The specific detectivity of ZnO HT was measured at 7.54×10^9 Jones, a noticeable improvement from the 4.10×10^9 Jones of ZnO COP. The carrier mobility, lifetime and diffusion length of the ZnO HT based device were found to be $0.0014 \text{ cm}^2 \text{ V}^{-1} \text{ s}^{-1}$, 72.35 μs and 72.37 μm respectively which are again superior to its counterpart. The faster and better charge transport is facilitated by the rod like morphology of the former. The study demonstrates improved device performance of rod like ZnO based Schottky diode and provides detail analysis of the Al/ZnO interface which can be beneficial for future research on metal-semiconductor junction.

1. Introduction

For a long time, zinc oxide (ZnO) has been the centre of intensive research and it continues to be so due to its optical transparency, non-toxic environment friendly nature, simple cost effective synthesis procedure and promising applications. Due to hexagonal wurtzite crystal structure and noncentro symmetry of the oxygen atom in tetrahedral coordination geometry, ZnO exhibits exciting properties [1,2]. Equipped with these favourable attributes, ZnO has been extensively used for electronic, optoelectronic, and electrochemical applications such as Schottky diodes, lasers, thin-film transistors, piezoelectric devices, light-emitting diode, photovoltaic cell and gas sensors [3–18].

Among them, metal-semiconductor Schottky barrier diodes (SBDs) are one of the most important devices for radio frequency (RF) electronics, optoelectronics, and fast switching device application. Not only that, they offer an interesting platform for material characterization [19–21]. The performance of a Schottky diode is influenced by the

material properties and especially, by the morphology of the materials. Over the past decade, application of rod like structures of ZnO has received widespread attention due to a large surface-to-volume ratio with reduced dimension [2]. Significant time and effort is being devoted for high-quality ZnO-based Schottky diode fabrication and their characterization using a variety of techniques [22–27]. The morphology of ZnO can change depending upon the synthesis technique and that change can affect its performance in a Schottky device. To have a good understanding of the metal-semiconductor interface, along with current-voltage (I–V) characteristics, capacitance-voltage (C–V) and impedance spectroscopy measurements can play a pivotal role. In addition, the analysis of charge transport from I–V and impedance spectroscopy is very important.

So, in this paper, we report the synthesis of ZnO with particle (ZnO COP) and rod like (ZnO HT) morphology by coprecipitation and hydrothermal method, respectively. Thereafter Al/ZnO SBD are fabricated and their photoresponse is compared. To investigate the Al/ZnO

* Corresponding author.

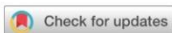
E-mail address: partha@phys.jdvu.ac.in (P.P. Ray).

<https://doi.org/10.1016/j.mssp.2021.105799>

Received 27 August 2020; Received in revised form 13 February 2021; Accepted 7 March 2021

Available online 23 March 2021

1369-8001/© 2021 Elsevier Ltd. All rights reserved.

Cite this: *New J. Chem.*, 2021, 45, 15920Received 3rd April 2021,
Accepted 26th July 2021

DOI: 10.1039/d1nj01629f

rsc.li/njc

4,4'-Bipyridine-based Ni(II)-metallogel for fabricating a photo-responsive Schottky barrier diode device†

Pubali Das,^a Santanu Majumdar,^b Arka Dey,^a Sourav Mandal,^b Atish Mondal,^b Sinchan Chakrabarty,^b Partha Pratim Ray^{*a} and Biswajit Dey^{†b}

A functionally advanced Ni(II)-metallogel (Ni-D-TA) was prepared through the sonication of nickel(II) chloride hexahydrate and 4,4'-dipyridyl and triethyl amine in an *N,N*-dimethyl formamide solvent at room temperature under ambient conditions. The rheological investigation proves the mechanical stability of the functional Ni-D-TA metallogel. FESEM microstructural analysis unveils a rock-like morphology with a self-assembled architecture of the Ni-D-TA metallogel. The optical and electrical properties of the metallogel were thoroughly examined, and the results indicate the semiconducting nature of Ni-D-TA. Electrical conductivity and photosensitivity show its capability in optoelectronic device application. Also, it is seen from the experimental studies that light irradiation endows the metallogel with better device parameters and charge transport properties. The rectification ratio increases to two-fold under illumination. This type of metallogel with photosensing Schottky behaviour advances the area of optoelectronic devices.

Issue 47, 2023

Previous

Next

From the journal:
Dalton Transactions

A dual-functional 2D coordination polymer exhibiting photomechanical and electrically conductive behaviours †

Samim Khan,^a Pubali Das,^b Sanobar Naaz,^a Paula Brandão,^c Aditya Choudhury,^d Raghavender Medishetty,^e Partha Pratim Ray^{†b} and Mohammad Hedayetullah Mir^{†a}

Author affiliations

Abstract

A photoactive two-dimensional coordination polymer (2D CP) [Zn₂(4-spy)₂(bdc)₂]_n (**1**) [4-spy = 4-styrylpyridine and H₂bdc = 1,4-benzendicarboxylic acid] undergoes a photochemical [2 + 2] cycloaddition reaction upon UV irradiation. Interestingly, the crystals of **1** show different photomechanical effects, such as jumping, swelling, and splitting, during UV irradiation. In addition, the CP was employed for conductivity measurements before and after UV irradiation *via* current density–voltage characteristics and impedance spectroscopy, which suggest that they are semiconducting in nature and can be used as Schottky diodes. Thus, this work demonstrates the potential dual applications of a 2D CP based on photosalient and conductivity properties.

In Situ Oxidation of Pyridyl-Dihydrobenzoimidazoquinazoline and the Synthesis of a Highly Luminescent Cd(II) Coordination Polymer: A Promising Candidate for Mutagenic Nitroaromatic Detection and Device Fabrication

Gurupada Bairy, Pubali Das, Basudeb Dutta, Saumitra Bhowmik, Partha Pratim Ray, and Chittaranjan Sinha*

Cite This: *Inorg. Chem.* 2023, 62, 12773–12782

Read Online

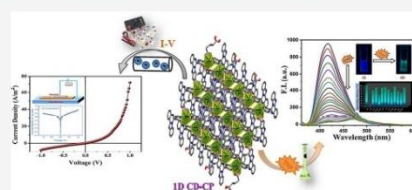
ACCESS |

Metrics & More

Article Recommendations

Supporting Information

ABSTRACT: Pyridyl-substituted imidazoquinoline, a potent fluorescent framework, is advantageous to architect multifunctional coordination networks for sensing and fabricating emergent electrical conductors. In this work, a Cd(II)-based one-dimensional (1D) coordination polymer (1D CP), $[\text{Cd}(\text{glu})_2(\text{pbiq})_2(\text{H}_2\text{O})]$, (**1**), $[\text{H}_2\text{glu} = \text{glutaric acid and pbiq} = 4-(6-(\text{pyridin-4-yl})\text{benzo}[4,5]\text{imidazo}[1,2-c]\text{quinazoline})]$, has been structurally confirmed by single-crystal X-ray crystallography. The H-bonding and $\pi\cdots\pi$ interactions built a three-dimensional (3D) supramolecular structure that strongly emits at 416 nm in acetonitrile suspension. Potentially intrusive nitroaromatics (NAs) and trinitrophenol (TNP) selectively quench the strong emission of **1**, and the highest quenching is noted in the case of TNP. A detection limit (limit of detection (LOD)) of 1.51×10^{-7} M for TNP is determined. The band gap (3.31 eV) of **1** recognizes semiconducting behavior, and an electronic device is fabricated. The correlation of current vs voltage (I - V plot) reveals a substantial non-ohmic electrical conductivity of **1** (Λ : $1.10 \times 10^{-5} \text{ S m}^{-1}$) along with a low energy barrier (Φ_B : 0.69), and the series resistance (R_s) becomes 6.21 k Ω .



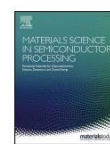
Materials Science in Semiconductor Processing 162 (2023) 107535



Contents lists available at ScienceDirect

Materials Science in Semiconductor Processing

journal homepage: www.elsevier.com/locate/mssp



Improvement of charge kinetics of MoS₂ nano-petal based Schottky device by incorporation of W: A comparative study of structural, optical, and electrical properties

Baishakhi Pal^a, Pubali Das^a, Joydeep Datta^{a,b}, Utpal Gangopadhyay^c, Partha Pratim Ray^{a,*}

^a Department of Physics, Jadavpur University, Kolkata, 700032, India

^b Department of Physics, Techno India University, Kolkata, 700091, India

^c Meghnad Saha Institute of Technology, Kolkata, 700150, India

ARTICLE INFO

Keywords:

MoS₂ and MoWS₂ nanocomposites
Schottky diode
Current density-Voltage
Charge transport parameters
Metal semiconductor junction
Impedance spectroscopy analysis

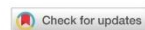
ABSTRACT

Molybdenum Tungsten Di-Sulphide is a semiconducting alloy of different TMD (transition metal dichalcogenide) materials that has enormous tunable structural, optical, and electrical attributes. In this research, we have performed the hydrothermal synthesis of Mo_{1-x}W_xS₂ nanocomposites with different molar concentration of tungsten (i.e. $x = 0, 0.1, 0.2, 0.3$) and fabricated Al/Mo_{1-x}W_xS₂/ITO structured Schottky Barrier diodes. Characterization of their structural, optical, and charge transport attributes are compared. In this alloy formation, the amount of W (tungsten) concentration has a great impact on the particle size of composites. The transportation of charges via the metal-semiconductor junction is the basis for the superiority of thin film semiconductor devices like the Schottky diode. The diode parameters as well as charge transfer characteristics were analyzed by Impedance Spectroscopy and the theory of SCLC (space charge limited current). The calculated mobility and transit time for the Mo_{0.8}W_{0.2}S₂ device are $5.65 \times 10^{-4} \text{ m}^2 \text{ V}^{-1} \text{ s}^{-1}$ and 1.59 ns respectively. These results are better than the rest of the devices. Dramatic conductivity enhancement for the Mo_{0.8}W_{0.2}S₂-based Schottky device is observed. As a result, this work not only investigates Al/MoWS₂ interface in detail but also explains the faster and better charge transport of the Mo_{0.8}W_{0.2}S₂-based device from a structural perspective.



From the journal:
CrystEngComm

Exploration of Cl \cdots Cl and $\pi\cdots\pi$ stacking contacts along with the conductivity properties of a Cu-MOF featured with paddle-wheel SBUs†



Sanobar Naaz,^a Pubali Das,^b Souvik Mukherjee,^c Samim Khan,^b Goutam Pramanik,^d Prasanta Ghosh,^b Antonio Frontera,^e Partha Pratim Ray^{*b} and Mohammad Hedayetullah Mir^{*a}

Author affiliations

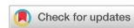
Abstract

A Cu(II)-based metal–organic framework (MOF) [Cu(muco)(3,5-DCP)]_n (**1**) has been synthesized by using linear rigid aliphatic dicarboxylic acid, *trans,trans*-muconic acid (H₂muco) and 3,5-dichloropyridine (3,5-DCP) as an auxiliary ligand. The MOF adopts a square-grid two-dimensional (2D) structure with paddle-wheel [Cu₂(OOC)₄] robust secondary building units (SBUs). The 3,5-DCP ligands are perpendicularly projected from the SBUs at both sides and undergo interdigitation *via* antiparallel $\pi\cdots\pi$ stacking interactions among 3,5-DCP ligands to fabricate three-dimensional (3D) supramolecular architecture. The $\pi\cdots\pi$ interactions favour the formation of Cl \cdots Cl stacking contacts. These non-covalent interactions are further validated by density functional theory (DFT) calculation. In addition, the synthesized MOF is tested for conductivity measurements *via* current density–voltage characteristics, as well as impedance spectroscopy, which reveal that the MOF is semiconducting in nature and can be used as a Schottky diode.



From the journal:
New Journal of Chemistry

Fabrication of Schottky barrier diodes utilizing carboxylate bridged trinuclear mixed valence cobalt(III/I/II) complexes of tetradentate N₂O₂ donor reduced Schiff base ligands†



Sudip Rhunia,^a Pubali Das,^b Snehasis Banerjee,^c Rosa M. Gornila,^d Michael G. B. Drew,^e Antonio Frontera,^b Partha Pratim Ray^b and Shouvik Chattopadhyay^{*a}

Author affiliations

Abstract

Three mixed-valence trinuclear cobalt(III)–cobalt(II)–cobalt(III) complexes, [Co^{II}{(μ-L¹)(μ-OAc)Co^{III}(OAc)}₂]}·2.67H₂O (**1**), [Co^I{(μ-L¹)(μ-OOCPh)Co^{III}(DMSO)_{0.6}(OOCPh)_{0.2}}(ClO₄)_{1.6}} (**2**) and [Co^{II}{(μ-L²)(μ-OOCPh)Co^{III}(DMSO)_{0.75}(OOCPh)_{0.25}}(ClO₄)_{1.5}} (**3**), have been synthesized using two tetradentate N₂O₂ donor 'reduced Schiff base' ligands, H₂L¹ [1,3-bis(2-hydroxybenzylamino)2,2-dimethylpropane] and H₂L² [2,2'-(1,1'-(propane-2,2-diylidimino)diethylidene)diphenol], and acetate or benzoate as anionic co-ligands. These complexes have been characterized by spectroscopic measurements and their solid state structures have been determined by single crystal X-ray diffraction analysis. The cobalt(III)–cobalt(II)–cobalt(III) skeletons of complexes **1** and **2** are linear, centrosymmetric; but in complex **3**, it is non-centrosymmetric. Both the central cobalt(II) and terminal cobalt(III) atoms are hexa-coordinated in all three complexes. The structure directing role of several noncovalent interactions in the solid state of the complexes has been investigated focusing on the H-bonding interactions mediated by the co-crystallized water molecules in **1** and the perchlorate counterions in **2** and **3**. Thermo-gravimetric analysis (TGA) provided a thermal driven



(https://www.espublisher.com/journals/id/es-materials-manufacturing)

From The Journal:

ES Materials & Manufacturing

(https://www.espublisher.com/journals/id/es-materials-manufacturing) Volume 19, 2023

(https://www.espublisher.com/journals/volumearticles/es-materials-manufacturing/2023/volume-19)

In quest of New Energy Material: 3D Mn (II)-coordination Polymer, the Schottky Device and Theoretical Interpretation

Authors

Authors and affiliations

Manik Shit, Pubali Das, Sukanya Paul, Arnab Samnta, Sk. Mohammad Aziz, Partha Pratim Ray, and Chittaranjan Sinha

Abstract

Single crystal X-ray structure of amino-isophthalato bridged Mn (II) co-ordination polymer, $\{[Mn(asp)(H_2O)](H_2O)_2\}_n$ (1) [H_2asp = 5-aminoisophthalic acid] is determined to support previously characterized structure of the polymer. The Tauc's plot obtained from UV-Visible spectra has determined the optical band gap, 2.53 eV, which corroborates the semiconducting nature. Mn(II) centre is coordinated by four carboxylate-O (one chelated carboxylate-O,O and two monodentate carboxylate-O), one H_2O and one $-NH_2$ (of asp^{2-}) to constitute MnO_5N

Inorganic Chemistry

pubs.acs.org/IC

Article

Cu(II)-Based Molecular Hexagons Forming Honeycomb-like Networks Exhibit High Electrical Conductivity

Sanobar Naaz, Pubali Das, Samim Khan, Basudeb Dutta, Sourav Roy, Antonio Frontera,* Partha Pratim Ray,* and Mohammad Hedayetullah Mir*

Cite This: *Inorg. Chem.* 2022, 61, 19828–19837

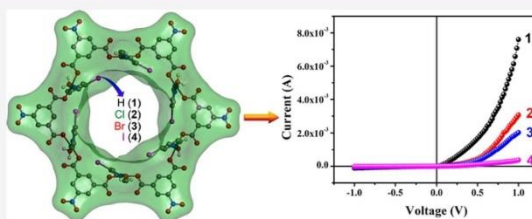
Read Online

ACCESS |

Metrics & More

Article Recommendations

Supporting Information



ABSTRACT: Four new Cu(II)-based hexagonal complexes with the metallomacrocyclic formulae $[Cu_6(5-nip)_6(3-py)_6(H_2O)_{12}]$ (1), $[Cu_6(5-nip)_6(3-Clpy)_6(H_2O)_{12}]$ (2), $[Cu_6(5-nip)_6(3-Brpy)_6(H_2O)_{12}]$ (3), and $[Cu_6(5-nip)_6(3-Ipy)_6(H_2O)_{12}]$ (4) have been synthesized using 5-nitroisophthalic acid (H_2S-nip) and pyridine (py)/3-halopyridine (3-Xpy; X = Cl, Br, and I) ligands. The structural features and supramolecular interactions of compounds 1–4 have been investigated using the single-crystal X-ray diffraction (SCXRD) technique. Interestingly, the hexagonal complexes undergo hydrogen bonding and $\pi \cdots \pi$ stacking interactions to form fascinating two-dimensional (2D) honeycomb-like structures. The synthesized complexes exhibit high electrical conductivity, arising from charge transport through space via $\pi \cdots \pi$ contacts. However, complexes containing 3-Brpy (3) and 3-Ipy (4) exhibit photosensitivity due to the presence of halogens with a larger size and lower ionization energy. The conductivity results are also in accordance with the theoretical prediction calculated by density functional theory (DFT) study.

Halogen \cdots Halogen and π -Hole Interactions in Supramolecular Aggregates and Electrical Conductivity Properties of Cu(II)-Based 1D Coordination Polymers

Published as part of a *Crystal Growth and Design* virtual special issue on Emerging Investigators 2022

Sanobar Naaz, Pubali Das, Antonio Frontera, Basudeb Dutta, Samim Khan, Partha Pratim Ray, and Mohammad Hedayetullah Mir*

 Cite This: *Cryst. Growth Des.* 2022, 22, 5189–5197

 Read Online

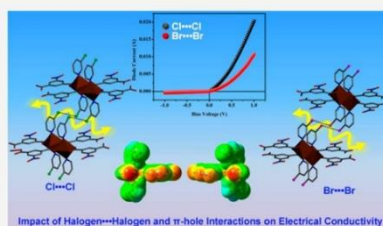
ACCESS |

 Metrics & More

 Article Recommendations

 Supporting Information

ABSTRACT: The two isostructural one-dimensional coordination polymers (1D CPs) [Cu(5-nip)(3-Clpy)₂]_n (**1**) and [Cu(5-nip)(3-Brpy)₂]_n (**2**) have been synthesized using a 5-nitroisophthalic acid (H₂5-nip) linker and the meta-substituted 3-chloropyridine (3-Clpy)/3-bromopyridine (3-Brpy) auxiliary ligands. The structural architectures and supramolecular interactions of the CPs have been investigated by single-crystal X-ray diffraction (SCXRD) and density functional theory (DFT) studies, respectively. The SCXRD study reveals that CPs **1** and **2** form a 1D double-chain structure with carboxylato-bridged cyclic secondary building units (SBUs). Interestingly, both CPs involve type I halogen \cdots halogen (X \cdots X) interactions combined with π \cdots π stacking interactions to generate a three-dimensional (3D) supramolecular network. Moreover, both CPs exhibit interesting X \cdots N π -hole interactions involving a nitro group as the electron acceptor. Both CPs show electrical conductivity in the semiconducting regime and behave as Schottky diodes. However, CP **1** has a higher electrical conductivity in comparison to CP **2**.



JADAVPUR UNIV on December 14, 2023 at 07:14:33 (UTC).
rimguidelines for options on how to legitimately share published articles.

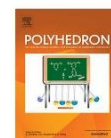
Polyhedron 201 (2021) 115159



Contents lists available at ScienceDirect

Polyhedron

journal homepage: www.elsevier.com/locate/poly



Fabrication of a halopyridine appended Co(II) based 1D coordination polymer for efficient charge transportation

Sanobar Naaz^a, Pubali Das^b, Samim Khan^a, Basudeb Dutta^a, Suvendu Maity^c, Prasanta Ghosh^d, Partha Pratim Ray^{b,*}, Mohammad Hedayetullah Mir^{a,*}

^a Department of Chemistry, Aliah University, New Town, Kolkata 700 156, India

^b Department of Physics, Jadavpur University, Jadavpur, Kolkata 700 032, India

^c Department of Chemistry, Jadavpur University, Jadavpur, Kolkata 700 032, India

^d Department of Chemistry, R. K. M. Residential College, Narendrapur, Kolkata 700 103, India



ARTICLE INFO

Article history:

Received 7 February 2021

Accepted 10 March 2021

Available online 17 March 2021

Keywords:

Co(II)

Crystal structure

Electrical conductivity

Hirshfeld surface analysis

Schottky diode

ABSTRACT

A new halopyridine appended Co(II) based coordination polymer (CP), [Co(3-clpy)₂(fum)₂(H₂O)₂]_n (**1**) [3-clpy = 3-Chloropyridine and H₂fum = fumaric acid] has been synthesized and characterized by elemental analysis and single crystal X-ray diffraction (SCXRD) technique. Compound **1** crystallizes in monoclinic space group *P*2₁/*c*. Herein, the ditopic linker H₂fum acts as bridging ligand in the formation of a one dimensional (1D) CP. The 1D chains are interconnected via hydrogen bonding interactions leading to 2D sheet. The 3-clpy ligands of one chain facilitate π \cdots π stacking interactions with adjacent chain leading to 3D supramolecular assembly which generally promotes better charge transport in the material. Hirshfeld surface analysis has also been performed to check the non covalent interactions in the crystal packing. Interestingly, the compound **1** shows electrical conductivity and reveals Schottky barrier diode behavior.

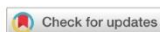
© 2021 Elsevier Ltd. All rights reserved.



From the journal:

Dalton Transactions

Electrically conductive Cu(II)-based 1D coordination polymer with theoretical insight†



Sakhiul Islam,^a Pubali Das,^b Saswati Maiti,^{cd} Samim Khan,^{de} Suvendu Maity,^e Prasanta Ghosh,^{fg} Atish Dipankar Jana,^{gh}
^{*c} Partha Pratim Ray^{gh} ^{*b} and Mohammad Hedayetullah Mir^{gh} ^{*a}

Author affiliations

Abstract

A nitro-functionalized Cu(II)-based one-dimensional coordination polymer (1D CP) [Cu(nip)(4-phpy)]_{2,n} (**1**) (H₂nip = 5-nitroisophthalic acid and 4-phpy = 4-phenylpyridine) was synthesized and characterized by elemental analysis, powder X-ray diffraction (PXRD) and single crystal X-ray diffraction (SCXRD). In the solid-state self-assembly of **1**, two sets of weak intermolecular forces, CH $\cdots\pi$ interaction among the axially bound 4-phpy ligands and $\pi\cdots\pi$ interaction among bridging nip ligands from adjacent 1D coordination polymeric chains led to 3D supramolecular packing. Interestingly compound **1** exhibited electrical conductivity in the semiconducting regime and behaved as a Schottky barrier diode.



From the journal:

New Journal of Chemistry

Two zinc(II)-based coordination polymers with flexible dicarboxylate and pyridine mixed ligands: effect of $\pi\cdots\pi$ interactions on electrical activity†

Akhtaruzzaman,^a Pubali Das,^b Samim Khan,^a Suvendu Maity,^c Sanobar Naaz,^a Sakhiul Islam,^a Prasanta Ghosh,^{de} Partha Pratim Ray,^{*b} and Mohammad Hedayetullah Mir^{gh} ^{*a}

Author affiliations

Abstract

Two novel coordination polymers (CPs) [Zn(*cis*-1,4-chdc)(4-phpy)]_n (**1**) and [Zn(*cis*-1,4-chdc)(py)]_n (**2**) (1,4-H₂chdc = 1,4-cyclohexanedicarboxylic acid, 4-phpy = 4-phenylpyridine and py = pyridine) were synthesized and characterized by elemental analysis, infrared spectroscopy, single-crystal X-ray diffraction, powder X-ray diffraction and thermogravimetric analyses. Both compounds formed a one-dimensional (1D) chain-like structure constructed by Zn₂(CO₂)₄ paddle-wheel dimers interconnected via double strands of *cis*-1,4-chdc-bridges, whereby pyridine-based ligands were decorated as arms on both sides of Zn₂ dimers. In compound **1**, polymeric 1D chains underwent self-assembly via $\pi\cdots\pi$ stacking interactions among 4-phpy ligands to form a 2D network, whereas this type of interaction was absent in **2**. Interestingly, both compounds exhibited electrical conductivity and revealed Schottky barrier diode behavior. However, compound **1** showed better electrical conductivity (1.09 $\times 10^{-3}$ S m⁻¹) with respect to compound **2** (6.01 $\times 10^{-5}$ S m⁻¹) because of $\pi\cdots\pi$ interactions.

Double advantages of 2D coordination polymer of coumarinyl-pyridyl Schiff base decorated Zn(II): The fabrication of Schottky device and Anti-carcinogenic activity

Sukanya Paul, Basudeb Dutta, Pubali Das, Satyajit Halder, Manik Shit, Partha Pratim Ray, Kuladip Jana, Chittaranjan Sinha✉

First published: 17 June 2023
<https://doi.org/10.1002/aoc.7160>

Pubali Das, Satyajit Halder, and Manik Shit contributed equally.

Abstract

A 2D coordination polymer, $[Zn_2(BDC)_4(QPR)_2(H_2O)]_n$ (**Zn(II)-CP**) ($BDC^{2-} = 1,4$ -benzenedicarboxylato; $QPR = 7$ -[[pyridin-4-ylmethylene]-amino]-chromen-2-one), is presumably the first reported on coumarinyl-pyridyl framework with terephthalato linker. The optical band gap, 2.91 eV, is obtained from the Tauc's plot that insists to fabricate an optically stimulated semiconducting device, and the electrical conductivity exhibited (Λ) is $8.07 \times 10^{-3} \text{ S m}^{-1}$ (dark) and $9.26 \times 10^{-3} \text{ S m}^{-1}$ (light). The cytotoxicity in the selected human cancer cell lines like HeLa, MDA-MB 231, and HepG2 cells in relative to the normal kidney epithelial (NKE) cell line has been examined, and its efficacy is observed highest in inhibiting proliferation of HeLa cells (IC_{50} , 21.02) compared with other cancer cells (IC_{50} : 42.22 [HepG2] and 46.37 [MDA-MB 231]). Further, the **Zn(II)-CP** possess intracellular reactive oxygen species (ROS) generation and caspase-3/7 activation leading to G2/M cell cycle arrest and apoptotic cell death in HeLa cell line. This novel coumarinyl-pyridyl ligand appended Zn(II)-CP has been employed for the fabrication of semiconducting device, which is quite impressive in view of existing energy crisis civilization; in addition, the compound has excellent bio-activity.

Materials Research Bulletin 118 (2019) 110507



Contents lists available at ScienceDirect

Materials Research Bulletin

journal homepage: www.elsevier.com/locate/matresbu



Effect of graphene on improved photosensitivity of MoS₂-graphene composite based Schottky diode

Soumi Halder^a, Baishakhi Pal^a, Arka Dey^{a,b}, Sayantan Sil^a, Pubali Das^a, Animesh Biswas^{a,c}, Partha Pratim Ray^{a,*}

^a Department of Physics, Jadavpur University, Kolkata, 700 032, India

^b Department of Condensed Matter Physics and Material Sciences, S. N. Bose National Centre for Basic Sciences, Block JD, Sec. III, Salt Lake, Kolkata, 700106, India

^c Sreegopal Banerjee College, Bagati, Mogra, Hooghly, 712148, India



ARTICLE INFO

Keywords:
 Schottky barrier diode
 MoS₂
 Current density-voltage
 Photosensitivity
 Charge transport phenomena

ABSTRACT

In this work, MoS₂ and MoS₂-Graphene (MGC) composite have been synthesized by hydrothermal process followed by their structural, optical and electrical characterization. The current density-voltage measurements have been performed at room temperature by fabricating Al/MoS₂ and/or MGC/TTO configured sandwich structured metal-semiconductor (MS) thin film Schottky devices. Under light and dark conditions, various parameters of our synthesized material based devices like rectification ratio, series resistance, barrier height, etc. have been measured and compared between the two. All the measured electrical properties show improvement for the composite based diodes, noteworthy the photosensitivity which has been increased by almost 33 times, signifying its potential application in photosensitive devices.



Contents lists available at ScienceDirect

Applied Surface Science

journal homepage: www.elsevier.com/locate/apsusc

Full Length Article

Improving performance of device made up of CuO nanoparticles synthesized by hydrothermal over the reflux method

Rajkumar Jana, Arka Dey, Mrinmay Das, Joydeep Datta, Pubali Das, Partha Pratim Ray*

Department of Physics, Jadavpur University, Kolkata 700 032, India



ARTICLE INFO

Article history:

Received 22 August 2017

Revised 14 April 2018

Accepted 28 April 2018

Available online 4 May 2018

Keywords:

CuO nanoparticles

Schottky barrier diode (SBD)

Photoresponse

Impedance spectroscopy

Electrical transport properties

ABSTRACT

In this work, we have prepared copper (II) oxide (CuO) nanoparticles (NPs) via reflux (CuO (R)) and hydrothermal (CuO (H)) methods. The electrical parameters like rectification ratio, ideality factor and barrier height were compared between two synthesized CuO NPs after fabricating Al/CuO/ITO schottky barrier diode (SBD). Under dark, rectification ratio increased by 37% for CuO (H) than CuO (R). In a similar manner, photoresponse also significantly improved by a huge 93%. Impedance Spectroscopy measurements establish that CuO (H) shows better charge transport and lower carrier recombination compared to CuO (R). The enhanced device performance of the hydrothermally synthesized CuO based schottky diode can be attributed to the reduction in lattice defect density and its good thin film properties.

© 2018 Elsevier B.V. All rights reserved.



Contents lists available at ScienceDirect

Materials Chemistry and Physics

journal homepage: www.elsevier.com/locate/matchemphys

Experimental and theoretical overview on bias dependent Debye relaxation and conduction mechanism of $\text{Cd}_{1-x}\text{Zn}_x\text{S}$ film and its significance in signal transport network

Joydeep Datta, Mrinmay Das, Arka Dey, Sayantan Sil, Rajkumar Jana, Soumi Halder, Pubali Das, Partha Pratim Ray*

Department of Physics, Jadavpur University, Kolkata, 700 032, India



HIGHLIGHTS

- Impedance Spectroscopy studies of $\text{Cd}_{1-x}\text{Zn}_x\text{S}$ ($x = 0, 0.4, 0.8$) were carried out.
- Bias dependent relaxation process and conduction mechanism of grain and grain boundary is analyzed.
- Relaxation time is derived theoretically and experimentally using deconvolution and simulation.
- Electrical modulus and ac conductivity is discussed for conduction mechanism.
- The improvement in conductivity is found for $\text{Cd}_{0.6}\text{Zn}_{0.4}\text{S}$.

ARTICLE INFO

Article history:

Received 3 November 2017

Received in revised form

21 February 2018

Accepted 24 March 2018

Available online 6 April 2018

Keywords:

Nanostructured materials

Impedance spectroscopy

Grain and grain boundary relaxation

Electronic circuit

Bias dependent AC conductivity


ABSTRACT

In this literature, bias dependent relaxation and conduction mechanism of grain and grain boundary of $\text{Cd}_{1-x}\text{Zn}_x\text{S}$ ($x = 0, 0.4, 0.8$) are discussed with the help of impedance spectroscopy. To get the insight of relaxation and conduction significance in signal transport network, we have simulated the experimental impedance value with appropriate circuit. The simulation provides bias dependent grain and grain boundary resistance and capacitance. It shows that the resistance of grain and grain boundary decreases with the increase in bias and is found to be lesser for $\text{Cd}_{0.6}\text{Zn}_{0.4}\text{S}$. Using various models we have found that the crystallite size of $\text{Cd}_{0.6}\text{Zn}_{0.4}\text{S}$ is lowest with respect to the other samples and exhibits lower grain and grain boundary resistance with better relaxation. We have tried to correlate the bias dependent grain and grain boundary conduction mechanism with crystallite size using Mandurah model. So, this literature has tried to enlighten the bias dependent relaxation and conduction behavior of $\text{Cd}_{1-x}\text{Zn}_x\text{S}$ and the impact of grain and grain boundary in the signal transporting network.

© 2018 Elsevier B.V. All rights reserved.



Gaussian Distribution of Inhomogeneous Barrier Height of Al/ZnS/ITO Schottky Barrier Diodes

Arka Dey, Rajkumar Jana, Joydeep Dhar, Pubali Das, Partha Pratim Ray  

Show more 

 Share  Cite

<https://doi.org/10.1016/j.matpr.2017.10.193> 

[Get rights and content](#) 

Abstract

The current–voltage (I–V) measurements on Al/ZnS Schottky barrier diodes in the temperature range 303 – 423 K by the step of 15 K were carried out. The forward I–V characteristics were analyzed on the basis of the thermionic emission theory. The temperature dependence I–V parameters such as ideality factor (n) and barrier height (ϕ_{b0}) have been explained on the basis of inhomogeneity. An abnormal increase of apparent barrier height and decrease of ideality factor with increasing temperature have been explained due to the barrier height inhomogeneities on the basis of the thermionic emission theory with Gaussian distribution. Experimental results reveal the existence of a single Gaussian distribution with apparent barrier height value ($\overline{\phi_{b0}}$) of 1.091 eV and standard deviations (σ_s) of 0.18 V. Richardson constant (A^*) was obtained as $8.49 \times 10^{-2} \text{ A.m}^{-2}\text{K}^{-2}$ from the $\ln(I_0/T^2)$ vs. q/kT plot, which is far from the calculated value of $5.6 \times 10^5 \text{ A.m}^{-2}\text{K}^{-2}$. The modified Richardson plot of $\ln(I_0/T^2) - (q^2\sigma_s^2/2k^2T^2)$ gives $\overline{\phi_{b0}}$ and A^* values as 1.093 eV and $6.07 \times 10^5 \text{ A.m}^{-2}\text{K}^{-2}$, without using the temperature coefficient of the barrier height. This obtained value of A^* is extremely close to the previously calculated value. So, the temperature dependence of the forward bias I–V characteristics of the Schottky device can be successfully explained on the basis of the thermionic emission mechanism with a single Gaussian distribution of the barrier heights.